Molybdenum speciation and phase associations across redox environments

Jennifer Rodley

Submitted in accordance with the requirements for the degree of Doctor of Philosophy

The University of Leeds

School of Earth and Environment

September 2020

The candidate confirms that the work submitted is her own, except where work which has formed part of jointly authored publications has been included. The contribution of the candidate and the other authors to this work has been explicitly indicated below. The candidate confirms that appropriate credit has been given within the thesis where reference has been made to the work of others.

The work presented in Chapter 3 of this thesis forms a jointly authored publication currently in preparation.

Candidate's contribution (J Rodley) – developed and tested the sequential extraction method, prepared and analysed synthetic minerals for use in experiments, conducted sorption experiments, collected and analysed XANES, interpreted data, prepared the manuscript; S. W. Poulton – formed the initial concept , aided with method development; aided in data interpretation, commented on the manuscript; C. L. Peacock – aided with method development, aided in data interpretation; aided with collection and analysis of XANES; J. F. W. Mosselmans – aided with collection of XANES; T. Goldberg – collected and supplied the Aarhus Bay samples that formed part of the method testing and provided Fe speciation, Mn, porewater, and total organic carbon (TOC) data for them; H. Brumsack – collected and supplied the Demerara Rise 1258 samples that formed part of the method testing; C. März – collected and supplied the Demerara Rise 1261 samples that formed part of the method testing; Y. Xiong – collected and supplied the Lake Cadagno samples that formed part of the method testing and provided Fe speciation, total Mo and TOC data for them; S. Reid – ICP-MS analysis; F. Bowyer – Fe speciation, Fe total digests and TOC analysis.

The work presented in Chapter 4 of this thesis forms a jointly authored publication currently in preparation.

Candidate's contribution (J Rodley) – developed the initial concept, prepared and analysed synthetic minerals, conducted sorption experiments; conducted Mo sequential extraction and pyrite removal experiments, developed the micro-thin section preparation technique, prepared samples for XANES, collected and analysed XANES, interpreted data, prepared the manuscript; C. L. Peacock – aided with development of the initial concept, aided with collection and analysis of XANES, commented on the manuscript; J. F W. Mosselmans – aided with the collection and analysis of XANES, commented on the manuscript; S. W. Poulton – collected and supplied the Lake Cadagno samples; R. Guilbaud – collected and supplied the Golfo Dulce sample; Y. Xiong – collected and supplied the Lake Cadagno sample.

The work presented in Chapter 5 of this thesis forms a jointly authored publication currently in preparation.

Candidate's contribution (J. Rodley) – developed the initial concept, prepared samples for XANES, collected and analysed XANES, interpreted data, prepared the manuscript; C. L. Peacock – aided in collection and analysis of XANES, aided with data interpretation, commented on the manuscript; J. F. W. Mosselmans – aided in collection of XANES; M. Krom – collected and supplied the Eastern Mediterranean sample; T. Goldberg – collected the and supplied the Aarhus Bay samples and provided Fe speciation, Mn, Al, porewater, total digest and TOC data for it; R. Guilbaud – collected and supplied the Golfo Dulce samples and provided Fe speciation and TOC data for them; J. Thompson – collected and supplied the Lake La Cruz samples and provided iron speciation, porewater, total digest and TOC data for them; Y. Xiong – collected and supplied the Lake Cadagno samples and provided iron speciation, porewater, total digest and TOC data for them; F. Bowyer – Fe speciation, Fe total digests and TOC analysis.

The work presented in Chapter 6 of this thesis forms a jointly authored publication currently in preparation.

Candidate's contribution (J. Rodley) – developed the initial concept, Mo sequential extraction experiments, prepared samples for XANES, collected and analysed XANES, interpreted data, prepared the manuscript; S. W. Poulton – aided in data interpretation, commented on the manuscript; C. L. Peacock – assisted with collection and analysis of XANES, aided with data interpretation; T. Goldberg – collected and supplied the Aarhus Bay samples and provided Fe speciation, Mn, Al, Mo isotope, porewater, total digest and TOC data for them.

Acknowledgements

I would like to begin by thanking my supervisor, Caroline Peacock for her endless support and encouragement, for convincing me to carry on when I was ready to give in and for sharing her incredible experience of synchrotrons and the associated intricacies like cafeteria times and locations of the best-stocked vending machines. Her own incredible successes during my PhD have been inspirational I'd also like to thank my other supervisors, Simon Poulton and Fred Mosselmans who have shared their immense wealth of knowledge with me, often after weeks of lab work that have left me feeling more confused than when I started. I must thank the exceptional Lab Manager and technicians at the University of Leeds, Andy Connelly, Stephen Reid, Harri Wyn Williams, Fiona Keay and Lesley Neve, who have helped immensely throughout the development of my research. My thanks go to Tina Geraki at Diamond Light Source who has gone out of her way to help me understand the scientific concepts that felt unfathomable and also to Steve Keylock at Diamond who made my thoughts and sketches a reality. Thank you to members of the Cohen Geochemistry Group who have helped during lab disasters, equipment failures, and general head-scratching moments, I also feel compelled to mention Jane Francis who convinced me from being a University PA teaching myself A Level Geology at home, to an undergraduate at the University, that I could go as far as doing a PhD, which to me had been unimaginable

I'd like to thank my family, especially my mum, who have been very understanding when I've had to cancel plans or lock myself away in my office and for being there at the last minute when I've found myself with free time. My friends in the University Veg Society, particularly Ellie Craig, have been wonderful at providing me with a much-needed distraction from all things molybdenum (mainly with food) and giving me a safe space to vent. My good friend Dorota Karasek has been a constant source of support in all kinds of ways and has been

boundless in her encouragement and understanding. I can't forget Jeff Dawson, my Blewbury landlord who became a friend while I worked at Diamond Light Source, as he introduced me to Pimms o'clock! Thank you also to my current manager, Sarah Burdall, for being so understanding about my need for last-minute annual leave to finish chapters and for being a shoulder when I've needed it.

Finally, my wonderful fiancé, Adrian Bisset, despite being able to use the time to watch sports, has been abandoned for too long. I'd like to thank him for encouraging me to come into my office day after day when I'd lost my motivation, for doing more than his share of the house and garden jobs, for finding weird and wonderful ways to keep my spirits up, and for keeping me fed! Our life is about to be very different!

To everyone who has been part of my life during this adventure, thank you, thank you thank you.

Abstract

Molybdenum (Mo) concentrations and isotopic compositions in marine sediments are commonly used as palaeoredox proxies, where high concentrations and heavy isotopes indicate deposition beneath a euxinic water column, while low concentrations and light isotopes indicate deposition beneath an oxic water column. X-ray absorption near edge spectroscopy (XANES) is also used to examine Mo phase associations in sediments and experimental sorption studies. However, there remains an incomplete understanding of Mo sequestration pathways in sediments and of Mo phase associations across redox environments. This precludes the Mo proxy from identifying intermediate redox environments, including ferruginous conditions, important in Earth history. To address these unknowns and eventually extend application of the Mo proxy, a novel Mo sequential extraction method has been developed to identify how Mo is partitioned in sediments, by targeting operationally defined sedimentary Mo pools. A Mo XANES library of standards was also developed to complement sequential extraction and provide an additional means of identifying Mo phase associations and speciation in sediment samples. These two techniques were used to investigate Mo in sediments deposited under known redox conditions, independently and in combination with Fe speciation and Mo isotopes.

Results indicate that Mo does not follow a unique sequestration pathway in sediments deposited beneath oxic, nitrogenous, ferruginous or euxinic water columns and highlight the importance of Fe (oxyhydr)oxides for Mo sequestration under oxic and euxinic waters. Mo sequestration to magnetite is also observed in all four environments and this Mo pathway is under-represented in the literature. XANES show that Mo can become fully thiolated in sulfidic porewaters beneath oxic water columns, as well as during sequestration beneath euxinic water columns. Mo isotopes from sediments beneath oxic waters are also shown to

reach seawater values, which could be misinterpreted as indicating deposition in a euxinic setting. Results underline the requirement for multiple redox proxies when reconstructing palaeo-environments.

Table of contents

Table of figures

Table of tables

Chapter 1 Introduction

This introductory chapter provides context for the research and an overview of molybdenum (Mo) in terms of its general chemistry and uses. Current understanding of Mo and its behaviour in marine sediments is outlined, particularly with respect to its use as a palaeoredox proxy. Aims and objectives of the research are then given before the thesis structure provides an overview of each data chapter.

1.1 Background context

1.1.1 Redox history of the oceans

The fossil record shows that the Earth has provided the chemical environments required for life to evolve and thrive, but changes in these critical chemical conditions may also have negatively impacted and impeded evolution. For example, the evolution of the first large multicellular heterotrophic eukaryotes (the Ediacaran fauna) did not occur until ~580 million years ago (Ma) following an ocean oxygenation event at the end of the Gaskiers Glaciation (Canfield et al., 2007) and since this early appearance of animals, the evolutionary record has been punctuated by five major, and numerous minor extinction events. These extinctions and evolutionary progress are strongly connected with other Earth system processes and therefore an understanding of the redox history of the Earth's oceans, which ultimately influences the atmosphere and biosphere, is critical to elucidating these links.

Although the modern oceans are predominantly oxic, alternative redox environments such as nitrogenous (nitrite accumulation in the water column), ferruginous (anoxic and non-sulfidic) and euxinic (anoxic and sulfidic), exist in some areas and it is reasonable to suggest that these environments also existed in the past. Through the development of a range of geochemical proxies, evidence from the rock record shows that ocean chemistry has changed throughout

geological time, switching between euxinic, ferruginous and oxic conditions on a local and global scale (Anbar and Knoll, 2002; Canfield et al., 2007; Canfield et al., 2008; Dahl et al., 2011; Guilbaud et al., 2015; Kendall et al., 2010; Poulton et al., 2004; Poulton and Canfield, 2011). Marine sedimentary rocks can preserve geochemical indicators of redox conditions at the time of their deposition and a large amount of research has already identified ancient redox conditions using techniques such as trace metal concentrations (e.g. Kendall et al., 2010; Wirth et al., 2013), iron speciation (e.g. Guilbaud et al., 2015; Poulton et al., 2004), total organic carbon concentrations (e.g. Canfield et al., 2007; Dahl et al., 2011), and various isotopic compositions (e.g. Anbar and Knoll, 2002; Archer and Vance, 2008) recorded in these rocks. This research has revealed a complex ocean redox history that has changed on local and global scales between euxinic, ferruginous and oxic conditions (Figure 1.1).

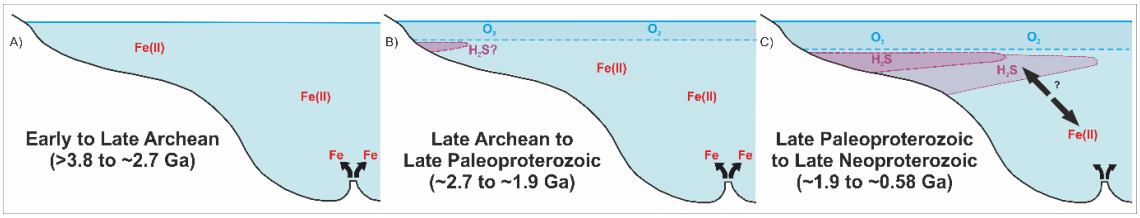

Figure 1.1 *A cartoon showing the evolution of redox conditions during the Precambrian: A) ferruginous oceans dominate throughout most of the Archean; B) between the late Archean and Late Palaeoproterozoic transient, spatially restricted euxinic conditions develop below oxygenated surface waters in continental margin/slope settings but the deep ocean remains ferruginous; C) coastal euxinic conditions extend at least 100 km from the palaeoshoreline from ~1.9 Ga, titrating Fe(II) from the ferruginous water column which continues to dominate the deep oceans (after Poulton and Canfield, 2011).*

Early Earth oceans were characterised by predominantly ferruginous conditions at depth with some euxinic areas/periods (Canfield et al., 2008; Poulton et al., 2004). The widespread deposition of banded iron formations (BIFs) is indicative of ferruginous oceans during the Archean and shows that iron (Fe) was present in the water column (Holland, 2006). Had deep waters been sulfidic, this iron would have formed, and been deposited as, pyrite rather than

the Fe (hydr)oxides observed in BIFs. Ferruginous conditions extended into the Palaeoproterozoic, ending ~1.8 Ga when global BIF deposition ceased (Poulton et al., 2004). At this time productive continental margins are believed to have been oxygenated to depths of several hundred metres (Kendall et al., 2010) and this is supported by evidence from the fossil record which shows photosynthetic eukaryotes were restricted to shoreline environments (Anbar and Knoll, 2002; Javaux et al., 2001). Although a transition to euxinic conditions is indicated during the mid-Proterozoic (Poulton et al., 2004), Poulton et al. (2010) and Poulton and Canfield (2011) suggest that a sulfidic wedge began to develop beneath oxygenated surface waters at continental margins ~2.7 Ga creating layered redox conditions at these locations. Although this sulfidic wedge may have extended >100 km from the palaeoshoreline, the deep ocean remained ferruginous. The sulfidic wedge was sufficient for pyrite deposition in these environments, documenting euxinic conditions in the geological record. At the Meso-Neoproterozoic boundary ~1 Ga, a global change from euxinic to ferruginous mid-depth waters occurred, possibly as a result of the peneplanation of Rodinia which promoted chemical weathering over physical weathering, increasing the flux of highly reactive Fe relative to sulfate (Guilbaud et al., 2015). This change affected the entire ocean with ubiquitous ferruginous conditions (below the oxycline) throughout the early Neoproterozoic, effectively removing the sulfidic wedge at continental margins. Guilbaud et al. (2015) also suggest that this switch from euxinic to ferruginous conditions promoted eukaryotic evolution as the oceans no longer contained toxic sulfide levels. These ferruginous conditions appear to have continued until the terminus of the Gaskiers Glaciation ~580 Ma. Canfield et al. (2007) used a range of geochemical proxies (Fe speciation, total organic carbon, pyrite sulfur concentrations and the isotopic composition of sulfur) to suggest that the Gaskiers glaciation ~580 Ma was a critical event in oxygenating the ocean. Their data indicate that during the glaciation the oceans were predominantly ferruginous but immediately following the glacial terminus, the oceans became oxygenated to a level that enabled Ediacaran biota to evolve. They further

suggest that the glacial melting increased oceanic nutrient loads stimulating primary production and therefore carbon burial which caused an increase in atmospheric oxygen levels.

Although a great deal of progress has been made in understanding the redox history of the oceans and how this has affected the atmosphere and biosphere, uncertainties remain regarding the spatial and temporal extent of redox conditions. It is therefore necessary to continue to develop and refine palaeoredox proxies that can address these uncertainties.

1.1.2 Molybdenum as a palaeoredox proxy

Mo is ideal as a palaeoredox proxy due to its bimodal behaviour in different redox environments and it has been used extensively in terms of its bulk concentration in sediments (e.g. Adelson et al., 2001; Hetzel et al., 2009; März et al, 2009) and isotopes (e.g. Chen et al., 2015; Dahl et al., 2010a; Poulson et al., 2006). Under oxic conditions, Mo exists as the molybdate anion (MoO_4) which may adsorb to Mn and Fe (oxyhydr)oxides in the water column. These particulates are then delivered to sediments but MoO_4 is released in anoxic porewaters and diffuses back into the water column resulting in generally low sediment Mo concentrations with upper sediment enrichments reflective of Mo cycling.

However, as waters become sulfidic, MoO_4 undergoes a series of sulfidation steps via a series of thiomolybdates (MoO_xS_{4-x}) towards the Mo sulfidic endmember, tetrathiomolybdate (MoS_4). These thiomolybdates are highly reactive and likely adsorb to Fe minerals and organic matter (Bostick et al., 2003; Coveney and Glascock, 1989; Tribovillard et al., 2004).

This bimodal behaviour leads to high Mo concentrations in euxinic environments and low concentrations in oxic environments, a feature that is recorded in sediments making it a useful

tool for identifying these chemical conditions. However, it is currently not used to identify ferruginous or indeed nitrogenous environments and little research has been done into Mo cycling in these settings.

1.2 Molybdenum Overview

1.2.1 Molybdenum in the environment

Molybdenum is ubiquitous in the environment with concentrations the upper crust of ~1-2 ppm (Taylor and McLennan, 1985). Mo is readily solubilised under oxidative weathering and levels in soils are ~1-2 ppm (Barceloux and Barceloux, 1999). Riverine Mo concentrations are highly variable with average estimates for world rivers at ~0.42 µg/L but much higher values in China (up to 20 µg/L) and India (up to 8.6 µg/L) compared to lower reported values from rivers in France (0.05-2.15 µg/L; Smedley and Kinniburgh, 2017, and references therein). Mo is also an essential component of nitrogenase which is essential to nitrogen-fixing organisms (George et al., 2007), a cofactor in over 60 enzymes (Stiefel, 1977) and an essential trace element for human health (National Academy of Sciences, 1989). It is the most abundant trace metal in the oceans (~105 nM; Collier, 1985) and, as a redox-sensitive element, has excellent potential as a palaeoredox but an incomplete understanding of its mechanistic behaviour in the water column and in marine sediments limits its use as a palaeoredox tool for 'intermediate' ocean redox states (e.g. ferruginous) which have likely dominated ocean redox throughout much of Earth history.

As mentioned, Mo is an important element in the biological fixation of nitrogen as the FeMo cofactor in the MoFe protein that forms nitrogenase (George et al., 2007). This enzyme catalyses the reduction of dinitrogen (N_2) to biologically available ammonium (NH_4) and this has been the driver for the bioavailability of nitrogen since early Earth history (Boyd, at al.

2015). There exists the potential for Mo nitrogenase to be made inactive by oxygen but gene recruitment in bacteria has resulted in the development of a number of strategies to protect from this, including temporal decoupling, spatial decoupling and metabolic decoupling (Boyd et al., 2015). These strategies facilitate exploitation of oxic environments which would otherwise be uninhabitable in terms of the bioavailability of nitrogen. It is possible, in Mo-limited environments for vanadium or Fe to substitute for Mo in the protein structure but this is rare and is strongly regulated by the abundance of Mo. X-ray absorption spectroscopy (XAS) studies suggest that Mo is present in nitrogenase as a Mo-Fe-S cubane believed to be [$MoFe_3S_4$] (George et al., 2007). X-ray absorption near-edge structure (XANES) studies suggest that Mo is surrounded primarily by sulfur ligands with no Mo=O bonds present (Cramer et al., 1978).

Although the principal Mo ore is molybdenite (MoS_2), several forms of Mo occur naturally as wulfenite ($PbMoO_4$), powellite ($Ca(MoW)O_4$) and ferrimolybdite ($Fe_2MoO_3O_{12}.8H_2O$) with generally all Mo mined from hydrothermal deposits and the majority of Mo mined in China (Braithwaite, 1994; Brown et al., 2020). The physical properties of Mo (high melting point, high density and thermal conductivity) make it an ideal component in metal alloys as it increases hardness, strength (including at elevated temperatures), weldability and corrosion resistance and this is its main commercial use (Figure 1.2; International Molybdenum Association, 2018). Mo is particularly important for stainless steels in improving corrosion resistance and is used in ferritic, austenitic and duplex grade steels in industries such as automotive, shipbuilding, aircraft and aerospace; drilling, mining and processing; energy generation; and chemical and petrochemical processing (International Molybdenum Association, 2018). Alloy manufacture dominates Mo use, but recognition of its essential role in nitrogenase led to its addition to commercial fertilisers to improve crop health and yields (International Molybdenum Association, 2018). ^{99}Mo is a fission product used to generate

^{99m}Tc used for imaging in nuclear medicine (Smedley and Kinniburgh, 2017 and references therein).

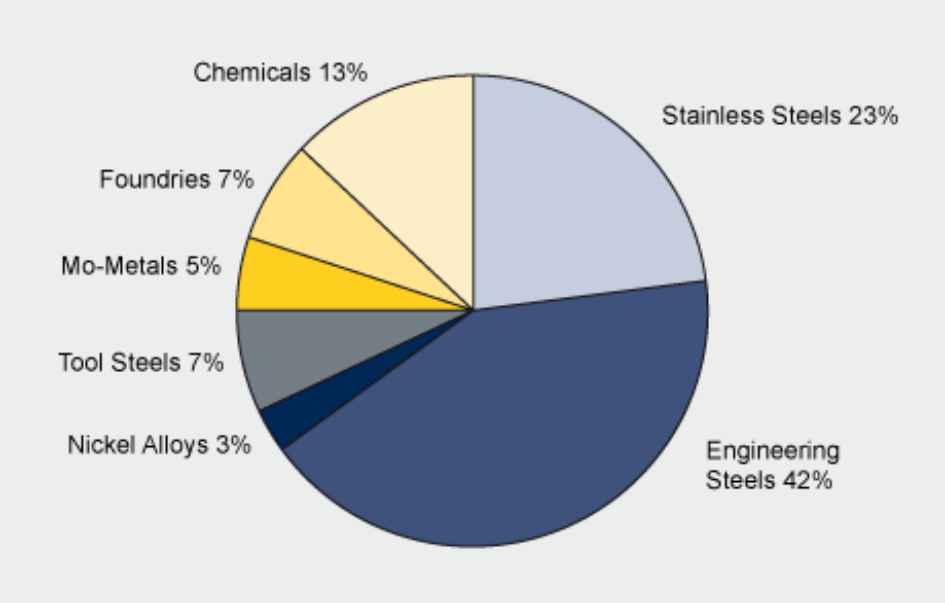

Figure 1.2 *Main uses of Mo produced from mine ore as at 2018 (International Molybdenum Association, 2018).*

1.2.2 Molybdenum geochemistry

Mo is number 42 in the periodic table with an electron configuration of [K]4d^{5}5s^1, with 4d, 5s and 5p valency orbitals and six valency electrons available for chemical bonding (Green, 1994). It is a Group VI transition metal in the 4d-block between niobium and technetium, with an atomic weight of 95.94 g/mol. Identified by Carl Wilhelm Scheele in 1778, Mo was later shown to have five oxidation states from Mo(II) to Mo(VI) with the most predominant species existing as Mo(IV) and Mo(VI) (Barceloux and Barceloux, 1999). The most common species in oxic waters is the conservative tetrahedral molybdate anion, Mo(VI)O_4^{2-} which is generally cycled between the sediments and water column via adsorption to and reductive release from Mn and Fe (oxyhydr)oxides (Figure 1.6). While this species is prevalent at pH >5, below pH 5, protonated species such as $HMoO_4^-$ and H_2MoO_4 (molybdic acid) become important (Anbar,

2004) and experimental work on adsorption of MoO_4 to goethite showed that at pH 3-4 Mo exists as polymer species such as $HMo_7O_{24}^{5-}$, $H_2Mo_7O_{24}^{4-}$ and $H_3Mo_7O_{28}^{3-}$ (Arai, 2010). Mo is highly mobile in oxidising fluids and is therefore easily transferred to solution during oxidative weathering (Anbar, 2004). Once in the oxic ocean, Mo is relatively unreactive, leading to a long residence time of 800 kyr (Morford and Emerson, 1999). Within the transition elements, Mo lies between oxophilic transition elements such as yttrium and zirconium and transition elements that show a preference for sulfur over oxygen such as rhodium and palladium and Mo does also have a high affinity for sulfur ligands (Green, 1994). This is evident in euxinic waters where tetrathiomolybdate ($Mo(VI)S_4$) dominates and is the end-product of a series of sulfidation steps. These sulfidation steps convert MoO_4 to MoS_4 via the substitution of oxygen with sulfur in the Mo tetrahedra ($MoO_4 \rightarrow MoO_3S \rightarrow MoO_2S_2 \rightarrow MoOS_3 \rightarrow MoS_4$) (Figure 1.3).

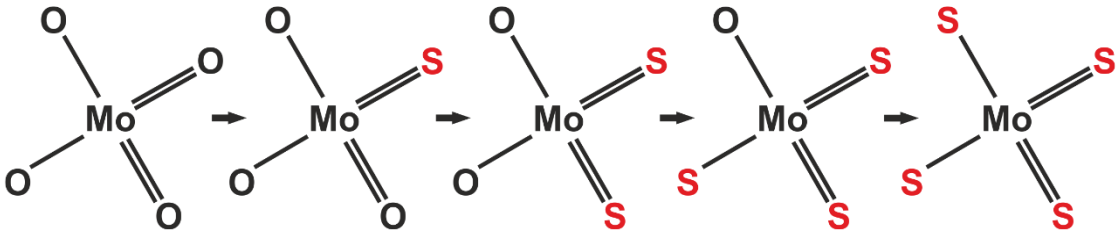

Figure 1.3 *Chemical structure of molybdate and tetrathiomolybdate showing intermediate thiomolybdates (after National Center for Biotechnology Information, 2004).*

1.3 Molybdenum behaviour in different minerals and organic matter

Mo sorption to minerals and organic matter has been widely investigated for both MoO_4 and MoS_4 (e.g. Bibak and Borggaard, 1994; Bostick et al., 2003; Xu et al., 2006). pH plays an important role across adsorbents as Mo adsorbs at lower pH but then sorption at higher pH rapidly decreases, displaying a reverse adsorption curve. The point at which sorption begins to decrease is dependent on factors such as the sorbent, Mo concentrations and the presence of any competitive anions (Goldberg and Forster, 1998; Gustafsson, 2003). For example,

Gustafsson (2003) found that where phosphate is present during Mo adsorption to ferrihydrite, the adsorption envelope shifts by ~2 pH units negatively showing a decrease in sorption from pH 4. The predominant Mo species in oxic waters is MoO_4 but at low pH (pH <4) experimental work suggests that HMo_4 and HMo_3O_7 take over as the dominant Mo species (Arai, 2010; Bibak and Borggaard, 1994). Water column chemistry also plays an important role in the reactivity of Mo. In oxic waters molybdate behaves conservatively but as sulfide concentrations increase, Mo is transformed to thiomolybdates and becomes highly reactive (Helz et al., 1996).

1.3.1 Mn (oxyhydr)oxides

Shimmield and Price (1986) suggested that Mn (oxyhydr)oxides play an important role in the cycling of Mo in oxic environments by identifying a constant ratio for Mo/Mn of 0.002 in sediments and ferromanganese nodules and Dahl et al. (2013a) suggest that Mo enrichments in Mn-nodules are very high (up to 300-700 ppm) as a result of their slow formation. A Mn-shuttle is the proposed as one of the dominant mechanisms for delivering Mo to sediments in oxic environments (Kashiwabara et al., 2009; Scott and Lyons, 2012, Shimmield and Price, 1986; Tribovillard, 2006). In this shuttle, MoO_4 adsorbs to Mn (oxyhydr)oxides in the water column where it is eventually transported to the sediments (Figure 1.6). When the Mn (oxyhydr)oxides come into contact with anoxic porewaters Mn^{4+} is reduced to Mn^{2+}, releasing Mo which then diffuses back into the water column where it eventually adsorbs to Mn (oxyhydr)oxides again and the process is repeated. This Mn-shuttle results in transient surface sediment Mo enrichments (Adelson et al., 2001; Scott and Lyons, 2012) but as the Mo ultimately diffuses back into the overlying water column, Mo is not generally sequestered to sediments unless it is transformed to more reactive thiomolybdates in sulfidic porewaters. However, high Mo concentrations associated with Mn (oxyhydr)oxides have been observed with turbidite deposition which prevents oxygen diffusion to the sediments below it (McKay

and Pederson, 2014). It is suggested that the sediments below the turbidite become anoxic and high levels of organic matter promote bacterial sulfate reduction (BSR) which converts molybdate to highly reactive thiomolybdates that are easily sequestered from porewaters. Scholz et al. (2013) also suggest the Mn-shuttle may be an important factor for Mo enrichments in stratified water columns where Mo adsorbed to Mn-(oxyhydr)oxides is transported from oxic upper layers to the euxinic part of the water column where it is transformed to thiomolybdates in the presence of sulfide. These thiomolybdates are then sequestered to other minerals and become concentrated in sediments. Scholz et al. (2013) suggest that this may have been an important Mo pathway for Precambrian euxinic wedge environments proposed by Poulton and Canfield (2011). This is supported by Cheng et al. (2016) who interpret good linear relationships between Mn and high Mo/U ratios in Cambrian shales as the product of the Mn-shuttle operating at the margins of the euxinic wedge.

As with Mo adsorption to other minerals, pH plays an important role. Studies of MoO_4 adsorption to birnessite show that maximum adsorption is at pH 3 and decreases to near zero at pH 10 (Matern and Mansfeldt, 2015). These authors also showed that the presence of competitive anions can affect MoO_4 adsorption, with selenite (SeO_3^{2-}), reducing adsorption by up to 50% and phosphate (PO_4^{3-}), reducing adsorption by up to 40%. Sulfate (SO_4^{2-}), however, has a negligible effect on adsorption.

It was initially suggested that this adsorption process required a Mo reduction step (Shaw et al., 1990; Shimmield and Price, 1986), but subsequent XAS studies have indicated that Mo is not reduced during adsorption and remains as Mo(VI) (Kashiwabara et al., 2009; Scott and Lyons, 2012; Shimmield and Price, 1986; Tribovillard, 2006). Although Matern and Mansfeldt (2015) suggest that MoO_4 adsorption to birnessite should form an outer-sphere complex,

Kashiwabara et al. (2009) used XAS (specifically XANES) to propose that Mo forms an octahedrally coordinated inner-sphere complex on δMnO_2 with distorted symmetry.

1.3.2 Fe (oxyhydr)oxides

In oxic environments, MoO_4 adsorption to Fe (oxyhydr)oxides follows the same pathway as MoO_4 adsorption to Mn (oxyhydr)oxides and this is commonly known as the Mn and Fe shuttle (Cheng et al., 2016; Scholz et al., 2013). MoO_4 is delivered to sediments by adsorption to Fe (oxyhydr)oxides in the oxic water column. These Fe (oxyhydr)oxides are reduced in sulfidic porewaters, releasing Mo which then diffuses back into the water column. Cheng et al (2016), and Scholz et al. (2013) suggest this may also be important in the delivery of Mo to euxinic sediments above a euxinic wedge.

Following studies of the Peruvian continental margin with nitrogenous conditions in the water column which show coincident Fe and Mo enrichments in the water column and co-variation in porewaters, Scholz et al. (2017) propose that the Fe (oxyhydr)oxide shuttle is important in these environments to a greater extent that the Mn (oxyhydr)oxide shuttle. The authors suggest that Fe^{3+} is reduced in sulfidic porewaters, releasing any adsorbed Mo which is then transformed to thiomolybdates and retained in the sediments by Fe sulfides. Fe^{2+} then diffuses back into the overlying nitrogenous water column where it is oxidised with nitrate as a terminal electron acceptor and readsorbs MoO_4 in the water column again.

pH plays an important role in the adsorption of Mo to Fe (oxyhydr)oxides with increased adsorption at lower pH (Bibak and Borggaard, 1994; Gustafsson, 2003). Adsorption experiments for MoO_4 on ferrihydrite show that adsorption begins to decline from ~pH 6-7 (Gustafsson, 2003). The adsorption envelope is shifted negatively in the presence of PO_4^{2-} as MoO_4 is outcompeted for adsorption sites (Gustafsson, 2003).

Extended X-ray absorption fine structure (EXAFS) and XANES studies of Mo adsorption to ferrihydrite indicate this occurs by the tetrahedral adsorption of the molybdate anion, forming a weak outer-sphere complex with no Mo-Fe bonding and the nature of this bonding means that it is easily desorbed (Brinza et al., 2015; Das et al., 2016; Kashiwabara et al., 2009). These findings are in agreement with Gustafsson and Tiberg (2015) who support a tetrahedrally coordinated outer-sphere molybdate complex on ferrihydrite. Gustafsson and Tiberg (2015) further propose that Mo is adsorbed to ferrihydrite principally as an edge-sharing bidentate complex. Gustafsson and Tiberg (2015) and Kashiwabara et al. (2009) also use XAS studies to show that Mo is adsorbed to ferrihydrite as Mo(VI), indicating that a reduction step is not necessary for this process.

1.3.3 Crystalline Fe oxides

Mo adsorption to crystalline Fe oxides has been investigated in terms of the effect of pH, the presence of competitive anions, particle concentration, ionic strength and temperature (Arai, 2010; Bibak and Borggaard, 1994; Goldberg and Forster, 1998; Xu et al., 2006). Of these factors, pH has the strongest influence on Mo adsorption with some effect from PO_4^{3-} competition but the remaining factors showed little effect. As with adsorption to other minerals, MoO_4 and MoS_4 adsorption to goethite decreases with increasing pH with maximum adsorption (100%) observed at pH 4 for MoO_4 and pH 3-6 for MoS_4 with decreasing adsorption for both Mo species at pH >6 (Xu et al., 2006). The same study indicates that PO_4^{3-} competes with MoO_4 and MoS_4 for sorption sites, outcompeting MoO_4 to a greater degree, suggesting that MoS_4 likely forms stronger complexes. However, no competition from SO_4^{2-} and very little from SiO_4^{2-} was observed. Adsorption studies by Das and Hendry (2013) indicate that MoO_4 is adsorbed to hematite as a strong inner-sphere complex and it is therefore likely that both MoO_4 and MoS_4 adsorb to crystalline Fe oxides as inner-sphere complexes which would likely prevent desorption.

Das and Hendry (2013) and Das et al. (2016) investigated the adsorption of MoO_4 to hematite to determine sorption mechanisms. The authors propose that MoO_4 becomes irreversibly adsorbed via a strong inner-sphere complex. During aging, MoO_4 became incorporated into the hematite structure, as evidenced by the increase in the size of the hematite unit shell as a result of the larger ionic radius of Mo compared to Fe. The authors propose that a change from tetrahedral to octahedral coordination is reflected in the decreased intensity of the XANES pre-edge peak. However, Wharton et al. (2003) argue that octahedral coordination is precluded by the presence of any pre-edge features. Further XAS adsorption studies for MoO_4 on goethite by Arai (2010) indicate that Mo adsorption to goethite is tetrahedral except at low pH (pH 3-4) where different Mo-polymer species may adsorb octahedrally. Das and Hendry (2013) also observed a decrease in pH during adsorption experiments and assign this to the possibility that MoO_4 displaces H^+ ions during adsorption, therefore increasing the pH of the sorption solution.

Lang et al. (2000); and Lang and Kaupenjohann (2003) used pressure-jump relaxation (where materials are subjected to rapid pressure changes and the time taken to reach equilibrium when pressure is removed is measured, indicating inner- or outer-sphere bonding) and adsorption experiments to investigate MoO_4 adsorption to goethite. They suggest that both inner-sphere and outer-sphere Mo complexes on goethite are possible, as Mo adsorbs to outer adsorption sites before diffusing into pore spaces, leaving previously occupied surface sites free for further adsorption. The authors suggest that resistance to Mo diffusion increases during adsorption as the pore sizes in Fe oxides decrease away from the mineral surface.

Very little research has been done into Mo adsorption to magnetite in natural environments but experimental work by Verbinnen et al. (2012) suggests that for MoO_4, Mo bonds with Fe(III) in magnetite as an inner-sphere complex. This work shows that pH plays an important

role with maximum adsorption at pH 2-5 but decreasing adsorption above pH 5. The authors suggest that this is due to the magnetite surface becoming increasingly negatively charged, increasing repulsive forces between magnetite and MoO_4.

1.3.4 Organic matter

Current research suggests that organic matter may be an important sequestration pathway for Mo, particularly in euxinic or weakly euxinic environments. MoO_4, MoO_xS_{4-x} and MoS_4 adsorption have been investigated for a range of organic materials, including: humic acid (Bibak and Borggaard, 1994; Helz et al., 1996); fulvic acid (Gustafsson and Tiberg, 2015); activated carbon (Cruywagen and DeWet 1988); sulfate-reducing bacteria (Dahl et al., 2017; Tucker et al., 1997); and natural sediments and soils (Tribovillard et al., 2004; Wagner et al., 2017; Wichard et al., 2009). Coveney and Glascock (1989), observed a strong correlation between Mo and organic matter concentrations in Pennsylvanian black shales with a stronger correlation for terrestrial organic matter. Subsequent studies by Tribovillard et al. (2004) indicate a correlation with sulfurized organic matter in Mesozoic limestones and other research indicates that the sulfurization of organic matter enhances its scavenging ability (Helz et al., 1996), indicating that this is an important step in Mo sequestration with organic matter. The predominant factors affecting the sulfurization of organic matter, and therefore its capacity to sequester Mo, are organic matter and reactive Fe concentrations. Tribovillard et al. (2004) suggest that pyritization precedes the sulfurization of organic matter which may therefore be limited by high reactive Fe concentrations. These authors also used data from Mesozoic limestones and shales to suggest that organic matter concentrations are a primary control on sulfurization of organic matter due to the requirement for organic matter in BSR and this is supported by work from Zheng et al. (2000). Tribovillard et al. (2004) propose that: where total organic carbon (TOC) is <2%, there is no sulfidized organic matter; where TOC is 2-7%, sulfidized organic matter levels rise rapidly; and where TOC >7%, all organic matter is

sulfidized. A model proposed by Wagner et al. (2017) suggests either that where hydrogen sulfide (H_2S) > 11µM, MoO_4 reacts with dissolved organic matter to form Mo-organic complexes, promoting a change from tetrahedral to octahedral coordination before further reactions with H_2S transform these complexes to MoO_xS_{4-x}-organic complexes, or organic matter is sulfidized by reactions with H_2S before complexation with MoO_xS_{4-x}.

A study by Valdivieso-Ojeda et al. (2014) showed very high Mo enrichments associated with hypersaline microbial mats in Guerro Negro. The authors noted low reactive Fe concentrations and BSR, suggesting that organic matter may have become sulfidized, promoting the sequestration of Mo. The production of H_2S in this environment would also have promoted the transformation of MoO_4 to more reactive thiomolybdates, further promoting sequestration.

As with the minerals already described, pH is an important factor in Mo adsorption to organic matter, with research suggesting maximum adsorption is at a lower pH than with minerals (Bertine, 1972; and Bibak and Borggaard, 1994). Wagner et al. (2017) further suggest that MoO_4 is transformed to MoS_4 at a faster rate under low pH. As pH is lowered during BSR (Helz et al., 2011), BSR rates may influence the rate of MoO_4 transformation to oxy- and tetrathiomolybdates both in terms of reducing the pH and altering the levels of H_2S available for MoO_4 transformation. Coveney and Glascock (1989) observed very high Mo concentrations (>1000 ppm) in Pennsylvanian black shales and suggest that seepage from swamps along the palaeoshoreline acidified coastal waters and porewaters. It is possible that this reduction in pH promoted Mo sulfidation and therefore enhanced subsequent complexation with organic matter. In terms of the transformation of MoO_4 to MoS_4, Wagner et al. (2017) stress the importance of MoO_xS_{4-x} species in Mo sequestration suggesting that complete transformation to MoS_4 is not necessary for increased sequestration.

A reduction step from Mo(VI) to Mo(IV) also appears to be important for Mo complexation with organic matter (Dahl et al., 2017; Tucker et al., 1997; Wagner et al., 2017; Zheng et al., 2000). Experimental studies by Tucker et al. (1997) on MoO_4 complexation with sulfate-reducing bacteria indicate that Mo(VI) is reduced to Mo(VI) only in the presence of the bacteria, and also that Mo reduction is faster and more efficient in the presence of sulfide. They further propose that the bacterial reduction of Mo(VI) is by an enzymatic process rather than chemical reduction by sulfide or H_2. XANES and EXAFS studies from Dahl et al. (2017) also suggest that Mo in MoS_4 is reduced from Mo(VI) to Mo(IV) and immobilised at the cell surface of sulfate-reducing bacteria (living and dead). The authors suggest that this mechanism may be responsible for the sequestration of Mo to sediments in euxinic environments. They also suggest that Mo precipitates as Mo(IV)-sulfide compounds and this may explain the black Mo(IV) precipitate observed by Tucker et al. (1997) in their study. The similarity of XAS data for these experimental compounds with natural euxinic sediment samples indicate that this sequestration mechanism is important in natural environments (Dahl et al., 2017). XAS studies by Gustafsson and Tiberg (2015), however, suggest that MoO_4 adsorbed to fluvic acid is recovered as Mo(VI).

Organic matter may exist in the water column and sediments as discrete particles or as coatings on mineral surfaces. Lang and Kaupenjohann (2003) investigated the effect of organic coatings on MoO_4 adsorption to goethite and propose that organic coatings prevent the diffusion of MoO_4 from outer surface sorption sites to goethite micropores. Although the study indicated that this does not affect total adsorption, it does promote desorption as more Mo is adsorbed to goethite at the outer surface.

XAS studies of MoO_4 and MoS_4 complexation with organic matter support a change from tetrahedral to octahedral coordination, evidenced by the absence or reduced amplitude of the pre-edge feature (Gustafsson and Tiberg, 2015; Wagner et al., 2017).

1.3.5 Fe sulfide

Pyrite is thought to be an important host for Mo sequestration in euxinic environments, including in euxinic porewaters, although debate continues as to whether this is the primary host in the presence of organic matter. Chappaz et al. (2014) suggest that, in sediments from euxinic environments studied using laser ablation ICP-MS, only 0-20% of Mo is associated with pyrite grains with the remaining Mo in the groundmass. However, the beam size exceeded the size of some pyrite grains and therefore Mo association with pyrite may be underestimated. It was also noted in this study that the proportion of pyrite-hosted Mo decreased with increasing age of the samples, highlighting the possibility that Mo is released during recrystallisation of framboidal pyrite to euhedral pyrite. Investigations into the effects of thermal maturity on Mo partitioning by Ardakani et al. (2016) support the theory of Mo release from pyrite suggesting that thermochemical sulfate reduction during diagenesis leads to the recrystallisation of framboidal pyrite to euhedral pyrite, resulting in the release of Mo to porewaters and the surrounding matrix. These authors also propose that Mo may be reincorporated into euhedral pyrite. However, neither of these studies distinguish between Mo species. Investigations of Pennsylvanian black shales by Coveney and Glascock (1989) suggest that Mo is associated with the groundmass is in organic-rich layers but pyrite is also ubiquitous in these layers and therefore cannot be ruled out as the primary host. Breward et al. (2015) support pyrite as the primary host for Mo in Jurassic shales following a geochemical survey which indicated that the high Mo concentrations (up to 320 ppm) observed are hosted by fine-grained pyrite rather than organic phases.

Experimental studies into Mo adsorption to pyrite highlight the importance of sulfidized Mo species which become more reactive with increasing sulfidation. Bostick et al. (2003) and Xu et al. (2006) suggest that the sorption capacity on pyrite is much higher for MoS_4 than for MoO_4. Bostick et al. (2003) used XAS for Mo adsorbed to synthetic pyrite to propose that MoO_4 adsorbs to pyrite via a weak inner- or outer-sphere complex that retains its tetrahedral coordination. Adsorption is reversible as a result of pH changes with rapid desorption of MoO_4 from ~ pH 4.5. Experimental XAS studies by Freund et al. (2016) also suggest a weak outer-sphere complex for MoO_4 as the Mo-O bond lengths appear unaffected by adsorption to pyrite. Bostick et al. (2003) also investigated MoS_4 adsorption to pyrite and propose that MoS_4 adsorbs to pyrite via an irreversible, strong, inner-sphere complex that involves structural rearrangement to form a Mo-Fe-S cubane. Vorlicek et al. (2004) support the Mo-Fe-S cubane model but suggest that thiomolybdates are first reduced by zero-valent sulfur (S^0). Freund et al. (2016) also support substantial structural rearrangement during MoS_4 adsorption to pyrite, and a reduction step, and suggest the thiolated form of Mo is required for reduction. The formation of a strong inner-sphere complex on pyrite for MoS_4 suggests that pyrite may be a permanent sink for fully sulfidized Mo species and therefore, if Mo is released during pyrite recrystallisation, as proposed by Chappaz et al. (2014), it is unlikely it was adsorbed to pyrite as MoS_4. The importance of sulfidized Mo species for adsorption to Fe sulfide minerals was highlighted by Helz et al. (2004) in experimental studies of model systems. These authors propose that FeS acts as a transient scavenger for Mo noting that, although FeS scavenges MoO_4, scavenging rates are much higher for thiomolybdate species.

Geochemical conditions may also affect Mo adsorption to pyrite. Experimental studies by Bostick et al. (2003) indicate that excess sulfide inhibits Mo adsorption to pyrite. Additional experimental studies by Xu et al. (2006) indicate that PO_4^{3-} outcompetes Mo for surface sites on pyrite, although this effect is stronger for MoO_4 than for MoS_4. This bimodal competitive

effect was also highlighted by Freund et al. (2016). These authors investigated how Mo adsorbs to pyrite in the presence of a thiol-containing organic molecule (2MPA) and noted that for MoO_4, 2MPA outcompetes Mo for adsorption to pyrite and can even displace it. However, MoS_4 does not appear to be outcompeted. XAS data from this study suggest that MoS_4 can form a ternary structure on the pyrite surface, binding with both pyrite and a thiol-containing molecule. This is perhaps a mechanism that has been overlooked, with previous authors preferring to assign Mo sequestration to a single pathway.

1.3.6 Mo-sulfur species

Work implicating a reduction step via a reaction between thiomolybdates and zero-valent sulfur initially proposed by Vorlicek et al. (2004) has recently gained support from Dahl et al. (2013b) who suggest that it is one of the major mechanisms controlling Mo sequestration to sediments in the euxinic Lake Cadagno. During this process, molybdate becomes unstable in the water column when H_2S levels exceed 11 µM and begins to be converted to tetrathiomolybdate via a series of sulfidation steps, as discussed above. At the third sulfidation step, trithiomolybdate ($MoOS_3^{2-}$) reacts with zero-valent sulfur forming polysulfide rings which lead to a reduction from Mo(VI) to Mo(IV) (Figure 1.4; Vorlicek et al., 2004) These reduced Mo-polysulfides ($Mo^{IV}X(S_4)S^{2-}$, where X = either O or S) are readily scavenged by pyrite and amorphous FeS and in the case of pyrite, appear to be more readily scavenged than tetrathiomolybdate, the final sulfidized Mo species (Vorlicek et al., 2004; Dahl et al., 2013b).

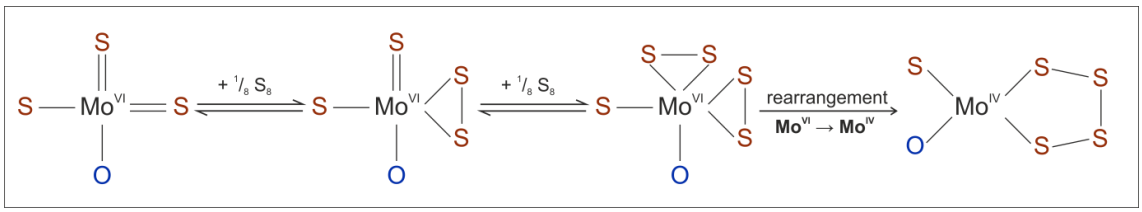

Figure 1.4 *Reaction scheme for trithiomolybdate and zero-valent sulfur proposed by Vorlicek, at al. (2004).*

1.3.7 Other sorption pathways

Although the adsorption pathways outlined above appear to dominate Mo sequestration, investigations have been undertaken to explore other potential sequestration mechanisms. One proposed pathway is that of an independent Mo-Fe-S colloid that forms under euxinic conditions. Experimental investigations by Vorlicek et al. (2018) suggest that, under euxinic conditions in the presence of Fe^{2+}, MoS_4 initially forms $FeMoS_4$ which, over a few hours by internal Mo self-reduction, irreversibly transforms to a non-crystalline Mo(IV) colloid of similar composition. The authors used EXAFS to investigate this colloidal Mo product and propose that it may be composed of inorganic polymers containing a cuboid $Fe_2Mo_2S_4^{4+}$ (Figure 1.5).

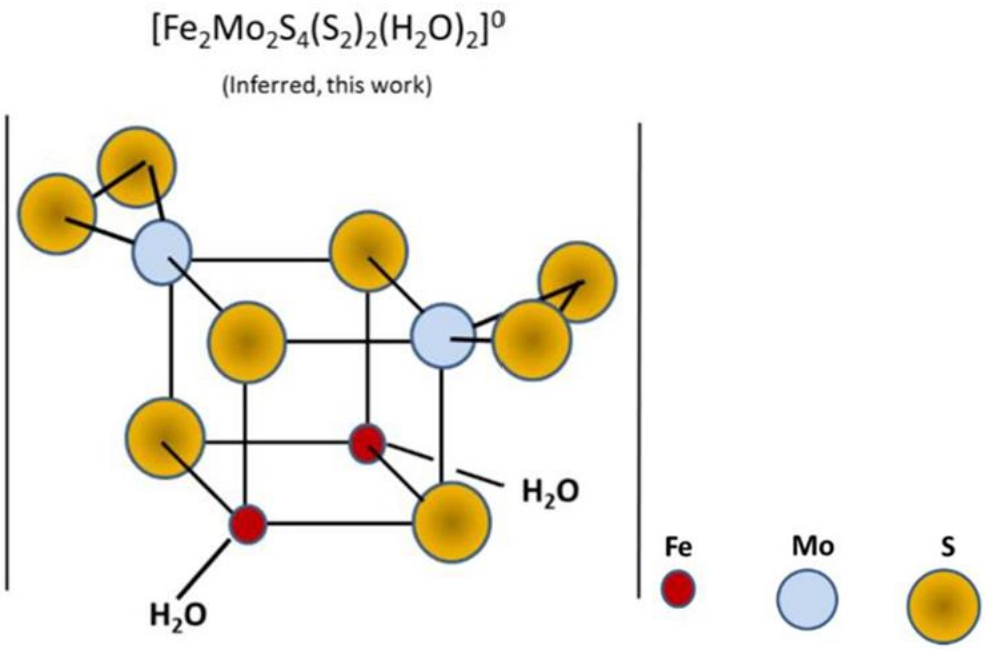

Figure 1.5 Hypothetical cuboid $Fe_2Mo_2S_4^{4+}$ proposed by Vorlicek et al. (2018).

Vorlicek et al. (2018) further suggest that these colloids may form on or within Fe(III)-bearing particles which means that these could act as the transport mechanism from the water column to the sediments where Mo is then permanently sequestered. This work supports that of Helz et al. (1996) who found a compact Mo-S-Fe cluster structure in black shales and under

experimental conditions using EXAFS. Zheng et al. (2000) investigated Mo sequestration in sulfidic porewaters of the Santa Barbara Basin and propose that the onset of Mo-Fe-S co-precipitation occurs at ~0.1 µM sulfide concentration whereas at ~100 µM sulfide concentration Mo precipitation occurs without Fe. Therefore, the Mo-S-Fe structure identified by Vorlicek et al. (2018) and Helz et al. (1996) may be somewhat controlled by sulfide concentrations.

1.4 Molybdenum behaviour under different water column redox conditions

1.4.1 Molybdenum in oxic environments

In oxic seawater, Mo behaves conservatively as the molybdate anion (MoO_4^{2-}) and generally remains in solution in the water column leading to low sediment concentrations. Its concentration in seawater is believed to be controlled by an equilibrium reaction in which Mo is temporarily removed from the water column via adsorption and desorption to Mn and Fe (oxyhydr)oxides. During this process, molybdate sorbs to Mn and Fe (oxyhydr)oxides in the water column and when these minerals are deposited, molybdate is released in anoxic porewaters and diffuses back into the water column (Figure 1.6). This mechanism facilitates the cycling of Mo, creating transient Mo enrichments in upper sediments (Scott and Lyons, 2012; Shimmield and Price, 1986). Consistent Mo/Mn ratios (~0.002) in Mn-rich sediments and ferromanganese deposits are observed from a range of sites (Shimmield and Price, 1986). Investigations of Mo isotopes reveal a heavy isotopic signature in seawater (δ^{98}Mo = 2.3 ‰) and observations of the light isotopic signature in Mn (oxyhydr)oxides (Mo = -0.7 ‰), indicate that these minerals preferentially adsorb isotopically light Mo, suggesting that it is this process that drives the overall seawater δ^{98}Mo values, further supporting Mn and Fe (oxyhydr)oxides

as sequestration pathways in oxic environments (Barling and Anbar, 2004; Kashiwabara et al., 2009; Scholz et al., 2013).

Experimental work from Kashiwabara et al. (2009) indicates different Mo adsorption processes for ferrihydrite and δMnO_2, which may explain the isotopic fractionation observed between seawater and ferromanganese nodules. Their data suggest that Mo is adsorbed to ferrihydrite as a tetrahedrally coordinated outer-sphere complex with the same symmetry and similar Mo-O bonding strength as MoO_4^{2-}, resulting in very low or no isotopic fractionation. On the other hand, Mo is adsorbed to δMnO_2 as an octahedrally coordinated inner-sphere complex with a symmetry distorted from MoO_4^{2-}, a larger oxygen coordination number and weaker bonding environment. This structure preferentially adsorbs lighter Mo isotopes and is therefore the most likely phase responsible for the seawater isotopic fractionation (Kashiwabara et al, 2009). The data for experimental δMnO_2 materials and ferromanganese nodules are in good agreement indicating that δMnO_2 is the host phase for Mo, further supporting the role of this mineral in Mo isotope fractionation in oxic seawater (Kashiwabara et al., 2009).

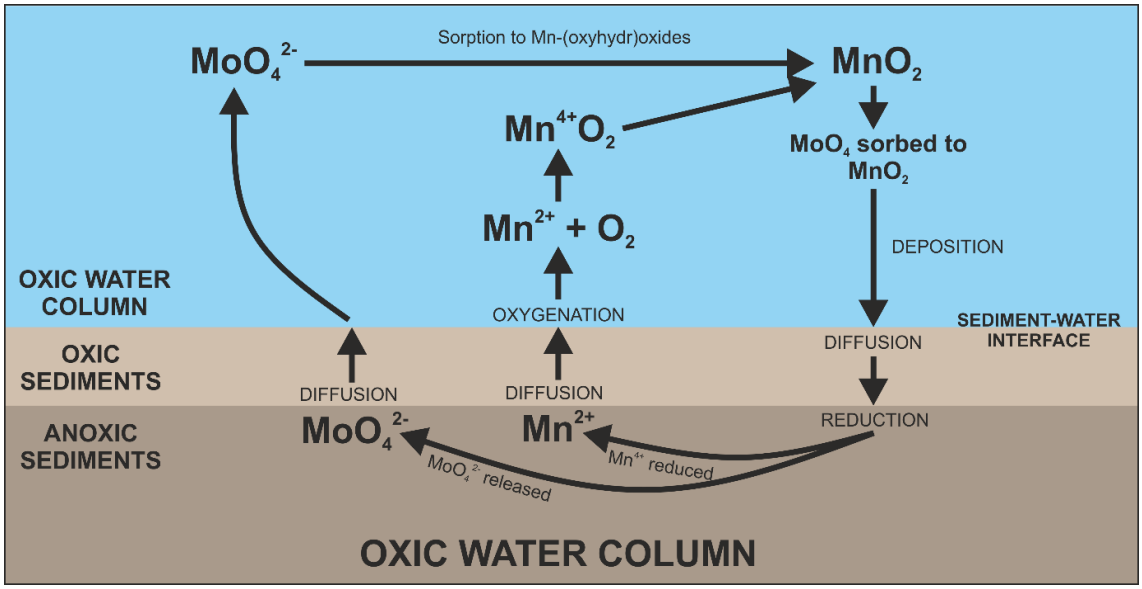

Figure 1.6 *A cartoon showing the behaviour of Mo under an oxic water column.*

Although Mo concentrations in oxic marine sediments tend to be low, extreme Mo enrichments of 300-700 ppm can be found in Mn nodules due to their very slow formation and this should be considered when using Mo concentrations as a palaeoredox tool (Dahl et al., 2013a).

1.4.2 Molybdenum in nitrogenous environments

A nitrogenous water column is one where nitrate (NO_3^-) is reduced and nitrite (NO_2^-) accumulates (Canfield and Thamdrup, 2009). Other than Scholz et al. (2017), very little research has been done on Mo cycling under a nitrogenous water column. The work done by Scholz et al. (2017) suggests that Mo is delivered to sediments adsorbed to Fe (oxyhydr)oxides. When these Fe minerals are then reduced in sediments, Mo is released during reduction in porewaters and then transformed to Mo-S-Fe complexes and retained in the sediment (Figure 1.7; Scholz et al., 2017).

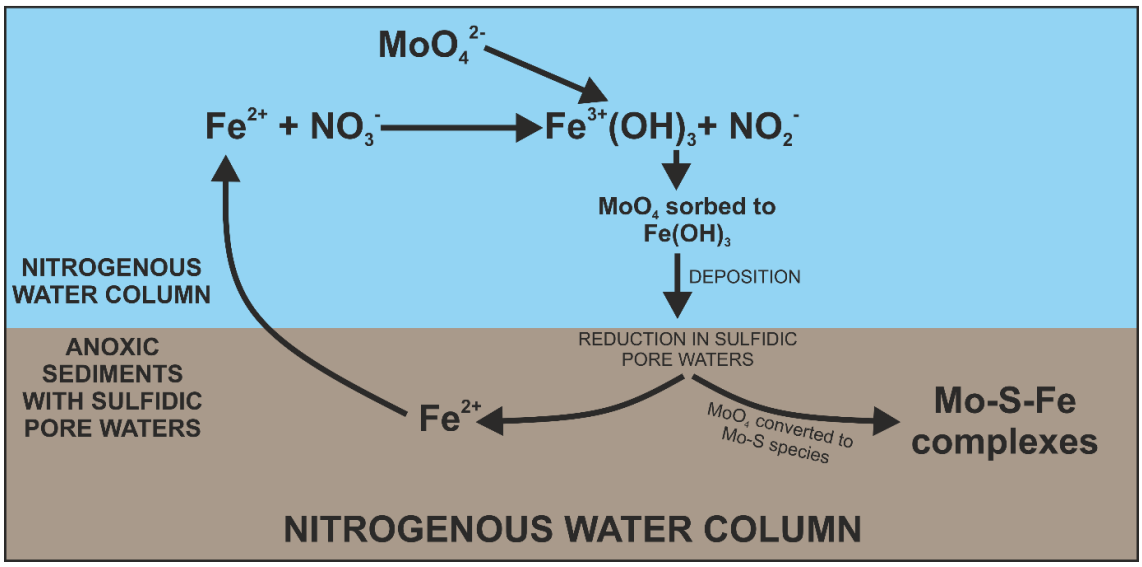

Figure 1.7 *A cartoon showing the behaviour of Mo under a nitrogenous water column (after Scholz et al., 2017).*

Although pronounced Mo enrichments were observed in water column Mn (oxyhydr)oxides, Scholz et al. (2017) suggest that during gravitational sinking through the water column these minerals are dissolved, releasing Mo, in contrast to Fe (oxyhydr)oxides which generally survive this process or are actually created in this setting due to the release of Fe^{2+} and its reoxidation with NO_3^-. These existing and newly formed Fe (oxyhydr)oxides are then available to adsorb Mo which has been released from Mn (oxyhydr)oxides and can then transport it to the sediments.

1.4.3 Molybdenum in ferruginous environments

A ferruginous water column is defined as an anoxic, non-sulfidic water column containing free aqueous ferrous iron (Fe(II); Poulton and Canfield, 2011). Unfortunately, although these environments have been widely investigated, Mo cycling in these settings has not. It is accepted that Mo adsorbs to Fe minerals (e.g. Bostick et al., 2003; Gustafsson, 2003; Lang and Kaupenjohann, 2003; Verbinnen et al., 2012) and it is therefore reasonable to suggest that these minerals play a part in Mo cycling. However, this particular environment requires further research into Mo behaviour under a ferruginous water column before a model can be developed.

1.4.4 Molybdenum in euxinic environments

The removal of Mo from the water column in euxinic environments is higher than in oxic environments by a factor of 200-5000 (with the upper end of this scale representative of fully euxinic environments and the lower end representative of non-euxinic environments but with sulfidic porewaters; Scott et al., 2008). However, the exact mechanisms of this increased Mo sequestration are still not fully understood. It is generally accepted that in the presence of H_2S concentrations >0.1 µM, molybdate is converted into a series of thiomolybdate complexes,

starting with oxythiomolybdates when H_2S concentrations are between ~0.1-11 µM, which progressively dominate Mo speciation and culminate in the formation of tetrathiomolybdate when H_2S >11 µM (Figure 1.8; Erickson and Helz, 2000; Helz et al., 1996; Zheng et al., 2000).

These thiomolybdates are extremely reactive and can be sequestered to sediments via scavenging onto Fe minerals and sulfidized organic matter (Figure 1.9; Helz et al., 1996; Zheng et al., 2000). Alternatively these complexes may react with zero-valent sulfur present in natural sulfidic waters to produce Mo(IV)-polysulfides which might similarly be scavenged by Fe minerals and/or organic matter (Figure 1.4; Dahl et al., 2013b; Vorlicek et al., 2004).

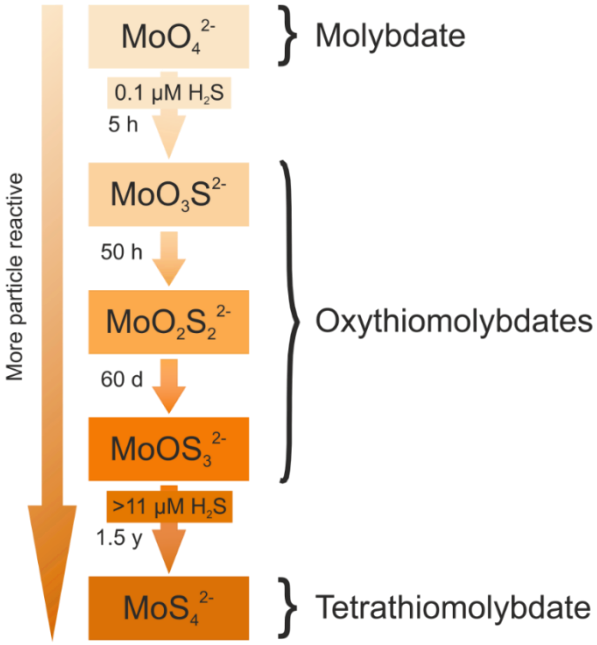

Figure 1.8 *Diagram showing the sulfidation steps from molybdate to tetrathiomolybdate in the presence of H_2S in the water column. After Dahl et al. (2017).*

There has been some debate over the importance of Fe sulfides and sulfidized organic matter in the sequestration of thiomolybdates. In euxinic environments where the geochemical switch has been activated, although both pyrite and sulfidized organic matter could act independently to sequester Mo, Tribovillard et al. (2004) suggest that both play important roles, arguing for the dominance of sulfidized organic matter as the final Mo host phase in Mesozoic limestones and shales. In this work Mo enrichments are found to be positively

correlated with sulfidized organic matter but not with pyrite or unsulfidized organic matter. These authors also identified a relationship between TOC and sulfidized organic matter (<2 % TOC – no sulfidized organic matter found; 2 – 7 % TOC – sulfidized organic matter levels rise rapidly; >7 – 10 % TOC – all organic matter present is sulfidized), which is further supported by other findings that TOC strongly correlates with Mo enrichments (e.g. Algeo and Lyons, 2006; Cruse and Lyons, 2004; Werne et al., 2002). Tribovillard et al. (2004) propose that under euxinic conditions pyrite forms prior to the sulfidation of organic matter and Mo-Fe-S clusters that form on pyrite surfaces are then trapped within the sediment. Once organic matter has been sulfidized it captures Mo in sediments as a secondary host and therefore these two processes act together to permanently sequester Mo. Coveney and Glascock (1989) found a similar correlation between Mo and organic matter in Pennsylvanian shales and went further to propose that Mo showed better correlations with terrestrial organic matter than with marine organic matter. However, Coveney and Glascock (1989) pointed out that the organic matter in their samples contained ubiquitous pyrite grains which could not be ruled out as the primary Mo host. This observation, although not noted by authors, may also apply to the Mesozoic limestones and shales studied by Tribovillard et al. (2004), suggesting either that pyrite within organic matter is the primary host for Mo and has not been recognised by Tribovillard et al. (2004) or that the pyrite observed within organic matter by Coveney and Glascock (1989) acted as the primary host for Mo before sulfidized organic matter formed and captured Mo from pyritic sediments.

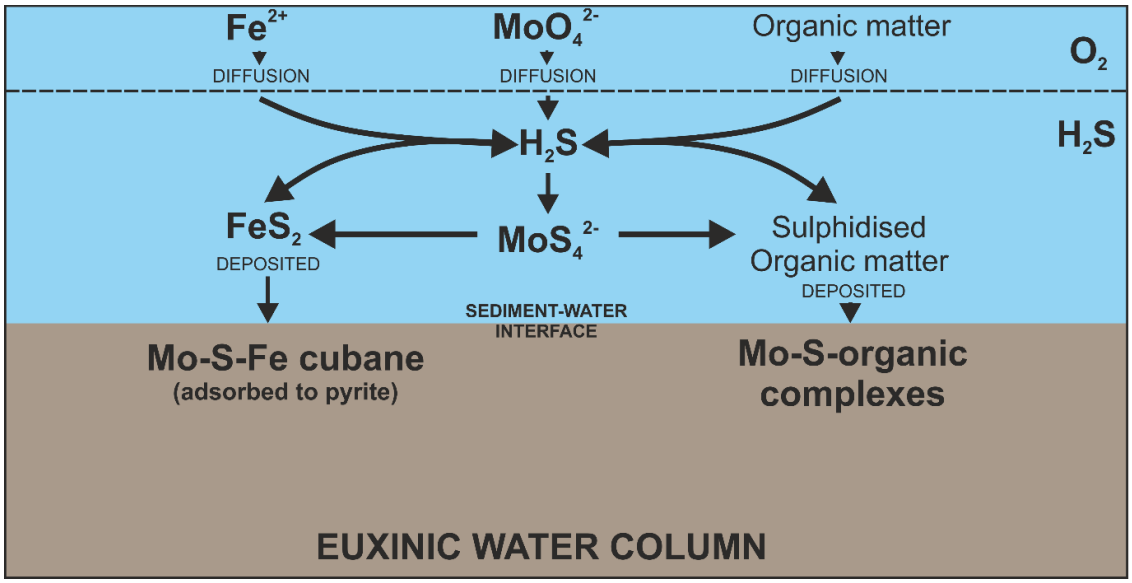

Figure 1.9 *A cartoon showing the behaviour of Mo under a euxinic water column.*

When Mo forms tetrathiomolybdate under sulfidic conditions it can adsorb to pyrite. EXAFS and XANES analyses of Mo adsorbed to pyrite from Bostick et al. (2003) show that during the adsorption process, MoS_4^{2-} undergoes extensive structural rearrangement to form a Mo-Fe-S cubane. The bond distances suggest that this process forms an inner-sphere complex indicative of irreversible adsorption. This finding is in agreement with SEM observations by Coveney and Glascock (1989) which show Mo occurs at or near the surface of pyrite framboids in Pennsylvanian shales, strengthening their suggestion that Mo enrichments observed within organic matter may actually be Mo adsorbed to pyrite grains within the organic matter, while casting doubt on the theory of Tribovillard et al. (2004) that pyrite acts as a primary host for Mo before it is captured by sulfidized organic matter. The proposal of the formation of a Mo-Fe-S cubane on pyrite surfaces receives additional support from the EXAFS data from Helz et al. (1996) which suggests the formation of a compact Mo-S-Fe cluster structure.

1.4.5 Molybdenum in other environments

An alternative explanation for high Mo concentrations has been proposed by Valdivieso-Ojeda et al. (2014). Following a study of modern hypersaline microbial mats in Guerro Negro, Mexico, Mo enrichment factors ((Mo/Al_{sample}) / ($Mo/Al_{background}$)) of up to 558 were observed. The microbial mats display microgradients of dissolved oxygen, H_2S, dissolved inorganic carbon and pH. The authors propose that as a result of these gradients, MoO_4 which adsorbs to Mn (oxyhydr)oxides in the top 4mm of the mats (the oxic zone), is released into H_2S-rich porewaters when it reaches the reduced part of the mat (Figure 1.10). In the presence of high H_2S concentrations (250 µM; Jørgensen and Des Marais, 1986) MoO_4 then is reduced to Mo(IV) and transformed to thiomolybdate-sulfides which are readily scavenged by organic matter and Fe sulfides. Valdivieso-Ojeda et al. (2014) carried out a sequential extraction on the microbial mat material and noted that a significant proportion of Mo (35 ± 18%) was released during the initial HCl extraction. Although this Mo reservoir is generally associated with Mo adsorbed to Mn oxides, the authors suggest that, in light of the H_2S concentrations in the mat, it is possible that some of the Mo in this fraction may be adsorbed to acid volatile sulfides (AVS) such as mackinawite and greigite as these minerals would be removed during the HCl extraction. The authors were not able to separate the AVS and Mn-oxide Mo fractions and therefore this cannot be verified.

Around 9 ± 4% of the Mo was removed in the HNO_3 step which targeted pyrite and organic matter. It must be noted, however, that Valdivieso-Ojeda et al (2014) did not separate Mo fractions between organic matter and pyrite and it is therefore unclear which of these known Mo sinks is responsible for the concentrations observed in this fraction.

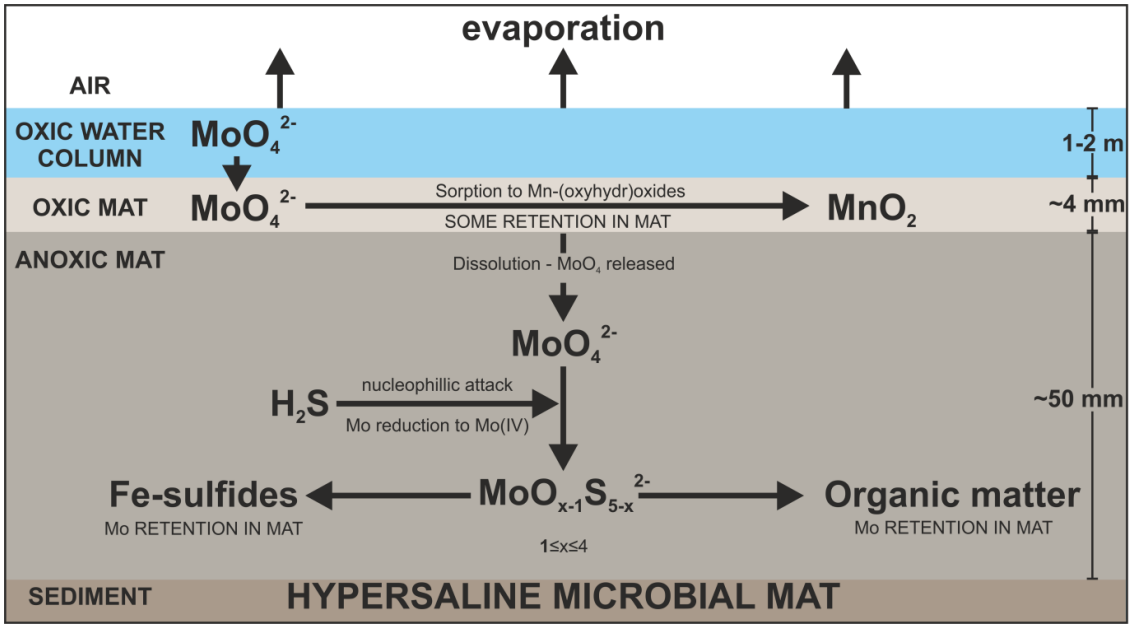

Figure 1.10 *A cartoon showing the Mo sequestration mechanism proposed by Valdivieso-Ojeda et al. (2014).*

1.5 Molybdenum isotopes

Mo has seven stable isotopes of varying abundance (Table 1.1; Hoefs, 2010) but it is generally the Mo^{98}/Mo^{95} and Mo^{97}/Mo^{95} isotope pairs that are used for geochemical interpretations (e.g. Poulson et al., 2006; Siebert et al., 2006; Tossell, 2005). Mo isotope values are generally presented as $\delta^{98}Mo$ where this is $[(^{98/95}Mo_{sample}/^{98/95}Mo_{standard})-1] \times 1000$ (Poulson et al., 2006). Due to the long residence time of Mo in oceans (800 kyr; Morford et al., 1999), seawater $\delta^{98}Mo$ is relatively uniform at ~2.3‰ which is in contrast to the lithogenic $\delta^{98}Mo$ value of 0.00‰ (Siebert et al., 2003) and riverine input which ranges from 0.2 to 2.3‰ (Archer and Vance, 2008). The near constant $\delta^{98}Mo$ value of seawater facilitates interpretations of palaeoenvironmental conditions through isotopic fractionations in ocean sediments. For example, an isotopic fractionation of ~3‰ is observed between Fe-Mn crusts (where $\delta^{98}Mo$ = -0.7‰) and seawater, as Mn and Fe (oxyhydr)oxides preferentially adsorb light Mo isotopes leaving seawater enriched in heavy isotopes (Poulson et al., 2006). As these deposits are created under known geochemical conditions, sediments with this light isotopic signature infer

deposition beneath an oxic water column. However, where an isotopic signature close to seawater value is observed, it is expected that deposition occurred beneath a euxinic water column with the isotopic value a result of near quantitative removal of Mo from the water column (e.g. Barling et al., 2001; Dahl et al., 2010a; Nägler et al., 2011).

Table 1.1 *Mo stable isotopes and their abundance (Hoefs, 2010).*

Mo isotope	**Abundance**
^{92}Mo	15.86%
^{94}Mo	9.12%
^{95}Mo	15.70%
^{96}Mo	16.50%
^{97}Mo	9.45%
^{98}Mo	23.75%
^{100}Mo	9.62%

Research into Mo isotopes includes experimental work to identify the δ^{98}Mo signature of specific minerals and observations of sediments from well-characterised redox environments (Figure 1.11). The combination of these observations suggests that the δ^{98}Mo signature becomes heavier as the environment it is deposited in becomes more reducing, with euxinic values close to those of seawater.

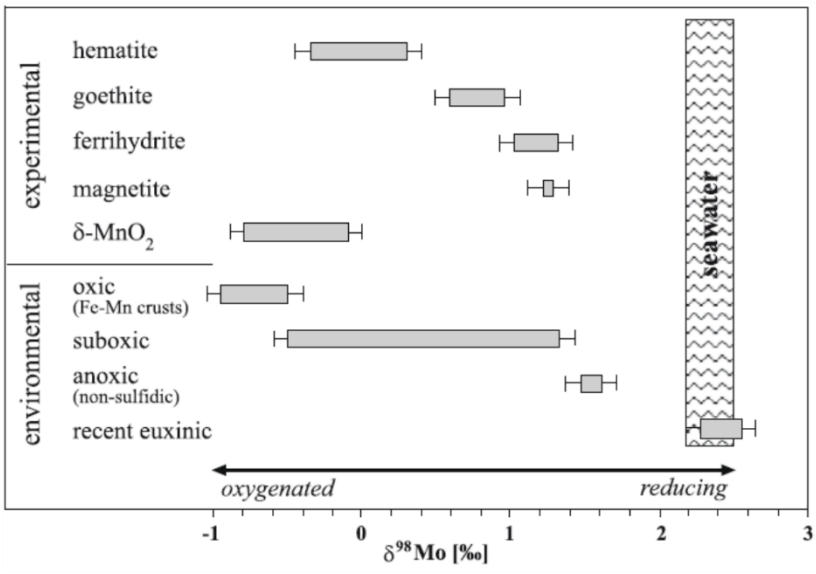

Figure 1.11 *A compilation of δ^{98}Mo values for Mo adsorbed to specific minerals during experimental work and the δ^{98}Mo signature from Mo deposited in known redox environments (Goldberg et al., 2009 and references therein).*

1.6 Summary of knowns and unknowns

To date Mo concentrations measured in marine sediments are used as a palaeoproxy for redox conditions in the contemporaneous overlying water column, where relatively low sediment concentrations are interpreted to reflect sediments deposited beneath oxic water columns and Mo cycling with Mn and Fe (oxyhydr)oxides (e.g. Adelson et al., 2001; Cheng et al., 2016; Scott et al., 2008), whilst relatively high sediment concentrations are interpreted to reflect sediments deposited beneath euxinic water columns (e.g. Breward et al, 2015; Cheng et al., 2016; Dahl et al., 2011; Hetzel et al., 2009; Scott et al., 2008) and sediments with porewater sulfide (e.g. Scott et al., 2012; Zheng et al., 2000). Work to date also uses Mo isotopic compositions to identify sediments deposited beneath oxic water columns via Mn and Fe cycling (e.g. Goldberg et al., 2012; Scholz et al., 2013) and those deposited beneath euxinic water columns (e.g. Dahl et al., 2010b). Despite the success of these Mo concentration and isotopic composition studies in elucidating palaeoredox conditions, they are restricted to identifying only end-member oxic or euxinic redox states, and are unable to determine

intermediate palaeoredox conditions, including nitrogenous and ferruginous. On the other hand, Mo speciation in sediments has the potential to elucidate a wider range of redox states because, by understanding the geochemical behaviour of Mo with respect to different sedimentary phases under different redox conditions and then determining Mo phase associations in sedimentary archives, it might be possible to infer palaeoredox conditions in these sediments and their contemporaneous overlying water columns. To date some methods have been used to infer Mo speciation in redox environments indirectly such as using Mo/TOC ratios (e.g. Dahl et al., 2011; Scholz et al., 2013; Tribovillard et al., 2004), Mo/Mn ratios (Shimmield and Price, 1986), observations of associations with minerals and organic matter using SEM and laser ablation-inductively coupled mass spectrometry analysis (e.g. Coveney and Glascock, 1989; Chappaz et al., 2014); and directly using XANES and EXAFS to determine Mo speciation in natural sediments (e.g. Ardakani et al., 2016; Dahl et al., 2013; Freund et al., 2016; Wagner et al., 2017), but our knowledge of Mo speciation across redox environments remains relatively limited and there remains significant debate regarding Mo sequestration pathways in these environments. In particular little research has been undertaken into Mo phase associations in sediments deposited beneath nitrogenous and ferruginous water columns, the latter of which has been shown to be important throughout Earth history (e.g. Poulton et al., 2010). In summary, an understanding of Mo speciation in sediments deposited under a range of redox environments is severely lacking but is critical to expanding the use of the Mo palaeoredox proxy for elucidating ancient ocean chemistry, particularly during early Earth conditions and key intervals in Earth's biogeochemical evolution, when ferruginous oceans are thought to have played an important role in the progressive habitability of the planet.

1.7 Aims and objectives

The aim of this research is to better understand the processes involved in Mo sequestration to sediments deposited under four different redox water columns (oxic, nitrogenous, ferruginous and euxinic) to expand the use of Mo as a palaeoredox proxy to nitrogenous and ferruginous environments. To develop this understanding, the following objectives were set:

To develop a wet chemical sequential extraction method for Mo that targets the main known Mo pools in marine sedimentary environments to facilitate identification of Mo phase associations in modern and ancient marine sediments (Chapter 3).

To develop a library of XANES reference standards for the main known Mo phase associations in marine sedimentary environments and subsequently characterise these standards both qualitatively and quantitatively to facilitate identification of Mo phase associations in modern and ancient marine sediments (Chapter 4).

To develop a detailed understanding of Mo phase associations in modern sediments deposited below oxic, nitrogenous, ferruginous and euxinic water columns using the XANES reference standards and XANES fingerprinting techniques (Chapter 5).

To investigate Mo geochemical behaviour in a modern environment with known geochemical conditions using the new sequential extraction and XANES fingerprinting techniques developed in this thesis (Chapter 6).

1.8 Thesis structure

The remainder of this study outlines the non-original methods and materials used in the research in Chapter 2.

The development of the sequential extraction method is then presented in Chapter 3. The main objectives of this research were to identify common sedimentary Mo pools and then develop a new sequential extraction protocol that targets Mo in all these sedimentary pools, by combining previously utilised trace metal extraction methods to target these pools, with consistent results. It was important to be able to extract Mo from low (~1 ppm) and high (>100 ppm) concentration sediments so that the method is valid for samples from a range of redox environments.

The library of Mo XANES standards are presented in Chapter 4. Standards for the majority of Mo pools identified in Chapter 3 are presented along with methods that use spectral characteristics and values to identify Mo oxidation and coordination. A fingerprinting technique to match unknown samples to standards is also shown and this method is tested against samples from different redox environments.

The fingerprinting techniques developed in Chapter 4 are then used in Chapter 5 to identify Mo phase associations in sediments deposited beneath oxic, nitrogenous, ferruginous and euxinic water columns. The samples are matched in terms of their XANES spectral characteristics and values and these sequestration pathways are discussed with respect to the local geochemistry.

Finally the sequential extraction and XANES fingerprinting methods developed in this work are used together to elucidate the geochemical history of a sediment core deposited beneath an oxic water column from Aarhus Bay, Denmark, in Chapter 6. These results are combined with Fe sequential extraction, TOC and Mo isotopes to present a model for Mo cycling in this environment.

1.9 References

Adelson, J. M., Helz, G. R., and Miller, C. V. 2001. Reconstructing the rise of recent coastal anoxia; molybdenum in Chesapeake Bay sediments. *Geochimica et Cosmochimica Acta.* **65** (2), pp. 237-252.

Algeo, T. J., and Lyons, T. W. 2006. Mo-total organic carbon covariation in modern anoxic marine environments: Implications for analysis of paleoredox and paleohydrographic conditions. *Paleoceanography.* **21**, pp. 1-23.

Anbar, A. D., and Knoll, A. H. 2002. Proterozoic Ocean Chemistry and Evolution: A Bioinorganic Bridge? *Science*. **297**, pp. 1137-1142.

Anbar, A. D. 2004. Molybdenum Stable Isotopes: Observations, Interpretations and Directions. *Reviews in Mineralogy & Geochemistry.* **55**, pp. 429-454.

Arai, Y. 2010. X-ray Absorption Spectroscopic Investigation of Molybdenum Multinuclear Sorption Mechanism at the Goethite-Water Interface. *Environmental Science and Technology.* **44**, pp. 3491-3496.

Archer, C., and Vance, D. 2008. The isotopic signature of the global riverine molybdenum flux and anoxia in the ancient oceans. *Nature Geoscientist.* **1**, pp. 597-600.

Ardakani, O. H., Chappaz, A., Sanei, H., and Mayer, B. 2016. Effect of thermal maturity on remobilization of molybdenum in black shales. *Earth and Planetary Science Letters*. **449**, pp. 311-320.

Barceloux, D. G., and Barceloux, D. 1999. Molybdenum. *Journal of Toxicology: Clinical Toxicology.* **37** (2), pp. 231-237.

Barling, J., Arnold, G. L., and Anbar, A. D. 2001. Natural mass-dependent variations in the isotopic composition of molybdenum. *Earth and Planetary Science Letters.* **193**, pp. 447-457.

Barling, J., and Anbar, A. D. 2004. Molybdenum isotope fractionation during adsorption by manganese oxides. *Earth and Planetary Science Letters.* **217**, pp. 315-329.

Bertine, K. K. 1972. The deposition of molybdenum in anoxic waters. *Marine Chemistry*. **1** (1), pp. 43-53.

Bibak, A., and Borggaard, O. K. 1994. Molybdenum adsorption by aluminium and iron oxides and humic acid. *Soil Science*. **158** (5), pp. 323-328.

Bostick, B. C., Fendorf, S., and Helz, G. R. 2003. Differential Adsorption of Molybdate and Tetrathiomolybdate on Pyrite (FeS_2). *Environmental Science and Technology.* **37** (2), pp. 285-291.

Boyd, E. S., Garcia Costas, A. M., Hamilton, T. L., Mus, F., and Peters, J. W. 2015. Evolution of Molybdenum Nitrogenase during the Transition from Anaerobic to Aerobic Metabolism. *Journal of Bacteriology.* **197** (9), pp. 1690-1699.

Braithwaite, E. R. 1994. Occurrence, extraction, production and uses of molybdenum. In: Braithwaite, E. R. and Haber, J. *Molybdenum: An outline of its chemistry and uses*. Amsterdam; Oxford: Elsevier, pp. 1-93.

Breward, N., Kemp, S. J., Ambrose, K., Powell, J. H., Morigi, A., and Wagner, D. 2015. Anomalous enrichment of molybdenum and associated metals in Lower Jurassic (Lias Group) black shales of central England, as revealed by systematic geochemical surveys. *Proceedings of the Geologists' Association.* **126**, pp. 346-366.

Brinza, L., Vu, H. P., Shaw, S., and Mosselmans, J. F. W. 2015. Effect of Mo and V on the Hydrothermal Crystallisation of Hematite from Ferrihydrite: An *in situ* Energy Dispersive X-

ray Diffraction and X-ray Absorption Spectroscopy Study. *Crystal Growth & Design*. **15** (10), pp. 4768-4780.

Brown, T. J., Idoine, N. E., Wrighton, C. E., Raycraft, E. R., Hobbs, S. F., Shaw, R. A., Everett, P., Kresse, C., Deady, E. A. and Bide, E. 2020. World Mineral Production 2014-18. Keyworth: British Geological Survey.

Canfield, D. E., Poulton, S. W., and Narbonne, G. M. 2007. Late-Neoproterozoic Deep Ocean Oxygenation and the Rise of Animal Life. *Science*. **315**, pp. 92-95.

Canfield, D. E., Poulton, S. W., Knoll, A. H., Narbonne, G. M., Ross, G., Goldberg, T., and Strauss, H. 2008. Ferruginous Conditions Dominated Later Neoproterozoic Deep-Water Chemistry. *Science.* **321**, pp. 949-952.

Canfield, D. E. and Thamdrup, B. 2009. Towards a consistent classification scheme for geochemical environments, or, Why we with the term 'suboxic' would go away. *Geobiology*. **7**, pp. 385-392.

Chappaz, A., Lyons, T. W., Gregory, D. D., Reinhard, C. T., Gill, B. C., Li, C., and Large, R. R. 2014. Does pyrite act as an important host for molybdenum in modern and ancient euxinic sediments? *Geochimica et Cosmochimica Acta*. **126**, pp. 112-122.

Chen, X., Ling, H., Vance, D., Shields-Zhou, G. A., Zhu, M., Poulton, S. W., Och, L. M., Jiang, S., Li, D., Cremonese, L., and Archer, C. 2015. Rise to modern levels of ocean oxygenation coincided with the Cambrian radiation of animals. *Nature Communications.* **6** (7142), pp. 1-7.

Cheng, M., Li, C., Zhou, L., Algeo, T. J., Zhang, F., Romaniello, S., Jin, C., Lei, L., Feng, L., Jiang, S. 2016. Marine biogeochemistry in the context of dynamically euxinic mid-depth waters. A case study of the lower Cambrian Niutitang shales, South China. *Geochimica et Cosmochimica Acta*. **183**, pp. 79-93.

Collier, R. W. 1985. Molybdenum in the Northeast Pacific ocean. *Limnology and Oceanography.* **30** (6), pp. 1351-1354.

Coveney, R. M., and Glascock, M. D. 1989. A review of the origins of metal-rich Pennsylvanian black shales, central U.S.A., with an inferred role for basinal brines. *Applied Geochemistry.* **4**, pp. 347-367.

Cramer, S. P., Hodgson, K. O., Gillum, W. O., and Mortenson, L. E. 1978. The Molybdenum Site of Nitrogenase, Preliminary Structural Evidence from X-Ray Absorption Spectroscopy. *Journal of the American Chemical Society.* **100** (11), pp. 3398-3407.

Cruse, A. M., and Lyons, T. W. 2004. Trace metal records of regional paleoenvironmental variability in Pennsylvanian (Upper Carboniferous) black shales. *Chemical Geology.* **206**, pp. 319-345.

Cruywagen, J. J., and De Wet, H. F. 1988. Equilibrium study of the adsorption of molybdenum (VI) on activated carbon. *Polyhedron.* **7** (7), pp. 547-556.

Dahl, T. W., Anbar, A. D., Gordon, G. W., Rosing, M. T., Frei, R., and Canfield, D. E. 2010a. The behaviour of molybdenum and its isotopes across the chemocline in the sediments of Lake Cadagno, Switzerland. *Geochimica et Cosmochimica Acta.* **74**, pp. 144-163.

Dahl, T. W., Hammarlund, E. U., Anbar, A. D., Bond, D. P. G., Gill, B. C., Gordon, G. W., Knoll, A. H., Nielsen, A. T., Schovsbo, N., H., and Canfield, D. E. 2010b. Devonian rise in atmospheric oxygen correlated to the radiations of terrestrial plants and large predatory fish. *PNAS*. **107**, pp. 19711-17915.

Dahl, T. W., Canfield, D. E., Rosing, M. T., Frei, R. E., Gordon, G. W., Knoll, A. H., and Anbar, A. D. 2011. Molybdenum evidence for expansive sulfidic water masses in ~750 Ma oceans. *Earth and Planetary Sciences Letters.* **311**, pp. 264-274.

Dahl, T. W., Ruhl, M., Hammarlund, E. U., Canfield, D. E., Rosing, M. T., and Bjerrum, C. J. 2013a. Tracing euxinia by molybdenum concentrations in sediments using handheld X-ray fluorescence spectroscopy (HHXRF). *Chemical Geology*. **360-251**, pp. 241-251.

Dahl, T. W., Chappaz, A., Fitts, J. P., and Lyons, T. W. 2013b. Molybdenum reduction in a sulfidic lake: Evidence from X-ray adsorption fine-structure spectroscopy and implications for the Mo paleoproxy. *Geochimica et Cosmochimica Acta.* **103**, pp. 213-231.

Dahl, T. W., Chappaz, A., Hoek, J., McKenzie, C. J., Svane, S., and Canfield, D. E. 2017. Evidence of molybdenum association with particulate organic matter under sulfidic conditions. *Geobiology*. **15** (2), pp. 311-323.

Das, S., and Hendry, M. J. 2013. Adsorption of molybdate by synthetic alkaline conditions: Effects of aging. *Applied Geochemistry*. **28**, pp. 184-201.

Das, S., Essilfie-Dughan, J., and Hendry, M. J. 2016. Sequestration of molybdate during transformation of 2-line ferrihydrite under alkaline conditions. *Applied Geochemistry*. **73**, pp. 70-80.

Erickson, B. E., and Helz, G. R. 2000. Molybdenum(VI) speciation in sulfidic waters: Stability and lability of thiomolybdates. *Geochimica et Cosmochimica Acta*. **64** (7), pp. 1149-1158.

Freund, C., Wishard, A., Brenner, R., Sobel, M., Mizelle, J., Kim, A., Meyer, D. A., and Morford, J. L. 2016. The effect of thio-containing organic molecule on molybdenum adsorption to pyrite. *Geochimica et Cosmochimica Acta.* **174**, pp. 222-235.

George, S. J., Igarshi, R. Y., Piamonteze, C., Soboh, B., Cramer, S. P., and Rubio, L. M. 2007. Identification of a Mo-Fe-S Cluster on NifEN by Mo K-Edge Extended X-ray Absorption Fine Structure. *Journal of the American Chemical Society.* **129**, pp. 3060-3061.

Goldberg, S., and Forster, H. S. 1998. Factors affecting molybdenum adsorption by soils and minerals. *Soil Science*. **163** (2), pp. 109-114.

Goldberg, T., Archer, C., Vance, D., Thamdrup, B., McAnena, A., and Poulton, S. W. 2009. Mo isotope fractionation during adsorption to Fe (oxyhydr)oxides. *Geochimica et Cosmochimica Acta.* **73**, pp. 6502-6516.

Goldberg, T., Archer, C., Vance, D., Thamdrup, B., McAnena, A., and Poulton, S. W. 2012. Controls on the Mo fractionations in a Mn-rich anoxic marine sediment, Gulmar Fjord, Sweden. *Chemical Geology*. **296**, pp. 73-82.

Green, M. L. H. 1994. An Introduction to the Chemistry of Molybdenum. In: Braithwaite, E. R. and Haber, J. *Molybdenum: An outline of its chemistry and uses*.

Guilbaud, R., Poulton, S. W., Butterfield, N. J., Zhu, M., and Shields-Zhou, G. A. 2015. A global transition to ferruginous conditions in the early Neoproterozoic oceans. *Nature Geoscience*. **8**, pp. 466-471.

Gustafsson, J. P. 2003. Modelling molybdate and tungstate adsorption to ferrihydrite. *Chemical Geology.* **200**, pp. 105-115.

Gustafsson, J. P., and Tiberg, C. 2015. Molybdenum binding to soil constituents in acid soils: An XAS and modelling study. *Chemical Geology*. **417**, pp. 279-288.

Helz, G. R., Miller, C. V., Charnock, J. M., Mosselmans, J. F. W., Pattrick, R. A. D., Garner, C. D., and Vaughan, D. J. 1996. Mechanism of molybdenum removal from the sea and its concentration in black shales: EXAFS evidence. *Geochimica et Cosmochimica Acta.* **60** (19), pp. 3631-3642.

Helz, G. R., Vorlicek, T. P., and Kahn, M. D. 2004. Molybdenum Scavenging by Iron Monosulfide. *Environmental Science & Technology.* **38**, pp. 4263-4268.

Helz, G. R., Bura-Nakić, E., Mikac, N., and Ciglenečki, I. 2011. New model for molybdenum behaviour in euxinic waters. *Chemical Geology*. **284**, pp. 323-332.

Hetzel, A. Böttcher, M. E., Wortmann, U. G., and Brumsack, H. 2009. Paleo-redox conditions during OAE 2 reflected in Demerara Rise sediment geochemistry (ODP Leg 207). *Palaeogeography, Palaeoclimatology, Palaeoecology.* **273**, pp. 302-328.

Hoefs, J. 2010. *Stable Isotope Geochemistry*. Berlin: Springer-Verlag.

Holland, H. D. 2006. The oxygenation of the atmosphere and oceans. *Philosophical Transactions of the Royal Society.* **361**, pp. 903-915.

International Molybdenum Association. 2018. *Uses of new molybdenum*. [Online]. Accessed 11 May 2020]. Available from https://www.imoa.info/molybdenum-uses/molybdenum-uses.php.

Javaux, E. J., Knoll, A. H., and Walter, M. R. 2001. Morphological and ecological complexity in early eukaryotic ecosystems. *Nature*. **412**, pp. 66-69.

Jørgensen, B. B., and Des Marais, D. J. 1986. Competition for sulfide among colorless and purple sulphur bacteria in cyanobacterial mats. *FEMS Microbiology Letters*. **38**, pp. 133-167.

Kashiwabara, T., Takahashi, Y., and Tanimizu, M. 2009. A XAFS study on the mechanism of isotopic fractionation of molybdenum during its adsorption on ferromanganese oxides. *Geochemical Journal.* **43**, pp. e31-e36.

Kendall, B., Reinhard, C. T., Lyons, T. W., Kaufman, A. J., Poulton, S. W., and Anbar, A. D. 2010. Pervasive oxygenation along late Archean ocean margins. *Nature Geoscience*. **3**, pp. 647-652.

Lang, F., Pohlmeier, A., and Kaupenjohann, M. 2000. Mechanism of molybdenum sorption to iron oxides using pressure-jump relaxation. *Plant Nutrient & Soil Science.* **163**, pp. 571-575.

Lang, F., and Kaupenjohann, M. 2003. Immobilisation of molybdate by iron oxides: effects of organic coatings. *Geoderma.* **113**, pp. 31-46.

März, C., Beckmann, B., Franke, C., Vogt, C., Wagner, T., and Kasten, S. 2009. Geochemical environment of the Coniacian-Santonian western tropical Atlantic at Demerara Rise. *Palaeogeography, Palaeoclimatology, Palaeoecology.* **273**, pp. 286-301.

Matern, K., and Mansfeldt, T. 2015. Molybdate adsorption by birnessite. *Applied Clay Science*. **108**, pp. 78-83.

McKay, J. L., and Pederson, T. F. 2014. Geochemical response to pulsed sedimentation: Implications for the use of Mo as a paleo-proxy. *Chemical Geology.* **382**, pp. 83-94.

Morford, J. L. and Emerson, S. 1999. The geochemistry of redox sensitive trace metals in sediments. *Geochimica et Cosmochimica Acta.* **63** (11/12), pp. 1735-1750.

Nägler, T. F., Neubert, N., Böttcher, M. E., Dellwig, O., and Schnetger, B. 2011. Molybdenum isotope fractionation in pelagic euxinia: Evidence from the modern Black and Baltic Seas. *Chemical Geology.* **289**, pp. 1-11.

National Academy of Sciences. 1989. *Recommended Dietary Allowances, tenth ed.* Washington DC: National Academy Press.

National Center for Biotechnology Information. PubChem Database. 2004. *Molybdate.* [Online]. [Accessed 09 May 2020]. Available from https://pubchem.ncbi.nlm.nih.gov/compound/Molybdate.

Poulson, R. L. 2006. Authigenic molybdenum isotope signatures in marine sediments. *Geology*. **34** (8), pp. 617-620.

Poulton, S. W., Fralick, P. W., and Canfield, D.E. 2004. The transition to a sulphidic ocean ~ 1.84 billion years ago. *Nature.* **431**, pp. 173-177.

Poulton, S. W., Fralick, P. W., and Canfield, D. E. 2010. Spatial variability in oceanic redox structure 1.8 billion years ago. *Nature Geoscience.* **3**, pp. 486-490.

Poulton, S. W., and Canfield, D. E. 2011. Ferruginous Conditions: A Dominant Feature of the Ocean through Earth's History. *Elements*. **7**, pp. 107-112.

Scholz, F., McManus, J., and Sommer, S. 2013. The manganese and iron shuttle in a modern euxinic basin and implications for molybdenum cycling at euxinic ocean margins. *Chemical Geology*. **355**, pp. 56-68.

Scholz, F., Siebert, C., Dale, A. W., and Frank, M. 2017. Intense molybdenum accumulation in sediments underneath a nitrogenous water column and implications for the reconstruction of paleo-redox conditions based on molybdenum isotopes. *Geochimica et Cosmochimica Acta*. **213**, pp. 400-417.

Scott, C., Lyons, T. W., Bekker, A., Shen, Y., Poulton, S. W., Chu, X., and Anbar, A. D. 2008. Tracing the stepwise oxygenation of the Proterozoic ocean. *Nature.* **452**, (7186), pp. 456-05.

Scott, C., and Lyons, T. W. 2012. Contrasting molybdenum cycling and isotropic properties in the euxinic versus non-euxinic sediments and sedimentary rocks: Refining the paleoproxies. *Chemical Geology.* **324-325**, pp. 19-27.

Shaw, T. J., Gieskes, J. M., and Jahnke, R. A. 1990. Early diagenesis in differing depositional environments: The response of transition metals in pore water. *Geochimica et Cosmochimica Acta.* **54**, pp. 1233-1246.

Shimmield, G. B., and Price, N. B. 1986. The behaviour of molybdenum and manganese during early sediment diagenesis – offshore Baja California, Mexico. *Marine Chemistry.* **19**. Pp. 261-280.

Siebert, C., Nägler, T. F., von Blanckenburg, F., and Kramers, J. D. 2003. Molybdenum isotope records as a potential new proxy for paleoceanography. *Earth and Planetary Science Letters*. **211**, pp. 159-171.

Siebert, C., McManus, J., Bice, A., Poulson, R., and Berelson, W. M. 2006. Molybdenum isotope signatures in continental margin marine sediments. *Earth and Planetary Science Letters.* **241**, pp. 723-733.

Smedley, P. L. and Kinniburgh, D. G. 2017. Molybdenum in natural waters: A review of occurrence, distribution and controls. *Applied Geochemistry*. **84**, pp. 387-432.

Stiefel, E. I. 1977. The coordination and bioinorganic chemistry of molybdenum. In: Lippiard, S. J. ed. *Progress in Inorganic Chemistry, vol. 22.* New York: John Wiley & Sons Inc.

Taylor, S. R. and McLennan, S. M. 1985. *The Continental Crust: Its Composition and Evolution.* Boston: Blackwell.

Tossell, J. A. 2005. Calculating the partitioning of the isotopes of Mo between oxidic and sulfidic species in aqueous solution. *Geochimica et Cosmochimica Acta.* **69** (12), pp. 2981-2993.

Tribovillard, N., Riboulleau, A., Lyons, T., and Baudin, F. 2004. Enhanced trapping of molybdenum by sulfurized organic matter of marine origin in Mesozoic limestones and shales. *Chemical Geology*. **213**, pp. 385-401.

Tribovillard, N., Algeo, T. J., Lyons, T., and Riboulleau, A. 2006. Trace metals as paleoredox and paleoproductivity proxies: An update. *Chemical Geology*. **232**, 12-32.

Tucker, M. D., Barton, L. L., and Thomson, B. M. 1997. Reduction and Immobilization of Molybdenum by *Desulfovibrio desulfricans. Journal of Environmental Quality.* **26**, pp. 1146-1152.

Valdivieso-Ojeda, J. A., Huerta-Diaz, M. A., and Delgadillo-Hinojosa, F. 2014. High enrichment of molybdenum in hypersaline microbial mats of Guerrero Negro, Baja California Sur, Mexico. *Chemical Geology.* **363**, pp. 341-354.

Verbinnen, B., Block, C., Hannes, D., Lievens, P., Vaclavikova, M., Stefusova, K., Gallios, G., and Vandecasteele, C. 2012. Removal of Molybdate Anions from Water by Adsorption on Zeolite-Supported Magnetite. *Water Environment Research.* **84** (9), pp. 753-760.

Vorlicek, T. P., Kahn, M. D., Kasuya, Y., and Helz, G. R. 2004. Capture of molybdenum in pyrite-forming sediments: Role of ligand-induced reduction by polysulfides. *Geochimica et Cosmochimica Acta*. **68** (3), pp. 547-556.

Vorlicek, T. P., Helz, G. R., Chappaz, A., Vue, P., Vezina, A., and Hunter, W. 2018. Molybdenum Burial Mechanism in Sulfidic Sediments: Iron-Sulfide Pathway. *ACS Earth and Space Chemistry.* **2** (6), pp. 565-576.

Wagner, M., Chappaz, A., and Lyons, T. W. 2017. Molybdenum speciation and burial pathway in weakly sulfidic environments: Insights from XAFS. *Geochimica et Cosmochimica Acta.* **206**, pp. 18-29.

Werne, J. P., Sageman, B. B., Lyons, T. W., and Hollander, T. J. 2002. An Integrated Assessment of a “Type Euxinic” Deposit: Evidence for Multiple Controls on the Black Shale Deposition in

the Middle Devonian Oatka Creek Formation. *American Journal of Science.* **302**, pp. 110-143.

Wharton, J. A., Ross, D. H., Treacy, G. M., Wilcox, G. D., and Baldwin, K. R. 2003. An EXAFS investigation of molybdate-based conversion coatings. *Journal of Applied Electrochemistry*. **33**, pp. 553-561.

Wichard, T., Mishra, B., Myneni, S. C. B., Bellenger, J., and Kraepiel, A. M. L. 2009. Storage and bioavailability of molybdenum in soils is increased by organic matter complexation. *Nature Geoscience.* **2**, pp. 625-629.

Wirth, S. B., Gilli, A., Niemann, H., Dahl, T. W., Ravasi, D., Sax, N., Hamann, Y., Peduzzi, R., Peduzzi, S., Tonolla, M., Lehmann, M. F., and Anselmetti, F. S. 2013. Combining sedimentological, trace metal (Mn, Mo) and molecular evidence for reconstructing past water-column redox conditions: The example of meromictic Lake Cadagno (Swiss Alps). *Geochimica et Cosmochimica Acta.* **120**, pp. 220-238.

Xu, N., Christodoulatos, C., and Braida, W. 2006. Adsorption of molybdate and tetrathiomolybdate onto pyrite and goethite: Effect of pH and competitive anions. *Chemosphere.* **62**, pp. 1726-1735.

Zheng, Y., Anderson, R. F., van Geen, A., and Kuwabara, J. 2000. Authigenic molybdenum formation in marine sediments: A link to pore water sulfide in the Santa Barbara Basin. *Geochimica et Cosmochimica Acta*. **64** (24), pp. 4165-4178.

Chapter 2 Methods

2.1 Materials

2.1.1 Sediment samples

2.1.1.1 Demerara Rise, 1261 samples (DR-1261)

The samples used are from a core collected in March 2003 which was recovered during ODP Leg 207 at Site 1261 located at ~5°N off the coasts of Suriname and French Guyana (Erbacher et al., 2004, März, 2019). A 120 cm core was collected and separated into 1 cm intervals (März et al., 2019). The samples used here are from depths of 4-5 cm (DR-1261-4-5) and 18-19 cm (DR-1261-18-19). The core is an organic carbon-rich black shale deposit that was deposited around the Coniacian-Santonian Oceanic Anoxic Event (März et al., 2008). The high TOC content; high S content; the presence of redox sensitive trace metals such as Cd, Mo, V and Zn, which are deposited under anoxic, sulfidic conditions; and intervals with lower concentrations of these, combined with elevated phosphorous and Fe oxide contents during these intervals; suggest that sediments were deposited under bottom waters that cycled between euxinic and anoxic non-sulfidic conditions (März et al., 2008). The high total Mo contents support deposition beneath a euxinic water column.

Geochemical analysis of the core shows that DR-1261-4-5 contains 0.006% Mn; 1.14 wt% total Fe; 1.92 wt% total S; 8.71 wt% TOC; 53.18 wt% $CaCO_3$; and 118.00 ppm Mo (Erbacher et al., 2004a; Erbacher et al., 2004b; März, 2019). Fe speciation and a separate chromous chloride extraction (for pyrite) on the sediments show that Fe is partitioned as: Fe_{carb} (Fe associated with carbonates) = 0.14 wt%; Fe_{ox} (Fe associated with amorphous and crystalline Fe oxides, excluding magnetite) = 0.07 wt%; Fe_{mag} (Fe in magnetite) = 0.02 wt%; and Fe_{py} (pyrite) = 0.39 wt% (Bowyer, 2019; Xiong, 2019).

For DR-1261-18-19 geochemical analysis shows it contains 0.006 wt% Mn; 1.09 wt% total Fe; 1.56 wt% total S; 6.51 wt% TOC; and 57.24 wt% $CaCO_3$ (Erbacher et al., 2004a; Erbacher et al., 2004b; März, 2019). Fe speciation and a separate chromous chloride extraction (for pyrite) on the sediments show that Fe is partitioned as: Fe_{carb} = 0.15 wt%; Fe_{ox} = 0.06 wt%; Fe_{mag} = 0.02 wt%; and Fe_{py} = 0.19 wt% (Bowyer, 2019; Xiong, 2019).

2.1.1.2 Demerara Rise, 1258 samples (DR-1258)

These samples, collected in spring 2003, are from Unit IV of core 1258B from the ODP, Leg 207 which was collected from the Demerara Rise ~380 km north of Suriname (Erbacher et al., 2004). Two samples are used in this study, DR-1258-1 and DR-1258-4. The unit represents the Cenomanian/Turonian boundary event (OAE 2; ca. 95 Ma), a period of ocean anoxia and enhanced carbon burial (Hetzel et al., 2009). Hetzel et al. (2009) characterise the section as generally anoxic with temporary euxinic periods and note a linear relationship between TOC and organic sulfur, suggesting that organic matter is sulfurized. A positive correlation between Mo and sulfidized organic matter was also observed, leading to the suggestion that organic matter is an important sequestration pathway for Mo (Hetzel et al., 2009). Hetzel et al. (2009) suggest that the high ratios of reactive to total Fe indicate pyrite formation in the water column and sediments and therefore euxinic conditions. The Mo concentrations in these samples of 73.00 and 117.00 ppm are also indicative of the euxinic conditions.

Geochemical analysis of the core shows that DR-1258-1 contains 1.62 wt% total Fe; 8.57 wt% TOC; 1.95wt% total S; and 73.00 ppm Mo (Hetzel et al., 2009). Fe speciation and a separate chromous chloride extraction (for pyrite) on the sample show that Fe is partitioned as: Fe_{carb} = 0.08 wt%; Fe_{ox} = 0.07 wt%; Fe_{mag} = 0.03 wt%; and Fe_{py} = 0.63 wt% (Bowyer, 2019; Xiong, 2019).

For DR-1258-4 geochemical analysis shows that it contains 3.27 wt% total Fe; 5.69 wt% TOC; 3.03 wt% total S; and 117.00 ppm Mo.(Hetzel et al., 2009). Fe speciation and a separate chromous chloride extraction (for pyrite) on the sediments show that Fe is partitioned as: Fe_{carb} = 0.22 wt%; Fe_{ox} = 0.13 wt%; Fe_{mag} = 0.04 wt%; and Fe_{py} = 1.69 wt% (Bowyer, 2019; Xiong, 2019).

2.1.1.3 USGS Green River Shale standard (USGS-GRS)

This sample is the USGS Green River Shale, SGR-1b standard reference material, collected in 1999 from the Eocene Mahogany Formation of the Green River Shale, Colorado, a petroleum- and carbonate-rich shale facies (USGS, 2016). The samples are organic-rich with a total carbon content of 28 wt% and TOC content of 24.8 wt% (USGS, 2016). The primary source of organic matter is algal with a minor contribution from higher plants (Ingram et al., 1983). Total S content is 1.53 wt% (± 0.11); total Fe (expressed as Fe_2O_3) is 4.19 wt% and total Mo is 35.00 ppm (USGS, 2016). Pyrite is the second most abundant Fe phase in the Green River Formation after Fe-carbonates (Cole et al., 1978). This sample was used in the sequential extraction method testing to assess the validity of the method against a known standard rather than material from a known geochemical environment.

Fe speciation and a separate chromous chloride extraction (for pyrite) on the sample show that Fe is partitioned as: Fe_{carb} = 0.97 wt%; Fe_{ox} = 0.06 wt%; Fe_{mag} = 0.10 wt%; and Fe_{py} = 0.33 wt% (Bowyer, 2019, Xiong, 2019).

2.1.1.4 Aarhus Bay samples (AB-1B)

The samples used here were collected in summer 2009 from Station 6 in Aarhus Bay which is on the Baltic Sea-North Sea transition on the East Coast of Jutland, Denmark. A Rumohr corer was used to collect undisturbed sediment which was then transferred into the laboratory the

same day and stored at 6 °C before processing. Within 48 h of sampling, porewaters were removed and cores were sliced into 0.5 or 2 cm sections and added to centrifuge tubes in a glove bag under a nitrogen atmosphere before being frozen and freeze dried to remove any remaining porewaters (Goldberg, 2019).

Aarhus Bay sediments are characterised by Thamdrup et al. (1994) through direct chemical measurements as follows. The oxic zone in the sediments is 1- 5 mm thick, below which sediments become anoxic with sulfate reduction resulting in sulfidic porewaters. However, although H_2S is continually produced in the upper 3.5 cm below the oxic zone, it is undetectable as it is completely consumed in redox reactions. FeS_2 concentrations increase downcore but dominate at all depths in terms of reduced sulfur compounds. A large pool of Mn reduction and intense cycling occurs in the top 2 cm of the sediments whereas Fe reduction extends to 6 cm below the sediment-water interface. FeS_2 concentrations increase downcore but dominate at all depths in terms of reduced sulfur compounds. A significant pool of sedimentary non-FeS bound Fe^{2+} is found in the top 2 cm, below which it declines as FeS increases.

In the sample used for the sequential extraction (AB-1B-3), TOC is 3.73 wt%; total Fe is 2.74 wt%; and total Mo is 1.65 ppm (Goldberg, 2019). Fe speciation and a separate chromous chloride extraction (for pyrite) on the sample show that Fe is partitioned as: Fe_{carb} = 0.23 wt%; Fe_{ox1} = 0.45 wt% (amorphous Fe (oxyhydr)oxides); Fe_{ox2} = 0.22 wt%; Fe_{mag} = 0.09 wt%; and Fe_{py} = 0.29 wt%. Porewater Fe is 97.2 µM, porewater Mn is 22.5 µM, and porewater Mo is 45.7 nM at 2.5 cm depth (Goldberg, 2019). This sample was chosen to represent a low-Mo environment to test the efficacy of the method for samples with low Mo concentrations.

The sample used for XANES in Chapters 3, 4 and 6 (AB-1B-2) is bulk untreated sediment from 1.5 cm depth. TOC is 3.69 wt% and total Fe is 2.80 wt% (Goldberg, 2019). Fe speciation and a separate chromous chloride extraction (for pyrite) on the sample show that Fe is partitioned as: Fe_{carb} = 0.19 wt%; Fe_{ox1} = 0.39 wt%; Fe_{ox2} = 0.21 wt%; Fe_{mag} = 0.09 wt%; and Fe_{py} = 0.22 wt% (Goldberg, 2019).

2.1.1.5 Lake Cadagno samples (LC-1A)

These samples were collected in summer 2014 from the part of Lake Cadagno, Switzerland where deposition takes place beneath a euxinic water column (46°33'44''N, 8°42'41''E; Xiong et al., 2019). Short gravity cores (up to 35 cm) were taken from a permanently moored platform and were stored upright, refrigerated at 4°C until processing, which was within 6 h. Cores were split into 1-2 cm sections under a nitrogen atmosphere in a glove bag and stored in 50 mL centrifuge tubes. While under a nitrogen atmosphere, porewater was extracted from all samples using Rhizons®. Sediment samples were then removed from the glove bag, immediately frozen, freeze-dried and then stored frozen prior to analysis (Xiong et al., 2019).

The samples are from organic-rich shales in the euxinic part of Lake Cadagno, a meromictic lake which is permanently stratified. The water column redox-transition zone, which is a few m thick, is located between 10 m – 12 m deep and separates the upper oxic layer from the lower anoxic layer (Del Don et al., 2001). In the euxinic part of the water column, sulfide concentrations range from ~20-70 µM (Xiong et al., 2019).

Sample LC-1A-5 which was used in the sequential extraction (Chapter 3), is from a depth of 8.75 cm. TOC is 12.12 wt%, total Fe is 4.81 wt% and porewater sulfide is 730 µM (Xiong, 2019). Fe speciation and a separate chromous chloride extraction (for pyrite) show that Fe is

partitioned as: Fe_{ox1} = 0.27 wt%; Fe_{ox2} = 0.91 wt%; Fe_{mag} = 0.34 wt%; and Fe_{py} = 0.89 wt% (Xiong et al., 2019).

Sample LC-1A-6 was also used in the sequential extraction (Chapter 3) and is from a depth of 11.25 cm. TOC is 8.88 wt%, total Fe is 5.16 wt% and porewater sulfide is 571 µM (Xiong, 2019). Fe speciation and a separate chromous chloride extraction (for pyrite) show that Fe is partitioned as: Fe_{ox1} = 0.02 wt%; Fe_{ox2} = 0.92 wt%; Fe_{mag} = 0.46 wt%; and Fe_{py} = 0.94 wt% (Xiong et al., 2019).

Initial screening of multiple XANES scans from 15 sediment samples deposited beneath the same euxinic water column resulted in four XANES spectral types, EUX-1, EUX-2, EUX-3 and EUX-4 from four different sediment samples (Chapter 5).

EUX-1 is a mixture of samples from 21.25 and 29.0 cm deep. The combined material was treated to remove Mn and Fe oxides and silicates using the sequential extraction method (Chapter 3) but then an additional chromous chloride extraction was performed to remove pyrite (Acholla and Orr (1993) to isolate a pure Mo-organic fraction (Section 2.1.4). The organic material was washed with deoxygenated 18.2MΩ cm Type 1 deionized water and air-dried under a nitrogen atmosphere. As the EUX-1 sample is a combination of two sediment samples the geochemical data is therefore presented as ranges between the two. Porewaters contain 2.69 – 370.50 µM sulfide and 0.79 – 45.48 µM Fe(II) (Xiong, 2019). In the sediment TOC is 2.12 – 2.51 wt% and total Fe is 5.70 – 7.00 wt% (Xiong, 2019). Fe speciation shows that Fe is partitioned as: Fe_{ox1} = 0.26 – 0.98 wt%; Fe_{ox2} = 0.56 – 1.12 wt%; Fe_{mag} is 0.15 – 0.69 wt%; and Fe_{py} is 2.43 – 3.94 wt% (Xiong et al., 2019).

EUX-2 is from bulk, untreated sediment from a depth of 4.75 cm and porewaters contain 855.25 µM sulfide and 0.17 µM Fe(II) (Xiong). In the sediment TOC is 12.95 wt% and total Fe is 4.32 wt% (Xiong). Fe speciation shows that Fe is partitioned as: Fe_{ox1} = 1.64 wt%; Fe_{ox2} = 0.83 wt%; Fe_{mag} = 0.08 wt%; and Fe_{py} = 0.46 wt% (Xiong et al., 2019).

The remaining samples used in Chapter 5 (EUX 3 and 4) were treated to remove Mo phases using the methods outlined in Chapter 3. EUX-3 (29.0 cm depth) is sediment that was treated to remove Mn and Fe-oxides, apart from magnetite. Porewaters contain 2.69 µM sulfide and 45.48 µM Fe(II) (Xiong, 2019). In the sediment TOC is 2.12 wt% and total Fe is 5.70 wt% (Xiong, 2019). Fe speciation data shows that Fe is partitioned as: Fe_{ox1} = 0.98 wt%; Fe_{ox2} = 1.12 wt%; Fe_{mag} = 0.15 wt%; and Fe_{py} = 0.15 wt% (Xiong, 2019). EUX-4 is a mixture of samples from the same core that were treated to remove Mn and Fe-oxides and silicates leaving only Mo associated with organic material and pyrite.

2.1.1.6 Golfo Dulce

The nitrogenous samples used in this study in Chapters 4 and 5 are bulk, untreated sediment from the 22-24 cm depth section of a short core originally collected from the anoxic sediments of Golfo Dulce, a nitrogenous basin in Costa Rica in spring 2008 (Guilbaud, 2015; Poulton, 2016). Once collected, the core was immediately processed under a nitrogen atmosphere where porewaters were removed before sediments were frozen and transported to the University of Leeds where they were freeze-dried and frozen until immediately prior to use (Poulton, 2016). The Golfo Dulce basin in Costa Rica is a 200 m deep tropical fjord with anoxic waters below 100 m and nitrogenous conditions are indicated by N_2 production in the water column (Thamdrup et al., 1996; Dalsgaard et al., 2003; Ferdelman et al., 2006).

TOC in these samples is 1.36 wt% and Fe speciation and a separate chromous chloride extraction (for pyrite) on the sediments show that Fe is partitioned as: Fe_{carb} = 0.61 wt%; Fe_{ox1} = 0.82 wt%; Fe_{ox2} = 0.95 wt%; Fe_{mag} = 0.75 wt%; and Fe_{py} (pyrite) = 0.41 wt% (Guilbaud, 2019).

2.1.1.7 Eastern Mediterranean sample

The Eastern Mediterranean sample was collected in summer 2014 approximately 25km west of Haifa, Israel (32 41.0449N 34 42.4279E) using a gravity core (Krom, 2015). Upon collection, the core was transferred into an anaerobic atmosphere for processing, where porewaters were removed and the core was frozen, freeze dried and stored frozen (Krom, 2015). Aspostolia-Maria et al. (2020) show that seawater in the area the sample was collected from is oxygenated (based on data from Boyer at al., 2013).

The sample used in Chapter 5 for OX1 is bulk, untreated sediment from the 1 cm depth section. Fe sequential extraction and pyrite extraction on this sample shows that Fe_{ox1} = 0.82 wt%; Fe_{ox2} = 2.23 wt%; Fe_{mag} = 0.57 wt%; and Fe_{py} = 0.002 wt%. The presence of pyrite indicates the presence of dissolved sulfide in porewaters.

2.1.1.8 Lake La Cruz

The ferruginous sample used in Chapter 5 is from a of 23.75 cm from a core collected from Lake La Cruz, Spain in summer 2014 using a gravity corer which was then processed under a nitrogen atmosphere (Thompson, 2018). Porewaters were filtered using Rhizons® and aliquots were immediately analysed for dissolved Fe(II) and P. Sediment samples were frozen prior to and during transport to the labs where they were then freeze-dried. Samples remained frozen until immediately prior to use (Thompson 2018). Lake La Cruz is an Fe-rich meromictic lake with anoxic waters below ~14 m (Rodrigo et al., 2001). The ferruginous conditions in waters below the chemocline arise as a result of low sulfate concentrations which allow the

accumulation of Fe(II) originating from the underlying Fe-rich marls (Miracle et al., 1992; Julia et al., 1998).

TOC in this sample is 8.9 wt% and total Fe is 0.73 wt% (Thompson, 2015). Porewaters for this sample are characterised by 0.9 µM S^{2-}, 432.9 µM dissolved Fe(II) and 1.4µM dissolved SO_4, while Fe speciation and a separate chromous chloride extraction (for pyrite) on the sample show that Fe is partitioned as: Fe_{ox1} = 0.02 wt%; Fe_{ox2} = 0.11 wt%; Fe_{mag} = 0.004 wt%; and Fe_{py} = 0.10 wt% (Thompson, 2015).

2.1.2 Synthetic minerals

2.1.2.1 δMnO₂

δMnO_2 was prepared after Villalobos et al., (2003). 1280 mL of 197.7 mM potassium permanganate ($KMnO_4$) was added to 1440 mL of 486.1 mM sodium hydroxide (NaOH) while stirring. 1280 mL of 296.6 mM manganese chloride tetrahydrate ($MnCl_2 \cdot 4H_2O$) was then added over ~35 m to form a black precipitate. The solution was left to settle for ~ 4 h before the majority of the supernatant was removed. The pH of the remaining supernatant was checked (as it is expected to be ~ pH 7) and adjusted if necessary. The remaining solution was transferred to 250 mL Nalgene bottles which were centrifuged at 4642 x g for 20 m before the supernatant was removed and discarded. The remaining paste was mixed with 1 M sodium chloride (NaCl) and shaken for 1 h. The NaCl wash cycle was repeated five times with the last wash taking place overnight. 18.2 MΩ·cm MilliQ water (hereafter referred to as MQ) was then added and the solution was shaken for 1 h before the pH was checked (this is expected to be ~ pH 12.8). The MQ wash cycle was repeated 10 times with wash periods ranging from 30 m to overnight. The pH of the slurry was adjusted to pH 8. pH adjustments were made using 10% (hydrochloric acid) HCl and 1 M (sodium hydroxide) NaOH. The paste was transferred to weigh boats and air dried before being ground to a fine powder and frozen until required. Where

using δMnO_2 slurry for experiments, a gravimetric analysis was performed by removing 1 mL of slurry and air-drying before weighing to determine g/mL. Slurries were refrigerated until required.

2.1.2.2 Ferrihydrite

Ferrihydrite was prepared after Cornell and Schwertmann (2003). 580 mL of 1M NaOH was added to 1 L of 0.2 M iron nitrate ($Fe(NO_3)_3 \cdot 9H_20$) while stirring. The pH of the solution was monitored while adding the last 80 mL of NaOH to ensure it did not exceed pH 7. The solution was transferred to a 5 L beaker and washed three times a day for 5 days by adding MQ to ~4 L then removing and discarding the supernatant once the ferrihydrite precipitate had settled. The pH of the solution was then measured again and raised to pH 7 by the dropwise addition of 5 M NaOH. The remaining slurry was transferred to 250 mL Nalgene bottles which were centrifuged to condense the slurry into one 250 mL Nalgene bottle. The slurry was poured into weigh boats and oven-dried overnight at 40°C before being ground into a fine powder and frozen until required. Where using ferrihydrite slurry for experiments, a gravimetric analysis was performed by removing 1 mL of slurry and air-drying before weighing to determine g/mL. Slurries were refrigerated until required.

2.1.2.3 Goethite

Goethite was prepared after Cornell and Schwertmann (2003). 50 mL of 1M $Fe(NO_3)_3 \cdot 9H_2O$ was added to 90mL of 5M potassium hydroxide (KOH) and 560 mL of MQ in a 1 L Nalgene bottle. The sealed bottle was then oven-heated for 60 h at 70°C. The supernatant was removed and the goethite precipitate was washed with MQ water before being oven-dried overnight at 50°C. The material was then ground to a powder and frozen until required. Where using goethite slurry for experiments, a gravimetric analysis was performed by

removing 1 mL of slurry and air-drying before weighing to determine g/mL. Slurries were refrigerated until required.

2.1.2.4 Magnetite

Magnetite was prepared anoxically after Cornell and Schwertmann (2003). A 3.33 M KOH/0.27 M KNO_3 solution was prepared under normal laboratory conditions and then degassed with N_2 for 1 h before storing in the anaerobic chamber. A 0.3 M Fe(II) solution was prepared under a nitrogen atmosphere. In the anaerobic chamber 560 mL of the 0.3 M Fe(II) solution was heated in a Schott bottle to 90°C then 240 mL of the 3.33 M KOH/0.27 M KNO_3 solution was added by dropwise addition over several minutes. The mixture was heated at 90°C for 60 m with stirring and once cooled added to 250 mL Nalgene bottles and removed from the anaerobic chamber. The magnetite slurry was centrifuged and the supernatant discarded. The remaining paste was washed with MQ water three times and the remaining slurry was oven-dried at 50°C overnight.

2.1.2.5 Organic analogues

5 M phosphoric and acetic acids (H_3PO_4 and CH_3CO_2H) and 187.5 mM tannic acid ($C_{76}H_{52}O_{46}$) were all used to act as organic analogues for the Mo standards. Acids were purchased from Sigma Aldrich and were prepared with MQ.

2.1.2.6 Pyrite

Synthetic pyrite was purchased from Strem Chemicals in line with previous Mo-pyrite adsorption experiments (Bostick et al., 2003; Xu et al., 2006). To remove oxidised species, pyrite was washed successively with MQ, 0.5 M HCl and 0.01 M sodium sulfide ($Na_2S{\cdot}9H_2O$) under a nitrogen atmosphere after Bostick et al., (2003). The washed pyrite was left to air-dry in the anaerobic chamber and then remained stored under a nitrogen atmosphere until required.

2.1.3 Molybdenum adsorption to synthetic minerals

MoO_4 and MoS_4 were adsorbed to dry minerals and mineral slurries after Peacock and Sherman (2004). Stock solutions of Na_2MoO_4 and $(NH_4)_2MoS_4$ were prepared to 1000 ppm Mo. 2 g of dry mineral or mineral slurry equivalent was added to 50 mL centrifuge tubes with the Mo stock solution and 0.1 M NaCl up to 40 ml. The amount of Mo stock solution added was adjusted according to the amount of Mo sorption required. Initial pH was adjusted to pH 5.5 and centrifuge tubes were shaken end-over end for 2 h. pH was measured and, if necessary, adjusted to pH 5.5 and tubes were shaken end-over-end for a further 24 h. The final pH was recorded and tubes were centrifuged for 4 m at 4643 x g. The supernatant was removed and discarded and then samples were washed three times in MQ before being either freeze dried or air dried. For pyrite and all minerals with MoS_4 adsorbed, sorption was completed under a nitrogen atmosphere using deoxygenated solutions.

2.1.3.1 Molybdenum solutions

For the molybdate solutions, stock solutions of Na_2MoO_4 purchased from Sigma Aldrich were made volumetrically using MQ. The sodium molybdate was stored in the laboratory at room temperature.

For tetrathiomolybdate, stock solutions of $(NH_4)MoS_4$ purchased from Sigma Aldrich were made volumetrically using degassed MQ under a nitrogen atmosphere. Stock solutions were mainly discarded if not used immediately but some were frozen on the same day they were made at -20°C then defrosted and used at a later date to prevent alteration. The ammonium tetrathiomolybdate was sealed in a minimum of three zip-lock bags in the anaerobic chamber and stored in the laboratory toxics fridge when not in use.

2.1.4 Separating organic material using the chromous chloride method

Acholla and Orr (1993) showed that a chromous chloride extraction can remove pyrite from a sample, leaving the organic fraction intact and suitable for XANES analysis. Therefore, using this method, an organic Mo fraction from Lake Cadagno was separated to confirm the presence of organic-Mo in this euxinic environment utilising XAS techniques. The organic + pyrite fraction was isolated initially by performing the sequential extraction, up to and including the Mo_{sil} extraction, on 60 samples, each weighing ~0.05 g, from the euxinic part of Lake Cadagno to remove Mn and Fe oxides and silicates.

Remaining material from the samples was then combined by adding four samples to 50 mL centrifuge tubes (15 tubes in total). 40 mL of MQ was then added to each tube and samples were shaken for 90 m. Samples were centrifuged at 4643 x g for 6 m and the supernatant was removed and discarded. Material from the 15 centrifuge tubes was condensed into three tubes by washing samples out with MQ so that each of the three remaining tubes contained 40 mL of water. Samples were centrifuged again at 4643 x g for 6 m and the supernatant discarded before they were finally condensed into one 50 mL centrifuge tube with 40 mL of MQ which was removed and discarded following centrifugation. The final sample was frozen overnight then freeze-dried and the final combined weight was 0.4 g.

The chromous chloride extraction (after Acholla and Orr, 1993) was then performed to remove pyrite from the sample, leaving only the organic fraction intact. 250 mL of acidified 2 M chromous chloride (made to volume with 0.5 M HCl) was added to a 500 mL Schott bottle with zinc pellets and nitrogen gas bubbled through the solution until it turned blue, indicating that it had been reduced. 80 mL of this reduced solution ($CrCl_2$) was added to a syringe (Figure 2.1) with 40 mL of concentrated HCl. 0.4 g of the freeze-dried sample was added to a reaction vessel with 20 mL of ethanol under a nitrogen atmosphere in an anaerobic chamber and the

vessel was sealed. This was transferred to a fume cupboard outside of the anaerobic chamber and nitrogen gas was immediately pumped through the vessel to prevent oxidation of the sample. A collection flask containing 140 mL 3% silver nitrate ($AgNO_3$) was connected to the reaction vessel. While the reaction vessel was heated, the $CrCl_2$/HCl solution was added dropwise and a dark precipitate was observed in the collection flask to the point where it became difficult to see further precipitation. The collection flask was therefore replaced halfway through the experiment. After this point the $AgNO_3$ in the flask changed colour to pale brown but no further precipitate was observed so the reaction was deemed to be complete after all of the $CrCl_2$/HCl solution had been added. Once cooled, the reaction vessel was disconnected, sealed immediately with parafilm and returned to the anaerobic chamber.

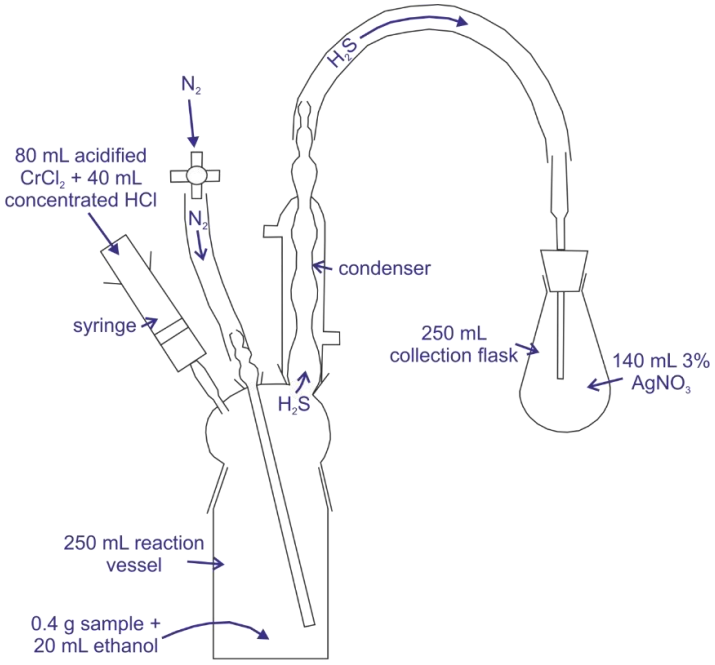

Figure 2.1 *Experimental set-up for chromous chloride pyrite extraction (after Acholla and Orr, 1993).*

The solution from the reaction vessel was passed through a Whatman No. 40 filter paper and the main residue was added to a 50 mL centrifuge tube and shaken with deoxygenated MQ. Three washes with deoxygenated MQ were carried out in the anaerobic chamber with the organic residue left to settle between washes. To test for the presence of chloride, 10 mL of

the supernatant from each wash was shaken with 2-3 drops of 5% HNO_3 + 2-3 drops of 1.7% $AgNO_3$ and these reactions indicated that all the chloride had been removed. Following these washes the organic residue was left to air-dry in the anaerobic chamber. The sample was added to a Kilner jar in the anaerobic chamber with two sachets of AnaeroGen™ to prevent oxidation during transportation to the Diamond Light Source synchrotron and the jar was opened under an argon atmosphere in the anaerobic chamber at DLS. The sample was made into a pressed pellet with cellulose and sealed between three layers of Kapton film in the DLS anaerobic chamber before it was presented to the beam.

2.2 Iron sequential extractions

2.2.1 Fe sequential extraction procedures

Fe sequential extractions were performed by other workers for this study in a similar way to Mo sequential extractions (Chapter 3) with ~50 mg sediment being treated with various extractants with centrifugation and removal of the supernatant between steps.

For modern sediments (Aarhus Bay, Eastern Mediterranean, Golfo Dulce, Lake Cadagno and Lake La Cruz) the procedures are based on the method used by Goldberg et al. (2012) and Xiong et al. (2019) and a modified version of the method of Poulton and Canfield (2005). Specifically the Fe_{ox1} extraction removes Fe associated with Fe (oxyhydr)oxides by treating sediment with 5 mL of 0.5 M HCl for 1 h (any Fe(II) removed in this extraction is measured immediately by the ferrozine method (spectrophotometrically) and this fraction is subtracted from the Fe_{ox1} total); the Fe_{ox2} fraction removed Fe in crystalline Fe oxides by treating sediment with 10 mL of sodium dithionite for 2 h; and the Fe_{mag} extraction removes Fe in magnetite by treating sediment with ammonium oxalate for 6 h.

For ancient sediments (Demerara Rise and USGS Green River Shale), a modified version of the extraction outlined in Poulton and Canfield (2005) was used. Specifically the Fe_{carb} extraction removes Fe associated with carbonates by treating sediment with 10 mL of sodium acetate (buffered to pH 4.8 with acetic acid) at 50°C for 2 h; the Fe_{ox} extraction removes Fe associated with Fe oxides, excluding magnetite, by treating sediment with 10 mL of sodium dithionite for 2 h; and the Fe_{mag} extraction removes Fe in magnetite by treating sediment with ammonium oxalate for 6 h.

Alongside both the modern and ancient Fe sequential extractions, pyrite Fe (Fe_{py}) was determined on separate samples of 0.5-1.0 g using the two-step boiling HCl and chromous chloride distillation ($Cr(II)Cl_2$) method which extracts and traps sulfide phases as Ag_2S. The boiling HCl distillation removes acid volatile sulfides (AVS; 8 mL used) and the $Cr(II)Cl_2$ distillation removes pyrite sulfur (5 mL used). Fe_{py} was then calculated stoichiometrically from the Ag_2S mass for FeS (AVS) and FeS_2 (pyrite; Canfield et al., 1986; Fossing and Jørgensen, 1989).

All sequential extractions were measured using a Thermo Scientific iCE-3000 series flame atomic absorption spectrometer (AAS).

2.2.2 Fe sequential extraction and pyrite removal solutions

0.5 M hydrochloric acid (HCl) was made volumetrically by adding ARISTAR® Hydrochloric acid fuming 37% (from VWR Chemicals) to MQ. Solutions were stored in the laboratory at room temperature.

Sodium dithionite was made volumetrically using trisodium citrate dehydrate, 99% ($Na_3C_6H_5O_7{\cdot}H_2O$) from Alfa Aesar (58.82 g for 1 L); sodium dithionite from Fisher Scientific (50 g

for 1 L), glacial acetic acid from Sigma Aldrich (20 mL for 1 L); and MQ. The solution was prepared immediately before use and was not stored for further extractions.

Ammonium oxalate was made volumetrically using ammonium oxalate monohydrate ACS reagent ≥99% ($(NH_4)_2C_2O_2 \cdot H_2O$) from Sigma-Aldrich (28.42 g for 1 L); oxalic acid dihydrate laboratory reagent grade ($C_2H_2O \cdot 2H_2O$) from Fisher Scientific (21.43 g for 1 L); and MQ. Solutions were stored in the laboratory at room temperature.

1 M sodium acetate was made volumetrically (82.03 g for 1 L) with glacial acetic acid from Sigma Aldrich to buffer to pH 4.8 and MQ.

For AVS removal by distillation, 50% hydrochloric acid (HCl) was made volumetrically by adding ARISTAR® Hydrochloric acid fuming 37% (from VWR Chemicals) to MQ. Solutions were stored in the laboratory at room temperature.

For pyrite removal by distillation 6M $Cr(II)Cl_2$ solution was made volumetrically using Sigma Aldrich Chromium (II) Chloride in 50% HCl (ARISTAR® Hydrochloric acid fuming 37%).

2.3 Total digests

2.3.1 Total digest procedure

Total concentrations of Mo, Fe, Mn and Al were determined by total digest. ~0.1 g of sediment was added to a ceramic crucible and samples were ashed for 8 h at 550°C. Samples were then washed into Teflon pots with 5 mL of HNO_3 and 2 mL of HF and 2 drops of $HClO_4$ were added. Samples were heated until fully evaporated and any residual HF was neutralised with 2 mL of 0.8 M H_3BO_3 which was heated until fully evaporated. Solids were resolubilised with either 50% HCl or concentrated HNO_3 under heat until the solution was clear, Solutions

were then transferred to 100 mL volumetric flasks and Teflon beakers and funnels were rinsed 5x with MQ to ensure complete transfer. Once completely cooled, flasks were made up to volume with MQ and inverted 10x to mix. ~12 mL of the solution was stored for analysis and the remainder was discarded. Mo, Fe and Al total digests were analysed by ICP-MS with almost all samples except for Aarhus Bay analysed at the University of Leeds and Aarhus Bay samples analysed at the University of Bristol). The non-silicate Mn fraction, consisting of Mn oxides, Mn carbonates and particulate Mn^{2+}, was determined on a separate sediment sample by treatment with hydroxylamine-HCl for 24 h (Poulton and Canfield, 2005). Mn was determined by AAS.

2.3.2 Total digest solutions

Concentrated nitric acid 69% ARISTAR® for trace analysis (HNO_3) from VWR Chemicals was added directly to samples to wash them from ceramic crucibles to Teflon pots. 2 mL of analytical reagent grade hydrofluoric acid 40% (HF) from Fisher Scientific was added directly to samples. Concentrated hydrochloric acid (ARISTAR® Hydrochloric acid fuming 37% from VWR Chemicals) was added directly to samples.

2.4 Total organic carbon (TOC) analysis

For all samples except the Aarhus Bay samples, carbonate phases were removed with 10% HCl to determine total inorganic carbon (TIC) and TOC was measured on a LECO C/S analyser at the University of Leeds. For the Aarhus Bay samples, carbonate phases were removed by pre-treatment of samples with 4 N HCl before TOC was measured on a LECO CS244.

2.5 Porewater analysis

Porewaters were extracted from the sediment in centrifuge tubes or directly from the cores using Rhizon® samplers (generally with a 0.1 µM pore diameter) into sample containers under

a nitrogen atmosphere. Fe(II) and sulfide analyses were performed on a spectrophotometer. For porewater Fe(II) analysis, 1 mL of porewater was added to 0.5 mL of a 0.02 M ferrozine solution (Viollier, et al., 2000). For sulfide analysis, 1 mL of porewater was added to 50 µL of 20% Zn-acetate and sulfide was determined via the methylene-blue method (Cline, 1969). Porewater Mn and Mo were analysed by ICP-MS (Element2) at the University of Bristol or ICP-MS at the University of Leeds.

2.6 Mo isotope analysis

Mo isotope analyses were completed by Goldberg (2019) to determine δ^{98}Mo in the Aarhus Bay samples, ~50 mg of sediment was dissolved in Teflon beakers with HNO_3/HF (0.75 mL and 3 mL respectively) with heating for 48 h. In preparation for ion-exchange purification of Mo and isotopic analysis, solutions were spiked with a mixed ^{97}Mo-^{100}Mo tracer. Using the methods of Archer and Vance (2008) and Goldberg et al. (2009), a pure Mo fraction was obtained using Bio-Rad AGMP-1 anion resin. Mo isotope measurements were completed at the University of Bristol using a ThermoFinnigan Neptune MC-ICP-MS. Solutions were presented to the MC-ICP-MS in a 2% (v/v) HNO_3 solution and mass discrimination correction was achieved using the double spike method described in Siebert et al. (2001) and Archer and Vance (2008). Mo isotopes are reported relative to an internal CPI Mo ICP-MS standard in the delta per mil notation ($\delta^{98}Mo = (^{98/95}Mo_{sample} / {}^{98/95}Mo_{standard}) \times 1000$) after Archer and Vance (2008) (for further method description see Goldberg et al., 2012). Reproducibility of the measured δ^{98}Mo ratios on the CPI standard and replicate samples was better than 0.08‰ (see Archer and Vance, 2008).

2.7 Trace metals cleaning procedures

To address the potential issue of contamination from polypropylene centrifuge tubes (Braithwaite, 1994), a series of blanks (i.e. samples with reagents but no sediment sample)

were run for steps 3, 5, 7, 9, 11 and 13 of the sequential extraction. Two blank samples for each reagent (one of which used glassware and plasticware rinsed 5 x in MQ, then added to a 1% HNO_3 acid bath overnight before being rinsed again 5 x in MQ, and one of which used untreated glassware and plasticware) were analysed by ICP-MS to determine whether there was any Mo contamination from the reagents, glassware or plasticware. As the method development had not been completed for Mo in the ICP-MS at that point, ppb concentrations were determined using a standard additions technique. The blanks showed Mo contamination of <5 ppb (Figure 2.2 and Table 2.1) which appeared to be the result of reagent contamination rather than contamination from glassware or plasticware as the results did not correlate with HNO_3 cleaned glassware/plasticware.

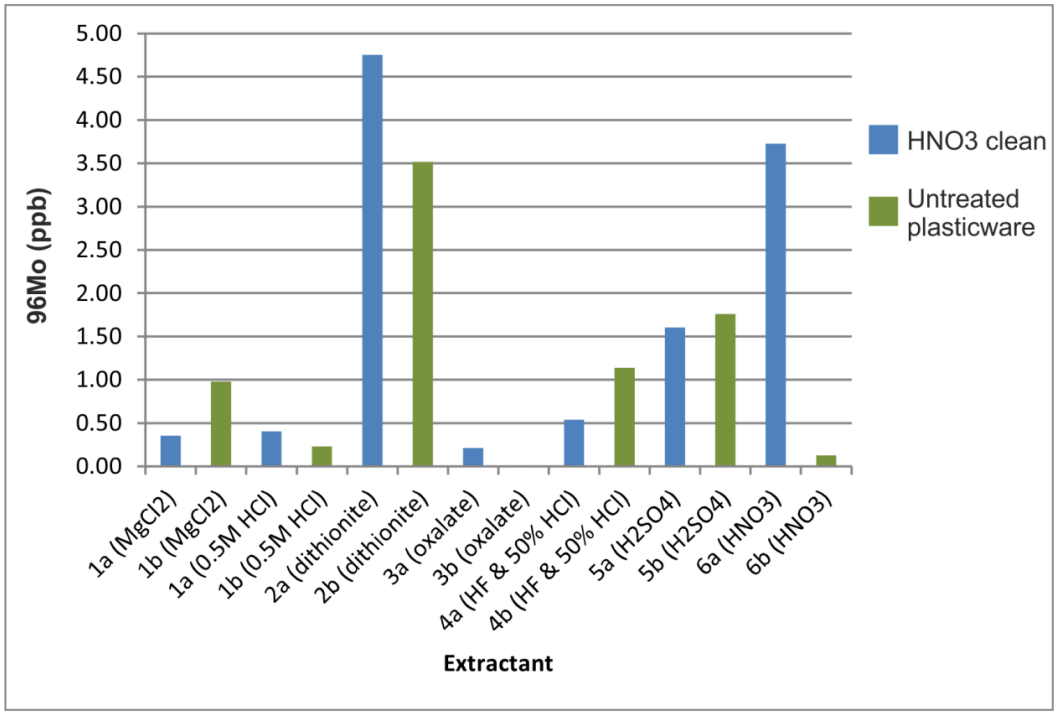

Figure 2.2 *Mo concentrations in blanks run using reagents from the Mo sequential extraction for pre-cleaned glassware and plasticware and glassware and plasticware that had not been pre-cleaned.*

Table 2.1 *Mo concentrations from a set of blanks to identify potential contamination from reagents and plasticware for a) HNO_3 clean glassware/plasticware and b) untreated glassware/plasticware.*

Blank	*96Mo (ppb)	Extractant	HNO_3-clean
1a	0.35	$MgCl_2$	Y
1b	0.98	$MgCl_2$	N
1a	0.41	0.5 M HCL	Y
1b	0.23	0.5 M HCL	N
2a	4.75	Dithionite	Y
2b	3.52	Dithionite	N
3a	0.21	Oxalate	Y
3b	0.01	Oxalate	N
4a	0.54	HF & 50% HCl	Y
4b	1.14	HF & 50% HCl	N
5a	1.60	H_2SO_4	Y
5b	1.76	H_2SO_4	N
6a	3.73	HNO_3	Y
6b	0.13	HNO_3	N

It was therefore determined that there was no requirement to pre-clean glassware or plasticware prior to use for trace metals analysis, although unopened bags of centrifuge tubes and pipette tips were kept in the Mo clean area of the lab and used only for the Mo extractions. Contamination in the Mo_{ox2} fraction (10 mL sodium dithionite) was the highest at 4.75 ppb and when compared to the lowest total Mo value from an oxic core held in Leeds (1.3 ppm) this introduces an error of 0.38%. To identify any contamination two blanks are included with each sample run. Although the blank results did not indicate contamination from glassware or plasticware, cleaning protocols for trace metals analysis were introduced to reduce contamination risks. An area of the lab was allocated for trace metals work with a separate sink, drying oven and set of pipettes. All glassware was rinsed 5 x in MQ, then added to a 1% HNO_3 acid bath overnight before being rinsed again 5 x in MQ.

2.8 Synchrotron sample preparation

Samples were presented to the synchrotron beam either as pressed pellets, micro-thin sections, powders or solutions.

2.8.1 Pressed pellets

Samples were made into pressed pellets both at Diamond Light Source and the University of Leeds by combining finely ground material with cellulose before applying pressure with either a hydraulic pellet press or a hand-held pellet press. Where possible the hydraulic press was used as this forms a more stable pellet. However, for air-sensitive samples, pellets were made using a hand-held pellet press in the anaerobic chamber. For these samples, pellets were then sealed between three layers of Kapton tape before they were removed from the chamber and immediately presented to the beam.

2.8.2 Micro-thin sections

The majority of natural samples presented to the synchrotron beam were prepared at the University of Leeds using a novel sample preparation protocol developed for this project (Figure 2.3).

Material that had either been extracted via the sequential extraction method (to represent specific Mo phases), or material that had not been treated (to represent bulk Mo in the sample) was embedded in Struers Epofix Resin in a 1 cm (diameter) circular mould on a glass slide to create blocks (Figure 2.3). These blocks were then cut and ground to ~120 µM on a Buehler PetroThin Thin Sectioning system before being polished to < 100 µM on a Buehler EcoMet® Grinder Polisher to create self-supporting micro-thin sections.

f 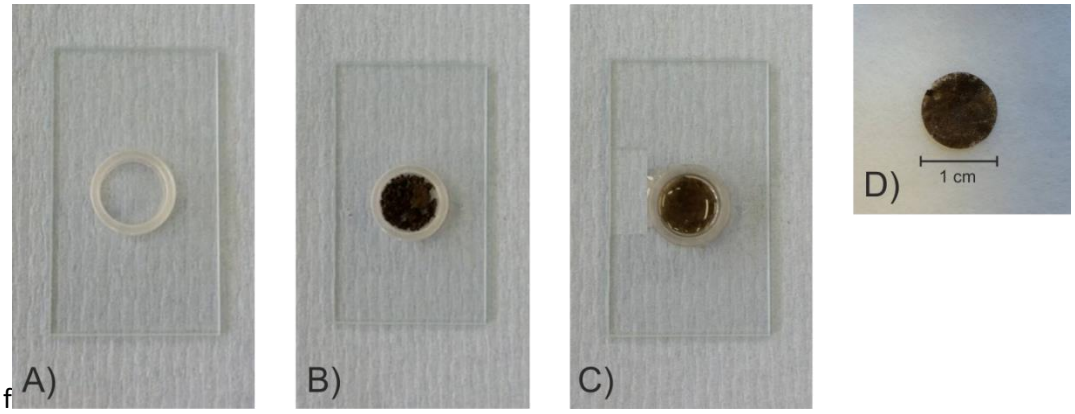

Figure 2.3 *Photographs of the procedure for making micro-thin sections: A) the mould is glued to a slide and grease is added to the outside of the mould and mould releasing agent to the inside; B) the sample is added to the mould ensuring good coverage over the slide; C) resin is added to the mould and left to set; D) the face of the resin block is cut and ground to give a flat surface and then the mould and resin block are removed from the slide, turned over and stuck back onto a slide with wax then ground and polished to <100 µM before removing and cleaning.*

2.8.3 Powders

In some cases there was either not enough material to make pressed pellets or samples were air sensitive and it proved difficult to make pellets anaerobically. For these samples materials was evenly spread onto Kapton tape (either in the main lab or anaerobic chamber depending on whether samples were air-sensitive) and then sealed between three further layers of Kapton tape before being presented to the beam.

2.8.4 Solutions

Some of the standards were presented to the beam as solutions. These were presented in polypropylene centrifuge tubes attached to the sample holder with Kapton tape. For air-sensitive samples, the tube lids were covered with parafilm and sealed with tape to prevent oxygen ingress.

2.9 ICP-MS analysis

ICP-MS was selected to determine Mo concentrations in sediments due to the low detection limits compared to inductively coupled plasma optical emission spectrometry (ICP-OES). Low parts per trillion (ppt) detection limits are possible with ICP-MS which makes it ideal for analysing diluted Mo fractions from sediments with already potentially low Mo concentrations.

Figure 2.4 provides an overview of the Thermo iCAP Qc ICP-MS used to analyse all samples in this study. Samples were diluted according to the sample matrix (Table 2.2) to reduce the levels of dissolved solids to acceptable levels (generally below 0.2%) to avoid compromising instrument stability. Each sample was made up to 10 mL with MQ and included 100 µL 100 ppb Rh standard to monitor for signal drift.

The following overview of the ICP-MS is from Thomas (2013). The autosampler removes some of the sample which is pumped into the nebuliser with a peristaltic pump where it is aspirated to convert it into a fine aerosol. Fine droplets are separated from larger droplets in the baffled cyclonic spray chamber by centrifugal force and it is these fine droplets that are transported to the plasma torch. The plasma torch consists of three concentric quartz tubes wrapped by a radiofrequency (RF) silver-coated copper coil at the end furthest from the spray chamber. Argon (Ar) gas is flowed between the middle and outer tubes at ~12-17 L/min and the sample aerosol generated in the nebuliser introduces the sample to the torch at ~1 L/min through the central injector tube. When an oscillating current is delivered to the RF coil, this creates a high intensity electromagnetic field in this area of the torch. A high-voltage spark is then delivered to the Ar gas which, in combination with the electromagnetic field, ionises the Ar atoms, forming a plasma which reaches temperatures from 6000 – 10000 K. The sample aerosol is injected into the plasma at high velocity, where it too is ionised, mainly by collision with energetic Ar electrons. This ion beam then enters the interface area where the pressure

differential between the plasma torch (760 torr) and the analyser region (10^{-6} torr) is reduced. The interface region consists of two nickel cones (a sampler cone and a skimmer cone) which both have very small orifices (1.1 mm for the sample cone and 0.5 mm for the skimmer cone) for the ion beam to pass through. A mechanical roughing pump maintains a vacuum of ~1-2 torr in this area which facilitates a two-step reduction in pressure as the beam passes through each cone. As the beam emerges from the second cone it is directed through a single extraction lens followed by a 90^{o} cylindrical ion lens (the Right Angular Positive Ion Deflection (RAPID) lens), both of which are maintained at a vacuum of 10^{-3} torr by a turbomolecular pump. The RAPID lens deflects the positive ion beam by 90^{o}, separating positive analyte ions and ensuring that particulates, neutral species and photons are discarded from the ion beam before it enters the mass analyser.

The ion beam then enters the collision cell where interferences from ions generated in the plasma with an identical mass-to-charge ratio to Mo are greatly reduced by passing the beam through a cloud of inert helium (He) gas. The last step before the detector is the quadrupole mass spectrometer which consists of four identical hyperbolic metallic rods. A direct current and a time-dependent alternating current are applied to opposite pairs of the rods and a specific ratio of these currents will only let ions of a selected mass to pass through by electrostatically steering the stable analyte ions down the middle of the rods and causing the unstable ions of different mass to pass through the rods and be ejected from the quadrupole. The remaining ions follow a curved path and hit the first dynode in a discrete dynode electron multiplier set off-axis. This releases electrons which are accelerated to the next dynode which releases more electrons and this electron cascade continues, producing an electrical pulse which is measured to count the ions.

The results are converted from Mo counts to Mo concentrations by comparison with a calibration curve in the Qtegra software. Solutions of known ppm Mo concentrations suited to the expected sample range of measurements are made using a standard solution (Inorganic Ventures 10 ppm (ug/mL) Molybdenum for ICP-MS) and results from these standards are used to make the calibration curve.

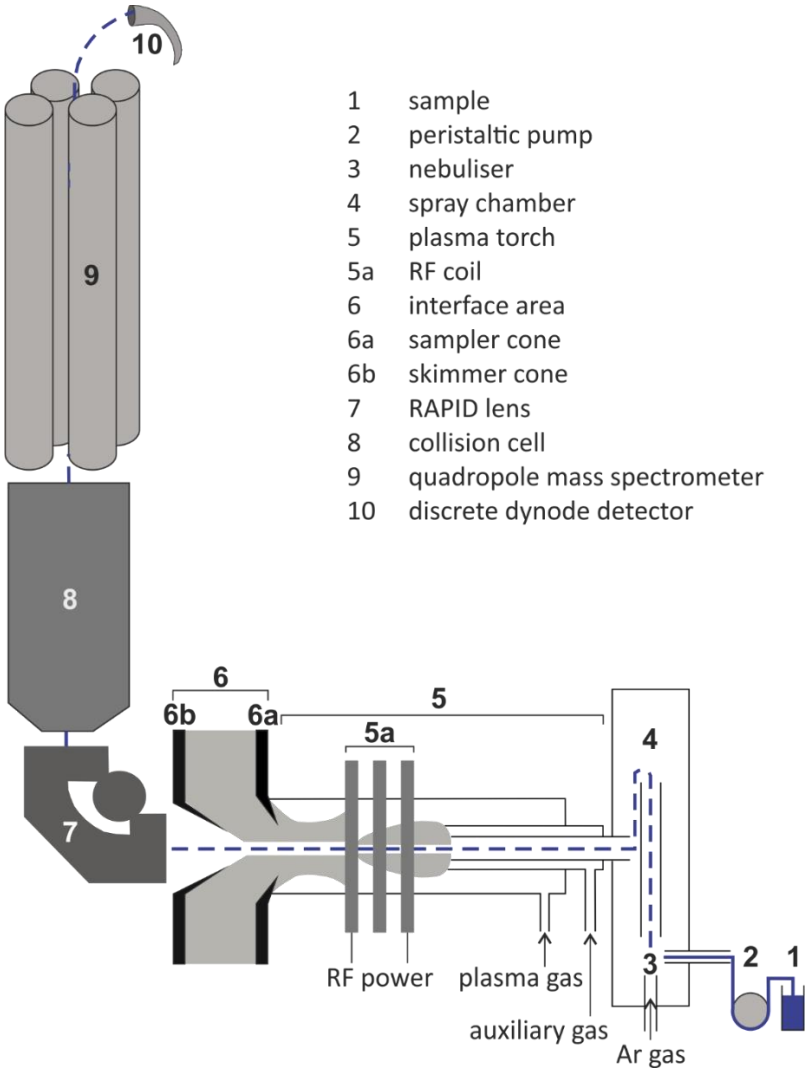

Figure 2.4 A schematic overview of an ICP-MS.

Before each ICP-MS run the machine is tuned in STD and KED modes using a tuning solution (Thermo Scientific TUNE B iCAP Q) to check for any errors before starting an analysis and a report to highlight any errors that need to be addressed before analysing samples is produced.

For every new Mo analysis on the ICP-MS, new peristaltic pump tubing was used and before every analysis the system was flushed with 2% HNO_3 to prevent sample contamination. At least two blanks (matrix diluted with MQ without any sample) were run with each ICP-MS analysis. To calculate the limit of detection (LOD) for any one run, a blank is measured six times and the LOD is calculated as 3 times the standard deviation of these measurements. The limit of quantification (LOQ) is calculated as 9 times the standard deviation of these measurements.

Table 2.2 *Dilutions used for ICP-MS analysis.*

Mo fraction	**Matrix**	**Dilution factor**
Mo_{WA} & Mo washes	pH 5.5 MQ	2
Mo_{SA}	pH 9 MQ	2
Mo_{ox1}	0.5 M HCl	2
Mo_{ox2}	Sodium dithionite	100
Mo_{mag}	Ammonium oxalate	50
Mo_{sil}	50% HCl	20
Mo_{org}	Conc. H_2SO_4	100
Mo_{py}	Conc. HNO_3	50
Mo-total	Conc. HNO_3 or HCl	2.5

2.10 Detecting oxygen in the anaerobic chamber

As an additional check, a titocene dichloride/acetonitrile solution was used to determine whether the anaerobic chamber at the University of Leeds was contaminated with oxygen (after Burgmayer, 1998). A colour change in the prepared solution upon contact with air from the initial dark blue indicates the presence of oxygen (a change to green indicates oxygen levels of >5 ppm; a change to yellow indicates oxygen levels of >20 ppm). 0.1 g of titocene dichloride was mixed with 20 mL of deoxygenated acetonitrile in a 50 mL centrifuge tube under anaerobic conditions. Zinc pellets were added to the tube and the solution was left until it turned dark blue. Once the colour change was observed the lid of the centrifuge tube was removed. The uncovered centrifuge tube was left overnight in the chamber and no colour change was observed, indicating that oxygen levels in the chamber were <5 ppm. Two tubes of solution were prepared to check if a colour change could be observed outside of the chamber. The second solution was opened outside of the chamber and an immediate colour change to yellow was observed, confirming the validity of the test. The original anoxic solution was stored in the chamber and opened each time the chamber was used to test for oxygen.

2.11 XRD analysis

Sample purity of the Mn and Fe oxides and Fe sulfide prior to Mo sorption was confirmed by XRD at Leeds using a Phillips PW1050 XRD for non-oxygen sensitive samples and a Brucker D8 Advance XRD for oxygen-sensitive samples. For Mn and Fe oxides, samples were finely ground before being packed into sample holders for analysis. Air-sensitive samples were finely ground and packed into airtight sample holders in the anaerobic chamber. Data were processed in Convex and matched to standards in DIFFRAC.EVA software packages.

2.12 pH measurements

pH measurements were made with a Hannah HI 9025 microcomputer pH meter. The pH reference electrode was filled with Thermo Scientific Orion Ag/Cl filling solution. The reference electrode was stored in 3 M KCl and sealed with parafilm to prevent evaporation when not in use. The pH probe was calibrated to pH 4 and pH 7 before each use with Fisher Chemical colour coded red. pH 4 traceable to NIST buffer solution (J/2826/15) and pH 7 (phosphate), traceable to NIST, stabilised (J/2855/15). pH adjustments were made by dropwise addition of 0.5 M HCl and 0.01-0.1 M NaOH.

2.13 References

Acholla, F. V., and Orr, W. L. 1993. Pyrite Removal from Kerogen without Altering Organic Matter: The Chromous Chloride Method. *Energy & Fuels*. **7**, pp. 406-410.

Archer, D., and Vance, D. 2008. The isotopic signature of the global riverine molybdenum flux and anoxia in the ancient oceans. *Nature Geoscientist.* **1**, pp. 597-600.

Aspostilia-Maria, M., Vassilios, V., and Sarantis, S. 2020. Dissolved oxygen variability in the Mediterranean Sea. *Journal of Marine Systems.* **208**, pp. 1-10.

Bostick, B. C.; Fendorf, S. and Helz, G. R. 2003. Differential Adsorption of Molybdate and Tetrathiomolybdate on Pyrite (FeS_2). *Environmental Science and Technology.* **37** (2), pp. 285-291.

Boyer, T. P., Antonov, J. I., Baranova, O. K., Coleman, C., Garcia, H. E., Grodsky, A., Johnson, D. R., Locarnini, R. A., Mishonov, A. V., O'Brien, T. D., Paver, C. R., Reagan, J. R., Seidov, D., Smolyar, I. V. and Zweng, M. M. 2013. *In: Levitus, Sydney, Mishonoc, Alexey (Eds.), World Ocean Database 2013, NOAA Atlas NESDIS 72.* **209**.

Bowyer, F. 2019. *Email to Jennifer Rodley, 14 August.*

Braithwaite, E. R. 1994. *Molybdenum: An Outline of its Chemistry and Uses*. Braithwaite, E. R. and Haber, J. eds. Amsterdam. Elsevier Science.

Burgmayer, S. J. N. 1998. Use of a titanium Metallocene as a Colorimetric Indicator for Learning Inert Atmosphere Techniques. *Journal of Chemical Education.* **75** (4), pp. 460-460.

Canfield, D. E., Raiswell, R., Westrich, J. T., Reaves, C. M., and Berner, R. A. 1986. The use of chromium reduction in the analysis of reduced inorganic sulfur in sediments and shales. *Chemical Geology*. **54**, pp. 149-155.

Cline, S. H. and Black, C. A. 1969. Spectrophotometric determination of hydrogen sulfide in natural waters, *Limnology and Oceanography*. **14**, pp. 454-458.

Cole, R. D., Lui, J., Smith, G. V., Hinckley, C. C., and Saporoschenko, M. 1978. Iron partitioning in oil shale of the Green River Formation Colorado: a preliminary Mössbauer study. *Fuel*. **57**, pp. 514-520.

Cornell, R. M., and Schwertmann, U. 2003. *The Iron Oxides*. 2nd ed. Weinheim: WILEY-VCH Verlag GmbH & Co.

Dalsgaard, T., Canfield, D. E., Petersen, J., Thamdrup, B., Acuña-González. 2003. N_2 production by the anammox reaction on the anoxic water column of Golfo Dulce, Costa Rica. *Nature*. 422, pp. 606-608.

Del Don, C., Hanselmann, K. W., Peduzzi, R., and Bachofen, R. 2001. The meromictic alpine Lake Cadagno: Orographical and biogeochemical description. *Acquatic Sciences*. **63**, pp. 70-90.

Erbacher, J., Mosher, D. C., Malone, M. J., et al. 2004a. Leg 207 Summary. *Proceedings of the Ocean Drilling Program, Initial Reports*. **207,** pp. 1-89.

Erbacher, J., Mosher, D. C., Malone, M. J., et al. 2004b. Site 1258. *Proceedings of the Ocean Drilling Program, Initial Reports.* **207**, pp. 1-117.

Ferdelman, T. G., Thamdrup, B., Canfield, D. E. Glud, R. N., Kuever, J., Lillebaek, R., Ramsing, N. B., and Wawer, C. 2006. Biogeochemical controls on the oxygen, nitrogen and sulfur distributions in the water column of Golfo Dulce: an anoxic basin on the Pacific coast of Costa Rica revisited. *Rev. Biol. Trop.* **54** (1), pp. 171-191.

Fossing, H. and Jørgensen, B. B. 1989. Measurement of bacterial sulfate reduction in sediments: Evaluation of a single-step chromium reduction method. *Biogeochemistry*. **8**, pp. 205-222.

Goldberg, T., Archer, C., Vance, D., Thamdrup, B., McAnena, A., and Poulton, S. W. 2009. Mo isotope fractionation during adsorption to Fe (oxyhydr)oxides. *Geochimica et Cosmochimica Acta.* **73**, pp. 6502-6516.

Goldberg, T., Archer, C., Vance, D., Thamdrup, B., McAnena, A., and Poulton, S. W. 2012. Controls on the Mo fractionations in a Mn-rich anoxic marine sediment, Gulmar Fjord, Sweden. *Chemical Geology*. **296**, pp. 73-82.

Goldberg, T., 2019. *Email to Jennifer Rodley*, 30 May.

Guilbaud, R., 2015. *Email to Jennifer Rodley*, 21 July.

Hetzel, A. Böttcher, M. E., Wortmann, U. G., and Brumsack, H. 2009. Paleo-redox conditions during OAE 2 reflected in Demerara Rise sediment geochemistry (ODP Leg 207). *Palaeogeography, Palaeoclimatology, Palaeoecology.* **273**, pp. 302-328.

Ingram, L. L., Ellis, J., Crisp, P. T., and Cook, A. C. 1983. Comparative study of oil shales and shale oils from the Mahogany Zone, Green River Formation (U.S.A.) and Kerosene Creek Seam, Rundle Formation (Australia). *Chemical Geology*. **38**, pp. 185-212.

Julia, R., Burjachs, F., Dasi, M. J., Mezquita, F., Miracle, M. R., Roca, J. R., Seret, G., Vicente, E. 1998. Meromixis origin and recent trophic evolution in the Spanish lake La Cruz. *Aquatic Sciences.* **60**, pp. 279-299.

Krom, M., 2015. *Email to Jennifer Rodley*, 09 January.

März, C., Poulton, S. W., Beckmann, B., Küster, K., Wagner, T., and Kasten, S. 2008. Redox sensitivity of P cycling during marine black shale formation: Dynamics of sulfidic and anoxic, non-sulfidic bottom waters. *Geochimica et Cosmochimica Acta*. **72**, pp. 3703-3717.

März, C. 2019. *Email to Jennifer Rodley, 30 July.*

Miracle, M. R., Vicente, E., Pedrós-Alió. 1992. Biological studies of Spanish meromictic and stratified karstic lakes. *Limnetica.* **8**, pp. 59-77.

Peacock, C. L., and Sherman, D. M. 2004. Copper(II) sorption onto goethite, hematite and lepidocrocite: a surface complexation model based on ab initio molecular geometrics and EXAFS spectroscopy. *Geochimica et Cosmochimica Acta*. **12**, pp. 2623-2637.

Poulton, S. W., and Canfield, D. E. 2005. Development of a sequential extraction procedure for iron: implications for iron partitioning in continentally derived particulates. *Chemical Geology*. **214**, pp. 209-221.

Poulton, S. W. 2016. *Conversation with Simon Poulton*, 08 June.

Poulton, S. W., 2019. *Email to Jennifer Rodley*, 24 July.

Rodrigo, M. A., Miracle, M. R. and Vicente, E. 2001. The meromictic Lake La Cruz (Central Spain). Patterns of Stratification. *Aquatic Sciences*. **63** (4), pp. 406-416.

Siebert, C., Nagler, T. F., and Kramers, J .D. 2001. Determination of molybdenum isotope fractionation by double-spike multicollector inductively coupled plasma mass spectrometry. *Geochemistry Geophysics Geosystems.* **2**, pp. 2000GC000124.

Thamdrup, B., Fossing, H., and Jørgensen, B. B. 1994. Manganese, iron and sulfur cycling in coastal marine sediment, Aarhus Bay, Denmark. *Geochimica et Cosmochimica Acta.* **58** (23), pp. 5515-5129.

Thamdrup, B., Canfield, D. E., Ferdelman, T. G., Glud, R. N., and Gundersen, J. K. 1996. A biogeochemical survey of the anoxic basin Golfo Dulce, Costa Rica. *Revista de Biologia Tropical.* **44**, pp. 19-33.

Thomas, R. 2013. *Practical Guide to ICP-MS.* 3rd ed. Boca Raton: Taylor & Francis Group.

Thompson, J., 2015. *Email to Jennifer Rodley*, 24 February.

Thompson, J. 2018. *Iron and Phosphorous Cycling Under Ferruginous Conditions*. Ph.D. thesis. University of Leeds.

USGS. 2016. *U.S. Geological Survey Certificate of Analysis, Green River Shale, SGR-1.* [Online]. [Accessed 01 November 2018]. Available from: https://crustal.usgs.gov/geochemical_reference_standards/shale.html.

Viollier, E., Inglett, P. W., Hunter, K., Roychoudhury, A. N. and Van Cappellen, P. 2000. The ferrozine method revisited: Fe(II)/Fe(III) determination in natural waters. *Applied Geochemistry*. **15**, pp. 785-790.

Villalobos, M., Toner, B., Bargar, J., and Sposito, G. 2003. Characterization of the manganese oxide produced by *Pseudomonas putida* strain MnB1. *Geochimica et Cosmochimica Acta.* **67** (14), pp. 2649-2662.

Xiong, Y., 2019. *Email to Jennifer Rodley*, 18 October.

Xiong, Y., Guilbaud, R., Peacock, C. L., Cox, R. P., Canfield, D. E., Krom, M. D., and Poulton, S. W. 2019. Phosphorous cycling in Lake Cadagno, Switzerland: A low sulfate euxinic ocean analogue. *Geochimica et Cosmochimica Acta*. **251**, pp. 116-135.

Xu, N.; Christodoulatos, C., and Braida, W. 2006. Adsorption of molybdate and tetrathiomolybdate onto pyrite and goethite: Effect of pH and competitive anions. *Chemosphere*. **62**, pp. 1726-1735.

Chapter 3 Development of a sequential extraction technique for the phase partitioning of molybdenum in marine sediments

3.1 Introduction

As the most abundant trace metal in the ocean (Collier, 1985), Mo has been used extensively as a palaeoredox proxy to identify the temporal and spatial extent of oxic and euxinic conditions in ancient oceans (e.g. Cheng et al., 2016; Dahl et al., 2011; Kendall et al., 2010). In addition, Mo has been used to identify environments which may have had sulfidic porewaters beneath an oxic water column (Scott and Lyons, 2012). These techniques have commonly utilised bulk concentrations in sediments, and the utility of Mo as a redox indicator relates to its bimodal behaviour under different redox conditions. Under oxic conditions, Mo exists as the molybdate (MoO_4) anion and although this can adsorb to Mn and Fe (oxyhydr)oxides in the water column, it is generally released in anoxic porewaters where it may then diffuse back into overlying bottom waters (Goldberg et al., 2012; Scholz et al., 2013; Shimmield and Price, 1986). However, in the presence of sulfide, MoO_4 forms thiomolybdates (MoO_xS_{4-x}) which are highly reactive and easily sequestered to sediments. Therefore, low Mo concentrations (<2 ppm) are generally indicative of oxic environments, intermediate Mo concentrations (2 – 25 ppm) indicate sulfidic porewaters, and high Mo concentrations (>60 ppm) indicate deposition beneath a euxinic water column (Scott and Lyons, 2012). While these methods are useful in identifying oxic vs. euxinic conditions, they do not provide insight into the phase associations responsible for Mo sequestration, and restrict the use of Mo to these end-member redox environments, limiting the use of Mo for identifying other redox settings such as ferruginous and nitrogenous.

Sequential extraction techniques are used to isolate fractions within sediments to identify sequestration pathways for a range of minerals. By treating bulk sediments with specific

extractants, target phases can be removed for analysis with little effect on remaining fractions which are then removed with another extractant. The concentrations from these individual fractions can then be used to develop a picture of the sequestration mechanisms of the target mineral in sediments.

Several sequential extraction methods have gained significant attention for their use in developing models of ocean geochemistry in modern and ancient environments. The Fe sequential extraction developed by Poulton and Canfield (2005) isolates six operationally defined sediment Fe fractions: 1) Fe_{carb} (carbonate-associated Fe); 2) Fe_{ox1} (easily reducible oxides including ferrihydrite and lepidocrocite); 3) Fe_{ox2} (reducible oxides including goethite, hematite and akageneite); 4) Fe_{mag} (magnetite); 5) Fe_{PRS} (poorly reactive sheet silicate Fe); and 6) Fe_{py} (pyrite). Comparison of highly reactive Fe phases (Fe_{HR}) with total Fe (Fe_T) indicates whether sediments were deposited under oxic or anoxic water columns and is an important indicator of the extent of ferruginous water masses in ancient oceans. For example, Canfield et al. (2007) used this method to help show that ocean chemistry was dominated by ferruginous conditions during the Gaskiers glaciation which became oxic following glacial melting and Canfield et al. (2008) used the method to suggest that parts of the deep ocean remained ferruginous at this time. The method has been used extensively to define the temporal and spatial extent of oxic and ferruginous ocean conditions through geological time.

Trace metals also provide important information on ocean geochemistry and methods have been developed to isolate trace metal pools within sediments. Tessier et al. (1979) developed a trace metal sequential extraction with five operationally defined pools: 1) exchangeable fraction; 2) bound to carbonates; 3) bound to iron and manganese oxides; 4) bound to organic matter, and 5) residual. The method has been used in a variety of ways, for example: to determine trace metal contamination in soils (Spahic et al., 2019) and estuarine tidal mudflats

(Nasnodkar and Nayak, 2018); to distinguish between mobile and mobilizable trace metal fractions in Antarctic sediments (Casalino et al., 2013); and to provide information on changing palaeocean chemistry (Neuhuber et al., 2007; Rao et al., 2006). This method, however, does not include a pyrite fraction which is considered an important host for trace metals (Huerta-Diaz and Morse, 1992; Large et al., 2009; Large et al., 2014). Huerta-Diaz and Morse (1990) subsequently developed a new method for trace metal sequential extraction that identified four trace metal pools: 1) reactive (trace metals associated with amorphous and crystalline Fe and Mn (oxyhydr)oxides, carbonates and hydrous aluminosilicates; 2) silicate (trace metals associated with clay minerals); 3) organic (trace metals complexed with organic matter); and 4) pyrite (trace metals associated with pyrite). The method is widely used for applications such as assessing the extent and impact of environmental trace metal contamination (e.g. Diop et al., 2015; Merhaby et al., 2018), investigating trace metal diagenesis in modern sediments (Olson et al., 2017) and investigating palaeocean chemistry (Mongegnot et al., 1996).

The trace metals methods can be applied to Mo, but none include all the fractions that have been shown to be important Mo sinks in one sequential extraction. To better understand the sequestration pathways for Mo it is therefore necessary to combine methods to incorporate all relevant Mo pools.

Therefore, to address the limitations of current Mo proxies, a novel Mo sequential extraction method has been developed to identify the prevalence of six different potential Mo sinks in sediments: 1) Mn and Fe (oxyhydr)oxides, AVS and other reduced Fe mineral phases, and calcium carbonate; 2) crystalline Fe oxides; 3) magnetite; 4) Fe-silicates; 5) organic matter; and 6) pyrite. The method was tested on ancient and contemporary, oxic and euxinic sediment samples and gave good RSD values and comparisons with total Mo. This new method provides

a means of identifying Mo phase associations in sediments and can be applied to a range of ancient and modern redox environments.

3.2 Methods

3.2.1 Sequential extraction target phases

Following existing trace metal and Fe sequential extraction methods (Huerta-Diaz and Morse, 1990; Poulton and Canfield, 2005) and insights into potential Mo sequestration mechanisms (e.g. Gustafsson et al., 2003; Scholz et al., 2013; Chappaz et al., 2014; Dahl et al., 2017), six Mo fractions were identified as important Mo pools to determine the host mineral/organic phase of Mo in sediments (Table 3.1).

Table 3.1 *Operationally derived Mo sediment pools.*

Mo pool	Target Mo phases
Mo_{ox1}	– targets Mo strongly adsorbed or incorporated into Mn and Fe (oxyhydr)oxides; AVS and other reduced Fe mineral phases and Mo incorporated into calcium carbonates
Mo_{ox2}	– targets Mo strongly adsorbed or incorporated into goethite, akageneite and hematite
Mo_{mag}	– targets Mo strongly adsorbed or incorporated into magnetite
Mo_{sil}	– targets Mo incorporated into Fe silicates
Mo_{org}	– targets Mo associated with organic matter
Mo_{py}	– targets Mo strongly adsorbed or incorporated into pyrite, discrete Mo sulfides and other sulfide phases

3.2.2 Sequential extraction procedure

To isolate the fractions outlined in Table 3.1 and incorporate data from the Fe sulfide efficiency tests (see Section 3.2.5), different steps from the sequential extraction methods of Poulton and Canfield (2005; steps 3, 5 and 7 in Table 3.2) and Huerta-Diaz and Morse (1990; steps 9, 11 and 13 in Table 3.2) were adapted and combined to create a specialised sequential extraction procedure for Mo in sediments, incorporating two extractions at the beginning to remove weakly and very strongly adsorbed Mo (see Section 3.3.2), and wash steps between each extraction to remove readsorbed Mo (see Section 3.3.3).

The first extraction from Poulton and Canfield (2005; Mo_{ox1} in the Mo sequential extraction) targets easily reducible oxides including ferrihydrite and lepidocrocite; Mn oxides; AVS minerals and other reduced Fe mineral phases; and calcium carbonates. This step has been revised to use 0.5 M HCl as an extractant over hydroxylamine HCl (Xiong et al., 2019) and it is this updated method that is incorporated into the Mo extraction. Mo is thought to readily adsorb to these Fe phases in the water column (Cheng et al., 2016; Scholz et al., 2013) and therefore dissolving them will release any adsorbed or incorporated Mo into solution. This is also the case with the second (Mo_{ox2}) extraction which targets reducible oxides such as goethite, hematite and akageneite; and the third extraction (Mo_{mag}) which targets magnetite (Poulton and Canfield, 2005).

The Mo_{sil}, Mo_{org}, and Mo_{py} steps of the Mo sequential extraction are adapted from the trace metals sequential extraction developed by Huerta-Diaz and Morse (1990). The Mo_{sil} fraction removes any Mo incorporated into Fe silicates and the Mo_{org} extraction removes any Mo complexed with organic matter. Although Huerta-Diaz and Morse (1990) present this as an optional step, Mo associated with organic matter is thought to be an important sequestration pathway (e.g. Tribovillard et al., 2004; Wagner et al., 2017; Wichard et al., 2009) and it was

therefore included in the Mo sequential extraction as a permanent step. Mo adsorption to pyrite is well-documented (e.g. Bostick et al., 2003; Tribovillard et al., 2004; Poulson Brucker et al., 2012) and therefore the final step of the Huerta-Diaz and Morse (1990) method was included in the Mo sequential extraction as Mo_{py}.

For reasons outlined in Section 3.3.2, two extractions were incorporated into the method at the beginning of the sequential extraction to remove weakly adsorbed (Mo_{WA}) and strongly adsorbed (Mo_{SA}) Mo. In this way, the sequential extractions ($Mo_{ox1, ox2, mag, sil, org, and py}$) only remove Mo incorporated into or very strongly adsorbed to the targeted fractions. The washes in between the extractions are to prevent any readsorption of Mo to sediment fractions that have not yet been extracted and it is therefore essential that the wash is completed immediately after the preceding extraction (see Section 3.3.3). The combined Mo sequential extraction shown in Table 3.2 is performed on a sample size of ~50 mg measured directly into 15 mL polypropylene centrifuge tubes. All extractions are carried out in the same tubes unless a dilution needed to be carried out during the Mo_{org} or Mo_{py} steps (see below). MQ was used for all solutions and the extractions were performed, as outlined in Table 3.2, with a pH 5.5 MQ wash between each extraction from step 3 onwards to address the potential readsorption of Mo between extractions (Tessier et al., 1979). Concentrations for each extraction and the associated subsequent wash are summed to give an overall concentration for that fraction and therefore when discussing results Mo_{ox1} refers to Mo_{ox1E} + Mo_{ox1W}; Mo_{ox2} refers to Mo_{ox2E} + Mo_{ox2W}, etc.

It was observed that during the Mo_{org} extraction, where samples are organic-rich, this extraction can result in problems centrifuging material, creating an insoluble buoyant layer above the supernatant. Where this becomes apparent after centrifuging, the sample (sediment and supernatant) is washed into a 50 mL centrifuge tube with an additional 40 mL of

MQ. After centrifuging, 10 mL of the supernatant is removed for analysis, 30 mL is removed and discarded and the remaining 10 mL with the solid sample is washed back into the original 15 mL centrifuge tube. This sample is then centrifuged and the supernatant removed and discarded.

Table 3.2 *Steps in the Mo sequential extraction showing extractants and target Mo pools.*

Step	Reagents	Mo pool extracted
1. Mo_{WA}	10 mL pH 5.5 18.2MΩ cm Type 1 deionized water (shake for 1 h)	Weakly adsorbed Mo
2. Mo_{SA}	10 mL pH 9 18.2MΩ cm Type 1 deionized water (shake for 1 h)	Strongly adsorbed Mo
3. Mo_{ox1E}	10 mL 0.5 M HCl (shake 1 h)	Mo very strongly adsorbed to or incorporated into Mn oxide, ferrihydrite and lepidocrocite; Mo associated with AVS and other reduced mineral phases; and Mo incorporated into carbonates
4. Mo_{ox1w}	10 mL pH 5.5 18.2MΩ cm Type 1 deionized water (shake for 1 h)	Mo readsorbed following the Mo_{ox1} extraction
5. Mo_{ox2E}	10 mL sodium dithionite (shake 2 h)	Mo very strongly adsorbed to or incorporated into goethite, akageneite and hematite
6. Mo_{ox2w}	10 mL pH 5.5 18.2MΩ cm Type 1 deionized water (shake for 1 h)	Mo readsorbed following the Mo_{ox2} extraction
7. Mo_{magE}	10 mL ammonium oxalate (shake 6 h)	Mo very strongly adsorbed to or incorporated into magnetite
8. Mo_{magw}	10 mL pH 5.5 18.2MΩ cm Type 1 deionized water (shake for 1 h)	Mo readsorbed following the Mo_{mag} extraction

9. Mo_{silE}	2 mL HF, evaporated, then 10 mL 50% HCl to resolubilise (hand-shake or shake for 10 m if necessary)	Mo incorporated into Fe silicates
10. Mo_{silw}	10 mL pH 5.5 18.2MΩ cm Type 1 deionized water (shake for 1 h)	Mo readsorbed following the Mo_{sil} extraction
11. Mo_{orgE}	10 mL concentrated H_2SO_4 (shake 2 h)	Mo associated with organic matter
12. Mo_{orgw}	10 mL pH 5.5 18.2MΩ cm Type 1 deionized water (shake for 1 h)	Mo readsorbed following the Mo_{org} extraction
13. Mo_{pyE}	10 mL concentrated HNO_3 (shake for 2 h)	Mo very strongly adsorbed to or incorporated into pyrite and crystalline sulfide phases.
14. Mo_{pyw}	10 mL pH 5.5 18.2MΩ cm Type 1 deionized water (shake for 1 h)	Mo readsorbed following the Mo_{py} extraction

MQ is used in all cases where solutions or dilutions are required. All samples are centrifuged at 4643 x g for between 4 to 12 minutes (depending on the nature of the samples), after which ~8 mL of the supernatant is removed for analysis and the remainder carefully removed and discarded. Due to the nature of the samples and the potentially low Mo concentrations, any remaining supernatant is removed with a 100 µL pipette and discarded to reduce the chance of removing sediment with the supernatant. Following an appropriate dilution in MQ, samples are analysed for Mo concentrations by ICP-MS.

3.2.3 Sequential extraction solutions

The following solutions are used in the sequential extraction procedure.

0.5 M hydrochloric acid (HCl) was made volumetrically by adding ARISTAR® Hydrochloric acid fuming 37% (from VWR Chemicals) to MQ. Solutions were stored in the laboratory at room temperature.

Sodium dithionite was made volumetrically using trisodium citrate dehydrate, 99% ($Na_3C_6H_5O_7 \cdot H_2O$) from Alfa Aesar (58.82 g for 1 L); sodium dithionite from Fisher Scientific (50 g for 1 L), glacial acetic acid from Sigma Aldrich (20 mL for 1 L); and MQ. The solution was prepared immediately before use and was not stored for further extractions.

Ammonium oxalate was made volumetrically using ammonium oxalate monohydrate ACS reagent ≥99% ($(NH_4)_2C_2O_2 \cdot H_2O$) from Sigma-Aldrich (28.42 g for 1 L); oxalic acid dihydrate laboratory reagent grade ($C_2H_2O \cdot 2H_2O$) from Fisher Scientific (21.43 g for 1 L); and MQ. Solutions were stored in the laboratory at room temperature.

2 mL of analytical reagent grade hydrofluoric acid 40% (HF) from Fisher Scientific was added directly to samples. 50% HCl was made volumetrically by adding ARISTAR® Hydrochloric acid fuming 37% (from VWR Chemicals) to MQ.

Concentrated sulfuric acid 93% NORMATOM for trace metals analysis (H_2SO_4) was from VWR Chemicals was added directly to samples and was stored at room temperature in the laboratory fume cupboard.

Concentrated nitric acid 69% ARISTAR® for trace analysis (HNO_3) from VWR Chemicals was added directly to samples and was stored at room temperature in the laboratory fume cupboard.

MQ washes were prepared using 18.2 MΩ·cm MilliQ water. pH adjustment was made with 10% HCl (ARISTAR® Hydrochloric acid fuming 37% from VWR Chemicals) and 0.1 M NaOH from Sigma Aldrich.

3.2.4 Sequential extraction materials

3.2.4.1 Sediment samples

To test the repeatability of the Mo sequential extraction, it was tested on ancient and modern samples as outlined in Table 3.3 (see Sections 2.1.1 for full details).

Table 3.3 *Details of the samples used in the Mo sequential extraction.*

Sample	Environment
DR-1261-4-5 & DR-1261-18-19	These samples are from organic carbon-rich black shales from the Coniacian-Santonian Oceanic Anoxic Event. Sediments were deposited under bottom waters that cycled between euxinic and anoxic non-sulfidic conditions (März et al., 2008).
DR-1258-1 & DR-1261-4	These samples are Turonian, middle to late Albian shales from a section that has been characterised as generally anoxic with temporary euxinic periods (Hetzel et al., 2009).
USGS-GRS	This sample is the USGS Green River Shale, SGR-1b standard reference material. The standard is from the Mahogany Formation of the Green River Shale, Colorado, a petroleum- and carbonate-rich shale facies (USGS, 2016).
AB-1B 1 to 10	These samples are from Station 6 in Aarhus Bay, which is on the Baltic Sea-North Sea transition on the East Coast of Jutland, Denmark and are characterised by Thamdrup et al. (1994) as having an oxic zone in the sediments is 1- 5 mm thick, below which sediments become anoxic with sulfate reduction resulting in sulfidic porewaters.
LC-1A-5 & LC-1A-6	These organic-rich black shales are from the permanently stratified meromictic Lake Cadagno in Switzerland. The redox-transition zone, which is a few m thick, is located between 10 m – 12 m deep and

	separates the upper oxic layer from the lower anoxic layer (Del Don et al., 2001). Samples were collected from the euxinic part of the lake where deposition takes place beneath a euxinic water column (Xiong et al., 2019.

3.2.4.2 Synthetic minerals

The sequential extraction was also performed on Mo adsorbed to a variety of synthetic minerals to test the efficiency of the method (see Section 3.2.5 and Section 3.3.1).

Ferrihydrite and goethite were synthesised after Cornell and Schwertmann (2003; full details are in Section 2.1.2). Ferrihydrite was synthesised by combining iron (III) nitrate ($Fe(NO_3)_3{\cdot}9H_2O$) with NaOH, and goethite by combining $Fe(NO_3)_3{\cdot}9H_2O$ with potassium hydroxide (KOH) before heating for 60 h at 70°C. Fe sulfide (pyrite) was purchased from Strem Chemicals and was used under anoxic conditions. The pyrite was washed consecutively in deoxygenated MQ, 0.5 M hydrochloric acid (HCl) and 0.1 M sodium sulfide (Na_2S) solutions to remove any oxidised surface species (Bostick et al., 2003). Mo was adsorbed to ferrihydrite, goethite and pyrite using the general method of Peacock and Sherman (2004). Specifically 2 g of the mineral (either as a dry mineral or a dry-weight equivalent of a mineral slurry) was added to a 50 mL centrifuge tube with 39.95 mL of a 0.1 M sodium chloride (NaCl) background electrolyte and 450 µL of a 1000 ppm Mo stock solution (Na_2MoO_4 for ferrihydrite and goethite, and both Na_4MoO_4 and $(NH_4)_2MoS_4$ for pyrite). Solution pH was adjusted to pH 7 and samples were shaken end-over-end for 2 d. Ferrihydrite and goethite samples were then washed in MQ, air-dried and ground to a fine powder, while pyrite samples were washed in deoxygenated MQ and air-dried under a nitrogen atmosphere. Sample purity of the Fe oxides and Fe sulfide were confirmed by XRD using a Phillips PW1050 for non-oxygen sensitive samples and a Brucker D8 Advance for oxygen-sensitive samples prior to Mo adsorption.

3.2.5 Efficiency tests for Mo adsorbed to Fe oxides and Fe sulfides

After Poulton and Canfield (2005) and Huerta-Diaz and Morse (1990), single and sequential extractions were performed on MoO_4 adsorbed to ferrihydrite, goethite and pyrite, and MoS_4 adsorbed to pyrite (Table 3.4). Ferrihydrite is the first mineral to be extracted and therefore was not subjected to a sequential extraction. Goethite and pyrite were subjected to all sequential extraction steps up to and including the one that extracts the relative phase to test whether Mo is removed before the target phase. Mo concentrations were compared to those from total digests for these minerals.

Table 3.4 *Efficiency tests for Fe oxides and Fe sulfide.*

Mineral phase	Extraction
MoO_4 adsorbed to ferrihydrite	Single extraction – 0.5 M HCl, shaken for 1 h.
MoO_4 adsorbed to goethite	Sequential extraction – 0.5 M HCl, shaken for 1 h; sodium dithionite, shaken for 2 h.
MoO_4 adsorbed to pyrite and MoS_4 adsorbed to pyrite	Sequential extraction – 0.5 M HCl, shaken for 1 h; sodium dithionite, shaken for 2 h; ammonium oxalate shaken for 6 h; HF evaporated followed by 50% HCl; concentrated H_2SO_4, shaken for 2 h; concentrated HNO_3 shaken for 2 h.

3.2.6 Analysis by Inductively Coupled Inductively Coupled Mass Spectrometry (ICP-MS)

All supernatants were analysed by ICP-MS following appropriate dilutions (Table 3.5) and all dilutions included 100 µL of a 100 ppb Rh standard to monitor recovery rates during ICP-MS analysis.

Table 3.5 *Dilutions used for ICP-MS analysis.*

Mo fraction	Supernatant matrix	Dilution Factor	Procedure
Mo_{WA}, Mo_{ox1W}, Mo_{ox2W}, Mo_{magW}, Mo_{silW}, Mo_{orgW}, Mo_{pyW}	pH 5.5 MQ	2	4900 µL sample, 5000 µL MQ, 100 µL Rh standard.
Mo_{SA}	pH 9 MQ	2	4900 µL sample, 5000 µL MQ, 100 µL Rh standard.
Mo_{ox1E}	0.5 M HCl	2	4900 µL sample, 5000 µL MQ, 100 µL Rh standard.
Mo_{ox2E}	Sodium dithionite	100	100 µL sample, 9800 µL MQ, 100 µL Rh standard.
Mo_{magE}	Ammonium oxalate	50	200 µL sample, 9700 µL MQ, 100 µL Rh standard.
Mo_{silE}	50% HCl	20	500 µL sample, 9400 µL MQ, 100 µL Rh standard.
Mo_{orgE}	H_2SO_4	100	100 µL sample, 9800 µL MQ, 100 µL Rh standard.
Mo_{pyE}	HNO_3	50	200 µL sample, 9700 µL MQ, 100 µL Rh standard.
Mo_T	5% HCl	2.5	4000 µL sample, 5900 µL MQ, 100 µL Rh standard.

3.2.7 Chromous chloride extraction to separate organic matter

A sample of pure Mo-organic material was isolated from sediment core LC-1A from the euxinic part of the stratified Lake Cadagno (see Section 2.1.4). A sequential extraction was performed on the sediment to remove Mn and Fe oxides and silicates (Huerta-Diaz and Morse, 1990; Poulton and Canfield, 2005). A chromous chloride extraction was then performed to remove pyrite from the sample, leaving the remaining organic material suitable for XANES analysis (Acholla and Orr, 1993). The organic material was washed with deoxygenated MQ water and air-dried under a nitrogen atmosphere. For analysis at Diamond Light Source Ltd (DLS) the sample was transported in a polypropylene centrifuge tube inside a Kilner jar with AnaeroGen™ sachets, sealed under a nitrogen atmosphere, and upon arrival at DLS was immediately transferred into an anaerobic chamber filled with an argon atmosphere where it was combined with cellulose to make a pressed pellet. The pellet was sealed between three layers of Kapton tape before being presented to the beam.

3.2.8 Total digests

Total digests (Mo_T) were performed using a HNO_3-HF-$HClO_4$ extraction. Samples of ~0.1 g were ashed in ceramic crucibles for 8 h at 550 °C. Samples were then washed into Teflon pots with 5 mL of HNO_3. 2 mL of HF and 2-3 drops of $HClO_4$ were added to samples before they were heated until they had evaporated to dryness. 2 mL of 0.8 M H_3BO_3 was added to neutralise any remaining HF and samples were again heated until they had evaporated to dryness. Precipitates were resolubilised by adding 5 mL of 50% HCl with heat until the solution was clear. This solution was transferred to 100 mL volumetric flasks, and Teflon pots and funnels were rinsed 5x with MQ to ensure complete transfer. Once completely cooled, flasks were made up to volume with MQ and inverted 10x to mix. ~12 mL of the solution was stored for analysis and the remainder was discarded.

3.2.9 XANES data collection and analysis

Micro-focus XANES spectra at the Mo K-edge (20,000 eV) were collected at DLS on hard X-ray beamline I18. For micro-focus scans the beam size was 2 x 2.5 µM, and XANES were collected in fluorescence mode using a 9-element solid-state Ge detector. During data collection the storage ring energy was 3.0 GeV and the beam current was 300 mA. The organic-Mo sediment sample (LC-1A) was finely ground and sealed between three layers of Kapton film under an argon atmosphere, before being moved to the beamline, after which the sample was attached to the sample stage with Kapton tape and presented to the beam. The pyrite-Mo sample (LC-1C) was presented to the beam as a self-supported micro-thin section, adhered to Kapton tape.

To reduce the signal to noise ratio multiple scans were taken at multiple *x, y* coordinates on each sample and merged. Before data collection, a series of XANES test scans were performed to monitor for photo-redox and beam damage. Multiple scans at the same *x, y* coordinates were performed and showed that beam induced effects manifest as a development or deterioration of the pre-edge feature and/or an energy shift of the main absorption edge. During data collection, scans showing evidence of these changes compared to the first scan at the given *x, y* coordinate were discarded from the merge. Generally, a minimum of three XANES scans were merged for each sample. For high Fe samples, aluminium sheets were placed in front of the detector to attenuate Fe fluorescence. At the start of data collection Mo foil reference scans were collected for energy calibration. The first peak in the first derivative of the Mo(0) foil was assigned to 20,000 eV. This set the absolute energy scale for all characteristic spectral features, and all sample scans were calibrated to this scale in order to correct for monochromator drift.

Data were processed using Athena 0.9.26 (Ravel and Newville, 2005). For background subtraction the pre-edge was fit to a linear function and the post-edge to one 2nd-order polynomial segment. Data were then normalised.

3.3 Results and discussion

3.3.1 Method validation on Fe oxides and Fe sulfide

To test the selectivity of extractions for Mo very strongly adsorbed to or incorporated into Fe oxides and Fe sulfide, the single Mo_{ox1E} extraction was performed on ferrihydrite with MoO_4 adsorbed; a partial sequential extraction including the Mo_{ox1E} and Mo_{ox2E} steps was performed on goethite with MoO_4 adsorbed; and the full sequential extraction including the Mo_{ox1E}, Mo_{ox2E}, Mo_{magE}, Mo_{silE}, Mo_{orgE} and Mo_{pyE} extractions was performed on pyrite with MoO_4 adsorbed and pyrite with MoS_4 adsorbed (Table 3.7). The Mo_{ox1E} extraction on the MoO_4 adsorbed to ferrihydrite shows that 106.4% of total Mo adsorbed is removed, therefore demonstrating the efficacy of the extraction. MoO_4 adsorbed to goethite should be removed by the Mo_{ox2E} extraction which is the second step in the sequential extraction. Therefore the sequential extraction was performed up to and including this step. The Mo_{ox1E} extraction removed 0.7% of total Mo adsorbed and the Mo_{ox2E} extraction removed 95.1%, indicating that the target phase was successfully removed by the Mo_{ox2} extraction. MoO_4 and MoS_4 adsorbed to pyrite should both be removed by the Mo_{pyE} extraction and therefore the sequential extraction was performed up to and including this step. For MoO_4 adsorbed to pyrite 63% of Mo was removed in the Mo_{ox1E} extraction and only 0.7% in the target Mo_{pyE} extraction. For MoS_4 adsorbed to pyrite, 55.9% of Mo was removed in the Mo_{ox1E} extraction; 3.7% in the Mo_{ox2E} extraction; 9.3% in the Mo_{magE} extraction; 15.7% in the Mo_{silE} extraction; and 2.0% in the target Mo_{pyE} extraction.

The tests on synthetic minerals indicate that the sequential method is effective for Mo adsorbed to ferrihydrite and goethite but not for pyrite. It appears that Mo adsorbed to pyrite, particularly MoS_4, is removed in extractions that precede the Mo_{py} extraction step, predominantly in the Mo_{ox1E} extraction. This suggests that Mo may be loosely adsorbed to pyrite and therefore easily removed with 0.5 M HCl.

Table 3.6 *Percentage Mo extracted in the target extraction from all extractions up to and including the target extraction.*

Mineral phase	Total Mo (ppm)	% removed by target extraction	% of total Mo removed
Ferrihydrite-MoO_4	357.0	106.4	106.4
Goethite-MoO_4	178.6	95.1	95.8
Pyrite-MoO_4	21.48	0.7	63.6
Pyrite-MoS_4	190.1	0.1	79.9

3.3.2 Extractions to remove weakly and strongly adsorbed Mo

To prevent pyrite Mo from being included in the Mo_{ox1} extraction, two additional extraction steps were incorporated into the sequential extraction at the start of the procedure to remove weakly adsorbed Mo (Mo_{WA}) and strongly adsorbed Mo (Mo_{SA}). The Mo_{WA} extraction is designed to remove weakly adsorbed Mo that may potentially reflect Mo cycling in sediments as well as Mo only loosely adsorbed to minerals that could potentially be removed in earlier extractions. The pH of this extraction lies within the range at which Mo commonly adsorbs to most of the significant substrates for adsorption in marine sediments, and hence any Mo removed mostly reflects weakly adsorbed Mo, rather than strongly adsorbed Mo. The pH of

the Mo_{SA} extractant is outside of the pH adsorption envelope for the Mo fractions identified for the sequential extraction and therefore has the potential to remove more strongly adsorbed Mo. Thus, after these first two extractions, the remaining Mo in the sediment is considered to be incorporated within the target phases, or very strongly adsorbed at the surface. It is possible that weakly and strongly adsorbed Mo from phases other than pyrite is also removed during these extractions but individual Mo phases cannot be separated in the Mo_{WA} or Mo_{SA} extractions. Sediments were therefore treated with pH 5.5 MQ (Mo_{WA}) and pH 9 MQ (Mo_{SA}) to remove weakly and strongly adsorbed Mo, respectively.

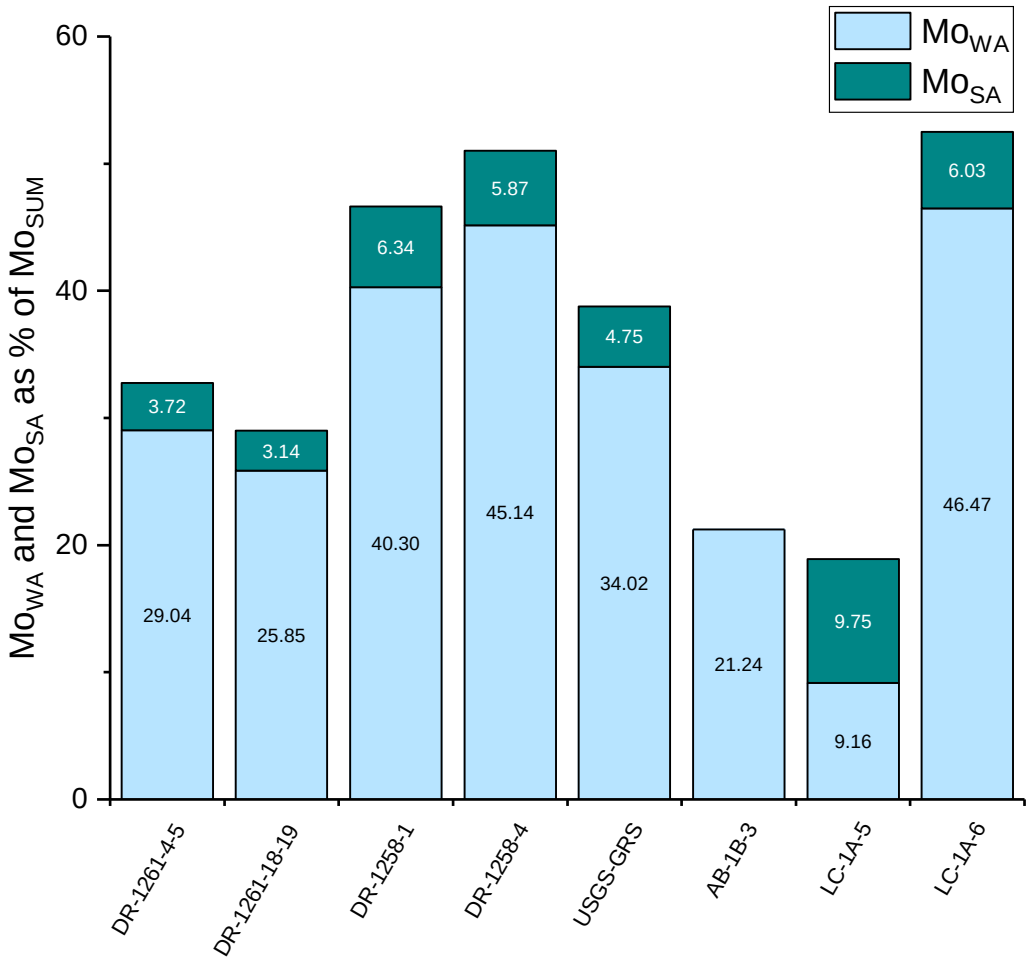

Figure 3.1 *Mo removed during Mo_{WA} and Mo_{SA} as a percentage of Mo_{SUM}.*

When the Mo sequential extraction was performed on sediment samples, the results from Mo_{WA} show that 9.16 – 46.47% of the summed Mo fractions (Mo_{SUM}) is removed in this step. The amount removed in Mo_{SA} is much lower at 0 – 9.75% of Mo_{SUM}. The initial two extractions therefore remove 18.91 – 52.50% of the total Mo extracted (Figure. 3.1). Given that the Mo_{WA} and Mo_{SA} extractions remove so much Mo, it is likely that the later stronger extractions, if performed without these initial steps, would also remove loosely and strongly bound Mo from non-targeted phases, giving higher Mo concentrations.

3.3.3 Readsorption washes

To prevent readsorption of Mo onto remaining sedimentary phases during the sequential extraction, wash steps were incorporated into the procedure (Mo_{ox1W}, Mo_{ox2W}, Mo_{magW}, Mo_{silW}, Mo_{orgW}, Mo_{pyW}). After each of the targeted extractions (Mo_{ox1E}, Mo_{ox2E}, Mo_{magE}, Mo_{silE}, Mo_{orgE}, Mo_{pyE}) the solid was treated with 10 mL of pH 5.5 MQ, shaken for 1 h. When tested on a range of ancient and modern sediments (Table 3.8) the data highlight the importance of these washes as significant amounts of Mo are removed when considering Mo from the wash as a percentage of the total Mo removed for that extraction (Mo_{ox1W} = 0.0 – 3.5%; Mo_{ox2W} = 11.5 – 83.8%; Mo_{magW} = 0.0 – 52.9%; Mo_{silW} = 0.0 – 27.26%; Mo_{orgW} = 0.0 – 4.92%; Mo_{pyW} = 0.0 – 31.80%). The Mo_{ox2} wash removes the most Mo, suggesting that Mo in this extraction is most easily readsorbed.

When the data from extractions that include the Mo_{WA}, Mo_{SA} and the readsorption wash steps are compared with extractions without any of these steps, the amount of Mo extracted is generally higher for those individual extractions without these additional extractions (Figure 3.2). This suggests either that sequential extractions without the Mo_{WA} and Mo_{SA} steps remove Mo that is weakly and strongly adsorbed to later Mo phases too early in the extraction; that extracted, dissolved Mo is readsorbed to later Mo phases and not included in

the results for the target phase; or a combination of both of these processes. The Mo removed in Mo_{ox1} in the sequential extraction without the Mo_{WA} and Mo_{SA} steps is much higher than the results for the sequential extraction including these steps (Figure 3.2). As this is the first step in this sequential extraction, it is likely that it has removed Mo weakly adsorbed to later target phases, giving abnormally high concentrations for Mo_{ox1}. As readsorption washes were also not included in this extraction, any dissolved Mo may also have readsorbed to later target phases, again giving abnormally high results. These data again highlight the importance of the Mo_{WA} and Mo_{SA} steps and the readsorption washes.

Table 3.7 *Washes as a percentage of all Mo recovered in the extraction step (i.e. Mo_x + Mo_{xW}). The highest percentage values are highlighted in grey for each sample.*

Extraction step	Wash as % of all Mo recovered (Mo_x + Mo_{xW})							
	DR-1261-4-5	DR-1261-18-19	DR-1258-1	DR-1258-4	USGS-GRS	AB-1B-3	LC-1A-5	LC-1A-6
Mo_{ox1}	3.49	2.95	1.21	1.68	0.00	0.00	1.02	0.91
Mo_{ox2}	51.06	60.20	63.78	83.75	51.79	11.72	37.33	49.43
Mo_{mag}	27.03	29.60	28.78	52.85	50.47	0.00	28.06	34.27
Mo_{sil}	11.60	11.32	11.87	23.25	27.26	0.00	1.90	1.26
Mo_{org}	1.52	1.98	4.92	4.39	0.00	0.00	0.00	0.00
Mo_{py}	13.90	12.29	31.80	22.19	3.11	0.00	4.39	2.87

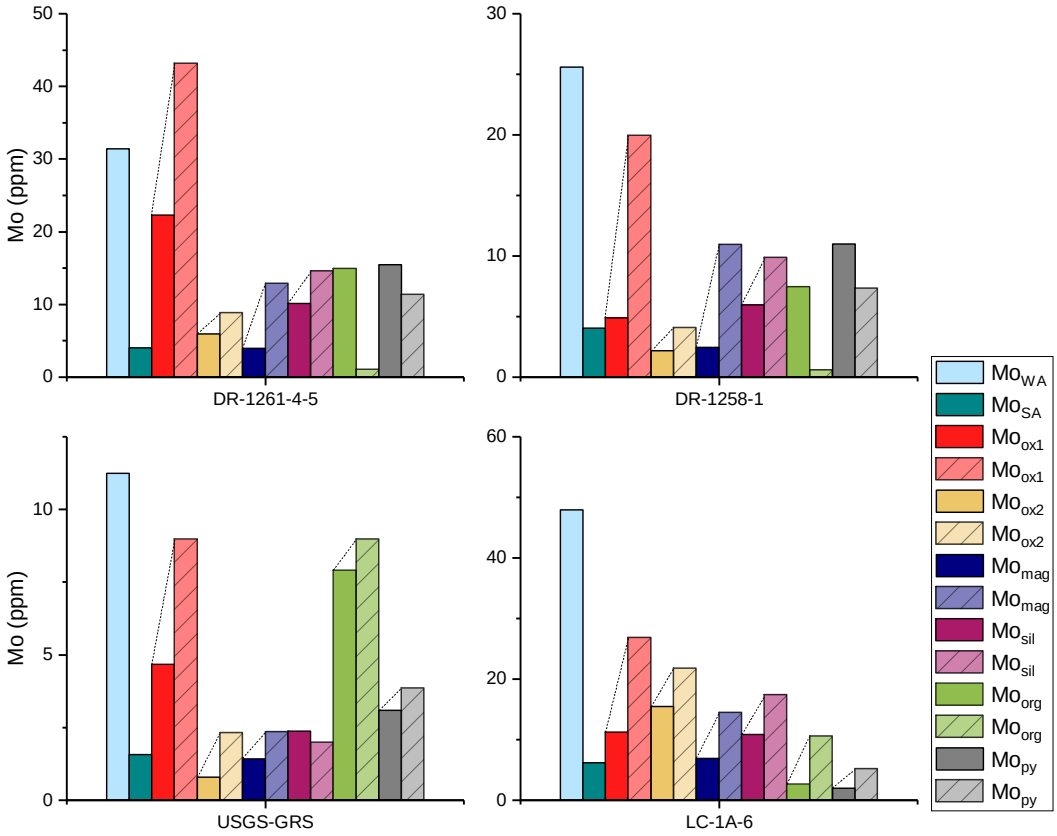

Figure 3.2 *Extractions including readsorption wash steps (block colour) compared with extractions without readsorption wash steps (pale, gridded colour) for a selection of samples.*

When the readsorption washes for individual samples are considered independently (Table 3.7), readsorption is highest for the Mo_{ox2} extraction for all samples but there is also considerable variability between individual samples. For example, the proportion of Mo recovered in the washes for all fractions, except Mo_{org} and Mo_{py} in the DR-1258 samples, is higher for DR-1258-4 than for DR-1258-1. DR-1258-4 has higher sulfur concentrations than DR-1258-1 and the apparently higher readsorption may reflect the presence of more sulfurized thiomolybdates in these samples which become more reactive and may therefore be more susceptible to readsorption. Unlike readsorption wash steps for any of the other samples, in the AB-1B-3 sample Mo is only recovered in the Mo_{ox2W} step. The fact that the Mo_{ox2W} step recovers more Mo than other wash steps may reflect either a greater exposure of surface sites

for readsorption after this extraction, or conversion of molybdate to thiomolybdates (which are more particle reactive) due to the presence of sulfide as an integral component of dithionite (Tessier et al., 1979).

3.3.4 Method validation using XANES

To test whether the sequential extraction steps Mo_{ox1E}, Mo_{ox2E}, Mo_{magE} and Mo_{silE} remove Mo complexed with organic matter before the Mo_{org} extraction, the sequential extraction was performed up to and including the Mo_{silE} step on material from the euxinic Lake Cadagno (LC-1C). A chromous chloride extraction was performed on the remaining solid to remove pyrite and therefore any Mo associated with pyrite, before the sample was washed and dried. XANES were collected on the remaining sample and compared with a library of standards (see Chapter 4 for full method details; Figure 3.3; Table 3.8).

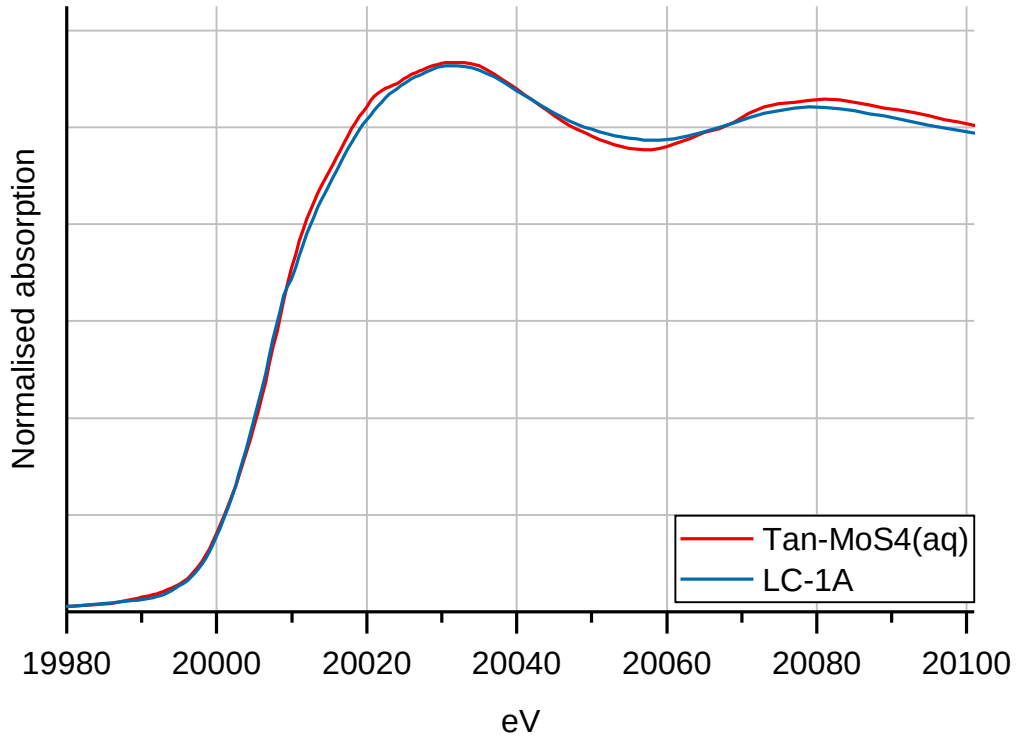

Figure 3.3 *XANES for the tannic acid-MoS_4 standard (Tan-MoS_4(aq)) and a sample from the euxinic part of Lake Cadagno, treated to remove all fractions except for the organic fraction (LC-1C).*

Using the library of standards, the best XANES match in terms of spectral shape and values is tetrathiomolybdate complexed with tannic acid (Tan-MoS_4(aq)), indicating Mo complexed with organic matter and therefore suggesting that organic matter and associated Mo is not affected by earlier extractions.

Table 3.8 *XANES spectral values for the Tan-MoS_4(aq) standard and the LC-1C sample (see Chapter 4 for full details on spectral value comparisons) .*

	Tan-MoS_4(aq)	**LC-1A**
E0 (eV)	20007.0	20007.1
E_M (eV)	20032.0	20030.8
E_S (eV)	-10.0	-9.9
E_C (eV)	20057.0	20059.3
E_D (eV)	20081.0	20078.9

To confirm whether the AB-1B-3 sample contained any Mo associated with pyrite (because this Mo was not included in the sequential extraction results), XANES were collected for a bulk sample (Figure 3.4; Table 3.9). When compared with a library of standards (Chapter 4), the best match was for MoS_4 adsorbed to pyrite (Py-MoS_4(ads)), indicating that Mo is adsorbed to pyrite in this sample. However, the sequential extraction data show that there is no Mo in the pyrite fraction. It is therefore likely that the pyrite Mo was removed in the Mo_{WA} extraction (this sample did not have any Mo in the Mo_{SA} extraction) and was therefore weakly adsorbed to pyrite. This highlights the importance of the initial extractions to remove weakly and

strongly adsorbed Mo, as Mo adsorbed to pyrite could have otherwise been potentially removed in the Mo_{ox1} extraction.

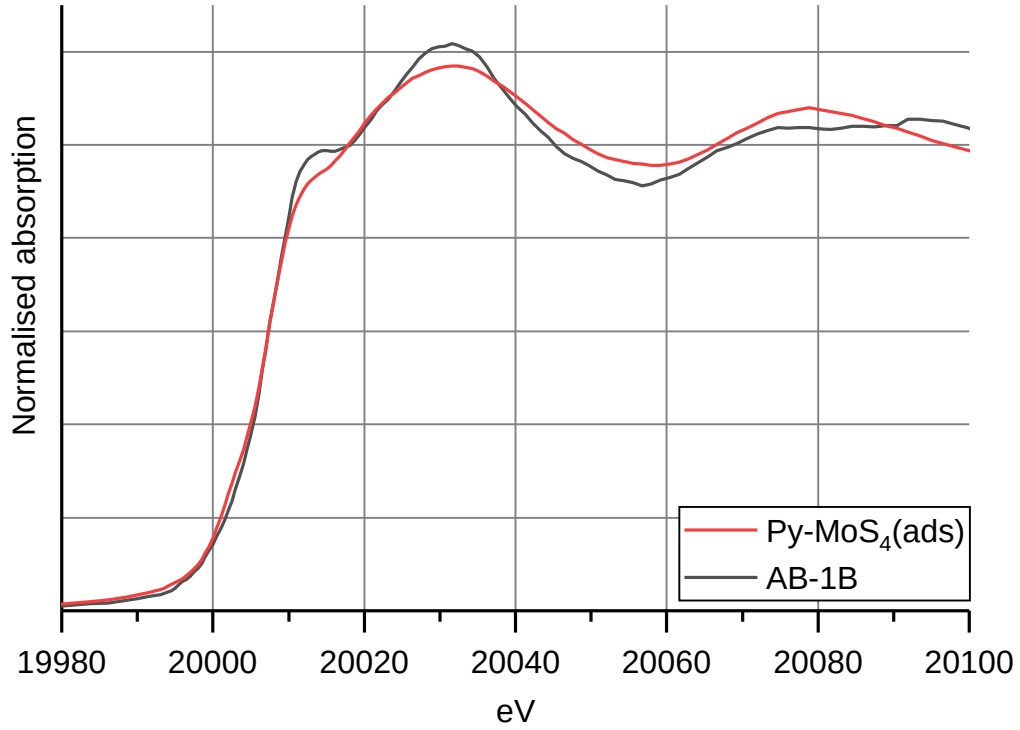

Figure 3.4 *XANES for the pyrite-MoS_4 standard (Py-MoS_4(ads)) and a bulk sample from AB-1B.*

Table 3.9 *XANES spectral values for the Py-MoS_4(ads) standard and the AB-1B sample (see Chapter 4 for details on spectral value comparisons).*

	Py-MoS_4(ads)	**AB-1B**
E0 (eV)	20007.2	20007.4
E_M (eV)	20032.0	20031.7
E_S (eV)	-9.8	-9.6
E_C (eV)	20059.0	20056.3
E_D (eV)	20079.0	20092.3

3.3.5 Reproducibility

The results for the extractions and associated washes for each Mo pool were combined to give an overall value (e.g. Mo_{ox1} is a combination of the Mo_{ox1E} 0.5 M HCl extraction and the Mo_{ox1W} pH 5.5 MQ wash). Extractions were performed on six repeats per extraction (i.e. 672 individual extractions). Excluding those extractions where no Mo was detected, the repeats give an average RSD value of 4.37% from a range of RSD values that are generally below 5% RSD (62.5% of all returned RSDs) with some values between 5-10% RSD (31.3% of all returned RSDs) and the remaining extractions returning results of zero. Mo concentrations in individual extractions range from 0.00-51.19 ppm Mo with an average value of 9.21 ppm Mo. The higher RSDs observed for some samples is a result of the small average concentrations, whereby a relatively small deviation from that average results in a lower degree of precision. Considering the overall sequential extraction results, reproducibility is good, with average RSD values for each individual extraction ranging from 2.94-6.27% (Appendix A).

3.3.6 Sequential extraction results compared with total Mo recovery

Mo concentrations for all extractions and washes were combined to give the summed Mo for each sample (Mo_{SUM}). This value was then compared with the total Mo (Mo_T) recovered either by total digest at Leeds or with published data for the samples used (Table 3.10). Overall, retrieval values are good, with 81.11% to 100.26% (average 92.03%) of Mo recovered in the sequential extractions when compared with Mo_T. Mo_{SUM} generally returns lower values than Mo_T and this is likely a result of minor sample loss during the procedure as the sequential extraction includes 14 individual steps. Some samples (e.g. AB-1B-3) already have low Mo concentrations and only a fraction of this total value is lost in the individual extractions (0.10 ppm). Therefore, even a small amount of sample loss can have a large effect on the Mo_{SUM} value. It is advisable to extract the supernatants from extractions and washes with a 10 mL pipette to remove around 9 mL of the supernatant for analysis, followed by a 100 µL pipette to

remove and discard any remaining supernatant. Careful pipetting should minimise sample loss.

Table 3.10 *Comparison of Mo retrieved during sequential extraction (Mo_{SUM}) with Mo retrieved from total digests (Mo_T). Data from [1]März at al. (2009); [2]Hetzel et al. (2009); [3]USGS (2016).*

Sample	Mo_{SUM} (ppm)	Mo_T (ppm)	Mo_{SUM} as % of Mo_T
DR-1261-4-5	108.12	[1]118.00	91.63
DR-1261-18-19	79.04	[1]87.00	90.85
DR-1258-1	63.50	[2]73.00	86.99
DR-1258-4	113.42	[2]117.00	96.94
USGS-GRS	33.04	[3]35.00	94.40
AB-1B-3	1.55	1.65	94.04
LC-1A-5	87.09	107.36	81.11
LC-1A-6	103.18	102.92	100.26

3.3.7 Sequential extraction to isolate Mo fractions

As the Mo_{WA} and Mo_{SA} extractions remove any weakly and strongly adsorbed Mo, each subsequent extraction and associated wash is considered to extract Mo from the specific target phase (either incorporated within the structure or very strongly adsorbed). Figure 3.5 shows the proportions of Mo extracted for each of the Mo fractions and these results indicate that Mo is associated with a variety of phases, each of which will be explored in further detail in sections 3.3.8 to 3.2.12 below.

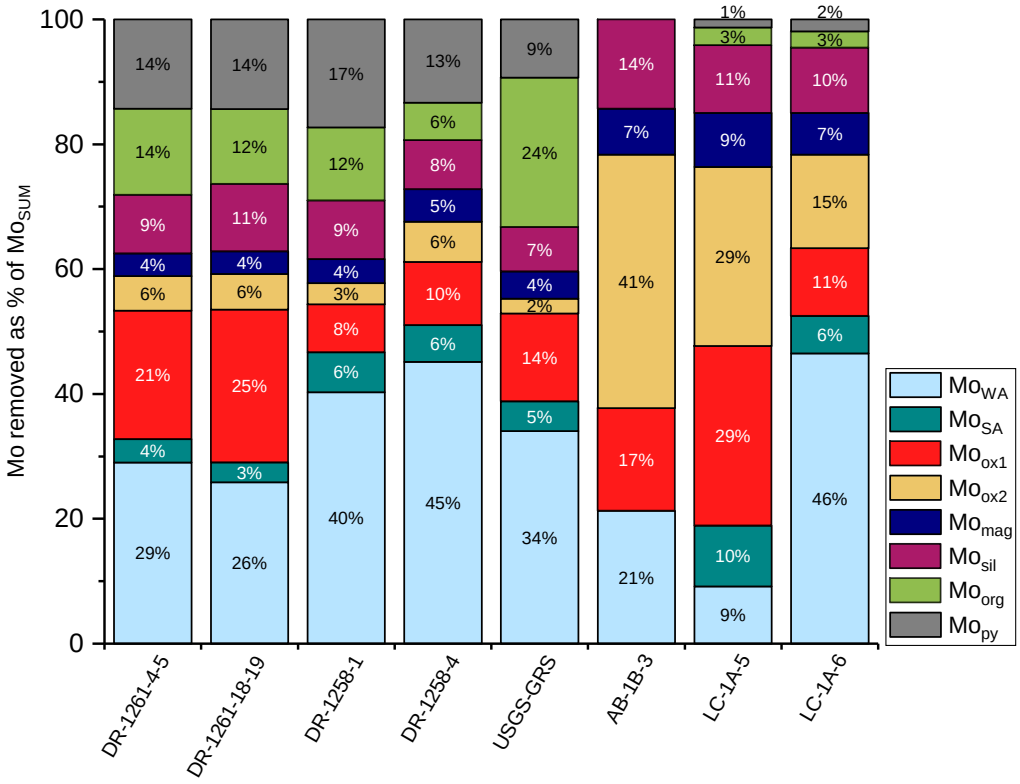

Figure 3.5 *Proportions of Mo extracted for each sequential extraction step as a percentage of* Mo_{SUM}.

3.3.8 Demerara Rise samples (DR-1261)

The Demerara Rise samples are from two different depths, but both are from sediments deposited below a generally euxinic water column. The results from the Mo sequential extraction are similar in terms of proportions extracted in each step (Figure 3.6). Mo_{WA} removed the most Mo from both samples (29.0% of Mo_{SUM} for DR-1261-4-5, and 25.9% for DR-1261-18-19). Mo_{SA} extracts a significantly lower proportion of Mo from both samples, removing only 3.7% of Mo_{SUM} from DR-1261-4-5 and 3.1% from DR-1261-18-19. Mo extracted from both samples is partitioned as $Mo_{WA} > Mo_{ox1} > Mo_{py} > Mo_{org} > Mo_{sil} > Mo_{ox2} > Mo_{SA} > Mo_{mag}$ (Figure 3.6). The significant association of Mo with the Mo_{ox1} fraction is perhaps surprising given the euxinic environmental setting, but this may reflect Mo incorporated into carbonate minerals or acid volatile sulfides, or potentially poorly crystalline Fe oxides that were not converted to pyrite. DR-1261-4-5 contains 53.2 wt% $CaCO_3$ and DR-1261-18-19

contains 57.2 wt% $CaCO_3$ and these high carbonate concentrations suggest that Mo removed in this extraction is likely associated with carbonate minerals.

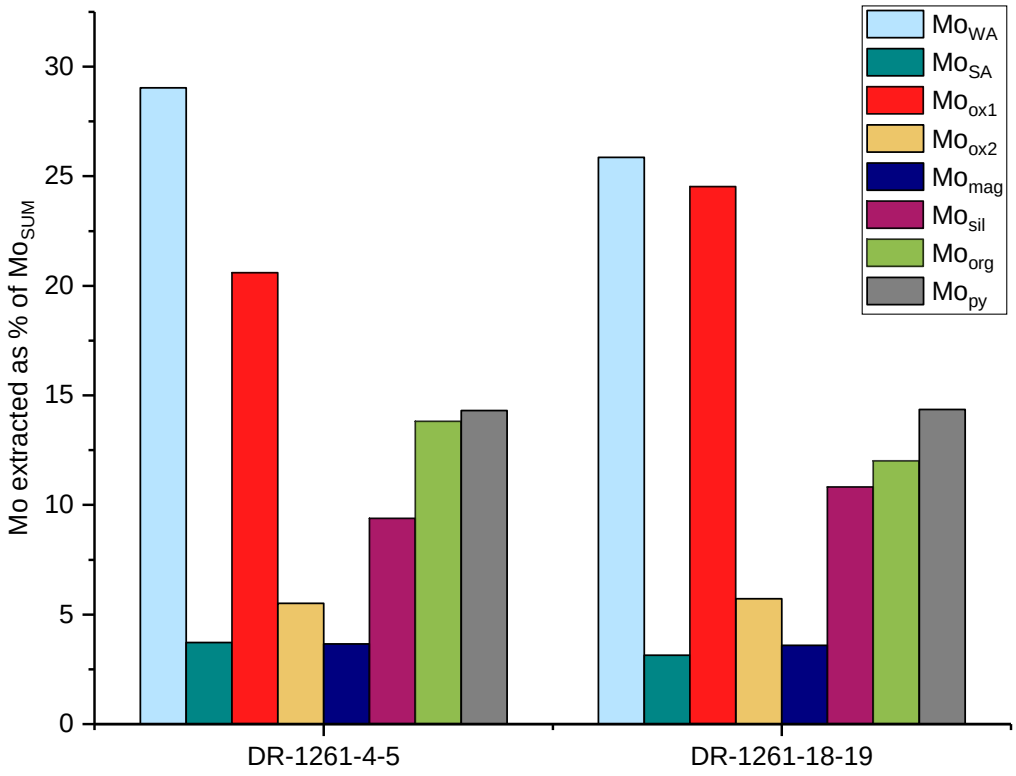

Figure 3.6 *Mo extracted from DR-1261 samples shown as a percentage of the total Mo extracted*.

The strong associations with the Mo_{org} and Mo_{py} fractions are less surprising as these are recognised Mo sequestration pathways in euxinic settings. Pyrite is frequent in all samples from this core (März et al., 2009) with 0.39 wt% Fe_{py} in DR-1261-4-5 and 0.19 wt% Fe_{py} in DR-1261-18-19, however, März et al. (2008) show that metal sulfides only account for ~25% of the total S pool and therefore propose that the majority of the S in this environment is associated with sulfurized organic matter. In support of this, März et al. (2009) noted a strong correlation of Mo/Al with both TOC/Al and S/Al. Given the presence of sulfurized organic matter, it would be reasonable to expect some of the Mo to be associated with this fraction. However, the sequential extraction results indicate that pyrite plays an equally, if not slightly more

important role in Mo sequestration for these samples. In DR-1261-4-5, Mo_{org} is 13.8% (14.9 ppm) of Mo_{SUM} and Mo_{py} is 14.3% (15.5 ppm) of Mo_{SUM}. In DR-1261-18-19, Mo_{org} is 12.0% (9.5 ppm) of Mo_{SUM} compared to Mo_{py} which is 14.4% (11.3 ppm) of Mo_{SUM}. In this environment, both sequestration pathways are in operation, but the Mo-pyrite pathway dominates. Nevertheless, weakly adsorbed Mo is the dominant pool, and it is not clear what phases this would originally have been associated with.

3.3.9 Demerara Rise samples (DR-1258)

The DR-1258 samples are from two different depths in the same core. Total Mo concentrations in the shallower sample are much lower (DR-1258-1 = 73.00 ppm) than the deeper sample (DR-1258-4 = 117.00 ppm). A major proportion of Mo is in Mo_{WA} (40.3% of Mo_{SUM} for DR-1258-1 and 45.1% of Mo_{SUM} for DR-1258-4), with less Mo being strongly adsorbed (Mo_{SA} is 6.3% of Mo_{SUM} for DR-1258-1 and 5.8% of Mo_{SUM} for DR-1258-4; Figure 3.7). For DR-1258-1 TOC is 8.57 wt% and Fe_{py} is 0.63 wt% with other Fe pools much lower (Fe_{carb} is 0.08 wt%; Fe_{ox} is 0.07 wt%; and Fe_{mag} is 0.03 wt%). In DR-1258-4 TOC is 5.69 wt% and Fe_{py} is 1.69 wt%, again with other Fe pools much lower (Fe_{carb} is 0.22 wt%; Fe_{ox} is 0.13 wt%; and Fe_{mag} is 0.04 wt%). Considering the proportions of the TOC and Fe_{py} pools it is possible that Mo in the Mo_{WA} fraction has been desorbed from one of these fractions. Mo is distributed between the remaining Mo pools, but Mo_{py} is the second most dominant fraction in both samples with values of 17.3% and 13.3% of Mo_{SUM} for DR-1258-1 and DR-1258-4 respectively (Figure. 3.7). However, the proportion of other Mo fractions varies between the two samples. In the shallower sample Mo is partitioned $Mo_{WA} > Mo_{py} > Mo_{org} > Mo_{sil} > Mo_{ox1} > Mo_{SA} > Mo_{mag} > Mo_{ox2}$ whereas in the deeper sample Mo is partitioned slightly differently as $Mo_{WA} > Mo_{py} > Mo_{ox1} > Mo_{sil} > Mo_{ox2} > Mo_{org} > Mo_{SA} > Mo_{mag}$. Hetzel et al. (2009) suggest that this environment was intermittently euxinic, evidenced by periodically higher Mo concentrations.

The sample with the higher Mo concentrations (DR-1258-4; 117.00 ppm Mo) is likely to represent deposition beneath a more strongly euxinic water column.

Hetzel et al. (2009) further suggest that Mo is predominantly associated with organic matter in this environment, as evidenced by a generally linear relationship between TOC and sulfurized organic matter. However, the data presented here indicate that, although organic matter is an important Mo sink, it is the pyrite sequestration pathway that dominates. The average ratio for TOC/total S is 4.22 in the unit these samples were collected from (Unit IV; Hetzel et al., 2009) and DR-1258-1 is close to this with a TOC/total S of 4.39. In this sample TOC is 8.6 wt% and the sequential extraction data suggest that organic matter is the second most significant sink for Mo after pyrite (Mo_{org} is 11.72% of Mo_{SUM}). However, in sample DR-1258-4, TOC/total S deviates from the general trend with a value of 1.88 and TOC is lower than the shallower sample at 5.7 wt%. In DR-1258-4 organic matter is only the 5th most significant sink (6.0% of Mo_{SUM}). Therefore, although the TOC/total S value suggests the organic matter in DR-1258-4 may be more sulfidized, it appears that it is the availability of TOC that affects the influence of this pool on Mo sequestration by organic matter and this may explain the difference in the association of Mo with organic matter between the two samples.

As with the DR-1261 samples, the Mo_{ox1} fraction is relatively significant, representing 7.7% of Mo_{SUM} for DR-1258-1 and 10.11% of Mo_{SUM} for DR-1258-4. This fraction reflects Mo associated with Mn oxides; ferrihydrite; lepidocrocite; AVS and other reduced phases; and calcium carbonates. Sample DR-1258-4 was likely deposited under a more strongly euxinic water column and this sample has a higher proportion of Mo in Mo_{ox1} which may reflect the association of Mo with AVS and other reduced phases. However, Fe speciation indicates that Fe oxides and Fe-carbonates persist in this environment and these phases cannot therefore be excluded as potential hosts for Mo in this fraction. Given the proposed geochemical

conditions of this environment, it is likely that Mo was transformed to thiomolybdates in the euxinic water column and therefore probable that Mo also adsorbed to pyrite in the water column.

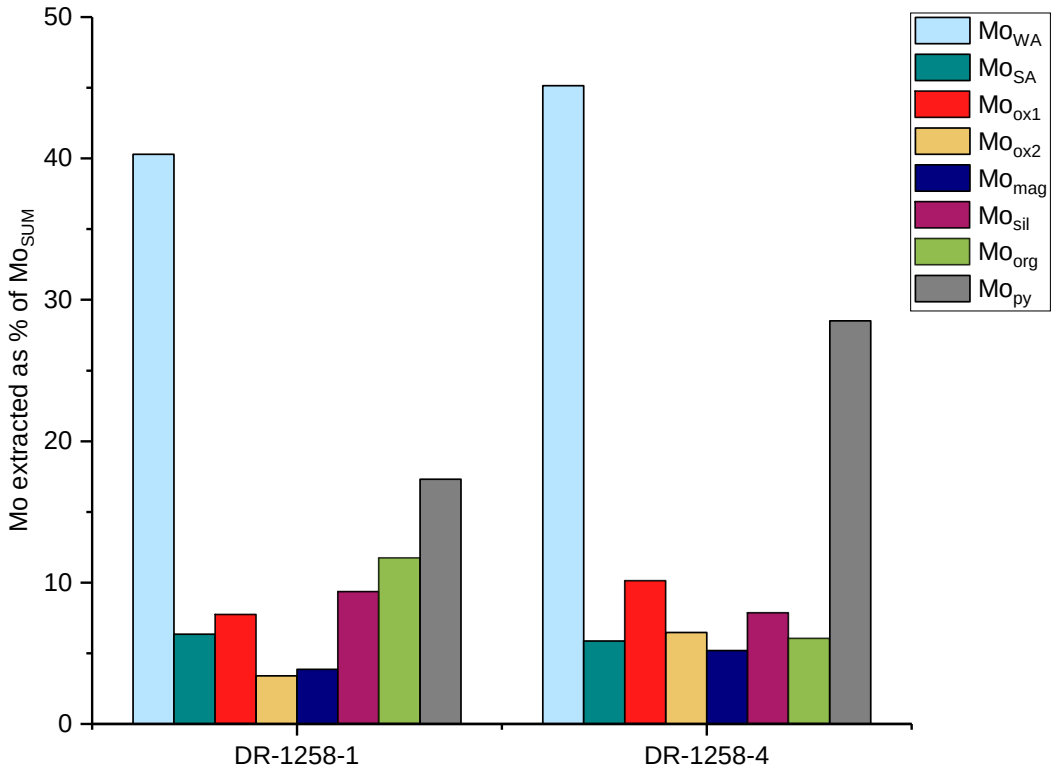

Figure 3.7 *Mo extracted from DR-1258 samples shown as a percentage of the total Mo extracted.*

3.3.10 USGS Green River Shale (USGS-GRS)

The initial extractions (Mo_{WA} and Mo_{SA}) remove a significant proportion of Mo from this sample (Mo_{WA} removes 34.0% of Mo_{SUM} and Mo_{SA} removes 4.8% of Mo_{SUM}). Of the remaining phases, Mo_{org} is the dominant phase (23.9% of the Mo_{SUM}; Figure 3.8), which is perhaps expected considering that the Green River Shale is organic-rich with a TOC content of 24.8 wt% (USGS, 2016). Ingram et al. (1983) suggest that there was bacterial reworking of organic matter during diagenesis, so Mo may have complexed with organic matter in the water column, in porewaters, or during this later bacterial alteration of organics. The Mo_{ox1} fraction is also significant, extracting 14.11% of the Mo_{SUM}. A study of Fe partitioning in the Green

River Shale indicates that the dominant Fe-bearing mineral is Fe-carbonate (Cole et al., 1978) and this is observed in the Fe speciation data which give a value of 0.97 wt% for Fe-carbonates. This fraction would be extracted during the Mo_{ox1} extraction and it is therefore likely that Mo adsorbed to Fe-carbonates (in this environment, Ca-ankerite or Fe-dolomite) was extracted during the Mo_{ox1} 0.5 M HCl extraction. However, Fe speciation also indicates that Fe oxides persist in this environment (Fe_{ox} which is amorphous and crystalline Fe oxides (excluding magnetite) is 0.06 wt%) and it is possible that some Mo in this fraction may be associated with Fe (oxyhydr)oxides. Cole et al. (1978) suggest that the second most dominant Fe-bearing mineral is pyrite and the Fe speciation data indicate that Fe_{py} is 0.63 wt%. The Mo_{py} fraction is the third highest Mo pool in this sample at 9.35% of Mo_{SUM}. Overall, the Mo fractions are in good agreement with the known potential Mo pools for this sample with Mo partitioning as: $Mo_{org} > Mo_{ox1} > Mo_{py} > Mo_{sil} > Mo_{mag} > Mo_{ox2}$.

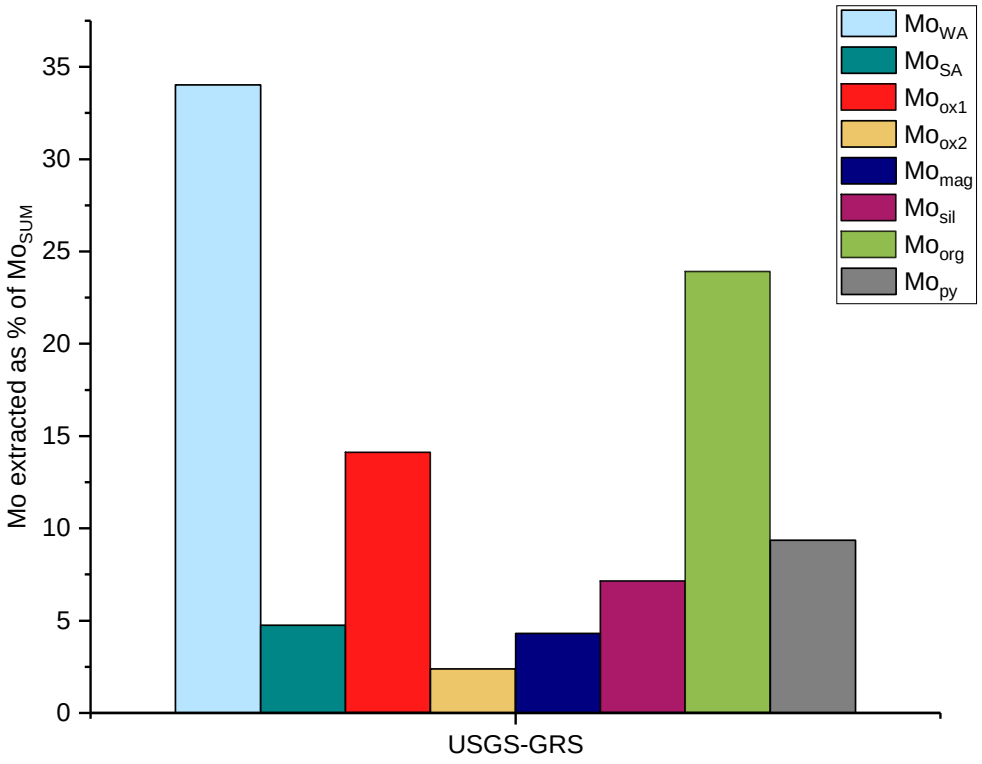

Figure 3.8 *Mo extracted from USGS-GRS samples shown as a percentage of the total Mo extracted.*

3.3.11 Aarhus Bay sample (AB-1B-3)

The initial extraction (Mo_{WA}) removed 21.2% of Mo_{SUM} from the AB-1B-3 sample and Mo_{SA} did not remove any Mo (Figure 3.9). The primary host for Mo identified from the sequential extraction is Mo_{ox2} which removes 40.6% of Mo_{SUM} and overall, the partitioning of Mo after Mo_{WA} is: $Mo_{ox2} > Mo_{ox1} > Mo_{sil} > Mo_{mag}$ with no Mo removed in either the Mo_{org} or Mo_{py} extractions. This sort of partitioning in an oxic environment is expected as MoO_4 adsorbs to Mn and Fe oxides in the water column before downwards transport to sediments (Shimmield and Price, 1986; Scott and Lyons, 2012; Scholz et al., 2013). Fe speciation data show that Fe_{ox1} is 0.45 wt%; Fe_{ox2} is 0.22 wt%; Fe_{mag} is 0.09 wt%; and Fe_{py} is 0.29 wt%. Mo has a strong affinity for pyrite (Bostick et al., 2003) and but the Mo speciation data indicate that there is no Mo in the Mo_{py} pool. This may be because Mo loosely or strong adsorbed to pyrite was removed in the Mo_{WA} and Mo_{SA} extractions but unfortunately it is not possible to confirm this from the sequential extraction data alone.

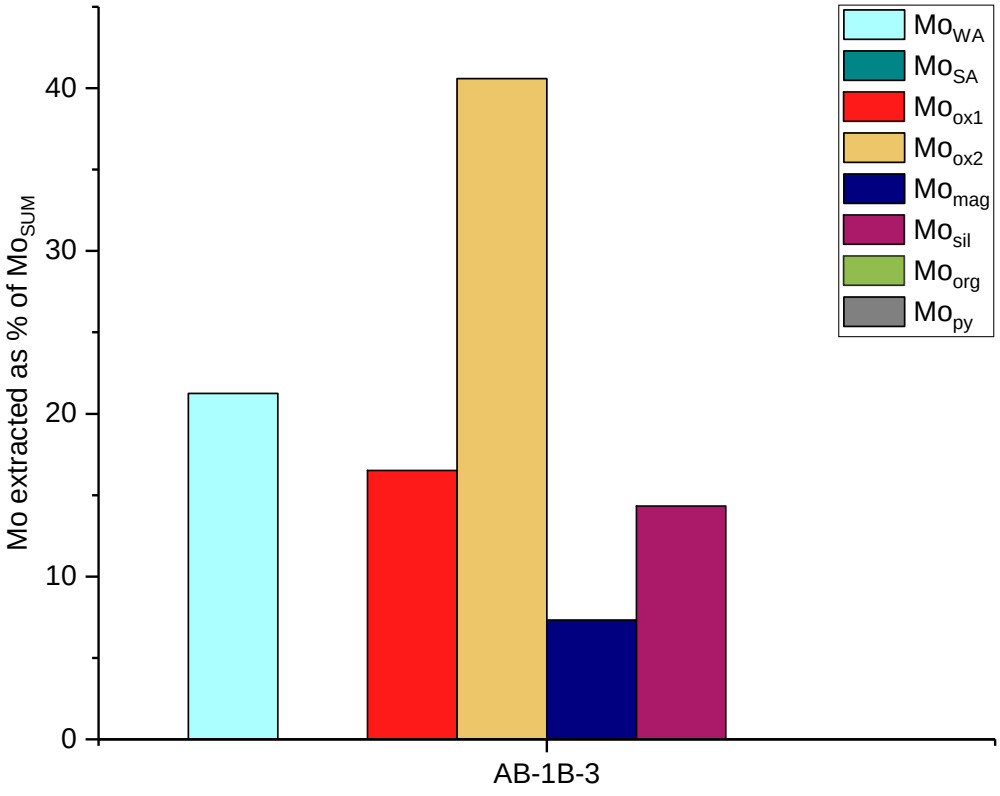

Figure 3.9 *Mo extracted from AB-1B samples shown as a percentage of the total Mo extracted.*

3.3.12 Lake Cadagno samples (LC-1A)

Although these are consecutive samples from the same core, Mo extracted in Mo_{WA} displays the lowest (LC-1A-5) and highest (LC-1A-6) values from any of the samples used in this study (Figure 3.10). The shallower sample (LC-1A-5) removes 9.16% of total Mo in Mo_{WA} and 9.75% of total Mo in Mo_{SA} whereas the slightly deeper sample (LC-1A-6) removes 46.47% of total Mo in Mo_{WA} and 6.03% of total Mo in Mo_{SA}. Although the Mo fractions in both samples differ proportionately, the same sequestration pathways are generally of the same relative importance. In LC-1A-5 Mo is partitioned as $Mo_{ox1} > Mo_{ox2} > Mo_{sil} > Mo_{mag} > Mo_{org} > Mo_{py}$ and in LC-1A-6 Mo is partitioned as $Mo_{ox2} > Mo_{ox1} > Mo_{sil} > Mo_{mag} > Mo_{org} > Mo_{py}$. It is clear from both samples that, although this is a euxinic environment, Fe oxides (both amorphous and crystalline) are important sequestration pathways for Mo. Another study of this environment shows that a minor amount of Fe in the ox1 fraction persists at depth (concentrations are only affected by underwater landslides) and Fe in the ox2 fraction is found at all depths in the core (Xiong et al., 2019). Fe speciation shows that for LC-1A-5 Fe_{ox1} is 0.27 wt%; Fe_{ox2} is 0.91 wt%; Fe_{mag} is 0.34 wt%; Fe_{py} is 0.89 wt% and TOC is 12.12 wt%. In LC-1A-6 Fe_{ox1} is 0.02 wt%; Fe_{ox2} is 0.92 wt%; Fe_{mag} is 0.46 wt%; Fe_{py} 0.94 wt%; and TOC is 8.88 wt%.

This is a stratified lake environment with a chemocline separating upper oxic waters from euxinic bottom waters. Mo may therefore have been sequestered to Fe oxides as: molybdate adsorbed to Fe oxides in oxic waters that escape sulfurization during downwards transport to sediments through the euxinic water column; thiomolybdates formed in euxinic waters that adsorb to Fe oxides in the euxinic water column before downwards transport to sediments, or; thiomolybdates in porewaters that adsorb to Fe oxides from the oxic upper waters that have survived sulfurization during downwards transport to sediments. Considering the amount of Mo that is associated with these fractions, it is unlikely that Mo remained as molybdate as this is a conservative species and more likely that Mo adsorbed to Fe oxides as a highly reactive

thiomolybdate which must have therefore occurred in the euxinic water column or porewaters.

As expected, organic matter and pyrite are also hosts for sedimentary Mo but in this environment, they both appear to play minor roles in Mo sequestration. Mo_{org} removes 2.8% of Mo_{SUM} in sample LC-1A-5 and 2.7% of Mo_{SUM} in sample LC-1A-6 and Mo_{py} removes 1.3% of Mo_{SUM} in LC-1A-5 and 2.0% of Mo_{SUM} in LC-1A-6. Compared to the Fe oxides (Mo_{ox1} and Mo_{ox2}), organic matter and pyrite play relatively minor roles in the sequestration of Mo in this environment. These data are supported by Fe sequential extraction data from Xiong et al. (2019) which show that Fe removed in the ox1 and ox2 extractions (amorphous and crystalline Fe oxides) accounts for 55.2% of total Fe in LC-1A-5 and 29.3% of total Fe in LC-1A-6.

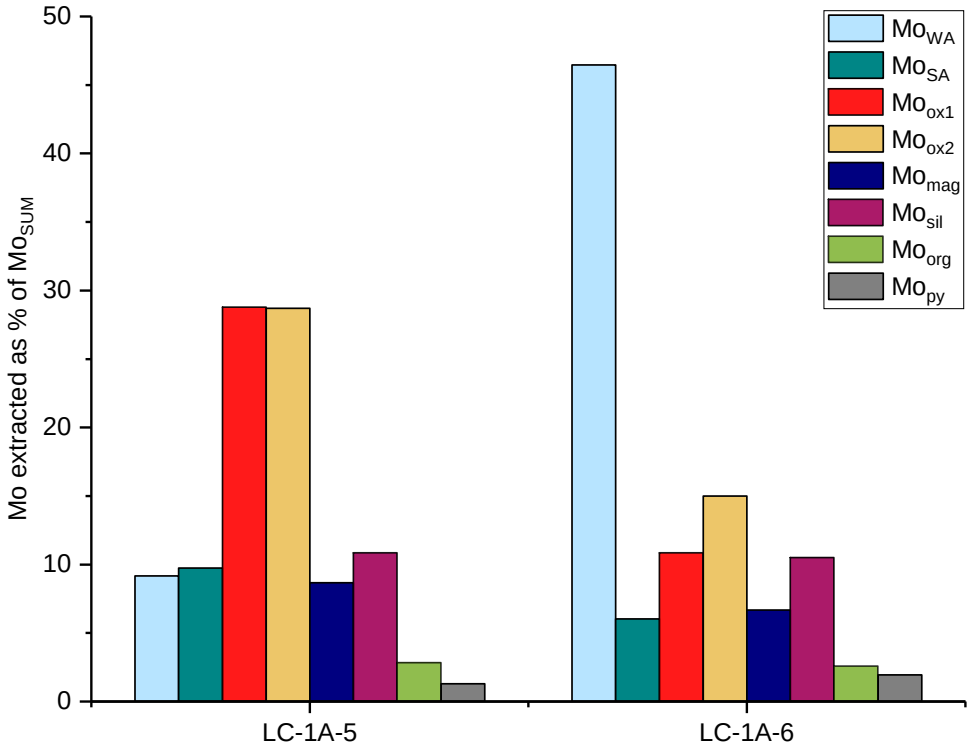

Figure 3.10 *Mo extracted from LC-1A samples shown as a percentage of the total Mo extracted.*

Conversely, Fe associated with pyrite is 18.4% of total Fe in LC-1A-5 and 18.3% of total Fe in LC-1A-6. Mo recovered in Mo_{py} is similar between samples, as is the Fe recovered in the pyrite extraction, whereas 57.5% of total Mo is removed in the Mo_{ox1} and Mo_{ox2} extractions in LC-1A-5 compared to 25.8% of total Mo in LC-1A-6 and these values mirror the Fe removed in the ox1 and ox2 extractions. It appears that Fe oxides in this environment exert a major control over the sequestration of Mo to sediments, significantly more so than organic matter or pyrite. However, weakly or strongly adsorbed Mo may have been removed during the Mo_{WA} and Mo_{SA} steps.

3.4 Conclusions

A novel sequential extraction method for Mo has been developed and tested on a range of sediment samples, both ancient and contemporary, oxic and euxinic. Repeatability is good, even in samples with very low (<2 ppm) Mo and Mo values from the sequential extraction are in good agreement with total Mo values, further validating the method. The incorporation of the Mo_{WA} and Mo_{SA} extractions at the beginning of the sequential extraction highlights the importance of removing weakly and strongly adsorbed Mo before commencing extractions as this Mo can be removed in the first extraction giving false results and can also be easily readsorbed, giving results that do not reflect the original phase associations in later extractions. The wash steps after each extraction are also shown to be important to address readsorption between extractions, particularly after Mo_{ox2E}. The combination of these extractions before, and washes during the sequential extraction prevent the smearing of Mo between extractions.

The sequential extraction was applied to samples from different redox environments and although generally consistent with expected phase associations, the prevalence of Mo in the

Mo_{ox1} and Mo_{ox2} fractions in anoxic and euxinic environments is surprising and highlights a sequestration mechanism that is generally under-represented in the literature.

3.5 References

Acholla, F. V., and Orr, W. L. 1993. Pyrite Removal from Kerogen without Altering Organic Matter: The Chromous Chloride Method. *Energy & Fuels.* **7**, pp. 406-410.

Bostick, B. C., Fendorf, S., and Helz, G. R. 2003. Differential Adsorption of Molybdate and Tetrathiomolybdate on Pyrite (FeS_2). *Environmental Science & Technology*. **37**, pp. 285-291.

Canfield, D. E., Poulton, S. W., and Narbonne, G. M., 2007. Late-Neoproterozoic Deep-Ocean Oxygenation and the Rise of Animal Life. *Science.* **315**, pp. 92-95.

Canfield, D. E., Poulton, S. W., Knoll, A. H., Narbonne, G. M., Ross, G., Goldberg, T., and Strauss, H. 2008. Ferruginous Conditions Dominated Later Neoproterozoic Deep-Water Chemistry. *Science.* **321**, pp. 949-952.

Casalino, C. E., Malandrino, M., Giacomino, A. and Abollino, O. 2013. Total and fractionation metal contents obtained with sequential extraction procedures in a sediment core from Terra Nova Bay, West Antarctica. *Antarctic Science.* **25** (1), pp. 83-98.

Chappaz, A., Lyons, T. W., Gregory, D. D., Reinhard, C. T., Gill, B. C., Li, C., and Large, R. R. 2014. Does pyrite act as an important host for molybdenum in modern and ancient euxinic sediments? *Geochimica et Cosmochimica Acta*. **126**, pp. 112-122

Cheng, M., Li, C., Zhou, L., Algeo, T. J., Zhang, F., Romaniello, S., Jin, C., Lei, L., Feng, L., Jiang, S. 2016. Marine biogeochemistry in the context of dynamically euxinic mid-depth waters. A case study of the lower Cambrian Niutitang shales, South China. *Geochimica et Cosmochimica Acta*. **183**, pp. 79-93.

Cole, R. D., Lui, J., Smith, G. V., Hinckley, C. C., and Saporoschenko, M. 1978. Iron partitioning in oil shale of the Green River Formation Colorado: a preliminary Mössbauer study. *Fuel*. **57**, pp. 514-520.

Collier, R. W. 1985. Molybdenum in the Northwest Pacific Ocean. *Limnology and Oceanography.* **30** (6), pp. 1351-1354.

Cornell, R. M., and Schwertmann, U. 2003. *The Iron Oxides*. 2nd ed. Weinheim: WILEY-VCH Verlag GmbH & Co.

Dahl, T. W., Canfield, D. E., Rosing, M. T., Frei, R. E., Gordon, G. W., Knoll, A. H., and Anbar, A. D. 2011. Molybdenum evidence for expansive sulfidic water masses in ~750 Ma oceans. *Earth and Planetary Sciences Letters.* **311**, pp. 264-274.

Dahl, T. W., Chappaz, A., Hoek, J., McKenzie, C. J., Svane, S., and Canfield, D. E. 2017. Evidence of molybdenum association with particulate organic matter under sulfidic conditions. *Geobiology*. **15** (2), pp. 311-323.

Del Don, C., Hanselmann, K. W., Peduzzi, R., and Bachofen, R. 2001. The meromictic alpine Lake Cadagno: Orographical and biogeochemical description. *Acquatic Sciences*. **63**, pp. 70-90.

Diop, C., Dewaelé, D., Cazier, F., Diouf, A. and Ouddane, B. 2015. Assessment of trace metals contamination level, bioavailability and toxicity in sediments from Dakar coast and Saint Louis estuary in Senegal, West Africa. *Chemossphere*. **138**, pp. 980-987.

Goldberg, T., Archer, C., Vance, D., Thamdrup, B., McAnena, A., and Poulton, S. W. 2012. Controls on the Mo fractionations in a Mn-rich anoxic marine sediment, Gulmar Fjord, Sweden. *Chemical Geology*. **296**, pp. 73-82.

Gustaffson, J. P. 2003. Modelling molybdate and tungstate adsorption to ferrihydrite. *Chemical Geology*. **200**, pp. 105-115.

Hetzel, A. Böttcher, M. E., Wortmann, U. G., and Brumsack, H. 2009. Paleo-redox conditions during OAE 2 reflected in Demerara Rise sediment geochemistry (ODP Leg 207). *Palaeogeography, Palaeoclimatology, Palaeoecology.* **273**, pp. 302-328.

Huerta-Diaz, M. A., and Morse, J. W. 1990. A Quantitative Method for Determination of Trace Metal Concentrations in Sedimentary Pyrite. *Marine Chemistry*. **29**, pp. 119-144.

Ingram, L. L., Ellis, J., Crisp, P. T., and Cook, A. C. 1983. Comparative study of oil shales and shale oils from the Mahogany Zone, Green River Formation (U.S.A.) and Kerosene Creek Seam, Rundle Formation (Australia). *Chemical Geology*. **38**, pp. 185-212.

Kendall, B., Reinhard, C. T., Lyons, T. W., Kaufman, A. J., Poulton, S. W., and Anbar, A. D. 2010. Pervasive oxygenation along late Archean ocean margins. *Nature Geoscience*. **3**, pp. 647-652.

Large, R. R., Danyushevsky, L., Hollit, C., Maslennikov, V., Maffre, S., Gilbert, S., Bull, S., Scott, R., Emsbo, P., Thomas, H., Singh, B. and Foster, J. 2009. Gold and Trace Element Zonation in Pyrite Using a Laser Imaging Technique: Implications for the Timing of Gold in Orogenic and Carlin-Style Sediment Hosted Deposits. *Economic Geology*. **104**, pp. 635-668.

Large, R. R., Halpin, J. A., Danyushevsky, L. V., Maslennikov, V. V., Bull, S. W., Long, J. A., Gregory, D. D., Lounejeva, E., Lyons, T. W., Sack, P. J., McGoldrick, P. J. and Calver, C. R. 2014. Trace element content of sedimentary pyrite as a new proxy for deep-time ocean-atmosphere evolution. *Earth and Planetary Science Letters*. **389**, pp. 209-220.

März, C., Poulton, S. W., Beckmann, B., Küster, K., Wagner, T., and Kasten, S. 2008. Redox sensitivity of P cycling during marine black shale formation: Dynamics of sulfidic and anoxic, non-sulfidic bottom waters. *Geochimica et Cosmochimica Acta*. **72**, pp. 3703-3717.

März, C., Beckmann, B., Franke, C., Vogt, C., Wagner, T., and Kasten, S. 2009. Geochemical environment of the Coniacian-Santonian western tropical Atlantic at Demerara Rise. *Palaeogeography, Palaeoclimatology, Palaeoecology.* **273**, pp. 286-301.

Merhaby, D., Ouddane, B., Net, S. and Halwani, J. 2018. Assessment of trace metals contamination in surficial sediments along Lebanese Coastal Zone. *Marine Pollution Bulletin.* **133**, pp. 881-890.

Mongenot, T., Tribovillard, N., Desprairies, A., Lallier-Vergès, E. and Laggoun-Defarge, F. 1996. Trace elements as palaeoenvironmental markers in strongly mature hydrocarbon source

rocks: the Cretaceous La Luna Formation of Venezuela. *Sedimentary Geology.* **103**, pp. 23-37.

Nasnodkar, M. R. and Nayak, G. N. 2018. Assessment of sediment quality using total and bioavailable concentration of metals in intertidal mudflats of a tropical (Vashishti) estuary, west coast of India. *Arabian Journal of Geosciences.* **11**, pp.1-14.

Olson, L., Quinn, K. A., Siebecker, G., Luther III, G. W., Hastings, D. and Morford, J. L. 2017. Trace metal diagenesis in sulfidic sediments: Insights from Chesapeake Bay. *Chemical Geology*. **452**, pp. 47-59.

Peacock, C. L., and Sherman, D. M. 2004. Copper(II) sorption onto goethite, hematite and lepidocrocite: a surface complexation model based on ab initio molecular geometrics and EXAFS spectroscopy. *Geochimica et Cosmochimica Acta*. **12**, pp. 2623-2637.

Poulson Brucker, R. L., McManus, J., and Poulton, S. W. 2012. Molybdenum isotope fractionation observed under anoxic experimental conditions. *Geochemical Journal*. **46**, pp. 201-209.

Poulton, S. W., and Canfield, D. E. 2005. Development of a sequential extraction procedure for iron: implications for iron partitioning in continentally derived particulates. *Chemical Geology*. **214**, pp. 209-221.

Rao, W., Chen, J., Luo, T. and Liu, L. 2006. Phosphorous geochemistry in the Luochuan loess section, North China and its paleoclimatic implications. *Quaternary International*. **144**, pp. 72-83.

Ravel, B., and Newville, M. 2005. ATHENA, ARTEMIS, HEPHAESTUS: data analysis for X-ray absorption spectroscopy using IFEFFIT. *Journal of Synchrotron Radiation.* **12**, pp. 537-541.

Scholz, F., McManus, J., and Sommer, S. 2013. The manganese and iron shuttle in a modern euxinic basin and implications for molybdenum cycling at euxinic ocean margins. *Chemical Geology.* **355**, pp. 56-68.

Scott, C., and Lyons, T. W. 2012. Contrasting molybdenum cycling and isotopic properties in the euxinic versus non-euxinic sediments and sedimentary rocks: Refining the paleoproxies. *Chemical Geology*. **324-325**, pp. 19-27.

Shimmield, G. B., and Price, N. B. 1986. The behaviour of molybdenum and manganese during early sediment diagenesis – offshore Baja California, Mexico. *Marine Chemistry*. **19**, pp. 261-280.

Spahić, M. P., Manojlović, D., Tančić, P., Cvetković, Z., Nikić, Z., Kovačević, R. and Sakan, S. 2019. Environmental impact of industrial and agricultural activities to the trace element content in soil of Srem (Serbia). *Environ Monit Assess*. **191**, pp. 1-22.

Tessier, A., Campbell, P. G. C., and Bisson, M. 1979. Sequential Extraction Procedure for the Sequential Extraction Procedure for the Speciation of Particulate Trace Metals. *Analytical Chemistry*. **51** (7), pp. 844-851.

Thamdrup, B., Fossing, H., and Jørgensen, B. B. 1994. Manganese, iron and sulfur cycling in coastal marine sediment, Aarhus Bay, Denmark. *Geochimica et Cosmochimica Acta.* **58** (23), pp. 5515-5129.

Tribovillard, N., Riboulleau, A., Lyons, T., and Baudin, F. 2004. Enhanced trapping of molybdenum by sulfurized organic matter of marine origin in Mesozoic limestones and shales. *Chemical Geology*. **213**, pp. 385-401.

USGS. 2016. *U.S. Geological Survey Certificate of Analysis, Green River Shale, SGR-1.* [Online]. [Accessed 01 November 2018]. Available from: https://crustal.usgs.gov/geochemical_reference_standards/shale.html.

Wagner, M., Chappaz, A., and Lyons, T. W. 2017. Molybdenum speciation and burial pathway in weakly sulfidic environments: Insights from XAFS. *Geochimica et Cosmochimica Acta*. **206**, pp. 18-20.

Wichard, T., Mishra, B., Myneni, S. C. B., Bellenger, J., and Kraepiel, A. M. L. 2009. Storage and bioavailability of molybdenum in soils is increased by organic matter complexation. *Nature Geoscience.* **2**, pp. 625-629.

Xiong, Y., Guilbaud, R., Peacock, C. L., Cox, R. P., Canfield, D. E., Krom, M. D., and Poulton, S. W. 2019. Phosphorous cycling in Lake Cadagno, Switzerland: A low sulfate euxinic ocean analogue. *Geochimica et Cosmochimica Acta*. **251**, pp. 116-135.

Chapter 4 A library of molybdenum XANES standards

4.1 Introduction

Mo exists in oxic water columns as its conservative anion, molybdate (MoO_4^{2-}) and under these conditions Mo can be sequestered to sediments via sorption to manganese (Mn) and Fe (oxyhydr)oxides (Arai, 2010; Das et al., 2016; Gustaffson and Tiberg, 2015; and Scholz et al., 2013). However, as Mn and Fe (oxyhydr)oxides are buried into sulfidic porewaters they are expected to undergo reductive dissolution during which Mo desorbs, with the majority diffusing back into the overlying water column (Scholz et al., 2017; Shimmield and Price, 1986; Tribovillard, 2006). These processes can continually cycle Mo between oxic seawater and underlying sediments, and ultimately lead to low Mo sediment concentrations in sediments beneath oxic water columns. As sulfide concentrations increase in the water column, MoO_4 undergoes a series of sulfidation steps where the oxygen atoms are progressively replaced with sulfur atoms ($MoO_3S \rightarrow MoO_2S_2 \rightarrow MoOS_3$) to eventually convert MoO_4 to tetrathiomolybdate (MoS_4). These oxythiomolybdate (MoO_xS_{4-x}) and tetrathiomolybdate species are highly reactive and easily sequestered to sediments, leading to high Mo sediment concentrations in sediments underlying euxinic water columns (Cheng et al., 2016; Dahl et al., 2011; Scott et al., 2008; Wirth et al., 2013). This bi-modal behaviour of Mo has rendered Mo concentrations in marine sediments an attractive palaeoredox proxy, where high sediment Mo concentrations are used as a proxy for a palaeoeuxinic water column (Cheng et al., 2016; Dahl et al., 2011; Scott et al., 2008; Wirth et al., 2013). Although a lot of work has been done using Mo concentrations to infer palaeoredox, the proxy is generally only able to identify whether conditions were oxic or euxinic (e.g. Breward et al., 2015; Cheng et al., 2016; Kendall et al., 2010; and Scott et al., 2008). It is possible that with a better understanding of Mo sequestration to sediments across a range of redox environments, Mo concentrations and moreover, Mo speciation, could be used to distinguish an important range of intermediate

redox states, including ferruginous conditions, that are thought to have been prevalent during most periods of low ocean oxygenation through Earth's history (Canfield et al., 2008; Poulton and Canfield, 2011). To better understand Mo sequestration, researchers are increasingly using synchrotron radiation, specifically XANES spectroscopy, to try to elucidate Mo speciation in sediments and determine Mo sequestration mechanisms and pathways, and hence prevailing redox conditions (Dahl et al., 2013; Vorlicek et al., 2018; Wagner et al., 2017). This effort is severely hindered however, by a lack of published XANES standards for the sequestration of Mo by different sediment phases. To address this, a comprehensive library of Mo XANES standards has been developed that represent the main Mo sequestration pathways in sediments, specifically, Mo adsorbed to Mn and Fe (oxyhydr)oxides, and pyrite, and Mo complexed with organic acids. Detailed characterisation of this library is provided for future use and the library has been applied to determine Mo speciation and phase associations in natural sediments, highlighting its potential as a tool for determining Mo sequestration pathways in sediments and therefore its potential to help extend the Mo palaeoredox proxy.

4.2 Materials and Methods

4.2.1 Synchrotron radiation generation

Synchrotron radiation is generated when charged particles (at the Diamond Light Source synchrotron these are electrons) travel at close to light speeds in a curved path such as the one shown in Figure 2.1 (Winick, 1994; Diamond Light Source, 2020). The following description specifically describes the Diamond Light Source synchrotron (Diamond Light Source, 2020). Electrons evaporate from the surface of a high voltage cathode which is heated under a vacuum by a process of thermionic emission and are then accelerated in the linear accelerator (linac; Figure 4.1, 1) before they are injected into the booster synchrotron (Figure 4.1, 2). Here the electron energy is increased from 0.1 GeV to 3 GeV with a radio frequency voltage source and a series of bending magnets. When required, electrons are injected into the storage ring

(Figure 4.1, 3) which is made of 25 straight sections and 50 dipole magnets that form a closed loop with an orbit >560 m. Synchrotron light which is typically known as the 'beam' is channelled into beamlines (Figure 4.1, 4) where it passes through a shield (Figure 4.1, 5) into the optics hutch (Figure 4.1, 6) where it is filtered and focussed. It then enters the experimental hutch (Figure 4.1, 7) where the X-rays generated by the high energy electrons meet the sample and during the experiment this interaction is monitored and controlled from the control cabin (Figure 4.1, 8).

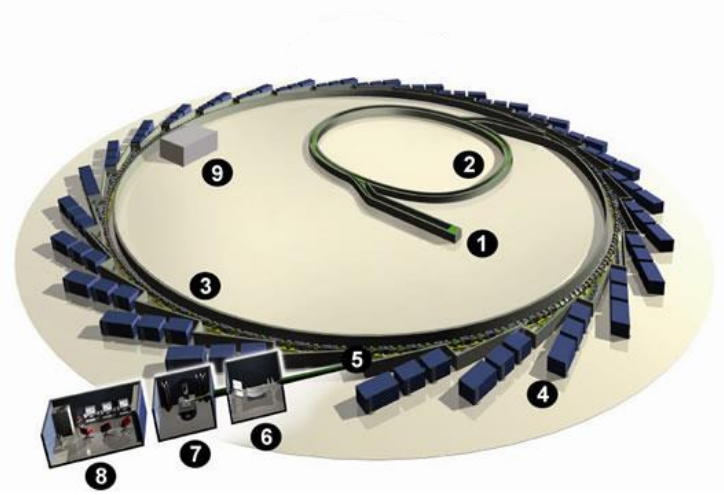

Figure 4.1 *Schematic diagram of the Diamond Light Source synchrotron showing: (1) the electron gun and linac; (2) the booster synchrotron; (3) the storage ring; (4) the beamlines; (5) front ends; (6) the optics hutch; (7) the experimental hutch; (8) the control cabin; (9) radiofrequency cavity (after Diamond Light Source 2020).*

4.2.2 The generation of XANES spectra

The generation of XANES spectra is explained by Calvin (2013) as follows. X-rays of a definite energy interact with the sample and cause a core electron to become excited to a higher energy state, or to be ejected, leaving a core hole. An electron from a higher energy shell falls to fill the core hole, producing a fluorescence emission in the process, and this emission can be measured. The process is then repeated with a slightly different X-ray energy to produce a spectrum. For example, Mo has a known K shell electron binding energy of 20,000 eV and therefore XANES are collected from 19980 eV to 20100 eV. The portion of the XANES scan before the Mo edge (20,000 eV) is therefore flat as the X-ray energy is not sufficient to excite a core electron. The features of the XANES spectra are explained in Section 4.3.1.

4.2.3 XAS techniques for the study of molybdenum

X-ray absorption spectroscopy (XAS) techniques have been used extensively for the study of Mo in terms of both XANES (e.g. Dahl et al., 2013; George et al., 2007; Vorlicek et al., 2018) and EXAFS investigations (e.g. Clausen et al., 1986; Helz et al., 1996; Kashiwabara et al., 2009). Early investigations by Cramer et al. (1976) identified a correlation between the absorbance edge position and the Mo oxidation state. It was suggested that as Mo becomes reduced from Mo(VI) the edge position decreases in eV and this work has been supported by subsequent XAS investigations (e.g. Cramer 1978; Essilfie-Dughan et al., 2011; Wharton et al., 2003). This phenomenon occurs because the edge energy corresponds to the energy required to excite a core level electron to an empty state (Henderson et al., 2014). Therefore, if there are less valence electrons, the effective nuclear charge is increased and it takes a greater amount of energy to remove the core electron (Pickering et al., 1995). The presence, absence and amplitude of a pre-edge peak on the main edge can also provide information on the Mo coordination environment. The pre-edge peak arises from 1s $\rightarrow$ 4d transitions which are dipole forbidden and is generally representative of the amount of p-d mixing (George et al., 2009). The presence of a high-amplitude peak indicates tetrahedral coordination (Arai, 2010; Dahl et al., 2013; Essilfie-Dughan et al., 2011; Vorlicek et al., 2018) whereas a suppressed peak generally reflects distorted octahedral coordination (Clausen et al., 1986; Wharton et al., 2003). The absence of a pre-edge peak eliminates tetrahedral coordination and is therefore indicative of an octahedral coordination environment (Clausen et al., 1986; Cramer et al., 1978; Wagner et al., 2017; Wharton et al., 2003). These features and their associated positions in eV are used in a XANES fingerprinting technique to match unknown Mo samples to known Mo standards by correlating these key characteristics in the XANES region (e.g. Brinza et al., 2015; Wagner et al., 2017; Wharton et al., 2003).

4.2.4 Development of the XAS technique

4.2.4.1 XANES collection

XANES for Mo standards were collected at the Diamond Light Source (DLS) Ltd. synchrotron on beamlines B18 (for bulk XANES) and I18 (for micro-focus XANES) during eight beamtime sessions during February 2015 and November 2017.

For natural samples micro-focus µ-XRF elemental maps (for Mo, Zr, Mn and Fe,) were collected for pressed pellets and self-supported micro-thin sections. Maps were generally collected at 20.4 keV with a pixel size of 10 x 10 µM and a count time of one second per pixel but these parameters were altered according to individual sample requirements. Maps were deadtime corrected and processed using custom beamline software. The maps were used to find Mo 'hot spots' to indicate where to collect Mo XANES. Mn and Fe were mapped to highlight any relationships with Mo. Zr was collected as this element has a Kβ_1 peak at 17667.8 eV which is similar to the Kα_1 from Mo (17479.34 eV) and therefore produces a signal in the µ-XRF maps that can lead to misidentification of Mo hot spots. The euxinic and nitrogenous environments both contained significant amounts of Zr in the samples as a result of the local lithology. Genuine Mo hot spots were identified by switching between Zr and Mo in the mapping software to determine genuine points of interest. A test scan was then performed on these locations to confirm the presence of Mo and it was at these points of interest (POIs) that XANES were collected. The Mo concentration and quality of XANES spectra obtained determined the number of scans that were collected from each POI. If a POI had a high Mo concentration, then more XANES were collected to be merged and reduce background noise. However, XANES were monitored and additional scans were abandoned if the XANES quality was poor. XANES were also monitored for photo-oxidation by observing any changes in amplitude of the pre-edge feature and white line. If it was deemed that photo-oxidation had started to occur then further XANES at this POI were abandoned. Generally, a minimum of

three XANES scans were merged for each sample. For high Fe samples, aluminium sheets were placed in front of the detector to attenuate Fe fluorescence.

XANES were collected in fluorescence mode and during collection storage ring energy was 3.0 GeV, the beam current was approximately 300 mA, and the beam size was ~2 x 2.5 µM for µ-focus XANES on I18 and 200 x 250 µM for bulk XANES on B18. A Si(111) double crystal monochromator was used to select photon energy for both beamlines with a 9-element solid state Ge detector or a 4 element Si drifts detector.

Files were calibrated by taking measurements for a Mo(0) foil in transmission mode. The first peak in the Mo(0) foil derivative was calibrated to 20,000.0 and the resulting energy shift was applied to files from that particular beamline session to correct for monochromator offset.

The $Mo(VI)O_4$(aq) reference was presented to the beam in a polypropylene centrifuge tube. The $Mo(VI)O_xS_{4-x}$(aq) and $Mo(VI)S_4$(aq) references were presented to the beam in sealed polypropylene centrifuge tubes. Samples for adsorbed and incorporated δMnO_2-MoO_4, ferrihydrite-MoO_4, goethite-MoO_4 and magnetite-MoO_4 were finely ground with cellulose nitrate and pressed into pellets, which were attached to the sample stage with Kapton tape and presented to the beam. Samples for adsorbed and incorporated δMnO_2-MoS_4, ferrihydrite-MoS_4, goethite-MoS_4, magnetite-MoS_4 and the $Mo(IV)S_3$ reference were finely ground and sealed between three layers of Kapton film under an argon atmosphere, before being moved to the beamline, after which samples were attached to the sample stage with Kapton tape and presented to the beam. The adsorbed pyrite-MoO_4 and pyrite-MoS_4 standards were presented to the beam in sealed polypropylene centrifuge tubes which were sealed under a nitrogen atmosphere to prevent oxidation. Samples for acetic acid-MoO_4, phosphoric acid-MoO_4, and tannic acid-MoO_4 were presented to the beam in polypropylene

centrifuge tubes. Samples for acetic acid-MoS_4, phosphoric acid-MoS_4, and tannic acid-MoS_4 were moved from anaerobic storage and presented to the beam as solutions inside sealed polypropylene centrifuge tubes. The organic-Mo sediment sample (LC-1A) was finely ground and sealed between three layers of Kapton film under an argon atmosphere, before being moved to the beamline, after which the sample was attached to the sample stage with Kapton tape and presented to the beam. The bulk nitrogenous sample (NIT-ST1) was presented to the beam as a micro-thin section, adhered to Kapton tape.

4.2.4.2 XANES processing

XANES data reduction was performed using Athena 0.9.26 (Ravel and Newville, 2005). Specifically Athena was used to calibrate from monochromator position (millidegrees) to energy (eV) and to average multiple spectra from individual samples. For background subtraction the pre-edge was fit to a linear function and the post-edge to one 2nd-order polynomial segment.

For each spectra, the derivative was selected as the first peak and groups of spectra for the same point were aligned to the first scan. XANES collected for a Mo(0) foil reference were calibrated to 20,000.0 in Athena to give a positive or negative energy shift by selecting the highest peak. This energy shift was then applied to any merged files acquired during that beamtime.

Individual XANES were assessed to identify any changes in the amplitude of the pre-edge feature or change in the white line and XANES from the same location where this was not apparent were merged to improve signal to noise ratio. Where appropriate, files were smoothed in Athena but all smoothed files were compared to the original to ensure pertinent

features and the positions of those features were retained in the smoothed spectra. Where this was not the case smoothed spectra were rejected and the original XANES were used.

4.2.5 Synthesis and characterisation of mineral and organic phases

Mn-oxide (δMnO_2) was synthesised after Villalobos et al. (2003) by combining manganese (II) chloride ($MnCl_2$), potassium permanganate ($KMnO_4$) and sodium hydroxide (NaOH). Ferrihydrite, goethite ($\alpha FeOOH$) and magnetite (Fe_3O_4) were synthesised after Cornell and Schwertmann (2003). Ferrihydrite was synthesised by combining iron (III) nitrate ($Fe(NO_3)_3 \cdot 9H_2O$) with NaOH; goethite by combining $Fe(NO_3)_3 \cdot 9H_2O$ with potassium hydroxide (KOH) before heating for 60 h at 70°C, and magnetite by combining iron (II) sulfate ($FeSO_4 \cdot 7H_2O$), KOH and potassium nitrate (KNO_3) under anaerobic conditions. Two batches of each mineral were made, one for Mo adsorption and one with Mo incorporated during mineral synthesis as described below.

Fe sulfide (pyrite) was purchased from Strem Chemicals and was used under anoxic conditions. The pyrite was washed consecutively in 18.2MΩ cm Type 1 deionized water, 0.5 M hydrochloric acid (HCl) and 0.1 M sodium sulfide (Na_2S) solutions to remove any oxidised surface species (Bostick et al., 2003).

Sample purity of the Fe (oxyhydr)oxides and Fe sulfide was confirmed by XRD using a Phillips PW1050 for non-oxygen sensitive samples and a Brucker D8 Advance for oxygen-sensitive samples (Appendix B).

Marine organic matter contains a variety of different functional groups, most abundantly carboxyl, phosphoric and hydroxyl groups (Hertkorn et al., 2006; Zark and Dittmar, 2018). To determine the XANES signature of Mo-carboxyl and Mo-phosphoric binding environments,

acetic and phosphoric acids were used as Mo-organic analogues (Moon and Peacock, 2011). Tannic acid was used as an analogue for Mo complexed with phenolic functional groups (Wagner et al., 2017).

4.2.6 Mo sorption to mineral and organic phases

Samples of molybdate (MoO_4) or tetrathiomolybdate (MoS_4) adsorbed and incorporated with Mn and Fe (oxyhydr)oxides and pyrite, and complexed with a range of organic phases, were prepared under either aerobic (MoO_4) or anaerobic conditions inside an anaerobic chamber (MoS_4), using MQ and analytical grade reagents at room temperature. pH meters were calibrated to ±0.1 pH units using Fisher Scientific pH 4 and pH 7 buffer solutions (traceable to NIST).

For MoO_4 or MoS_4 adsorbed to Mn and Fe (oxyhydr)oxides, the general method of Peacock and Sherman (2004) was followed. Specifically, 2 g of the mineral (either as a dry mineral or a dry-weight equivalent of a mineral slurry) was added to a 50 mL centrifuge tube with 38.39 mL of a 0.1 M sodium chloride (NaCl) background electrolyte and 1.61 mL of a 1000 ppm Mo stock solution (Na_2MoO_4 or $(NH_4)_2MoS_4$). Solution pH was adjusted to pH 7 and samples were shaken end-over-end for 2 d. The MoS_4 containing samples were prepared under a nitrogen atmosphere. Solid-to-solution ratio was 1:0.8 and the samples contained 2.3 wt% Mo at 100% adsorption. For MoO_4 incorporated into Fe-oxides, the general method of Brinza et al. (2015) was followed. Specifically, a 1000 ppm solution of MoO_4/MoS_4 was mixed with the KOH solution for goethite and the KOH/KNO_3 solution for magnetite prior to their mixing with $Fe(NO_3)_3 \cdot 9H_2O$ or $FeSO_4 \cdot 7H_2O$. Samples contained 3.1 wt% Mo at 100% incorporation.

For MoO_4 or MoS_4 adsorbed to pyrite, the general method of Bostick et al., (2003) was followed. Specifically, 2 g of the mineral was added to a 50 mL centrifuge tube with 36.16 mL

of 0.1 M NaCl background electrolyte and 3.84 mL of a 1000 ppm Mo stock solution (Na_2MoO_4 or $(NH_4)_2MoS_4$). Solution pH was adjusted to between pH 6.7-7.5 and samples were shaken end-over-end for 28 h. Both the MoO_4 and MoS_4 containing samples were prepared under a nitrogen atmosphere. Solid-to-solution ratio was 1:0.8 and the samples contained 7.7 wt% Mo at 100% adsorption.

All MoO_4 containing samples were washed in MQ, air-dried and ground to a fine powder, while MoS_4 containing samples were washed in deoxygenated MQ and air-dried under a nitrogen atmosphere. For analysis at Diamond Light Source Ltd. (DLS) all MoO_4 containing samples were transported as air-dried, finely ground powders in glass vials, while MoS_4 containing samples were added to polypropylene centrifuge tubes and transferred into Kilner jars sealed under a nitrogen atmosphere, with AnaeroGen™ sachets. Upon arrival at DLS, air-sensitive samples were immediately transferred into an anaerobic chamber filled with an argon atmosphere.

For MoO_4 or MoS_4 complexed with acetic- and phosphoric-acid, the general method of Moon and Peacock (2011) was followed. Specifically, acids were prepared to 5 M solutions and mixed in equal amounts with 0.05 M Na_2MoO_4 or $(NH_4)_2MoS_4$ solutions. For MoO_4 or MoS_4 complexed with tannic-acid, the general method of Wagner et al. (2017) was followed. Specifically, 5 mM Na_2MoO_4 or $(NH_4)_2MoS_4$ was mixed with 187.5 mM tannic acid in a 1:37.5 ratio. All MoS_4 samples were prepared under a nitrogen atmosphere in polypropylene centrifuge tubes. For analysis at DLS samples were transported as solutions in polypropylene centrifuge tubes in Kilner jars containing AnaeroGen™ sachets to prevent oxidation, sealed under a nitrogen atmosphere, and upon arrival at DLS were immediately transferred into an anaerobic chamber filled with an argon atmosphere.

A sample of pure Mo-organic material was isolated from sediment core LC-1A from the euxinic part of the stratified Lake Cadagno (Xiong et al., 2019, Section 2.1.4). Once other fractions had been removed, organic material was washed with deoxygenated MQ and air-dried under a nitrogen atmosphere. For analysis at DLS the sample was transported in a polypropylene centrifuge tube inside a Kilner jar with AnaeroGen™ sachets, sealed under a nitrogen atmosphere, and upon arrival at DLS was immediately transferred into an anaerobic chamber filled with an argon atmosphere.

A sample of bulk sediment was also taken from a sediment core from the anoxic, nitrogenous part of the Golfo Dulce Basin, Costa Rica (Poulton, 2019; Thamdrup et al., 1996). This sample was untreated with no Mo fractions chemically removed. The sample was finely ground and encased into EpoFix epoxy resin, polished to produce a self-supported micro-thin section ~60 µM thick (Section 2.8.2), and transported to DLS encased between glass slides to maintain physical stability.

A $Mo(VI)O_4(aq)$ reference in which Mo is present as Mo(VI) tetrahedrally coordinated by 4 oxygen atoms was prepared as a 1000 ppm Mo solution at DLS in a polypropylene centrifuge tube. A $Mo(VI)S_4(aq)$ reference in which Mo is present as Mo(VI) tetrahedrally coordinated by 4 sulfur atoms was prepared as a 500 ppm Mo solution and transported to DLS in a polypropylene centrifuge tube inside a Kilner jar with AnaeroGen™ sachets, sealed under a nitrogen atmosphere. Upon arrival at DLS the jar was immediately transferred into an anaerobic chamber filled with an argon atmosphere. A $Mo(VI)O_xS_{4-x}(aq)$ reference in which Mo is present as Mo(VI) tetrahedrally coordinated by both oxygen and sulfur atoms was prepared as a 500 ppm MoS_4 solution which was left exposed to air for >1 month to partially oxidise. The solution was transported to DLS in a sealed polypropylene centrifuge tube. A $Mo(IV)S_3(s)$ reference in which Mo is present as Mo(IV) trigonally coordinated by 3 sulfur atoms was

prepared anaerobically after Wang et al. (1997) by acidification of aqueous $(NH_4)_2MoS_4$ to <pH 3 with 0.1 M HCl. The resulting solid was air-dried under a nitrogen atmosphere. For analysis at DLS the solid was transferred in a polypropylene centrifuge tube inside a Kilner jar with AnaeroGen™ sachets, sealed under a nitrogen atmosphere. Upon arrival at DLS was immediately transferred into an anaerobic chamber filled with an argon atmosphere.

4.3 Results and discussion

A comprehensive library of XANES standards is presented that represents the main Mo sequestration pathways in sediments, specifically Mo sorbed to Mn and Fe (oxyhydr)oxides and pyrite, and Mo complexed with organic acids (Figure. 4.2). In order that these XANES standards can be used to determine Mo geochemistry in XANES spectra from sediments in which Mo geochemistry is unknown, 10 spectral features are defined that in combination are unique to each standard (Section 4.3.1). These spectral features are then used to characterise each XANES standard (Section 4.3.2). Finally the validity of the Mo XANES standards library is demonstrated by applying the XANES standards to characterise Mo speciation and phase associations in natural sediments (Section 4.3.3).

The XANES region is designated as the area between 19980 and 20100 eV (Bostick et al., 2003; Gustaffson and Tiberg, 2015).

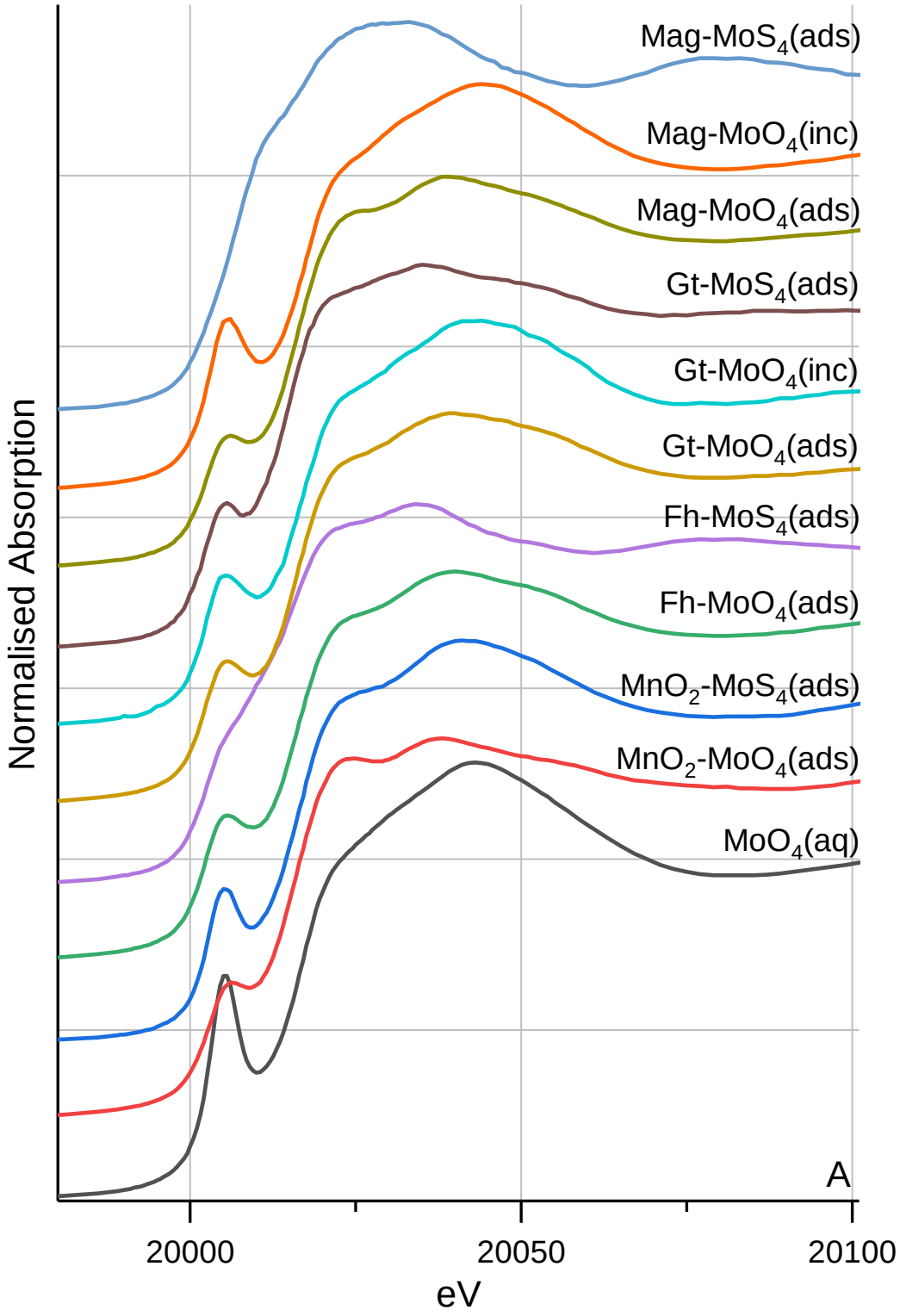
Mag-MoS4(ads)
Mag-MoO4(inc)
Mag-MoO4(ads)
Gt-MoS4(ads)
Gt-MoO4(inc)
Gt-MoO4(ads)
Fh-MoS4(ads)
Fh-MoO4(ads)
MnO2-MoS4(ads)
MnO2-MoO4(ads)
MoO4(aq)
A
Normalised Absorption
20000
20050
20100
eV

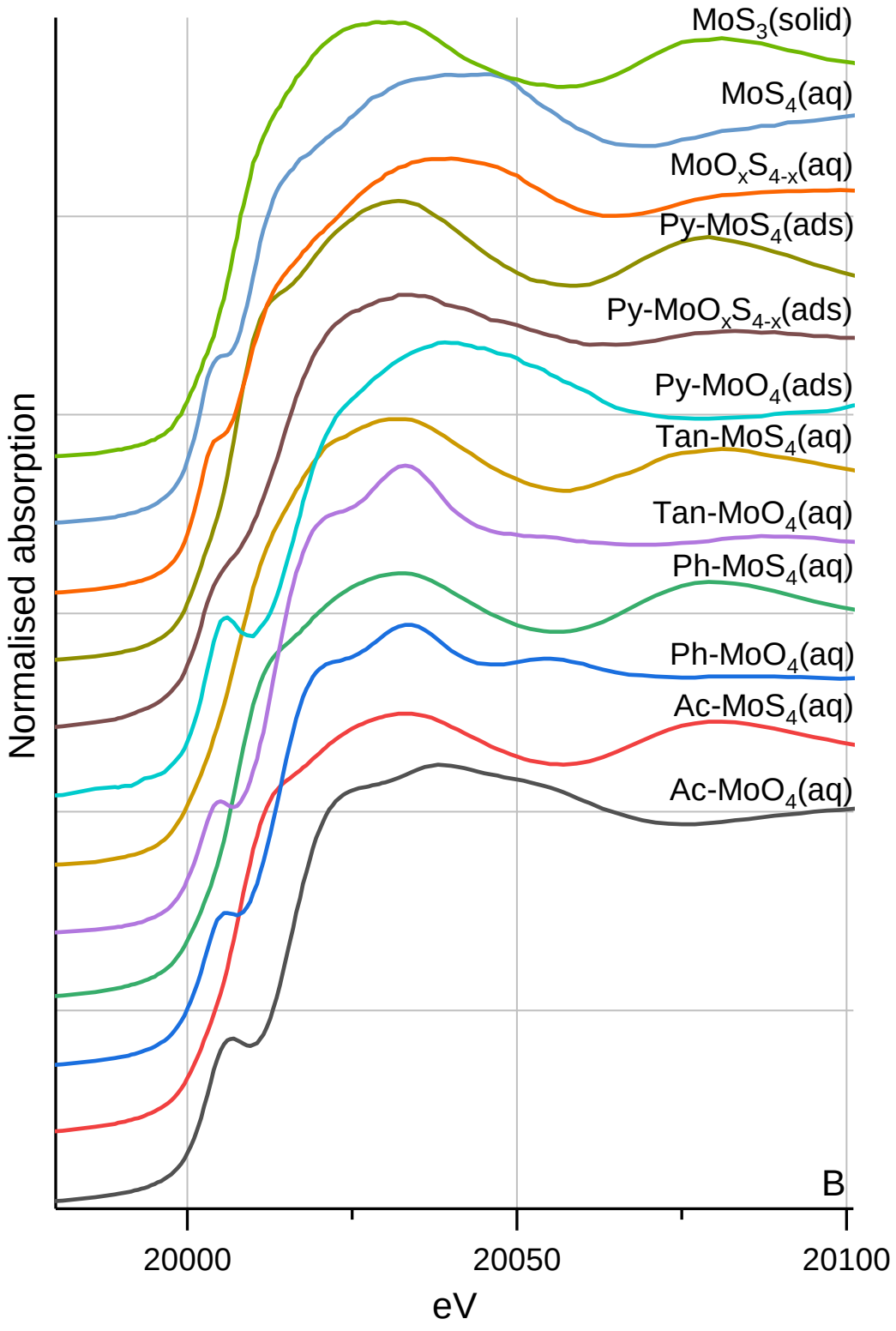

Figure 4.2 *Normalised XANES spectra for the Mo XANES standard library with MoO_4, MoO_xS_{4-x} or MoS_4 adsorbed (ads), incorporated into (inc), or complexed in solution (aq) with: A) manganese oxide (δMnO_2), ferrihydrite (Fh), goethite (Gt), magnetite (Mag); B) acetic acid (Ac), phosphoric acid (Ph), tannic acid (Tan) and pyrite (Py). Aqueous $Mo(VI)O_4$ (A), $Mo(VI)O_xS_{4-x}$ (B), $Mo(VI)S_4$ (B) and solid $Mo(IV)S_3$ (B) are included for reference.*

4.3.1 Characteristic Mo XANES spectral features

The spectral features used to characterise each Mo XANES standard are show in Figure 4.3 and Table 4.1 and described in detail below.

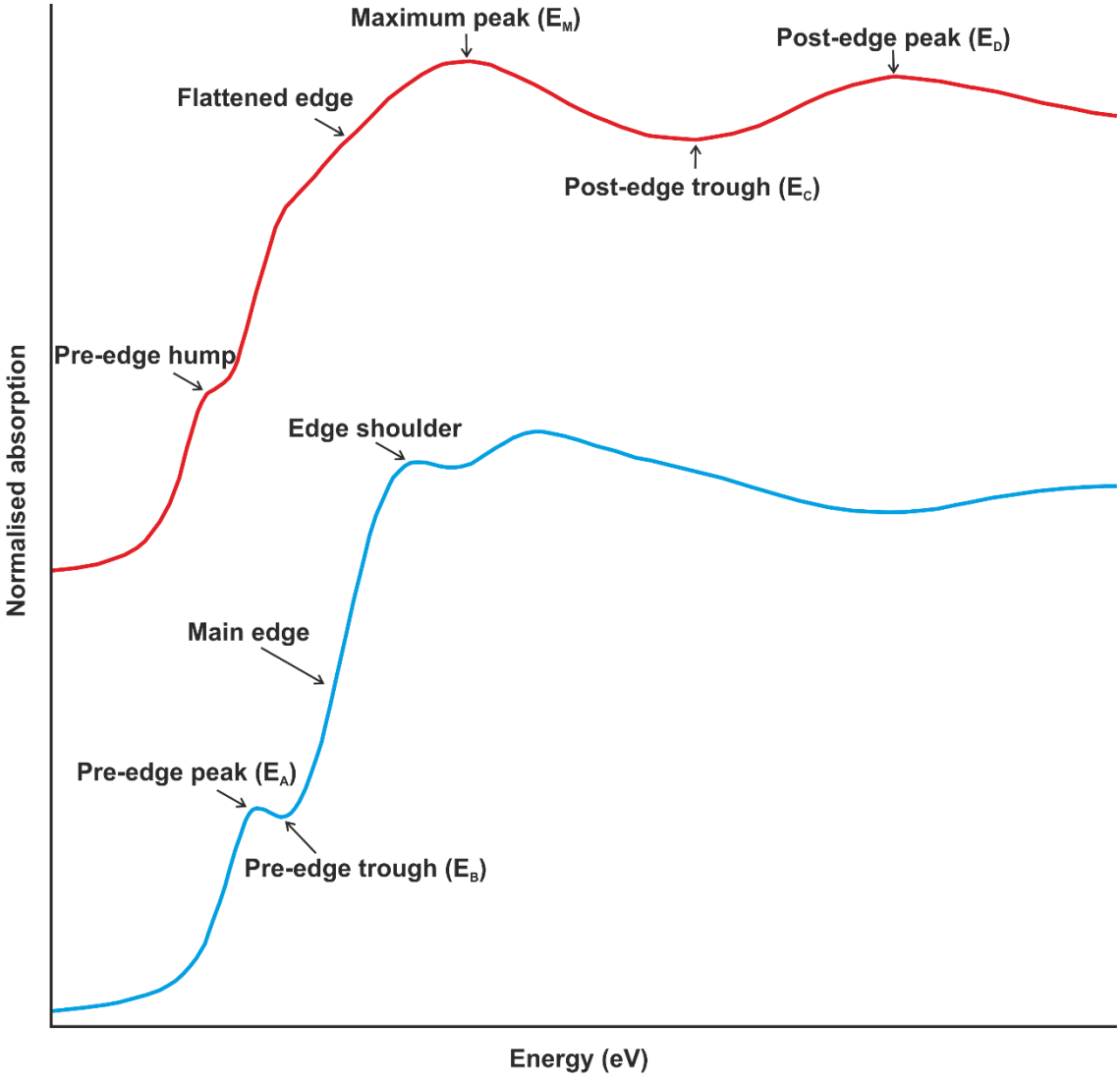

Figure 4.3 *Normalised generic XANES spectra showing spectral features used to characterise the Mo XANES standard library. Spectral features are listed and described in Table 4.1. Note two generic XANES spectra are shown to clearly display the different spectral features.*

Table 4.1 *Spectral features used to characterise the Mo XANES standard library. All features are measured on the normalised XANES spectra unless otherwise stated.*

SPECTRAL FEATURE	**DESCRIPTION**
1. E0	- the energy maxima of the peak in the first derivative of the normalised XANES spectrum that results from the main absorption edge
2. E_M	- the energy maxima of the peak of the main absorption edge
3. E_S	- the energy shift in the main absorption edge position (E0) of a standard relative to the $Mo(VI)O_4(aq)$ reference
4. E_A	- the energy maxima of the pre-edge peak
5. E_B	- the energy minima of the pre-edge trough following the pre-edge peak
6. E_C	- the energy minima of the post-edge trough following the maximum absorption peak
7. E_D	- the energy maxima of the first post-edge hump
Other features	
8. Pre-edge hump – a low amplitude pre-edge feature without an associated trough	
9. Flattened edge – a decrease in the gradient of the main absorption edge before the maximum absorption peak	
10. Edge shoulder – a feature towards the top of the main absorption edge before the maximum absorption peak	

4.3.1.1 Main absorption edge, E0 and E_S

The main absorption edge reflects the sudden increase in absorption energy due to the excitation of a core Mo electron and here is considered as the region after any pre-edge features and before any edge shoulders and/or the maximum absorption peak (Figure. 4.3). In general, the position of the main edge in energy space provides information on the oxidation state of the absorber atom (Cramer et al., 1978). The position and shape of the main edge in energy space also provides information on the local coordination environment around the absorber atom (Dahl et al., 2013). To characterise the position of the main edge in the XANES standards, the spectral feature E_M is defined as the energy maxima of the peak of the main absorption edge in the normalised XANES spectrum (Dahl et al., 2013; Dahl et al., 2017; Wagner et al., 2017), and E0 as the energy maxima of the peak in the first derivative of the normalised XANES spectrum that results from the main edge (Figure. 4.3; Table 4.1). To characterise the oxidation state of Mo in the XANES standards E_S is defined as the energy shift between the main edge position (E0) of a standard and E0 of the $Mo(VI)O_4(aq)$ reference in the normalised XANES spectrum (Figure. 4.4). A main edge position (E0) at lower energy is indicative of lower Mo oxidation state (Cramer, 1978; Essilfie-Dughan et al., 2011, George et al., 2007, Pickering et al., 1995; Wharton et al., 2003) and thus the E0 for more reduced standards should be lower than the E0 of the $Mo(VI)O_4(aq)$ reference (i.e. the energy shift E_S is relatively large), while the E0 for more oxidised standards should be more similar to the E0 of the $Mo(VI)O_4(aq)$ reference (i.e. the energy shift E_S is relatively small). To constrain the E_S value indicative of more reduced standards, it is noted that the main edge position of the $Mo(IV)S_3(s)$ reference is 10.4 eV lower than the $Mo(VI)O_4(aq)$ reference and therefore E_s is -10.4 eV. However, to consider the influence of the local coordination environment around the Mo absorber on the position of the main edge and thus E_s it is noted that the $Mo(VI)S_4(aq)$ reference also has a lower main edge position compared to the $Mo(VI)O_4(aq)$ reference with an E_s of -6.4 eV. To more precisely determine the E_S at or above which a standard can be

determined to contain reduced Mo, the E_S approach is calibrated by plotting each standard as E_M-E0 vs. E0-20,000 (Dahl et al., 2013) (Figure. 4.5). As expected, the Mo(IV)S_3(s) reference plots in the lowest and most left-hand position and defines the energy space for reduced Mo(IV), while the Mo(VI)S_4(aq) reference plots in the highest most left-hand position and defines the energy space for oxidised Mo(VI) coordinated by sulfur ligands (Dahl et al., 2013). Given this spatial differentiation there are five nominally Mo(VI)-containing MoS_4 standards that group closely with the Mo(IV)S_3(s) reference and thus appear to contain reduced Mo: Mag-MoS_4(ads), Ac-MoS_4(aq), Ph-MoS_4(aq), Tan-MoS_4(aq) and Py-MoS_4(ads), with E_S values of -9.7, -9.0, -9.5, -10.0 and -9.8 eV, respectively (Figure. 4.5; Appendix C). Based on this spatial grouping, $E_S \leq$ -9.0 eV is indicative of a standard that likely contains reduced Mo. It is noteworthy that the Mo(VI)O_xS_{4-x}(aq) reference plots halfway between the group of Mo standards that likely contain reduced Mo and the Mo(VI)S_4(aq) reference (Figure. 4.5), and also the E_S value is -7.7 eV, which, although above -9.0 eV, is significantly below that of the Mo(VI)S_4(aq) reference. Taken together these indicators suggest that the Mo(VI)O_xS_{4-x}(aq) reference may also contain reduced Mo. The apparent lack of reduced Mo in the Py-MoO_xS_{4-x}(ads) standard (Figure. 4.5; Appendix C) suggests that the adsorption of Mo(VI)O_xS_{4-x}(aq) to pyrite acts to stabilise Mo against reduction.

Overall the XANES spectra suggest that Mo in Mo(VI)S_4 is reduced during adsorption to magnetite and pyrite, and during complexation with some organics. This is in agreement with Tucker et al., (1997) whose investigations into Mo complexation with organic matter indicate a reduction step, and more recently with Dahl et al. (2013; 2017) who suggest that a reduction from Mo(VI) to Mo(IV) is an important step in the sequestration of Mo in euxinic environments, particularly when complexed with organic matter.

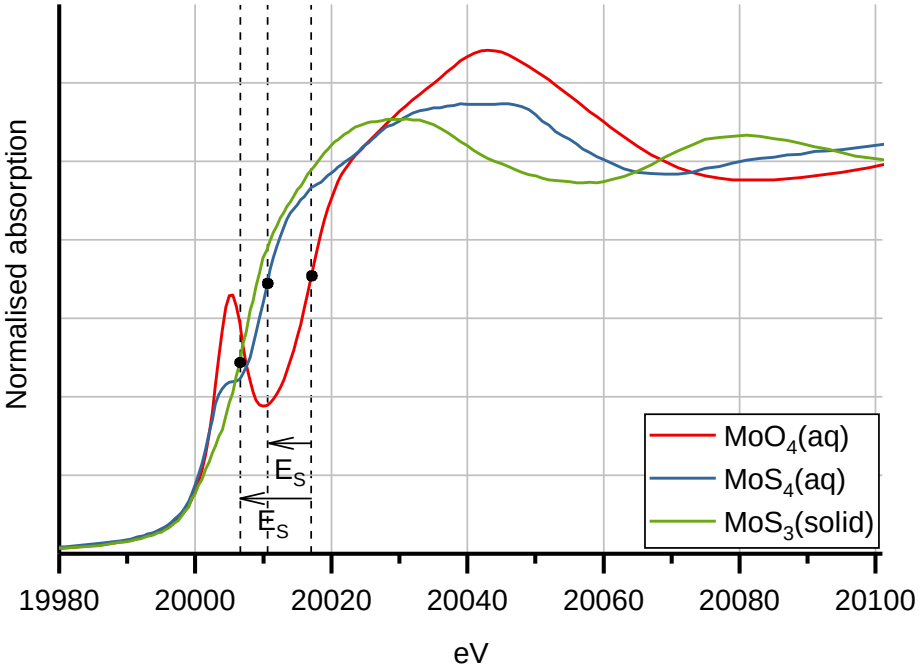

Figure 4.4 *Normalised XANES spectra for the Mo(VI)O_4(aq), Mo(VI)S_4(aq) and Mo(IV)S_3(s) references. Black circles denote the position of E0 on the normalised XANES spectrum of each reference. E_S is shown for the Mo(VI)S_4(aq) reference (-6.4 eV) and Mo(IV)S_3(s) reference (-10.4 eV).*

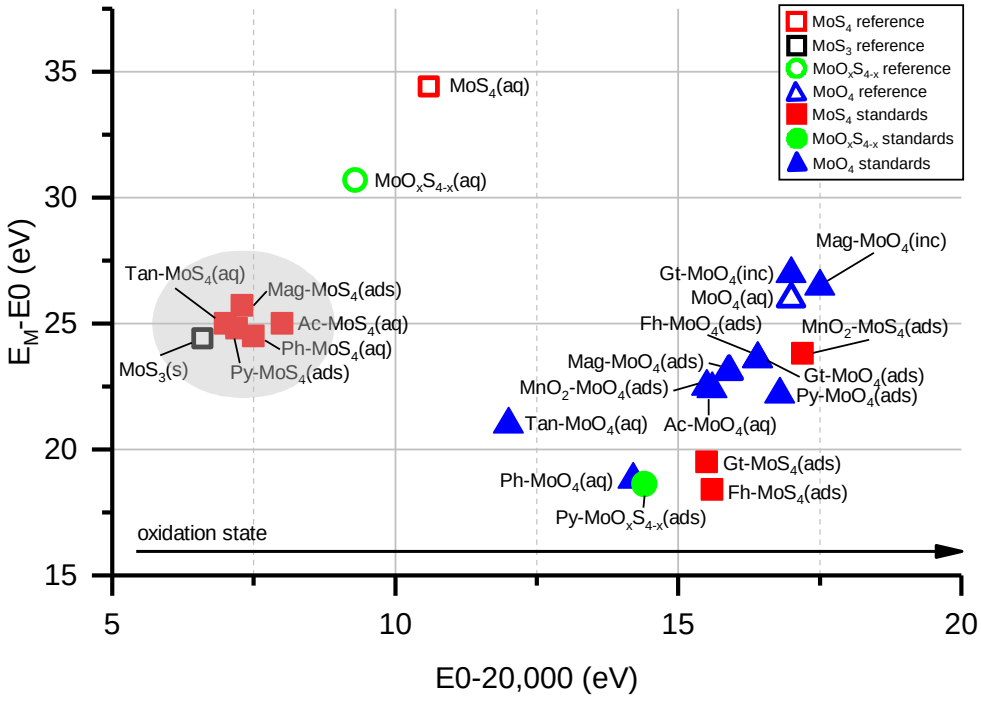

Figure 4.5 *Mo XANES standards and references plotted as E_M-E0 vs. E0-20,000 after Dahl et al. (2013). Standards in the shaded area likely contain reduced Mo.*

4.3.1.2 Pre-edge peak, pre-edge trough and pre-edge hump

The pre-edge peak (E_A) is defined as the energy maxima of a peak before the main edge, and the pre-edge trough (E_B) is defined as the energy minima of the trough immediately following E_A, both measured in the normalised XANES spectrum (Figure. 4.3; Table 4.1). A high-intensity pre-edge peak is largely a feature of 1s $\rightarrow$ 4p state transitions as these formally dipole forbidden (Essilfie-Dughan et al, 2011; Dahl et al, 2013).

The pre-edge hump describes the presence or absence of a less defined peak at the same energy as E_A, without a subsequent trough, observed in the normalised XANES spectrum (Figure. 4.3; Table 4.1). The intensity of the pre-edge feature is related to Mo coordination chemistry, with a well-defined pre-edge peak indicative of tetrahedrally coordinated Mo (Arai, 2010; Cramer et al., 1978; Essilfie-Dughan et al., 2011; Wharton et al., 2003, Wichard et al., 2009). Accordingly, the $Mo(VI)O_4(aq)$ and $Mo(VI)S_4(aq)$ references where Mo(VI) is tetrahedrally coordinated by 4 oxygen, or 4 sulfur atoms, respectively, display well-defined pre-edge peaks (Figure. 4.2). A decrease in the intensity of the pre-edge peak, such that it becomes a pre-edge hump, is indicative of a transition towards distorted octahedrally coordinated Mo (Clausen et al., 1986; Wichard et al., 2009), while a smooth main edge with no pre-edge features is considered to be indicative of octahedrally coordinated Mo (Arai, 2010; Cramer et al., 1978; Das et al., 2016; Essilfie-Dughan et al., 2011; Vorlicek et al., 2018; Wharton et al., 2003; Wichard et al., 2009). The $Mo(VI)O_xS_{4-x}(aq)$ reference where Mo(VI) is coordinated to a mixture of four oxygen/sulfur atoms displays a high-amplitude pre-edge hump rather than a pre-edge peak which can be indicative of tetrahedral or distorted octahedral coordination (Clausen et al., 1986; Wharton et al., 2003). The trigonally coordinated MoS_3 reference where Mo is coordinated by three sulfur atoms displays a smooth main edge with no pre-edge feature and therefore this spectral characteristic appears to reflect both octahedral and trigonal coordination.

The XANES standards show that δMnO_2-MoO_4(ads), δMnO_2-MoS4(ads), Fh-MoO_4(ads), Gt-MoO_4(ads), Gt-MoO_4(inc), Gt-MoS_4(ads), Mag-MoO_4(ads), Mag-MoO_4(inc), Ac-MoO_4(aq), Ph-MoO_4(aq), Tan-MoO_4(aq), Py-MoO_4(ads), and MoO_xS_{4-x}(aq) display well-defined pre-edge peaks and thus contain Mo in tetrahedral coordination (Figure. 4.2). These standards contain Mo in the same coordination as the Mo(VI)O_4(aq) or Mo(VI)S_4(aq) references used during their synthesis, and do not appear to have experienced a transition in coordination geometry during Mo adsorption or incorporation. This is in agreement with Das et al. (2016) who suggest that MoO_4 adsorbed to pyrite retains its tetrahedral coordination as an outer-sphere complex and Bostick et al. (2003) who observe that MoO_4 retains its structural coordination during adsorption to pyrite. The XANES standards for Fh-MoS_4(ads) and Py-MoO_xS_{4-x}(ads) display a pre-edge hump rather than a pre-edge peak and thus may contain some distorted octahedrally coordinated Mo (Figure. 4.2; Clausen et al., 1986; Wharton et al., 2003). The XANES standards for Mag-MoS_4(ads), Ac-MoS_4(aq), Ph-MoS_4(aq), Tan-MoS_4(aq), Py-MoS_4(ads) are without pre-edge peaks or pre-edge humps, and thus contain Mo in octahedral coordination (Figure. 4.2; Appendix C). These standards appear to have experienced a transition from tetrahedral to octahedral coordination during Mo adsorption or complexation, such that octahedral coordination appears to dominate for Mo-sulfur ligation. This is in agreement with previous work on Mo-organic complexes, proposing that when tetrahedrally coordinated Mo reacts with carboxyl and phenol groups in organic matter, it becomes octahedrally coordinated (Cruywagen and De Wet, 1988; Bibak and Borggaard, 1994). It is also supported by previous work on Mo-pyrite association, in which MoS_4 is reported to undergo structural rearrangement during uptake (Bostick et al., 2003). It is noteworthy that δMnO_2-MoS_4(ads) and Gt-MoS_4(ads) are the only standards containing tetrathiomolybdate species that display well-defined pre-edge features and thus contain Mo in tetrahedral coordination (Figure. 4.2; Appendix C). It therefore appears that during the adsorption of Mo(VI)S_4(aq) to these Mn and Fe (oxyhydr)oxides, a transition from tetrahedrally to octahedrally coordinated Mo is inhibited.

4.3.1.3 Post-edge trough and post-edge hump

The post-edge trough (E_C) is defined as the energy minima of the trough immediately after the maximum peak (E_M), measured in the normalised XANES spectrum (Figure. 4.3; Table 4.1). The post-edge hump (E_D) is defined as the energy maxima of the first (usually very broad) peak following E_M, measured in the normalised XANES spectrum (Figure. 4.3; Table 4.1). It should be noted that for several standards the post-edge hump lies outside the defined energy range for XANES but is nonetheless included as a characteristic spectral feature (Appendix C). In fact, the post-edge hump is a part of the EXAFS region and its spectral signature is most likely related to the distance between the central Mo absorber and the first coordination sphere. A lower E_D indicates a longer first coordination sphere distance and hence most likely octahedral coordination. A common feature of most standards that display a post-edge hump within the defined energy range for Mo XANES (19980 to 20100 eV) is the absence of any pre-edge features that are indicative of Mo in octahedral coordination (Arai, 2010; Cramer et al., 1978; Das et al., 2016; Essilfie-Dughan et al., 2011; Vorlicek et al., 2018; Wharton et al., 2003; Wichard et al., 2009; Appendix C). Only the Ph-MoO_4(aq) and Tan-MoO_4(aq) standards have both a post-edge hump and a medium amplitude pre-edge peak and are defined as containing Mo in tetrahedral coordination (Figure. 4.2; Appendix C). It is therefore possible that the presence of a post-edge hump in spectra that do not display any pre-edge features can be used as a secondary characteristic for Mo in octahedral coordination. Indeed, all of the standards presented here that have been characterised as containing Mo in octahedral coordination by the absence of any pre-edge features also include a post-edge hump within the XANES energy range.

4.3.1.4 Flattened edge and edge shoulder

A flattened edge describes the presence or absence of a decrease in the gradient of the main edge immediately before the maximum peak, measured in the normalised XANES spectrum

(Figure. 4.3; Table 4.1). An edge shoulder, or a less defined hump at the same energy, with or without an associated trough, describes the presence or absence of a peak on the main edge immediately before the maximum peak, measured in the normalised XANES spectrum (Figure. 4.3; Table 4.1). In addition to the measured characteristic spectral features described above, the presence or absence of these observed features facilitates the fingerprinting technique used to match XANES standards to natural sediments.

4.3.2 Characterisation of each Mo XANES standard

The characterisation of each Mo XANES standard with reference to the defined spectral features is listed in Appendix C and described in detail below for the main Mo sequestration pathways in natural sediments, specifically, Mo sorbed to Mn and Fe (oxyhydr)oxides, and pyrite, and Mo complexed with organic acids.

4.3.2.1 Reference $Mo(VI)O_4(aq)$, $Mo(VI)O_xS_{4-x}(aq)$, $Mo(VI)S_4(aq)$ and $Mo(IV)S_3(s)$

Characterisation of the Mo XANES spectral features for the $Mo(VI)O_4(aq)$ reference indicate that the main edge and associated parameters are present at: E_M = 20043.0 eV; E0 = 20017.0 eV, and as this reference is the standard by which others are compared to calculate E_S; E_s = 0.0 eV. The pre-edge region is characterised by a high-amplitude pre-edge peak with E_A at 20005.5 eV and E_B at 20010.0 eV. The post-edge region is characterised by E_C at 20083.0 eV with E_D outside of the XANES range. In addition, the $Mo(VI)O_4(aq)$ reference displays a flattened edge. In summary these spectral characteristics indicate that $Mo(VI)O_4(aq)$ contains largely oxidised Mo in mainly tetrahedral coordination.

Characterisation of the Mo XANES spectral features for the $Mo(VI)O_xS_{4-x}(aq)$ reference indicate that the main edge and associated parameters are present at: E_M = 20040.0 eV; E0 = 20009.3 eV; and E_s = -7.7 eV. The pre-edge region is characterised by a high-intensity pre-edge hump.

The post-edge region is characterised by E_C at 20063.0 eV with E_D at 20099.0 eV. In addition, the Mo(VI)O_xS_{4-x}(aq) reference displays a flattened edge. In summary these spectral characteristics indicate that Mo(VI)O_xS_{4-x}(aq) contains largely oxidised Mo in tetrahedral or distorted octahedral coordination.

Characterisation of the Mo XANES spectral features for the Mo(VI)S_4(aq) reference indicate that the main edge and associated parameters are present at: E_M = 20045.0 eV; E0 = 20010.6 eV; and E_s = -6.4 eV. The pre-edge region is characterised by a pre-edge hump. The post-edge region is characterised by E_C at 20069.0 eV with E_D outside of the XANES region. In addition, the Mo(VI)S_4(aq) reference displays a flattened edge. In summary these spectral characteristics indicate that Mo(VI)S_4(aq) contains largely oxidised Mo in mainly tetrahedral or distorted octahedral coordination.

Characterisation of the Mo XANES spectral features for the Mo(IV)S_3(s) reference indicate that the main edge and associated parameters are present at: E_M = 20031.0 eV; E0 = 20006.6 eV; and E_s = -10.4 eV. The pre-edge region is characterised by the absence of a pre-edge peak or hump. The post-edge region is characterised by E_C at 20057.0 eV with E_D at 20081.0 eV. In summary these spectral characteristics indicate that Mo(IV)S_3(s) contains largely reduced Mo in mainly octahedral coordination.

4.3.2.2 Mo sorbed to Mn-oxide

Characterisation of the Mo XANES spectral features for the δMnO_2-MoO_4(ads) standard indicate that the main edge and associated parameters are present at: E_M = 20038.0 eV; E0 = 20015.5 eV; and E_s = -1.5 eV. The pre-edge region is characterised by a pre-edge peak with E_A at 20006.0 eV and E_B at 20009.0 eV. The post-edge region is characterised by E_C at 20087.0 eV with E_D outside of the XANES range. In addition, the δMnO_2-MoO_4(ads) standard displays a

prominent edge shoulder and a slightly flattened edge. In summary these spectral characteristics indicate that δMnO_2-MoO_4(ads) contains largely oxidised Mo in mainly tetrahedral coordination.

Characterisation of the Mo XANES spectral features for the δMnO_2-MoS_4(ads) standard indicate that the main edge and associated parameters are present at: E_M = 20041.0 eV; E0 = 20017.2 eV; and E_s = +0.2 eV. The pre-edge region is characterised by a pre-edge peak with E_A at 20005.0 eV and E_B at 20009.0 eV. The post-edge region is characterised by E_C at 20079.0 eV with E_D outside of the XANES range. In addition, the δMnO_2-MoS_4(ads) standard displays an edge shoulder and a flattened edge. In summary these spectral characteristics indicate that δMnO_2-MoS_4(ads) contains largely oxidised Mo in mainly tetrahedral coordination.

4.3.2.3 Mo sorbed to Fe-(hydr)oxides

4.3.2.3.1 Ferrihydrite

Characterisation of the Mo XANES spectral features for the Fh-MoO_4(ads) standard indicate that the main edge and associated parameters are present at: E_M = 20040.0 eV; E0 = 20016.4 eV; and E_s = -0.6 eV. The pre-edge region is characterised by a pre-edge peak with E_A at 20005.5 eV and E_B at 20009.5 eV. The post-edge region is characterised by E_C at 20081.0 eV with E_D outside of the XANES range. In addition, the Fh-MoO_4(ads) standard displays a low-amplitude edge shoulder and a flattened edge. In summary these spectral characteristics indicate that Fh-MoO_4(ads) contains largely oxidised Mo in mainly tetrahedral coordination.

Characterisation of the Mo XANES spectral features for the Fh-MoS_4(ads) standard indicate that the main edge and associated parameters are present at: E_M = 20034.0 eV; E0 = 20015.6 eV; and E_s = -1.4 eV. The pre-edge region is characterised by a very low-amplitude pre-edge hump. The post-edge region is characterised by E_C at 20061.0 eV with E_D at 20081.0 eV. In

addition, the Fh-MoS_4(ads) standard displays a slight edge shoulder and a flattened edge. In summary these spectral characteristics indicate that Fh-MoS_4(ads) contains largely oxidised Mo in tetrahedral or distorted octahedral coordination.

4.3.2.3.2 *Goethite*

Characterisation of the Mo XANES spectral features for the Gt-MoO_4(ads) standard indicate that the main edge and associated parameters are present at: E_M = 20040.0 eV; E0 = 20016.4 eV; and E_s = -0.6 eV. The pre-edge region is characterised by a pre-edge peak with E_A at 20005.5 eV and E_B at 20009.5 eV. The post-edge region is characterised by E_C at 20077.0 eV with E_D outside of the XANES range. In addition, the Gt-MoO_4(ads) standard displays a slight edge shoulder and a flattened edge. In summary these spectral characteristics indicate that Gt-MoO_4(ads) contains largely oxidised Mo in mainly tetrahedral coordination.

Characterisation of the Mo XANES spectral features for the Gt-MoO_4(inc) standard indicate that the main edge and associated parameters are present at: E_M = 20044.0 eV; E0 = 20017.0 eV; and E_s = 0.0 eV. The pre-edge region is characterised by a pre-edge peak with E_A at 20005.5 eV and E_B at 20010.0 eV. The post-edge region is characterised by E_C at 20073.0 eV with E_D outside of the XANES range. In addition, the Gt-MoO_4(inc) standard displays a flattened edge. In summary these spectral characteristics indicate that Gt-MoO_4(inc) contains largely oxidised Mo in mainly tetrahedral coordination.

Characterisation of the Mo XANES spectral features for the Gt-MoS_4(ads) standard indicate that the main edge and associated parameters are present at: E_M = 20035.0 eV; E0 = 20015.5 eV; and E_s = -1.5 eV. The pre-edge region is characterised by a pre-edge peak with E_A at 20005.5 eV and E_B at 20008.0 eV. The post-edge region is characterised by E_C at 20071.0 eV with E_D outside of the XANES range. In addition, the Gt-MoS_4(ads) standard displays a

flattened edge. In summary these spectral characteristics indicate that Gt-MoS_4(ads) contains largely oxidised Mo in mainly tetrahedral coordination.

4.3.2.3.3 *Magnetite*

Characterisation of the Mo XANES spectral features for the Mag-MoO_4(ads) standard indicate that the main edge and associated parameters are present at: E_M = 20039.0 eV; E0 = 20015.9 eV; and E_s = -1.1 eV. The pre-edge region is characterised by a pre-edge peak with E_A at 20006.0 eV and E_B at 20009.0 eV. The post-edge region is characterised by E_C at 20079.0 eV with E_D outside of the XANES range. In addition, the Mag-MoO_4(ads) standard displays an edge shoulder and a flattened edge. In summary these spectral characteristics indicate that Mag-MoO_4(ads) contains largely oxidised Mo in mainly tetrahedral coordination.

Characterisation of the Mo XANES spectral features for the Mag-MoO_4(inc) standard indicate that the main edge and associated parameters are present at: E_M = 20044.0 eV; E0 = 20017.5 eV; and E_s = +0.5 eV. The pre-edge region is characterised by a pre-edge peak with E_A at 20006.0 eV and E_B at 20010.5 eV. The post-edge region is characterised by E_C at 20079.0 eV with E_D outside of the XANES range. In addition, the Mag-MoO_4(inc) standard displays a flattened edge. In summary these spectral characteristics indicate that Mag-MoO_4(inc) contains largely oxidised Mo in mainly tetrahedral coordination.

Characterisation of the Mo XANES spectral features for the Mag-MoS_4(ads) standard indicate that the main edge and associated parameters are present at: E_M = 20033.0 eV; E0 = 20007.3 eV; and E_s = -9.7 eV. The pre-edge region is characterised by the absence of any pre-edge features. The post-edge region is characterised by E_C at 20060.0 eV with E_D at 20079.0 eV. In addition, the Mag-MoS_4(ads) standard displays a flattened edge. In summary these spectral

characteristics indicate that Mag-MoS_4(ads) contains largely reduced Mo in mainly octahedral coordination.

4.3.2.4 Mo sorbed to pyrite

Characterisation of the Mo XANES spectral features for the Py-MoO_4(ads) standard indicate that the main edge and associated parameters are present at: E_M = 20039.0 eV; E0 = 20016.8 eV; and E_s = -0.2 eV. The pre-edge region is characterised by a pre-edge peak with E_A at 20006.0 eV and E_B at 20010.0 eV. The post-edge region is characterised by E_C at 20077.0 eV with E_D outside of the XANES range. In addition, the Py-MoO_4(ads) standard displays a flattened edge. In summary these spectral characteristics indicate that Py-MoO_4(ads)contains largely oxidised Mo in mainly tetrahedral coordination.

Characterisation of the Mo XANES spectral features for the Py-MoO_xS_{4-x}(ads) standard indicate that the main edge and associated parameters are present at: E_M = 20033.0 eV; E0 = 20014.4 eV; and E_s = -2.6 eV. The pre-edge region is characterised by a slight pre-edge hump. The post-edge region is characterised by E_C at 20065.0 eV with E_D at 20083.0 eV. In addition, the Py-MoO_xS_{4-x}(ads) standard displays a slightly flattened edge. In summary these spectral characteristics indicate that Py-MoO_xS_{4-x}(ads) contains largely oxidised Mo in tetrahedral or distorted octahedral coordination.

Characterisation of the Mo XANES spectral features for the Py-MoS_4(ads) standard indicate that the main edge and associated parameters are present at: E_M = 20032.0 eV; E0 = 20007.2 eV; and E_s = -9.8 eV. The pre-edge region is characterised by the absence of any pre-edge features. The post-edge region is characterised by E_C at 20059.0 eV with E_D at 20079.0 eV. In addition, the Py-MoS_4(ads) standard displays an edge shoulder and a flattened edge. In

summary these spectral characteristics indicate that Py-MoS_4(ads) contains largely reduced Mo in mainly octahedral coordination.

4.3.2.5 Mo complexed with organics

Characterisation of the Mo XANES spectral features for the Ac-MoO_4(aq) standard indicate that the main edge and associated parameters are present at: E_M = 20038.0 eV; E0 = 20015.6 eV; and E_s = -1.4 eV. The pre-edge region is characterised by a pre-edge peak with E_A at 20007.0 eV and E_B at 20009.5 eV. The post-edge region is characterised by E_C at 20075.0 eV with E_D outside of the XANES region. In addition, the Ac-MoO_4(aq) standard displays an edge shoulder and a flattened edge. In summary these spectral characteristics indicate that Ac-MoO_4(aq) contains largely oxidised Mo in mainly tetrahedral coordination.

Characterisation of the Mo XANES spectral features for the Ac-MoS_4(aq) standard indicate that the main edge and associated parameters are present at: E_M = 20033.0 eV; E0 = 20008.0 eV; and E_s = -9.0 eV. The pre-edge region is characterised by the absence of any pre-edge features. The post-edge region is characterised by E_C at 20057.0 eV with E_D at 20081.0 eV. In addition, the Ac-MoS_4(aq) standard displays a flattened edge. In summary these spectral characteristics indicate that Ac-MoS_4(aq) contains largely reduced Mo in mainly octahedral coordination.

Characterisation of the Mo XANES spectral features for the Ph-MoO_4(aq) standard indicate that the main edge and associated parameters are present at: E_M = 20033.0 eV; E0 = 20014.2 eV; and E_s = -2.8 eV. The pre-edge region is characterised by a pre-edge peak with E_A at 20005.5 eV and E_B at 20007.5 eV. The post-edge region is characterised by E_C at 20047.0 eV with E_D at 20054.0 eV. In addition, the Ph-MoO_4(aq) standard displays an edge shoulder and a

flattened edge. In summary these spectral characteristics indicate that Ph-MoO_4(aq) contains largely oxidised Mo in mainly tetrahedral coordination.

Characterisation of the Mo XANES spectral features for the Ph-MoS_4(aq) standard indicate that the main edge and associated parameters are present at: E_M = 20032.0 eV; E0 = 20007.5 eV; and E_s = -9.5 eV. The pre-edge region is characterised by an absence of any pre-edge features. The post-edge region is characterised by E_C at 20056.0 eV with E_D at 20079.0 eV. In addition, the Ph-MoS_4(aq) standard displays a flattened edge. In summary these spectral characteristics indicate that Ph-MoS_4(aq) contains largely reduced Mo in mainly octahedral coordination.

Characterisation of the Mo XANES spectral features for the Tan-MoO_4(aq) standard indicate that the main edge and associated parameters are present at: E_M = 20033.0 eV; E0 = 20012.0 eV; and E_s = -5.0 eV. The pre-edge region is characterised by a pre-edge peak with E_A at 20005.0 eV and E_B at 20007.0 eV. The post-edge region is characterised by E_C at 20071.0 eV with E_D at 20087.0 eV. In addition, the Tan-MoO_4(aq) standard displays an edge shoulder and a flattened edge. In summary these spectral characteristics indicate that Tan-MoO_4(aq) contains largely oxidised Mo in mainly tetrahedral coordination.

Characterisation of the Mo XANES spectral features for the Tan-MoS_4(aq) standard indicate that the main edge and associated parameters are present at: E_M = 20032.0 eV; E0 = 20007.0 eV; and E_s = -10.0 eV. The pre-edge region is characterised by the absence of any pre-edge features. The post-edge region is characterised by E_C at 20057.0 eV with E_D at 20081.0 eV. In addition, the Tan-MoS_4(aq) standard displays neither an edge shoulder nor a flattened edge. In summary these spectral characteristics indicate that Tan-MoS_4(aq) contains largely reduced Mo in mainly octahedral coordination.

4.3.2.6 Adsorbed vs. incorporated Mo

For all minerals synthesised in the experiments (δMnO_2, ferrihydrite, goethite and magnetite), MoO_4 was both adsorbed to and co-precipitated with each mineral, where co-precipitation is designed to result in structural incorporation of Mo into the mineral matrix. Differences between the XANES spectra for the adsorbed and co-precipitated standards are only observed however, for goethite and magnetite. The XANES spectra for MoO_4 adsorbed to and co-precipitated with δMnO_2 or ferrihydrite are indistinguishable using the spectral characteristics defined in this study. Because the XANES region is sensitive to Mo local coordination environment this suggests that molybdate does not become structurally incorporated into δMnO_2 or ferrihydrite and is thus limited to an adsorption pathway for sequestration in natural environments. This is supported by observations from Das et al. (2016); Gustaffson and Tiberg (2015); and Kashiwabara et al. (2009) who suggest that Mo only forms a weak outer-sphere complex with ferrihydrite. Brinza et al. (2015) also collected XANES for Mo adsorbed and co-precipitated with ferrihydrite and did not observe any significant differences, suggesting that Mo was not incorporated into the ferrihydrite structure.

4.3.3 Determining Mo sequestration pathways in natural sediments

To validate that the XANES standards are representative of Mo sequestration pathways in natural sediments, the organic fraction of a Mo-rich sediment core (LC-1A) from the euxinic part of the stratified Lake Cadagno (Xiong et al., 2019) was isolated. This was then subjected to Mo XANES analysis in order to characterise its spectral features and compare these with the Mo-organic standards. Other fractions that might sequester Mo, including pyrite, were removed from the sample by sequential extraction to leave only Mo complexed with organics. The spectrum is characterised using the characteristic spectral features described above (Table 4.2; Figure. 4.6). The main edge and associated parameters are present at: E_M = 20030.8 eV; E0 = 20007.1 eV; and E_s = -9.9 eV. The pre-edge region is characterised by the absence of any

pre-edge features; the main edge is smooth with neither an edge shoulder nor a flattened edge; and the post-edge trough E_C is at 20059.3 eV with a post-edge hump E_D in the XANES range at 20078.9 eV. The E_S value indicates that this sample contains reduced Mo, while the absence of pre-edge features and inclusion of a post-edge hump within the XANES range indicates the Mo is present in octahedral coordination.

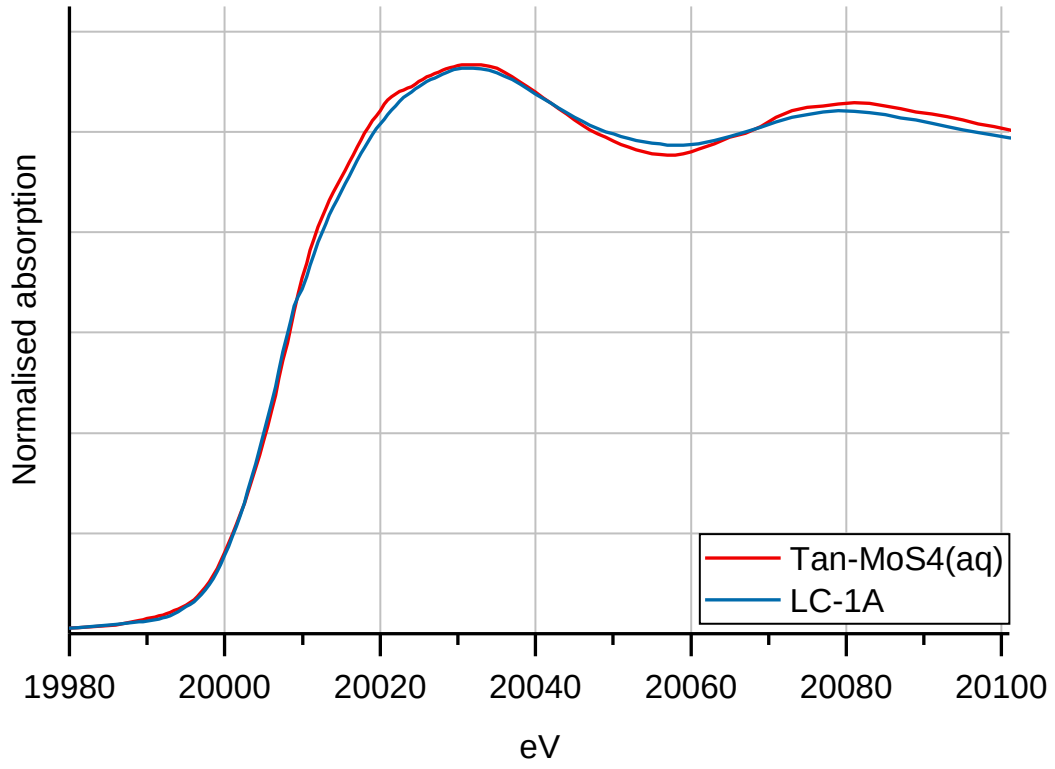

Figure 4.6 *XANES spectra for Tan-MoS_4(aq) standard and euxinic organic Mo sediment sample (LC-1A) showing similarities in spectral shape and features.*

On comparison with the standards in terms of the characteristic spectral features (Table 4.2) and overall spectral shape (Figure 4.6), this sediment sample is a very close match to the Tan-MoS_4(aq) standard, thus verifying that this standard is a good analogue for Mo sequestration by organic substances in natural sediments.

Table 4.2 *XANES spectral values for Tan-MoS_4(aq) and LC-1A.*

	Tan-MoS_4(aq)	**LC-1A**
E0 (eV)	20007.0	20007.1
E_M (eV)	20032.0	20030.8
E_S (eV)	-10.0	-9.9
E_C (eV)	20057.0	20059.3
E_D (eV)	20081.0	20078.9

To further validate that the XANES standards are able to determine Mo sequestration pathways in natural sediments, XANES were collected for a bulk sediment sample (NIT-ST1) from the anoxic, nitrogenous part of the Golfo Dulce Basin, Costa Rica (Guilbaud, 2015; Thamdrup et al., 1996). Again, the spectrum is characterised using the characteristic spectral features described above (Table 4.3; Figure 4.7). The main edge and associated parameters are present at: E_M = 20032.5 eV; E0 = 20007.0 eV; and E_s = -10.0 eV. The pre-edge region is characterised by the absence of any pre-edge features; the main edge is smooth without an edge shoulder but does display a flattened edge; and the post-edge trough E_C is at 20055.6 eV with a post-edge hump E_D in the XANES range at 20078.8 eV. The E_S value indicates that this sample contains reduced Mo, while the absence of pre-edge features and inclusion of a post-edge hump within the XANES range indicates the Mo is present in octahedral coordination. Overall the characteristic spectral features, and to some extent the overall spectral shape, are similar to both the Mag-MoS_4(ads) and Tan-MoS_4(aq) standards. The presence of a flattened edge, however, facilitates a match between the bulk sediment sample and the Mag-MoS_4(ads) standard, indicating that in this environment at least one of the sequestration pathways for Mo is as MoS_4 adsorbed to magnetite. Although little is known about the sequestration of Mo

in nitrogenous environments, Thompson et al. (2019) show that phosphorous is sequestered to magnetite in the same nitrogenous environment (Golfo Dulce) as the samples presented here. Chapter 5 also shows that magnetite operates as a Mo sink in a range of redox environments.

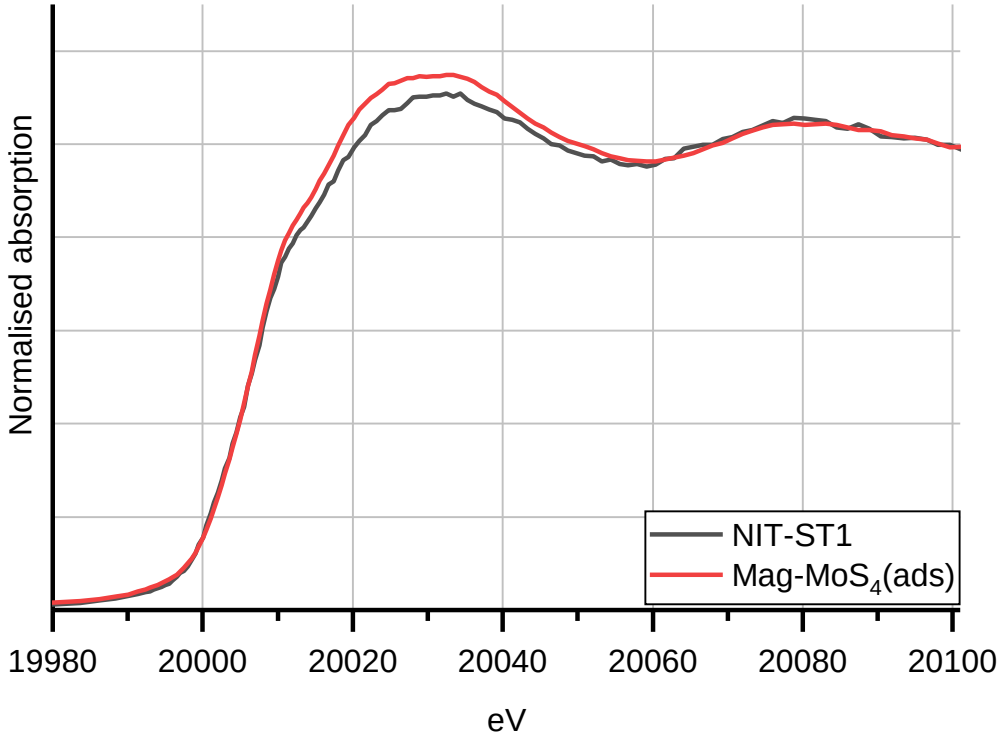

Figure 4.7 *XANES spectra for Mag-MoS_4(ads) standard and nitrogenous sediment sample (NIT-ST1) showing similarities in spectral shape and features.*

Table 4.3 *XANES spectral values for Mag-MoS_4(ads) and NIT-ST1.*

	Mag-MoS_4(ads)	**NIT-ST1**
E0 (eV)	20007.3	20007.0
E_M (eV)	20033.0	20032.5
E_S (eV)	9.7	10.0
E_C (eV)	20060.0	20055.6
E_D (eV)	20079.0	20078.8

4.4 Conclusions

A library of Mo XANES standards that represents the main Mo sequestration pathways in natural sediments is presented. By identifying a suite of characteristic spectral features, their associated positions in energy space and the relationships between these, a system has been developed that provides a fingerprint of different Mo sequestration pathways, that can be used to identify Mo oxidation state and coordination, and Mo host phases, in natural sediment samples.

The Mo XANES standards represent Mo sequestration mechanisms for the full range of sedimentary redox conditions and can therefore be used as a tool in future synchrotron analyses to determine Mo speciation and host phase association across a range of sedimentary environments.

4.5 References

Arai, Y. 2010. X-ray Absorption Spectroscopic Investigation of Molybdenum Multinuclear Sorption Mechanism at the Goethite-Water Interface. *Environ. Sci. Technol.* **44**, pp.8491-8496.

Bibak, A., and Borggaard, O. K. 1994. Molybdenum adsorption by aluminium and iron oxides and humic acid. *Soil Science*. **158**, pp. 323-328.

Bostick, B. C., Fendorf, S., and Helz, G. R. 2003. Differential Adsorption of Molybdate and Tetrathiomolybdate on Pyrite (FeS_2). *Environmental Science & Technology*. **37**, pp. 285-291.

Breward, N., Kemp, S. J., Ambrose, K., Powell, J. H., Morigi, A., and Wagner, D. 2015. Anomalous enrichment of molybdenum and associated metals in Lower Jurassic (Lias Group) black shales of central England, as revealed by systematic geochemical surveys. *Proceedings of the Geologists' Association.* **126**, pp. 346-366.

Brinza, L., Vu, H. P., Shaw, S., and Mosselmans, J. F. W. 2015. Effect of Mo and V on the Hydrothermal Crystallisation of Hematite from Ferrihydrite: An *in situ* Energy Dispersive X-ray Diffraction and X-ray Absorption Spectroscopy Study. *Crystal Growth & Design*. **15** (10), pp. 4768-4780.

Calvin, S. 2013. *XAS for Everyone*. Boca Raton. Taylor & Francis Group.

Canfield, D. E., Poulton, S. W., Knoll, A. H., Narbonne, G. M., Ross, G., Goldberg, T., and Strauss, H. 2008. Ferruginous Conditions Dominated Later Neoproterozoic Deep-Water Chemistry. *Science.* **321**, pp. 949-952.

Cheng, M., Li, C., Zhou, L., Algeo, T. J., Zhang, F., Romaniello, S., Jin, C., Lei, L., Feng, L., Jiang, S. 2016. Marine biogeochemistry in the context of dynamically euxinic mid-depth waters. A case study of the lower Cambrian Niutitang shales, South China. *Geochimica et Cosmochimica Acta*. **183**, pp. 79-93.

Clausen, B. S., Lengeler, B., and Topsoe, H. 1986. X-ray absorption spectroscopy studies of calcined Mo-Al_2O_3 and Co-Mo-Al_2O_3 hydrosulfurization catalysts. *Polyhedron*. **5** (1/2), pp. 199-202.

Cornell, R. M., and Schwertmann, U. 2003. *The Iron Oxides*. 2nd ed. Weinheim: WILEY-VCH Verlag GmbH & Co.

Cramer, S. P., et al. 1976. Molybdenum X-Ray Absorption Edge Spectra. The Chemical State of Molybdenum in Nitrogenase. *Journal of the American Chemical Society*. **98** (5), pp. 1287-1288.

Cramer, S. P., Hodgson, K. O., Gillum, W. O., and Mortenson, L. E. 1978. The Molybdenum Site of Nitrogenase, Preliminary Structural Evidence from X-Ray Absorption Spectroscopy. *Journal of the American Chemical Society.* **100** (11), pp. 3398-3407.

Cruywagen, J. J., and Heyns, J. B. B. 1988. Spectrophotometric Determination of the Thermodynamic Parameters for the First Two Protonation Reactions of Molybdate. *Polyhedron*. **7** (7), pp. 547-556.

Dahl, T. W., Canfield, D. E., Rosing, M. T., Frei, R. E., Gordon, G. W., Knoll, A. H., and Anbar, A. D. 2011. Molybdenum evidence for expansive sulfidic water masses in ~750 Ma oceans. *Earth and Planetary Sciences Letters.* **311**, pp. 264-274.

Dahl, T. W., Chappaz, A., Fitts, J. P., and Lyons, T. W. 2013. Molybdenum reduction in a sulfidic lake: Evidence from X-ray adsorption fine-structure spectroscopy and implications for the Mo paleoproxy. *Geochimica et Cosmochimica Acta.* **103**, pp. 213-231.

Dahl, T. W., Chappaz, A., Hoek, J., McKenzie, C. J., Svane, S., and Canfield, D. E. 2017. Evidence of molybdenum association with particulate organic matter under sulfidic conditions. *Geobiology*. **15** (2), pp. 311-323.

Das, S., Essilfie-Dughan, J., and Hendry, J. 2016. Sequestration of molybdate during transformation of 2-line ferrihydrite under alkaline conditions. *Applied Geochemistry*. **73**, pp. 70-80.

Diamond Light Source. 2020. *Bird's eye view of the synchrotron* [online]. [Accessed 16 March 2020]. Available from: https://www.diamond.ac.uk/Science/Machine/Components.html.

Esslifie-Dughan, J., Pickering, I. J., Jim Hendry, M., George, G. N., and Kotzer, T. 2011. Molybdenum Speciation in Uranium Mine Tailings Using X-Ray Absorption Spectroscopy. *Environ. Sci. Technol.* **45**, pp. 455-460.

George, S. J., Igarashi, R. Y., Piamonteze, C., Soboh, B., Cramer, S. P., and Rubio, L. M. 2007. Identification of a Mo-Fe-S Cluster on NifEN by Mo K-edge Extended X-ray Absorption Fine Structure. *Journal of the American Chemical Society.* **129**, pp. 3060-3061.

George, S. J., Drury, O. B., Fu, J., Friedricj, S., Doonan, C. J., George, G. N., White, J. M., Young, C. G., and Cramer, S. P. 2009. Molybdenum X-ray absorption edges from 200 to 20,000 eV: The benefits of soft X-ray spectroscopy for chemical speciation. *Journal of Inorganic Biochemistry*. **103**, pp. 157-167.

Guilbaud. 2019. *Email to Jennifer Rodley 21 July.*

Gustaffson, J. P., and Tiberg, C. 2015. Molybdenum binding to soil constituents in acid soils: An XAS and modelling study. *Chemical Geology*. **417**, pp. 279-288.

Helz, G. R., et al. 1996. Mechanism of molybdenum removal from the sea and its concentration in black shales: EXAFS evidence. *Geochimica et Cosmochimica Acta.* **60** (19), pp. 3631-3642.

Henderson, G. S., de Groot, F. M. F., and Moulton, B. J. A. 2014. X-ray Absorption Near-Edge Structure (XANES) Spectroscopy. *Reviews in Mineralogy & Geochemistry.* **78**, pp. 75-138.

Hertkorn, N., Benner, R., Frommberger, M., Schmitt-Kopplin, P., Witt, M., Kaiser, K., Kettrup, A., and Hedges, J. I. 2006. Characterization of a major refractory component of marine dissolved organic matter. *Geochimica et Cosmochimica Acta*. **70**, pp. 2990-3010.

Huerta-Diaz, M. A., and Morse, J. W. 1990. A Quantitative Method for Determination of Trace Metal Concentration in Sedimentary Pyrite. *Marine Chemistry*. **29**, pp. 119-144.

Kashiwabara, T., Takahashi, Y., and Tanimizu, M. 2009. A XAFS study on the mechanism of isotopic fractionation of molybdenum during its adsorption on ferromanganese oxides. *Geochemical Journal*. **43**, pp. e31-e36.

Kendall, B., Reinhard, C. T., Lyons, T. W., Kaufman, A. J., Poulton, S. W., and Anbar, A. D. 2010. Pervasive oxygenation along late Archean ocean margins. *Nature Geoscience*. **3**, pp. 647-652.

Moon, E. M., and Peacock, C. L. 2011. Adsorption of Cu(II) to *Bacillus subtilis*: A pH-dependent EXAFS and thermodynamic modelling study. *Geochimica et Cosmochimica Acta*. **75**, pp. 6705-6719.

Peacock, C. L., and Sherman, D.M. 2004. Copper (II) sorption onto goethite, hematite and lepidocrocite: a surface complexation model based on ab initio molecular geometries and EXAFS spectroscopy. *Geochimica et Cosmochimica Acta.* **12**, pp. 2623-2637.

Pickering, I. J., Brown, G. E., and Tokunaga, T. K. 1995. Quantitative Speciation of Selenium in Soils Using X-ray Absorption Spectroscopy. *Environmental Science and Technology.* **25** (8), pp. 2456-2459.

Poulton., S. W. 2019. *Email to Jennifer Rodley on 24 July.*

Poulton, S. W., and Canfield, D. E. 2011. Ferruginous Conditions: A Dominant Feature of the Ocean through Earth's History. *Elements*. **7**, pp. 107-112.

Ravel, B., and Newville, M. 2005. ATHENA, ARTEMIS, HEPHAESTUS: data analysis for X-ray absorption spectroscopy using IFEFFIT. *Journal of Synchrotron Radiation.* **12**, pp. 537-541.

Scholz, F., McManus, J., and Sommer, S. 2013. The manganese and iron shuttle in a modern euxinic basin and implications for molybdenum cycling at euxinic ocean margins. *Chemical Geology*. **355**, pp. 56-68.

Scholz, F., Siebert, C., Dale, A. W., and Frank, M. 2017. Intense molybdenum accumulation in sediments underneath a nitrogenous water column and implications for the reconstruction of paleo-redox conditions based on molybdenum isotopes. *Geochimica et Cosmochimica Acta*. **213**, pp. 400-417.

Scott, C., Lyons, T. W., Bekker, A., Shen, Y., Poulton, S. W., Chu, X., and Anbar, A. D. 2008. Tracing the stepwise oxygenation of the Proterozoic ocean. *Nature.* **452**, (7186), pp. 456-05.

Shimmield, G. B., and Price, N. B. 1986. The behaviour of molybdenum and manganese during early sediment diagenesis – offshore Baja California, Mexico. *Marine Chemistry*. **19**, pp. 261-280.

Thamdrup, B., Canfield, D. E., Ferdelman, T. G., Glud, R. N., and Gundersen, J. K. 1996. A biogeochemical survey of the anoxic basin Golfo Dulce, Costa Rica. *Revista de Biologia Tropical.* **44**, pp. 19-33.

Thompson, J A., Poulton, S. W., Guilbaud, R., Doyle, K. A., Reid, S., and Krom, M. D. 2019. Development of a modified SEDEX phosphorous speciation method for ancient rocks and modern iron-rich sediments. *Chemical Geology*. **524** (5), pp. 383-393.

Tribovillard, N., Algeo, T. J., Lyons, T., and Riboulleau, A. 2006. Trace metals as paleoredox and paleoproductivity proxies: An update. *Chemical Geology*. **232**, 12-32.

Tucker, M. D., Barton, L. L., and Thomson, B. M. 1997. Reduction and Immobilization of Molybdenum by *Desulfovibrio desulfuricans*. *Journal of Environmental Quality.* **26** (4), pp. 1146-1152.

Villalobos, M., Toner, B., Bargar, J., and Sposito, G. 2003. Characterization of the manganese oxide produced by *Pseudomonas putida* strain MnB1. *Geochimica et Cosmochimica Acta.* **67** (14), pp. 2649-2662.

Vorlicek, T. P., Helz, G. R., Chappaz, A., Vue, P., Vezina, A., and Hunter, W. 2018. Molybdenum Burial Mechanism in Sulfidic Sediments: Iron-Sulfide Pathway. *ACS Earth and Space Chemistry.* **2** (6), pp. 565-576.

Wagner, M., Chappaz, A., and Lyons, T. W. 2017. Molybdenum speciation and burial pathway in weakly sulfidic environments: Insights from XAFS. *Geochimica et Cosmochimica Acta.* **206**, pp. 18-29.

Wang, H. W., Skeldon, P., Thompson, G. E., Wood, G. C. 1997. Synthesis and characterization of molybdenum disulphide formed from ammonium tetrathiomolybdate. *Journal of Materials Science*. **32**, pp. 497-502.

Wharton, J. A., Ross, D. H., Treacy, G. M., Wilcox, G. D., and Baldwin, K. R. 2003. An EXAFS investigation of molybdate-based conversion coatings. *Journal of Applied Electrochemistry*. **33**, pp. 553-561.

Wichard, T., Mishra, B., Myneni, S. C. B., Bellenger, J., and Kraepiel, A. M. L. 2009. Storage and bioavailability of molybdenum in soils is increased by organic matter complexation. *Nature Geoscience.* **2**, pp. 625-629.

Winick, H. 1994. Introduction and overview. In: Winick, H. ed. *Synchrotron Radiation Sources.* Singapore: World Scientific Publishing Co. Pte. Ltd., pp. 1-17.

Wirth, S. B., Gilli, A., Niemann, H., Dahl, T. W., Ravasi, D., Sax, N., Hamann, Y., Peduzzi, R., Peduzzi, S., Tonolla, M., Lehmann, M. F., and Anselmetti, F. S. 2013. Combining sedimentological, trace metal (Mn, Mo) and molecular evidence for reconstructing past

water-column redox conditions: The example of meromictic Lake Cadagno (Swiss Alps). *Geochimica et Cosmochimica Acta.* **120**, pp. 220-238.

Xiong, Y., Guilbaud, R., Peacock, C. L., Cox, R. P., Canfield, D. E., Krom, M. D., and Poulton, S. W. 2019. Phosphorous cycling in Lake Cadagno, Switzerland: A low sulfate euxinic ocean analogue. *Geochimica et Cosmochimica Acta*. **251**, pp. 116-135.

Zark, M., and Dittmar, T. 2018. Universal molecular structures in natural dissolved organic matter. *Nature Communications*. **9**, pp. 1-8.

Chapter 5 Identification of molybdenum sequestration pathways in four water column redox environments using XANES

5.1 Introduction

Mo is used extensively as a palaeoredox proxy where both its concentration (e.g. Cheng et al., 2016; Dahl et al., 2013a; Hetzel et al., 2009) and isotopic signature (e. g. Chen et al., 2015; Dahl et al., 2010) recorded in sedimentary archives are used to infer palaeo redox conditions in these sediments and overlying water columns at the time of their deposition. Current use of this palaeoredox indicator is however, generally limited to interpretations of redox end member conditions (oxic, where the water column is oxygenated, and euxinic, where the water column is anoxic and sulfidic) due to the bimodal geochemical behaviour of Mo in most environments. Although present day oceans and lakes are predominantly oxic, alternative redox environments, such as nitrogenous (where nitrate reduction occurs in the water column; Scholz et al, 2017) and ferruginous (where Fe(II) is mobilised in the water column; Canfield and Thamdrup, 2009), exist and ferruginous environments in particular have been shown to potentially dominate oceans in the past (Guilbaud et al., 2015; Poulton and Canfield, 2011). The behaviour of Mo in these environments is poorly understood however, and thus the current use of the Mo palaeoredox proxy is limited to determining whether a palaeoenvironment was oxic or euxinic.

The use XANES to determine Mo speciation in sediments and thus the likely Mo and sediment geochemistry at the time of sedimentary deposition has also been used extensively in both experimental studies that define Mo speciation under different environmental parameters (e.g. Arai, 2010; Bostick et al., 2003; Freund et al., 2016) and in sediments (e.g. Ardakani et al., 2016; Dahl et al., 2013b) to infer palaeo-redox conditions. Again however, this approach is

generally limited to investigating and defining end-member redox states and has not been used to investigate Mo speciation under nitrogenous or ferruginous conditions or in sediments where intermediate redox conditions may have prevailed. The recent development of a comprehensive library of XANES standards for Mo associated with a range of sedimentary phases typical for Mo sequestration under a variety of redox regimes (Chapter 4) facilitates the identification of Mo speciation and thus sequestration pathways in sediments with known oxic, nitrogenous, ferruginous and euxinic redox conditions. Identification of Mo sequestration pathways in these four archetype redox environments can then be used to interpret Mo XANES spectra recorded in sediments with unknown redox history. To this end, this study examined Mo speciation in sediment samples representing four contemporary redox environments, specifically sediments deposited beneath oxic, nitrogenous, ferruginous and euxinic water columns. A large number of initial XANES spectra were recorded for the sediments from each redox environment, and then archetype XANES spectral types for each of these environments were identified by screening the initial spectra using a XANES fingerprinting approach (Chapter 4). Each redox environment was shown to host at least two different spectral types, which were matched to the XANES spectral library (Chapter 4) to identify prevalent Mo speciation and thus sequestration pathways indicative of oxic, nitrogenous, ferruginous and euxinic redox conditions.

5.2 Methods

5.2.1 Samples

To determine XANES spectral characteristics associated with different water column redox environments and determine potential matches of these characteristics to the Mo XANES library of standards (Chapter 4), samples for XANES analysis were prepared from modern sediment cores with known redox conditions, that represent sediments deposited beneath an

oxic water column, a nitrogenous water column, a ferruginous water column and a euxinic water column (full sample details in Section 2.1.1).

Samples from these four redox environments were analysed to collect as many different XANES spectra for each environment as possible, although XANES are more difficult to obtain from samples with lower Mo concentrations. The XANES were from bulk and treated samples that were presented to the beam as micro-thin sections, pressed pellets or powders (Section 2.8). XANES collection and processing methods are outlined in Section 4.2.4 and all samples studied in this chapter were collected on beamline I18. Once the spectra were processed and merged to create archetype XANES spectral types, they were then characterised using a targeted list of spectral features for each XANES scan together with identification of Mo redox state (as oxidised or reduced) and Mo coordination geometry (as tetrahedral or octahedral, or in some cases potentially displaying a distorted octahedral coordination; Chapter 4). Initial screening of all the different spectra collected revealed that at least two different XANES spectral types existed in each of the four redox environments, with four different spectral types observed in the euxinic environment, although the same spectral types were observed in multiple redox environments in some cases. These XANES spectral types were then compared to the Mo library of standards (Chapter 4) to match XANES spectral characteristics and determine Mo phase associations.

5.2.1.1 Samples deposited beneath an oxic water column (oxic samples)

Initial screening of multiple XANES scans from two sediment samples deposited beneath oxic water columns resulted in two XANES spectral types, OX-1 and OX-2 from two different sediment samples. The samples used to generate these spectral types are detailed in Section 2.1.1. For the OX1 sample (Section 2.1.1.7), a small amount of the freeze dried sediment was added to a Kilner jar with AnaeroGen™ sachets, sealed under a nitrogen atmosphere and

transported to DLS, where it was transferred into an argon atmosphere and made into a pressed pellet, then sealed between three layers of Kapton tape before being removed from the argon atmosphere and presented to the beam.

The sample that generated the OX-2 spectral type (Section 2.1.1.4) was made into a micro-thin section at Leeds and attached to Kapton tape at DLS where it was then presented to the beam.

5.2.1.2 Samples deposited beneath a nitrogenous water column (nitrogenous samples)

Initial screening of multiple XANES scans from three sediment samples deposited beneath the same nitrogenous water column resulted in two XANES spectral types, NIT-1 and NIT-2 from the same sediment sample (Section 2.1.1.6).

For the work here, small samples of the freeze dried sediment were added to a Kilner jar with AnaeroGen™ sachets, sealed under a nitrogen atmosphere and transported to DLS, where they were transferred into an argon atmosphere and made into pressed pellets, then sealed between three layers of Kapton tape before being removed from the argon atmosphere and presented to the beam.

5.2.1.3 Samples deposited beneath a ferruginous water column (ferruginous samples)

Initial screening of multiple XANES scans from two sediment samples deposited beneath the same ferruginous water column resulted in two XANES spectral types, FER-1 and FER-2 from the same sediment sample (Section 2.1.1.8).

For the work here, small samples of the freeze-dried sediment were made into micro-thin sections, attached to Kapton tape and presented to the beam; both FER-1 and FER-2 XANES scans were obtained from the same micro-thin section.

5.2.1.4 Samples deposited beneath a euxinic water column (euxinic samples)

Initial screening of multiple XANES scans from 15 sediment samples deposited beneath the same euxinic water column resulted in four XANES spectral types, EUX-1, EUX-2, EUX-3 and EUX-4 from four different sediment samples (Section 2.1.1.6).

For the work here, all samples excluding EUX-1 were made into micro-thin sections, attached to Kapton tape and presented to the beam. For EUX-1 the organic material (Section 2.1.4) was transported to DLS in a sealed Kilner jar with Anaergen sachets to prevent oxygen ingress and then made into a pressed pellet under an argon atmosphere and sealed between three layers of Kapton tape at DLS before it was presented to the beam.

5.2.2 Preparing samples for XANES analysis

Section 2.8 provides full details of sample preparation. Briefly, samples were either made into micro-thin sections or pressed pellets. Micro-thin sections were made in Leeds by embedding a small amount of material in Epothin epoxy resin in a 1 cm diameter mould. Sections were then ground and polished on both sides until the sections were <100 µM thick. Sections were adhered to the XANES sample mount plate using X-ray amorphous Kapton tape.

Pressed pellets were made at DLS, with or without cellulose. All pressed pellets used in this study were prepared under an argon atmosphere. These samples were transferred from freezers directly into a nitrogen-filled anaerobic chamber in Leeds, where they were defrosted and added (in centrifuge tubes) to Kilner jars with AnaeroGen™ sachets for transport to DLS. The Kilner jars were immediately transferred to an argon-filled anaerobic chamber upon arrival at DLS. Pressed pellets were made anaerobically and were sealed between three layers of Kapton tape. The pellets were removed from the chamber immediately prior to analysis on the beamline.

5.2.3 XANES data collection and processing

Data collection and processing followed the same procedures as those outlined in Section 4.2.4 and all XANES were collected on hard X-ray beamline I18.

5.2.4 Protocols for matching samples to standards

To determine XANES spectral characteristics associated with different sedimentary redox environments and determine potential matches of these characteristics to the Mo XANES standard library (Chapter 4), the XANES spectra for each sample were examined with respect to the spectral features listed in Table 5.1. The presence or absence and position of these features were used to match the XANES sample spectra to those from the Mo XANES standards library, that represent the likely Mo speciation pathways in sediments (Chapter 4).

The diagnostic spectral features that characterise Mo speciation and thus the Mo XANES standard library are described in detail in Chapter 4. Briefly, for ease of reference here, Mo in tetrahedral coordination is identified by the presence of a strong pre-edge feature and the absence of a post-edge hump in the XANES range (19980-20100 eV), whereas Mo in octahedral coordination is identified by the absence of a pre-edge feature and the presence of a post-edge hump in the XANES range. It should be noted that the presence of a low-amplitude pre-edge hump can be indicative of tetrahedral or distorted octahedral coordination (Chapter 4 and references therein). A Mo species is considered to be reduced if it has an energy shift (E_S) from the E0 of the MoO_4-aq standard of ≤ -9 eV (Chapter 4). It should be noted in particular that the XANES spectra in the Mo XANES standard library suggest that Mo(VI) in Mo(VI)S_4 is reduced during adsorption to magnetite and pyrite, and during complexation with some organics (Chapter 4; Dahl, et al., 2013b; Dahl et al., 2017).

Table 5.1 *Spectral features used to characterise the Mo XANES standard library. All features are measured on the normalised XANES spectra unless otherwise stated.*

SPECTRAL FEATURE	DESCRIPTION
1. E0	- the energy maxima of the peak in the first derivative of the normalised XANES spectrum that results from the main absorption edge
2. E_M	- the energy maxima of the peak of the main absorption edge
3. E_S	- the energy shift in the main absorption edge positions (E0) of a standard relative to the $Mo(VI)O_4(aq)$ reference
4. E_A	- the energy maxima of the pre-edge peak
5. E_B	- the energy minima of the pre-edge trough following the pre-edge peak
6. E_C	- the energy minima of the post-edge trough following the maximum absorption peak
7. E_D	- the energy maxima of the first post-edge hump
Other features	
8. Pre-edge hump – a low amplitude pre-edge feature without an associated trough	
9. Flattened edge – a decrease in the gradient of the main absorption edge before the maximum absorption peak	
10. Edge shoulder – a feature towards the top of the main absorption edge before the maximum absorption peak	

5.2.5 Geochemical analyses

Methods for porewater analysis, water column analysis, TOC analysis and Fe speciation are all outlined in Chapter 2.

5.3 Results

5.3.1 Sediments deposited beneath an oxic water column

Two XANES spectral types were identified in the oxic environments studied (Figure 5.1; Table 5.2). Characterisation of XANES spectral features for OX-1 indicate that the main edge and associated spectral parameters are present at: E_M = 20037.2 eV; E0 = 20018.6 eV; and E_S = -1.2 eV. The pre-edge region is characterised by the presence of a low-amplitude pre-edge hump and the post-edge region by E_C = 20068.0 eV and E_D = 20083.1 eV. OX-1 does not display a flattened edge or edge shoulder. These spectral characteristics indicate that OX-1 contains largely oxidised Mo in tetrahedral or distorted octahedral coordination. The best match for OX-1 from the library of standards is the Py-MoO_xS_{4-x}(ads) standard, which contains largely oxidised Mo in tetrahedral or distorted octahedral coordination (Chapter 4). Both XANES spectra have a slight pre-edge hump, an absence of any edge shoulder or flattened edge, and the inclusion of a post-edge hump within the XANES range in addition to similar spectral values.

Characterisation of XANES spectral features for OX-2 indicate that the main edge and associated spectral parameters are present at: E_M = 20031.6 eV; E0 = 20007.4 eV, and E_S = -9.6 eV. The pre-edge region is characterised by the absence of any pre-edge features and the post-edge region by E_C = 20056.7 eV and E_D = 20093.5 eV. In addition, OX-2 has an edge shoulder. These spectral characteristics indicate that OX-2 contains largely reduced Mo in mainly octahedral coordination. The best match for OX-2 from the library of standards is the Py-MoS_4(ads) standard, which contains largely reduced Mo (where Mo(VI) in Mo(VI)S_4 is reduced during adsorption to pyrite) in mainly octahedral coordination (Chapter 4). Both XANES spectra have a smooth edge with an absence of any pre-edge features, an edge shoulder and a flattened edge and a post-edge hump within the XANES range in addition to similar spectral values.

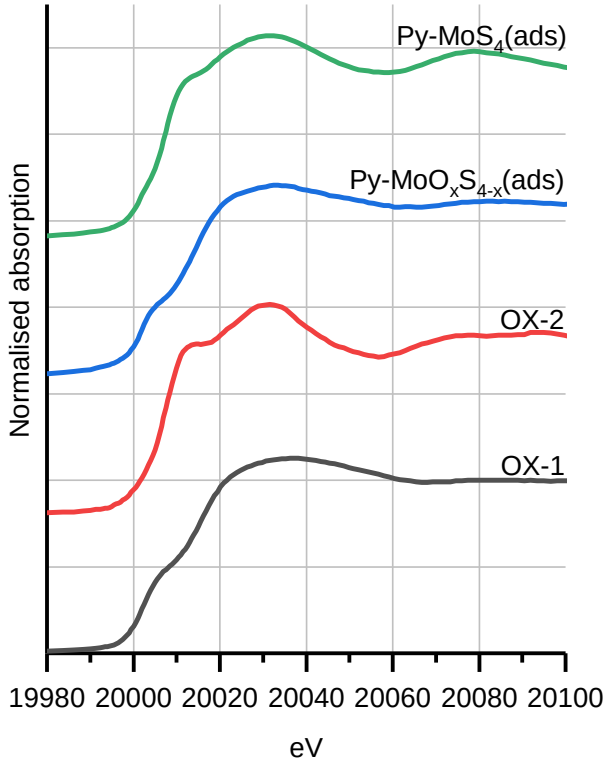

Figure 5.1 *XANES for Mo oxic spectral types and matching standards.*

Table 5.2 *XANES spectral values for oxic spectral types and Mo XANES standards.*

Standard or spectral type	E0 (eV)	E_M (eV)	E_C (eV)	E_D (eV)	E_S (eV)
OX-1	20015.8	20037.2	20068.0	20083.1	-1.2
Py-MoO_xS_{4-x}(ads)	20014.4	20033.0	20065.0	20083.0	-2.6
OX-2	20007.4	20031.6	20056.7	20093.5	-9.6
Py-MoS_4(ads)	20007.2	20032.0	20059.0	20079.0	-9.8

5.3.2 Sediments deposited beneath a nitrogenous water column

Two XANES spectral types were identified for samples from the nitrogenous environment (Figure 5.2; Table 5.3). Characterisation of XANES spectral features for the first spectral type

(NIT-1) indicate that the main edge and associated spectral parameters are present at: E_M = 20032.5 eV; E0 = 20007.6 eV, and E_S = -9.4 eV. The pre-edge region is characterised by the absence of any pre-edge features and the post-edge region by E_C = 20059.2 eV and E_D = 20078.8 eV. In addition, NIT-1 has a slight edge shoulder. These spectral characteristics indicate that NIT-1 contains largely reduced Mo in mainly octahedral coordination. The best match for NIT-1 from the library of standards is the Mag-MoS_4(ads) standard, which contains largely reduced Mo (where Mo(VI) in Mo(VI)S_4 is reduced during adsorption to magnetite) in mainly octahedral coordination (Chapter 4). Both XANES spectra have a smooth main edge with an absence of any pre-edge features, a flattened edge and the inclusion of a post-edge hump within the XANES range in addition to similar spectral values.

Characterisation of XANES spectral features for NIT-2 indicate that the main edge and associated spectral parameters are present at: E_M = 20035.3 eV; E0 = 20016.4 eV, and E_S = +0.6 eV. The pre-edge region is characterised by the presence of a slight pre-edge hump and the post-edge region by E_C = 20055.6 eV and E_D = 20078.8 eV. These spectral characteristics indicate that NIT-2 contains largely oxidised Mo in tetrahedral or distorted octahedral coordination. The best match for NIT-2 from the library of standards is the Py-MoO_xS_{4-x}(ads) standard, which contains largely oxidised Mo in tetrahedral or distorted octahedral coordination (Chapter 4). Both XANES spectra have a slight pre-edge hump and a slightly flattened edge with a post-edge hump in the XANES range in addition to similar spectral values.

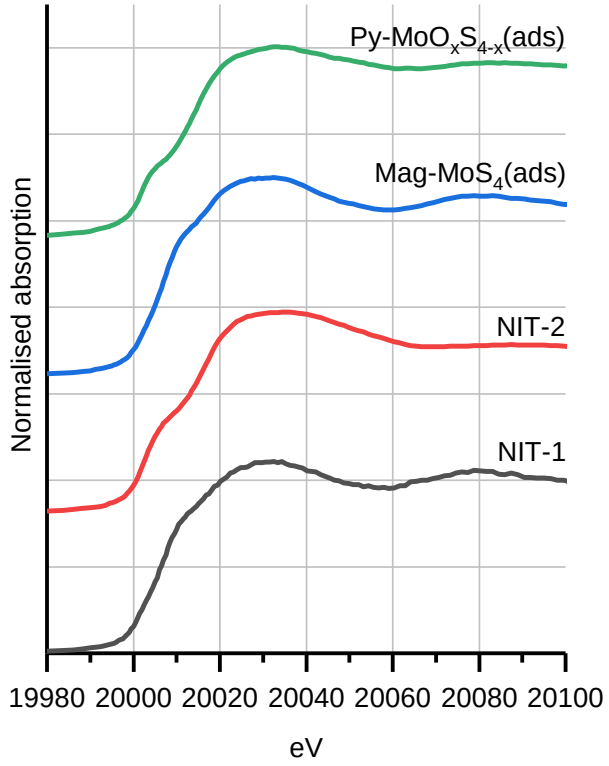

Figure 5.2 *XANES for Mo nitrogenous spectral types and matching standards.*

Table 5.3 *XANES spectral values for nitrogenous spectral types and Mo XANES standards.*

Standard or spectral type	E0 (eV)	E_M (eV)	E_C (eV)	E_D (eV)	E_S (eV)
NIT-1	20007.6	20032.5	20059.2	20078.8	-9.4
Mag-MoS_4(ads)	20007.3	20033.0	20060.0	20079.0	-9.7
NIT-2	20016.4	20035.3	20070.6	20087.4	-0.6
Py-MoO_xS_{4-x}(ads)	20014.4	20033.0	20065.0	20083.0	-2.6

5.3.3 Sediments deposited beneath a ferruginous water column

Two XANES spectral types were identified for samples from the ferruginous environment (Figure 5.3; Table 5.4). Characterisation of XANES spectral features for FER-1 indicate that the

main edge and associated spectral parameters are present at: E_M = 20029.8 eV; E0 = 20007.8 eV, and E_S = -9.2 eV. The pre-edge region is characterised by the absence of any pre-edge features and the post-edge region by E_C = 20057.9 eV and E_D = 20083.1 eV. In addition, FER-1 has a flattened edge. These spectral characteristics indicate that FER-1 contains largely reduced Mo in mainly octahedral coordination. The best match for FER-1 from the library of standards is the Mag-MoS_4(ads) standard, which contains largely reduced Mo (where Mo(VI) in Mo(VI)S_4 is reduced during adsorption to magnetite) in mainly octahedral coordination (Chapter 4). Both XANES spectra have a smooth main edge with an absence of any pre-edge features, a flattened edge and the inclusion of a post-edge hump within the XANES range in addition to similar spectral values.

Characterisation of XANES spectral features for FER-2 indicate that the main edge and associated spectral parameters are present at: E_M = 20034.4 eV; E0 = 20005.3 eV, and E_S = -11.7 eV. The pre-edge region is characterised by the absence of any pre-edge features and the post-edge region by E_C = 20057.9 eV and E_D = 20081.7 eV. These spectral characteristics indicate that FER-2 contains largely reduced Mo in mainly octahedral coordination. The best match for FER-2 is the Tan-MoS_4(ads) standard, which contains largely reduced Mo (where Mo(VI) in Mo(VI)S_4 is reduced during adsorption to tannic acid) in mainly octahedral coordination (Chapter 4). Both XANES spectra have a smooth main edge with an absence of any pre-edge features, flattened edge or edge hump and the inclusion of a post-edge hump in the XANES region in addition to similar spectral values.

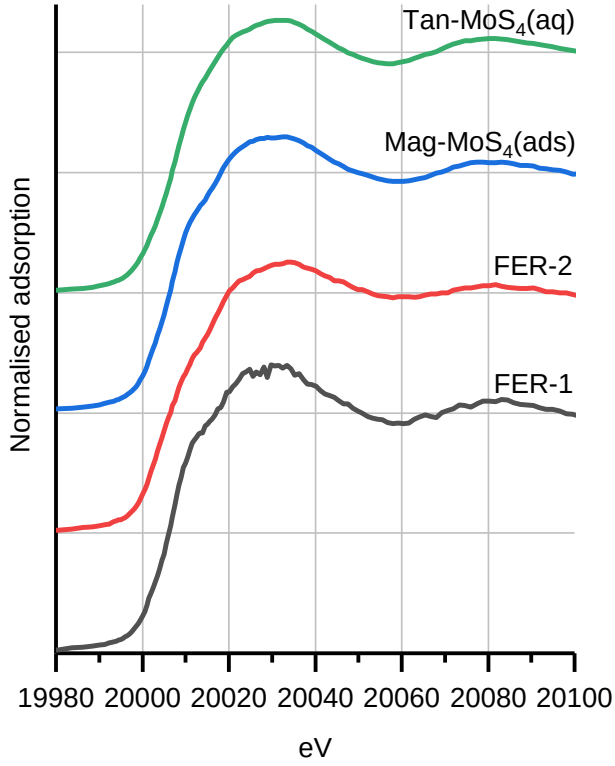

Figure 5.3 *XANES for Mo ferruginous spectral types and matching standards.*

Table 5.4 *XANES spectral values for ferruginous spectral types and Mo XANES standards.*

Standard or spectral type	E0 (eV)	E_M (eV)	E_C (eV)	E_D (eV)	E_S (eV)
FER-1	20007.8	20029.8	20057.9	20083.1	-9.2
Mag-MoS_4(ads)	20007.3	20033.0	20060.0	20079.0	-9.7
FER-2	20005.3	20034.4	20057.9	20081.7	-11.7
Tan-MoS_4(aq)	20007.0	20032.0	20057.0	20081.0	-10.0

5.3.4 Sediments deposited beneath a euxinic water column

Four XANES spectral types were identified four samples from the euxinic environment (Figure 5.4; Table 5.5). Characterisation of the XANES spectral features for EUX-1 indicate that the

main edge and associated spectral parameters are present at: E_M = 20030.8 eV; E0 = 20007.1 eV, and E_S = -9.9 eV. The pre-edge region is characterised by the absence of any pre-edge features and the post-edge region by E_C = 20059.3 eV and E_D = 20078.9 eV. These spectral characteristics indicate that EUX-1 contains largely reduced Mo in mainly octahedral coordination, with a best match to the Tan-MoS_4(ads) standard, which contains largely reduced Mo (where Mo(VI) in Mo(VI)S_4 is reduced during adsorption to tannic acid) in mainly octahedral coordination (Chapter 4). Both XANES spectra have a smooth main edge with an absence of any pre-edge features, flattened edge or edge hump and the inclusion of a post-edge hump in the XANES region in addition to similar spectral values.

Characterisation of the XANES spectral features for EUX-2 indicate that the main edge and associated spectral parameters are present at: E_M = 20040.2 eV; E0 = 20007.7 eV, and E_S = -1.2 eV. The pre-edge region is characterised by the presence of a pre-edge peak with spectral parameters present at: E_A = 20005.5 eV; and E_B = 20008.0 eV. The post-edge region is characterised by: E_C = 20055.6 eV and E_D = 20078.8 eV. These spectral characteristics indicate that EUX-2 contains largely oxidised Mo in mainly tetrahedral coordination. The best match for EUX-2 is the Py-MoO_4(ads) standard, which contains largely oxidised Mo in mainly tetrahedral coordination (Chapter 4). Both XANES have a pre-edge peak, a flattened edge and an absence of a post-edge hump within the XANES range in addition to similar spectral values.

Characterisation of XANES spectral features for EUX-3 indicate that the main edge and associated spectral parameters are present at: E_M = 20031.6 eV; E0 = 20014.3 eV, and E_S = -2.7 eV. The pre-edge region is characterised by the presence of a pre-edge hump and the post-edge region by E_C = 20061.6 eV and E_D = 20086.0 eV. These spectral features indicate that EUX-3 contains largely oxidised Mo in tetrahedral or distorted octahedral coordination. The best match for EUX-3 is the Py-MoO_xS_{4-x}(ads) standard, which contains largely oxidised Mo in

tetrahedral or distorted octahedral coordination (Chapter 4). Both XANES spectra have a slight pre-edge hump and a slightly flattened edge with a post-edge hump within the XANES region in addition to similar spectral values.

Finally, characterisation of XANES spectral features for EUX-4 indicate that the main edge and associated spectral parameters are present at: E_M = 20032.5 eV; E0 = 20007.0 eV, and E_S = -10.0 eV. The pre-edge region is characterised by the absence of any pre-edge features and the post-edge region by E_C = 20055.6 eV and E_D = 20078.8 eV. In addition, EUX-4 has an edge shoulder. EUX-4 contains largely reduced Mo in mainly octahedral coordination. The best match for EUX-4 is the Py-MoS_4(ads) standard, which contains largely reduced Mo (where Mo(VI) in Mo(VI)S_4 is reduced during adsorption to pyrite) in mainly octahedral coordination (Chapter 4). Both XANES spectra have a smooth main edge with an absence of any pre-edge features, an edge shoulder, flattened edge and the inclusion of a post-edge hump in the XANES region in addition to similar spectral values.

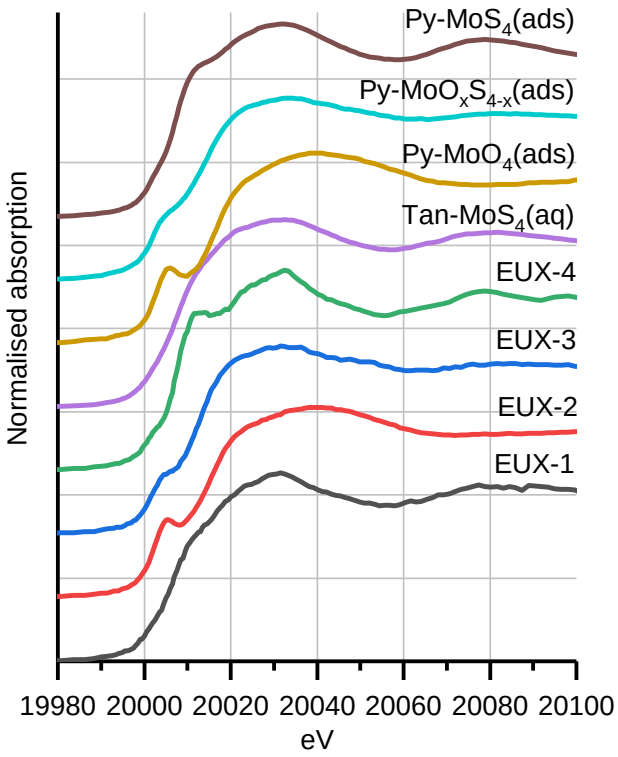

Figure 5.4 *XANES for Mo euxinic spectral types and matching standards.*

Table 5.5 *XANES spectral values for euxinic spectral types and Mo XANES standards.*

Standard or spectral type	E0 (eV)	E_M (eV)	E_C (eV)	E_D (eV)	E_S (eV)
EUX-1	20007.1	20030.8	20059.3	20078.9	-9.9
Tan-MoS_4-aq	20007.0	20032.0	20057.0	20081.0	-10.0
EUX-2	20015.8	20040.2	20072.0	-	-1.2
Py-MoO_4-ads	20016.6	20039.0	20077.0	-	-0.2
EUX-3	20014.3	20031.6	20061.6	20086.0	-2.7
Py-MoO_xS_{4-x}-ads	20014.4	20033.0	20065.0	20083.0	-2.6
EUX-4	20007.0	20032.5	20055.6	20078.8	-10.0
Py-MoS_4-ads	20007.2	20032.0	20059.0	20079.0	-9.8

5.4 Discussion

5.4.1 Sediments deposited beneath an oxic water column

The first oxic spectral type, OX-1, is identified from bulk, untreated sediment from the 1 cm depth section of a core originally collected from the anoxic sediments (deposited beneath an oxic water column) of the Eastern Mediterranean, approximately 25km west of Haifa, Israel. Fe sequential extraction for this samples shows that Fe_{ox1} = 0.82 wt%; Fe_{ox2} = 2.23 wt%; Fe_{mag} = 0.57 wt%; and Fe_{py} = 0.002 wt% suggesting that porewaters contained enough sulfide for pyrite production. The XANES match is for oxythiomolybdate adsorbed to pyrite and, as this is an oxic water column, this process must have occurred in the sediments. In addition, the conversion of MoO_4 to MoO_xS_{4-x} must have also occurred in the sediments either before or during adsorption to pyrite.

The second oxic spectral type OX-2 is identified from bulk, untreated sediment from the 1.5 cm depth section of a core originally collected from anoxic sediments at Station 6 in Aarhus Bay, on the Baltic Sea-North Sea transition on the East Coast of Jutland, Denmark. The 1.5 cm depth is below the oxic zone (1-5 mm), where sediments are anoxic with generally sulfidic porewaters (Thamdrup et al., 1994). In this core however, porewater sulfide is undetectable in the top 5 cm (Figure 5.5; Chapter 6), possibly due to complete consumption of sulfide by redox reactions (Thamdrup et al., 1994). Sulfide levels increase with depth from 5 cm, with a peak at 15 cm where levels reach 364 µM. Fe speciation data show that in the upper 5 cm of the sediments, Fe minerals are present as $Fe_{ox1} > Fe_{py} > Fe_{ox2} > Fe_{mag}$, and the data for this specific sample are in agreement (Figure 5.5; Chapter 6). The XANES match is for tetrathiomolybdate adsorbed to pyrite and, again as this is an oxic water column, this process (including the thiolation of molybdate) must have occurred in sulfidic porewaters.

Both the OX-1 and OX-2 spectral types indicate that Mo is sequestered in anoxic sediments deposited beneath an oxic water column as (oxy)thiomolybdate species (MoO_xS_{4-x} for OX-1 and MoS_4 for OX-2) adsorbed to pyrite (Figure 5.1). As the water columns at these sampling sites are oxic, it is likely that Mo exists there as MoO_4, which is then delivered to sediments, either by diffusion into the upper sediments or adsorbed to other mineral and/or organic phases, which are then reduced in the anoxic porewaters releasing Mo for secondary uptake by pyrite. If this is indeed the case, then, interestingly, it appears that Mo can be completely transformed to MoS_4 at Aarhus Bay. Sedimentation rates in Aarhus Bay are ~3.2 mm/y (Jensen et al., 1988; Rasmussen and Jørgensen, 1992) and therefore the sample used was deposited ~4.7 years before collection. Using calculations from Erickson and Helz (2000) on the kinetics of conversion of MoO_4 to MoS_4 which suggest this can occur in ~1.5 y, Mo in this environment is present in sulfidic porewaters for long enough to be completely transformed to tetrathiomolybdate. Although porewater sulfide is not detected at Aarhus Bay, the presence

of pyrite in the top 5 cm (0.22-0.56 wt%; Chapter 6) suggests that sulfide is present, but that it is completely consumed in redox reactions. Adsorption of this MoS_4 to pyrite is then commensurate with pyrite as a dominant phase in the sedimentary system (Figure 5.5), and in fact, pyrite has been proposed as a sink for Mo as MoS_4 in a number of studies (e.g. Bostick et al., 2003; Vorlicek et al., 2004; Xu et al., 2006). However, in the OX1 sample pyrite is 0.002 wt% suggesting that Mo adsorption to pyrite is occurring despite the fact that it is not a dominant phase, highlighting the importance of pyrite as a high affinity sink for Mo in agreement with Bostick et al., (2003).

Overall the XANES data suggest that in anoxic sediments deposited beneath an oxic water column Mo can be sequestered in the sediments in an oxidised (MoO_xS_{4-x}) and reduced (MoS_4) sulfidized form, through adsorption to pyrite, where Mo(VI) in $Mo(VI)S_4$ is reduced upon adsorption (Dahl, et al. 2013b; 2017). Both samples are from upper sediments where redox reactions occur and it is possible that the transformation of molybdate to thiomolybdates contributes to the consumption of sulfide in porewaters. It should be noted that this might not be the only sequestration mechanism.

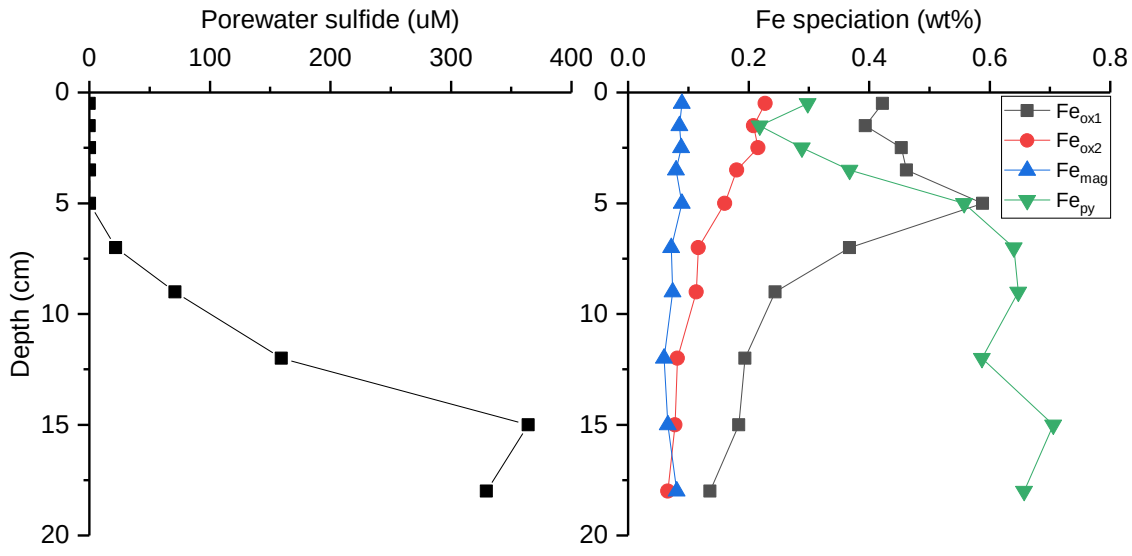

Figure 5.5 *Porewater sulfide and Fe speciation data for Aarhus Bay sediment core (Goldberg, 2019).*

5.4.2 Sediments deposited beneath a nitrogenous water column

The nitrogenous spectral types NIT-1 and NIT-2 are identified from bulk, untreated sediment from the 22-24 cm depth section of a core originally collected from the anoxic sediments of Golfo Dulce, where sediments are deposited beneath a nitrogenous water column, defined as a water column where nitrate (NO_3^-) is reduced and nitrite (NO_2^-) accumulates (Canfield and Thamdrup, 2009). Fe speciation data show that Fe minerals are generally present in the sediments as Fe_{ox2} > Fe_{mag} > Fe_{ox1} > Fe_{py}, although in the sample used here Fe_{py} > Fe_{ox1}. Specifically for the sample both XANES were recovered from, Fe_{ox2} = 0.9 wt%; Fe_{mag} = 0.8 wt%; Fe_{py} = 0.4 wt%; and Fe_{ox1} = 0.4 wt% (Figure 5.6; Guilbaud,2015). TOC ranges from 0.78 wt% to 1.53 wt% with concentrations generally higher in the upper sediments (Figure 5.6; Guilbaud, 2015).

Both the NIT-1 and NIT-2 spectral types indicate that Mo is sequestered in anoxic sediments deposited beneath a nitrogenous water column as (oxy)thiomolybdate species adsorbed to magnetite (NIT-1, with MoS_4) and pyrite (NIT-2, with MoO_xS_{4-x}) (Figure 5.2). As the water column at this sampling site is nitrogenous, with <1 µM sulfide in most of the water column (Ferdelman et al., 2006), it is likely that Mo exists here as MoO_4, and then similar to the oxic water column environments, is delivered to sediments, either by diffusion into the upper sediments or adsorbed to other mineral and/or organic phases, which are then reduced in the anoxic porewaters releasing Mo for secondary uptake by magnetite and pyrite. Again, if this is indeed the case, then it appears that Mo can be completely transformed to MoS_4 at Gulfo Dulce, despite the fact that porewater sulfide does not appear to accumulate. Specifically, investigations of the Golfo Dulce basin by Thamdrup et al. (1996) indicate that although bacterial sulfate reduction (BSR) is significant, H_2S does not accumulate in porewaters, potentially because nitrate acts as an oxidant, and the high sedimentation rate of reactive Fe phases consumes porewater sulfide before it has a chance to build up. However, MoO_4 may

also act as an oxidant in porewaters, consuming porewater sulfide, and transforming to molybdate to oxythiomolybdates in the process. Ultimately, the adsorption of the sulfidized Mo to pyrite is in accordance with Scholz et al. (2017) who suggest that in nitrogenous water column environments, Mo is delivered to sediments by particulate Fe (oxyhydr)oxides which are reduced in the sediments, leaving aqueous Fe^{2+} to diffuse back into the water column and Mo in the sediments to be sequestered to other minerals, where Fe sulfides in particular form the most likely final sink. With regards to the adsorption of Mo to magnetite, little research has been done into the role of magnetite in sequestering Mo in sediments, but work into the use of Mo as a palaeoatmosphere redox sensor shows that Mo is hosted in magnetite in granitic and basaltic rocks (Greaney et al., 2018), while experimental work suggests that highly reactive MoS_4 might adsorb to Fe(III) in porewater particulate magnetite as an inner-sphere complex (Verbinnen et al., 2012).

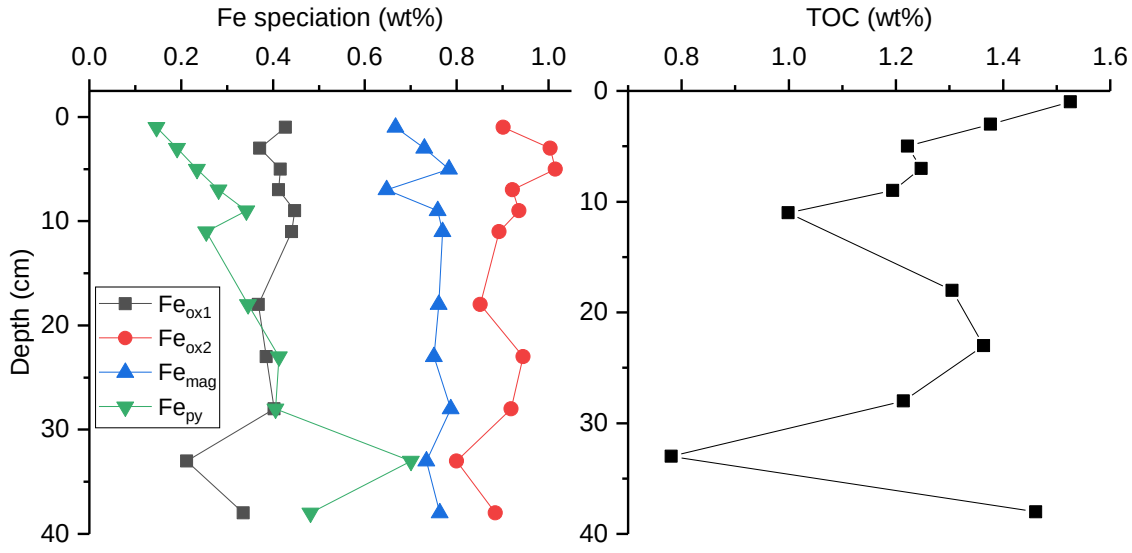

Figure 5.6 *Fe speciation and TOC data for Golfo Dulce sediment core (Guilbaud, 2015).*

Overall the XANES data suggest that in anoxic sediments deposited beneath a nitrogenous water column, Mo can be sequestered in the sediments in an oxidised (MoO_xS_{4-x}) and reduced sulfidized (MoS_4) form, through adsorption to pyrite and magnetite, respectively, where

Mo(VI) in $Mo(VI)S_4$ is reduced upon adsorption to magnetite (Chapter 4). It should be noted that this might not be the only sequestration mechanism.

5.4.3 Sediments deposited beneath a ferruginous water column

The ferruginous spectral types FER-1 and FER-2 are identified from bulk, untreated sediment from the 23.75 cm depth section of a core originally collected from the ferruginous sediments of Lake La Cruz, Spain, which are deposited beneath a ferruginous water column, defined as an anoxic, non-sulfidic water column containing free aqueous ferrous iron (Fe(II)) (Poulton and Canfield, 2011). Fe speciation data for the core indicate that Fe minerals are generally present in the sediments as $Fe_{py} > Fe_{ox2} > Fe_{mag} > Fe_{ox1}$ (Figure 5.7; Thompson, 2018). TOC throughout the core ranges from 3.6-11.1 wt% and is specifically 8.9 wt% for this sample (Figure 5.7; Thompson et al., 2018). Water column sulfide in this environment is generally low but porewater dissolved sulfide concentrations have pronounced peaks at 2.5 cm (1.7 µM dissolved sulfide) and 20.75 cm (3.1 µM dissolved sulfide) (Figure 5.8; Thompson et al., 2018).

Both the FER-1 and FER-2 spectral types indicate that Mo is sequestered in sediments deposited beneath a ferruginous water column as tetrathiomolybdate (MoS_4) adsorbed to magnetite and organic matter, as represented by tannic acid (Figure 5.3). As the water column at this sampling site is ferruginous, with generally low water column sulfide (Thompson et al., 2018), it is likely that Mo exists here as MoO_4, and then similar to the oxic and nitrogenous water column environments at Aarhus Bay and Golfo Dulce, respectively, is delivered to sediments, either by diffusion into the upper sediments or adsorbed to other mineral and/or organic phases, which are then reduced in the anoxic porewaters releasing Mo for secondary uptake by magnetite and organics. As with Aarhus Bay and Golfo Dulce, it appears that Mo can be completely transformed to MoS_4 at Lake La Cruz, despite the fact that porewater sulfide concentrations (Figure 5.8; Thompson et al., 2018) do not appear to reach the geochemical

switch point for conversion of MoO_4 to MoS_4 proposed by Helz et al. (1996). On the other hand, porewater dissolved sulfide concentrations do have pronounced peaks at 2.5 cm (1.7 µM dissolved sulfide) and 20.75 cm (3.1 µM dissolved sulfide) (Figure 5.8; Thompson et al., 2018), and the Fe speciation data (Figure 5.7; Thompson, 2018) suggest that enough dissolved sulfide was present for the formation of pyrite (Fe_{py}). Therefore, if sulfide was present in sufficient quantities for the transformation of Fe minerals to pyrite it may therefore have been sufficient to thiolate MoO_4 to MoS_4. In particular, the samples used were from a depth of 23.75 cm and given the sedimentation rate of 0.1-0.5 cm/y in Lake La Cruz (Romero-Viana et al., 2010), the sediments are a minimum of 47.5 y old. Erickson and Helz (2000) propose that, although each successive sulfidation step gets slower, MoO_4 can be transformed to MoS_4 in ~1.5 y, suggesting that even though porewater sulfide concentrations are low at this sampling site, Mo might be present in the sulfidic porewaters for a sufficient period to become thiolated. Ultimately, the adsorption of the sulfidized Mo to magnetite is in accordance with Poulton and Canfield (2011) who suggest that under ferruginous conditions a significant proportion of Fe minerals remain unsulfidized and this is reflected in the Fe speciation data for this core (Figure 5.7; Thompson, 2018). Of particular relevance, this sample shows that the Fe_{mag} pool is 0.004 wt% so magnetite persists in this anoxic environment. It is therefore likely that highly reactive MoS_4 present in porewaters adsorbed to Fe(III) in porewater particulate magnetite as an inner-sphere complex (Verbinnen et al., 2012). With regards to the complexation of Mo with organics, the organic matter sequestration pathway is well studied, both in experimental work (e.g. Bibak and Borggaard, 1994; Tucker et al., 1997; Dahl et al., 2017) and in sediments deposited under an anoxic and euxinic water columns (Hetzel et al., 2009; Dahl et al., 2010; Wagner et al., 2017), where strong correlations are observed between TOC and Mo concentrations (Coveney and Glascock, 1989; Tribovillard et al, 2004). Whilst there are no previous observations of Mo complexation to organics in anoxic sediments deposited under a ferruginous water column, TOC is 8.9 wt% in the sample studied here, and

TOC/Mo ratios for the Lake La Cruz core are generally ~0.7-1.1, showing a good correlation (Figure 5.9), that supports an organic complexation sequestration mechanism.

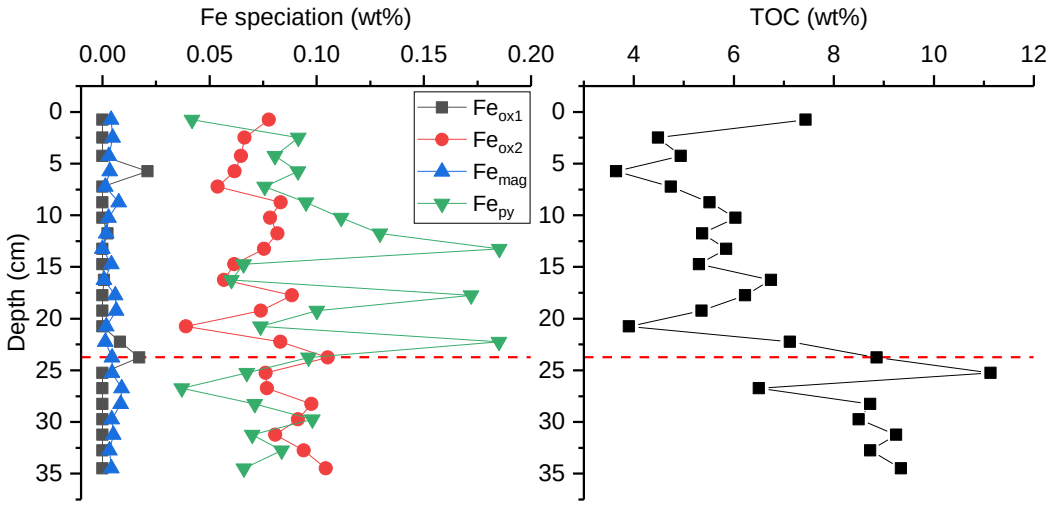

Figure 5.7 *Fe speciation and TOC data for Lake La Cruz sediment core (red dashed line shows the location of the sample used in this study; Thompson, 2018).*

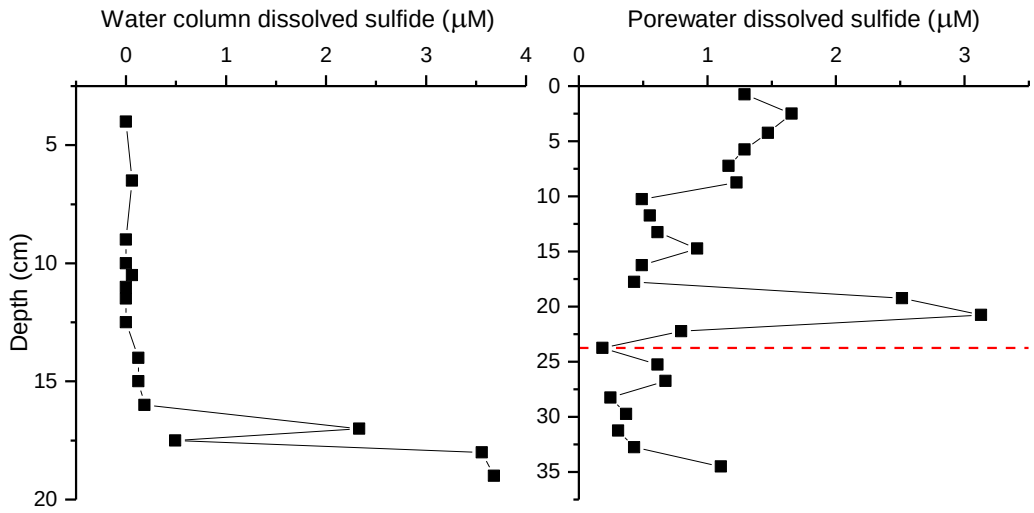

Figure 5.8 *Water column and porewater dissolved sulfide concentrations for the ferruginous Lake La Cruz (red dashed line shows the location of the sample used in this study; Thompson, 2018).*

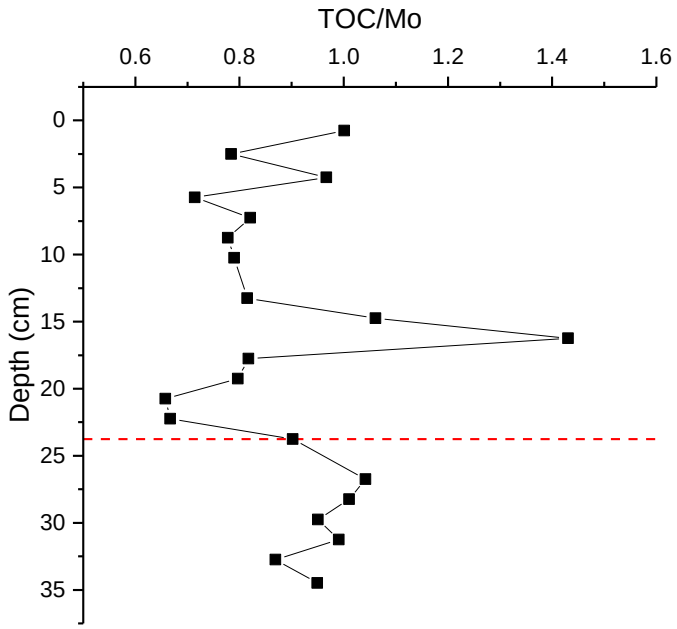

Figure 5.9 *TOC/Mo ratios for Lake La Cruz sediment core (red dashed line shows the location of the sample used in this study; Thompson, 2018).*

Overall the XANES data suggest that in ferruginous sediments deposited beneath a ferruginous water column Mo can be sequestered in the sediments in a reduced, sulfidized form (MoS_4), adsorbed to and complexed with magnetite and organics, respectively, where Mo(VI) in $Mo(VI)S_4$ is reduced upon adsorption to magnetite and organics (Dahl, et al., 2013b; 2017). It should be noted that these may not be the only sequestration mechanisms.

5.4.4 Sediments deposited beneath a euxinic water column

The euxinic spectral types EUX-1 – EUX-4 are identified from sediment cores collected from the euxinic sediments of Lake Cadagno, a 21 m deep meromictic lake in Switzerland with a euxinic monimolimnion that extends from a depth of 12 to 21 m and is separated from overlying oxic waters by a chemocline ~1 m thick (Del Don et al., 2001; Xiong et al., 2019). Fe speciation data for the sediments show that Fe minerals are generally present as $Fe_{ox1} > Fe_{ox2} > Fe_{mag} > Fe_{py}$ and TOC decreases downcore from 14.7 wt% at the sediment-water interface to 2.1 at a depth of

29 cm (Figure 5.10; Xiong et al., 2019). TOC/Mo ratios are fairly consistent to ~18 cm, after which they begin to increase, indicating that TOC concentration becomes disproportionately higher than Mo concentration at depth (Figure 5.12; Xiong et al., 2019). Water column sulfide is generally undetectable to ~12 m where then it increases with depth from 16.5 µM to 70.2 µM at the sediment-water interface (Figure 5.11; Xiong et al., 2019). Porewater sulfide is generally high ranging from 84.6 µM to 868.3 µM down to 24.25 cm depth but is much lower beneath this with 4.7 µM at 26.25 cm depth and 2.7 µM at 29.0 cm depth (Figure 5.11; Xiong et al., 2019).

The EUX-1 spectral type indicates that Mo is sequestered as thiomolybdate (MoS_4) complexed with organic matter (Figure 5.4). Research into Mo sequestration in sediments deposited beneath a euxinic water column also suggests an organic pathway for Mo removal, by identifying positive correlations between concentrations of Mo and sulfidized organic matter (März et al., 2008; Tribovillard et al., 2004). In the sediment core used here, Mo is strongly correlated with TOC to a depth of 18.25 cm, and thus there is a strong correlation between Mo and TOC at the depth from which samples were taken for XANES analysis. It should be noted that below 18.25 cm there is no correlation between Mo and TOC, but this is likely because the presence of a landslide in this section of the core prevents upwards diffusion of Mo (Xiong et al., 2019). The XANES spectrum also indicates that Mo(VI) in $Mo(VI)S_4$ is reduced upon adsorption to organics in agreement with experimental work that suggests that Mo can be adsorbed and reduced at the surface of particulate organic matter (Tucker et al., 1997; Dahl et al., 2017).

The EUX-2, EUX-3 and EUX-4 spectral types indicate that Mo is also sequestered as molybdate (MoO_4), (oxy)thiomolybdate (MoO_xS_{4-x}) and tetrathiomolybdate (MoS_4) adsorbed to pyrite, respectively. The presence of MoO_4 in the EUX-2 spectral type is surprising given the fact that

both the water column and sediments are sulfidic. By way of explanation, the existence of MoO_4 may indeed reflect the preservation of Mo as molybdate through the water column and/or in the sediments, or it may be a result of oxidation of the sample during or after its preparation for XANES analysis. However, all air-sensitive samples in this project were prepared and stored for XANES analysis under strict anaerobic conditions, and the XANES for this particular sample were collected < 1 month after preparation, compared to the OX-2 spectral type, which was exposed to air for a number of months before analysis, yet is matched to the Py-MoS_4 standard, and as such has not experienced oxidation. For these reasons it is unlikely that the EUX-2 spectral type represents an oxidised sample and may in fact indicate that not all Mo in a sulfidic environment is necessarily thiolated. Indeed, sequestration of Mo as MoO_4, MoO_xS_{4-x} and MoS_4 in Lake Cadagno is in agreement with earlier XAS work that identifies the presence of Mo-O and Mo-O-S bonds in the same euxinic environment (Dahl et al., 2013b).

Experimental work supports the suggestion that Mo is sequestered to sediments by pyrite, particularly as MoS_4 which forms an inner-sphere complex with irreversible adsorption, while MoO_4 only forms a weak outer-sphere complex (Bostick et al., 2003; Freund et al., 2016). Freund et al. (2016) further suggest that Mo(VI) in $Mo(VI)S_4$ is reduced during adsorption, which is observed here in the EUX-4 spectral type. Geochemical studies of sediments deposited in euxinic environments have also identified Mo associations with pyrite through SEM analysis (Coveney and Glascock, 1989), laser ablation ICP-MS (Chappaz et al., 2014) and X-ray diffraction analyses (Breward et al., 2015).

An earlier study of Mo in Lake Cadagno by Dahl et al. (2013b) suggests that Mo is removed onto sinking particles in the sulfidic water column. However, because the time required for transformation from MoO_4 to MoS_4 is ~1.5 y (Dahl et al., 2010) and the residence time of Mo in

the sulfidic zone of the water column at this sampling site is 80-130 days (Dahl et al., 2010), there is potentially only enough time for MoO_4 to be transformed to $MoOS_3$. The XANES collected here suggest that Mo associated with organic matter, and some of the Mo associated with pyrite, is present as MoS_4. The library of standards used does not include standards for organic matter associated with oxythiomolybdates and it may be possible that the XANES for thiomolybdate and oxythiomolybdate adsorbed to these phases are very similar. However, when looking at the XANES standards for Mo associated with pyrite as MoO_4, MoO_xS_{4-x} and MoS_4, clear differences are apparent in terms of the spectral shape (the deterioration of the pre-edge feature from a clear pre-edge peak for Py-MoO_4(ads) to a pre-edge hump for Py-MoO_xS_{4-x}(ads) and the absence of any pre-edge features for PyMoS_4(ads); and the development of a post-edge hump in the XANES range towards Py-MoS_4(ads)). It is therefore likely that the XANES collected are correctly matched with the standards identified and that Mo is retained in these sediments as MoS_4. This suggests that Mo retained as MoS_4 is fully thiolated in the sediments, rather than the water column, and may therefore have adsorbed or complexed with the identified mineral and organic phases below the sediment water interface.

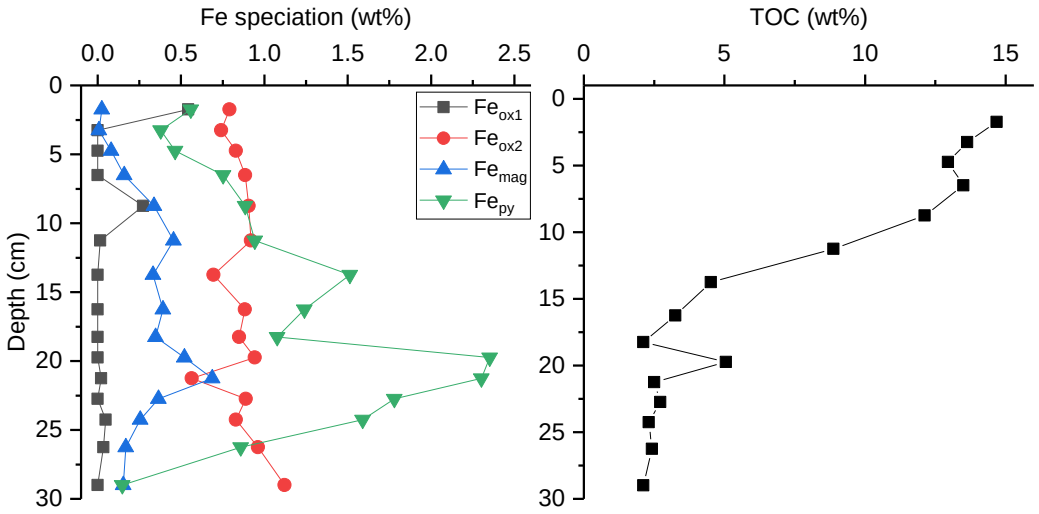

Figure 5.10 *Fe speciation and TOC data for Lake Cadagno sediment core (Xiong et al., 2019).*

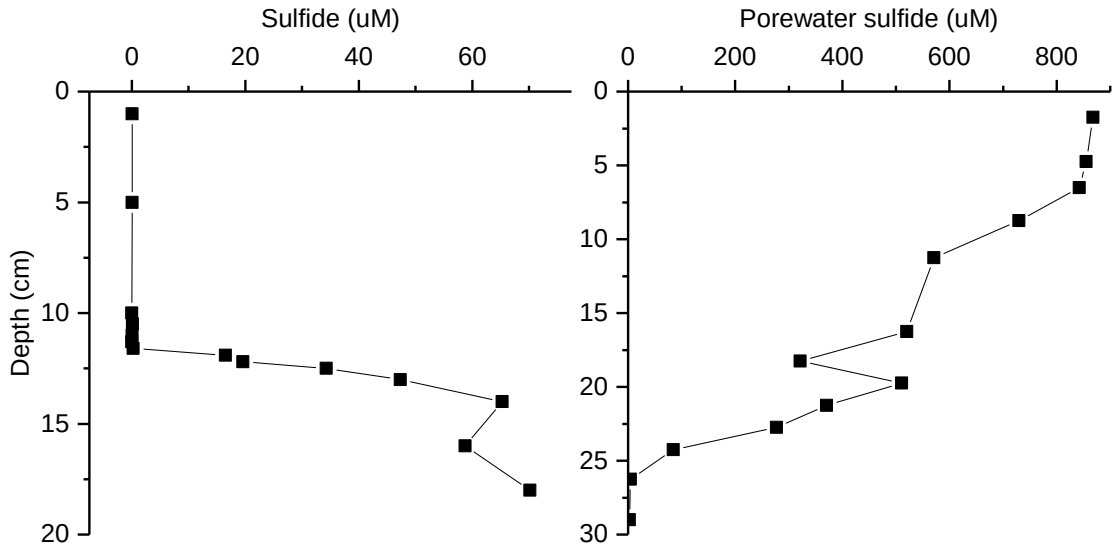

Figure 5.11 *Water column and porewater dissolved sulfide concentrations for the euxinic Lake Cadagno (Xiong et al., 2019).*

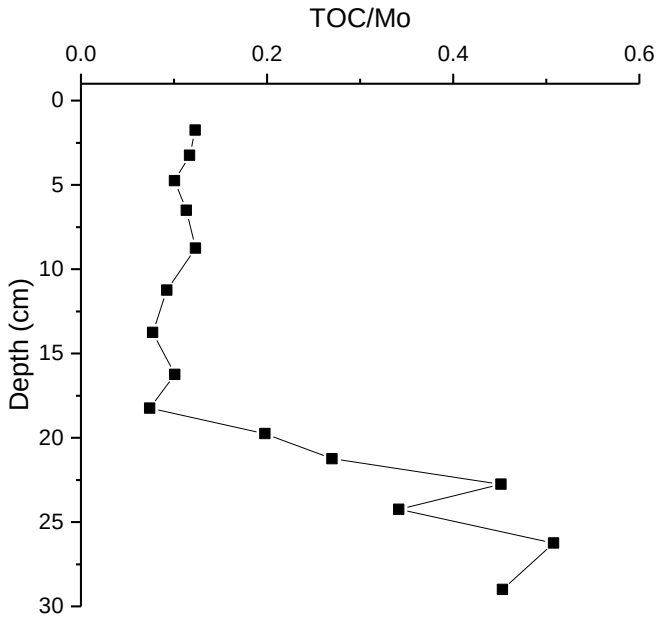

Figure 5.12 *TOC/Mo ratios for Lake Cadagno sediment core (Xiong et al., 2019).*

Overall the XANES data suggest that in sediments deposited beneath a euxinic water column Mo can be sequestered in the sediments in a reduced sulfidized form to organics, and as a spectrum of species (molybdate, oxythiomolybdate and thiomolybdate, the latter containing

reduced Mo) with pyrite. The importance of organic matter as the primary host for Mo in euxinic environments has been stressed in previous work (Coveney and Glascock, 1989; Dahl et al., 2017; Wagner et al., 2017) but it is clear from the current study that pyrite also plays an important role.

5.5 Conclusions

Mo sequestration pathways in sediments deposited beneath oxic, nitrogenous, ferruginous and euxinic water columns have been identified using XANES for the first time and previously unknown sequestration mechanisms have been identified. Multiple Mo phase associations are observed in all four redox environments with MoO_xS_{4-x} and MoS_4 adsorbed to pyrite in sediments deposited beneath an oxic water column; MoS_4 adsorbed to magnetite and MoO_xS_{4-x} adsorbed to pyrite observed in sediments deposited beneath a nitrogenous water column; MoS_4 adsorbed to magnetite and MoS_4 complexed with organic matter in sediments deposited beneath a ferruginous water column; and MoS_4 complexed with organic matter and MoO_4, MoO_xS_{4-x} and MoS_4 adsorbed to pyrite observed in sediments deposited beneath a euxinic water column. These results indicate that this method is a potentially useful palaeoredox tool in that it shows that XANES can be collected from sediments to identify spectral types; these XANES spectral types can be characterised using the methods identified in Chapter 4 and the XANES spectral types can be matched to known Mo species in the library of standards (Chapter 4). While this is a promising new tool, care needs to be taken as the data here indicate that the same spectral types are observed in different redox environments and generally only one known redox environment was studied. Therefore, this tool does not yet provide a clear set of Mo phase associations that facilitate identification of water column redox but does begin to identify previously unknown Mo sequestration pathways in these environments. To better calibrate the method, further known redox environments need to be studied to identify XANES spectral types. When using this method to develop robust

interpretations of palaeoenvironments it is also essential that Mo XANES are combined with other palaeo-redox techniques such as Mo concentrations, sequential extraction and isotopes, as well as other methods such as Fe sequential extraction.

Although pyrite has been identified as an important sequestration mineral for Mo in three of the redox environments studied, the pyrite-Mo pathway has surprisingly been identified in sediments deposited beneath an oxic water column, highlighting that identification of Mo associated with pyrite does not exclude oxic water columns from environmental interpretation of sediments. In addition, the XANES presented here indicate that Mo has been thiolated in this environment, which again may have previously been cause for misinterpretation of environmental conditions from sediments.

In all four environments Mo has been shown to have undergone partial or complete thiolation to MoO_xS_{4-x} and MoS_4, respectively. For the euxinic environment it is possible this happened either in the water column or porewaters but in the oxic, nitrogenous and ferruginous water columns the geochemical switch point of 11 µM sulfide (Helz et al., 1996) is not reached, limiting the transformation of MoO_4 to MoS_4 to the sediments, likely in sulfidic porewaters. MoO_4 has also been shown to survive transport through euxinic water column and sequestration in euxinic sediments. These observations again, could lead to misinterpretation of water column chemistry from Mo in sediments and therefore highlights the importance of using multiple geochemical proxies for water column interpretation from sediments.

Magnetite has been little studied as a sequestration mineral for Mo but has been identified as such in two of the environments studied here (sediments deposited beneath nitrogenous and ferruginous water columns) and this mechanism warrants further study. This is the first time

that Mo sequestered under a ferruginous water column has been studied and magnetite has been shown as one of the two sequestration pathways identified.

Finally, the XANES identify a mixture of oxic and reduced Mo species in three of the four environments studied, showing that a reduction step is not required for the sequestration of Mo to sediments.

5.6 References

Acholla, F. V., and Orr, W. L. 1993. Pyrite Removal from Kerogen without Altering Organic Matter: The Chromous Chloride Method. *Energy & Fuels.* **7**, pp. 406-410.

Arai, Y. 2010. X-ray Absorption Spectroscopic Investigation of Molybdenum Multinuclear Sorption Mechanism at the Goethite-Water Interface. *Environ. Sci. Technol.* **44**, pp. 8491-8496.

Ardakani, O. H., Chappaz, A., Sanei, H., and Mayer, B. 2016. Effect of thermal maturity on remobilization of molybdenum in black shales. *Earth and Planetary Science Letters*. **449**, pp. 311-320.

Bibak, A., and Borggaard, O. K. 1994. Molybdenum adsorption by aluminium and iron oxides and humic acid. *Soil Science*. **158**, pp. 323-328.

Bostick, B. C., Fendorf, S., and Helz, G. R. 2003. Differential Adsorption of Molybdate and Tetrathiomolybdate on Pyrite (FeS_2). *Environmental Science & Technology*. **37**, pp. 285-291.

Breward, N., Kemp, S. J., Ambrose, K., Powell, J. H., Morigi, A., and Wagner, D. 2015. Anomalous enrichment of molybdenum and associated metals in Lower Jurassic (Lias Group) black shales of central England, as revealed by systematic geochemical surveys. *Proceedings of the Geologists' Association.* **126**, pp. 346-366.

Canfield, D. E., and Thamdrup, B. 2009. Towards a consistent classification scheme for geochemical environments or, why we wish the term 'suboxic' would go away. *Geobiology*. **7**, pp. 385-392.

Chappaz, A., Lyons, T. W., Gregory, D. D., Reinhard, C. T., Gill, B. C., Li, C., and Large, R. R. 2014. Does pyrite act as an important host for molybdenum in modern and ancient euxinic sediments? *Geochimica et Cosmochimica Acta*. **126**, pp. 112-122.

Chen, X., Ling, H., Vance, D., Shields-Zhou, G. A., Zhu, M., Poulton, S. W., Och, L. M., Jiang, S., Li, D., Cremonese, L., and Archer, C. 2015. Rise to modern levels of ocean oxygenation coincided with the Cambrian radiation of animals. *Nature Communications.* **6** (7142), pp. 1-7.

Cheng, M., Li, C., Zhou, L., Algeo, T. J., Zhang, F., Romaniello, S., Jin, C., Lei, L., Feng, L., Jiang, S. 2016. Marine biogeochemistry in the context of dynamically euxinic mid-depth waters. A case study of the lower Cambrian Niutitang shales, South China. *Geochimica et Cosmochimica Acta*. **183**, pp. 79-93.

Coveney, R. M., and Glascock, M. D. 1989. A review of the origins of metal-rich Pennsylvanian black shales, central U.S.A., with an inferred role for basinal brines. *Applied Geochemistry*. **4**, pp. 347-367.

Dahl, T. W., Anbar, A. D., Gordon, G. W., Rosing, M. T., Frei, R., and Canfield, D. E. 2010. The behaviour of molybdenum and its isotopes across the chemocline in the sediments of Lake Cadagno, Switzerland. *Geochimica et Cosmochimica Acta.* **74**, pp. 144-163.

Dahl, T. W., Ruhl, M., Hammarlund, E. U., Canfield, D. E., Rosing, M. T., and Bjerrum, C. J. 2013a. Tracing euxinia by molybdenum concentrations in sediments using handheld X-ray fluorescence spectroscopy (HHXRF). *Chemical Geology*. **360-251**, pp. 241-251.

Dahl, T. W., Chappaz, A., Fitts, J. P., and Lyons, T. W. 2013b. Molybdenum reduction in a sulfidic lake: Evidence from X-ray adsorption fine-structure spectroscopy and implications for the Mo paleoproxy. *Geochimica et Cosmochimica Acta.* **103**, pp. 213-231.

Dahl, T. W., Chappaz, A., Hoek, J., McKenzie, C. J., Svane, S., and Canfield, D. E. 2017. Evidence of molybdenum association with particulate organic matter under sulfidic conditions. *Geobiology*. **15** (2), pp. 311-323.

Del Don, C., Hanselmann, K. W., Peduzzi, R., and Bachofen, R. 2001. The meromictic alpine Lake Cadagno: Orographical and biogeochemical description. *Acquatic Sciences*. **63**, pp. 70-90.

Erickson, B. E., and Helz, G. R. 2000. Molybdenum (VI) speciation in sulfidic waters: Stability and lability thiomolybdates. *Geochimica et Cosmochimica Acta*. **64** (7), pp. 1149-1158.

Ferdelman, T. G., Thamdrup, B., Canfield, D. E. Glud, R. N., Kuever, J., Lillebaek, R., Ramsing, N. B., and Wawer, C. 2006. Biogeochemical controls on the oxygen, nitrogen and sulfur distributions in the water column of Golfo Dulce: an anoxic basin on the Pacific coast of Costa Rica revisited. *Rev. Biol. Trop.* **54** (1), pp. 171-191.

Freund, C., Wishard, A., Brenner, R., Sobel, M., Mizelle, J., Kim, A., Meyer, D. A., and Morford, J. L. 2016. The effect of thio-containing organic molecule on molybdenum adsorption to pyrite. *Geochimica et Cosmochimica Acta.* **174**, pp. 222-235.

Greaney, A. T., Rudnick, R. L., Gasching, R. M., Whalen, J. B., Luais, B., and Clemens, J. D. 2018. Geochemistry of molybdenum in the continental crust. *Geochimica et Cosmochimica Acta*. **238**, pp. 35-54.

Guilbaud, R., Poulton, S. W., Butterfield, N. J., Zhu, M., and Shields-Zhou, G. A. 2015. A global transition to ferruginous conditions in the early Neoproterozoic oceans. *Nature Geoscience*. **8**, pp. 466-471.

Guilbaud, R., 2015. *Email to Jennifer Rodley*, 21 July.

Helz, G. R., Miller, C. V., Charnock, J. M., Mosselmans, J. F. W., Pattrick, R. A. D., Garner, C. D., and Vaughan, D. J. 1996. Mechanism of molybdenum removal from the sea and its concentration in black shales: EXAFS evidence. *Geochimica et Cosmochimica Acta.* **60** (19), pp. 3631-3642.

Hetzel, A. Böttcher, M. E., Wortmann, U. G., and Brumsack, H. 2009. Paleo-redox conditions during OAE 2 reflected in Demerara Rise sediment geochemistry (ODP Leg 207). *Palaeogeography, Palaeoclimatology, Palaeoecology.* **273**, pp. 302-328.

Jensen, H. S., Mortensen, P. B., Andersen, F. Ø., Ramusssen, E., and Jensen, A. 1998. Phosphorous cycling in a coastal marine sediment, Aarhus Bay, Denmark. *Limnology and Oceanography.* **40** (5), pp. 908-917.

März, C., Poulton, S. W., Beckmann, B., Küster, K., Wagner, T., and Kasten, S. 2008. Redox sensitivity of P cycling during marine black shale formation: Dynamics of sulfidic and anoxic, non-sulfidic bottom waters. *Geochimica et Cosmochimica Acta*. **72**, pp. 3703-3717.

Poulton, S. W., and Canfield, D. E. 2011. Ferruginous Conditions: A Dominant Feature of the Ocean through Earth's History. *Elements*. **7**, pp. 107-112.

Ramussen, H. and Jørgensen, B. B. 1992. Microelectrode studies of a seasonal oxygen uptake in a coastal sediment: role of molecular diffusion. *Marine Ecology Progress Series.* **81**, pp. 289-303.

Ravel, B., and Newville, M. 2005. ATHENA, ARTEMIS, HEPHAESTUS: data analysis for X-ray absorption spectroscopy using IFEFFIT. *Journal of Synchrotron Radiation.* **12**, pp. 537-541.

Romero-Viana, L., Keely, B. J., Camacho, A., Vicente, E., and Miracle, M. R. 2010. Primary production in Lake La Cruz (Spain) over the last four centuries: reconstruction based on sedimentary signal of photosynthetic pigments. *Journal of Paleolimnology*. **43**, pp. 771-786.

Scholz, F., Siebert, C., Dale, A. W., and Frank, M. 2017. Intense molybdenum accumulation in sediments underneath a nitrogenous water column and implications for the reconstruction of paleo-redox conditions based on molybdenum isotopes. *Geochimica et Cosmochimica Acta*. **213**, pp. 400-417.

Thamdrup, B., Fossing, H., and Jørgensen, B. B. 1994. Manganese, iron and sulfur cycling in coastal marine sediment, Aarhus Bay, Denmark. *Geochimica et Cosmochimica Acta.* **58** (23), pp. 5515-5129.

Thamdrup, B., Canfield, D. E., Ferdelman, T. G., Glud, R. N., and Gundersen, J. K. 1996. A biogeochemical survey of the anoxic basin Golfo Dulce, Costa Rica. *Revista de Biologia Tropical.* **44**, pp. 19-33.

Thompson, J. 2018. *Iron and Phosphorous Cycling Under Ferruginous Conditions.* Ph.D. thesis. University of Leeds.

Tribovillard, N., Riboulleau, A., Lyons, T., and Baudin, F. 2004. Enhanced trapping of molybdenum by sulfurized organic matter of marine origin in Mesozoic limestones and shales. *Chemical Geology*. **213**, pp. 385-401.

Tucker, M. D., Barton, L. L., and Thomson, B. M. 1997. Reduction and Immobilization of Molybdenum by *Desulfovibrio desulfuricans. Journal of Environmental Quality*. **26**, pp. 1146-1152.

Verbinnen, B., Block, C., Hannes, D., Lievens, P., Vaclavikova, M., Stefusova, K., Gallios, G., and Vandecasteele, C. 2012. Removal of Molybdate Anions from Water by Adsorption on Zeolite-Supported Magnetite. *Water Environment Research.* **84** (9), pp. 753-760.

Vorlicek, T. P., Kahn, M. D., Kasuya, Y., and Helz, G. R. 2004. Capture of molybdenum in pyrite-forming sediments: Role of ligand-induced reduction by polysulfides. *Geochimica et Cosmochimica Acta*. **68** (3), pp. 547-556.

Wagner, M., Chappaz, A., and Lyons, T. W. 2017. Molybdenum speciation and burial pathway in weakly sulfidic environments: Insights from XAFS. *Geochimica et Cosmochimica Acta*. **206**, pp. 18-20.

Xiong, Y., Guilbaud, R., Peacock, C. L., Cox, R. P., Canfield, D. E., Krom, M. D., and Poulton, S. W. 2019. Phosphorous cycling in Lake Cadagno, Switzerland: A low sulfate euxinic ocean analogue. *Geochimica et Cosmochimica Acta*. **251**, pp. 116-135.

Xu, N., Christodoulates, C., and Braida, W. 2006. Adsorption of molybdate and tetrathiomolybdate onto pyrite and goethite: Effect of pH and competitive anions. *Chemosphere*. **62**, pp. 1726-1735.

Chapter 6 Controls on molybdenum cycling during anoxic diagenesis in continental margin sediments: Aarhus Bay, Denmark

6.1 Introduction

Mo is ubiquitous in the Earth's oceans and its distinct behaviour in different redox environments makes it an ideal palaeoredox proxy. Mo is used as such in terms of its concentrations in marine sediments (e.g. Adelson et al., 2001; Hetzel et al., 2009; März et al., 2009) where low concentrations are used to infer deposition beneath an oxic water column as the unreactive molybdate anion is transiently cycled in upper sediments, and high concentrations are used to infer deposition beneath a euxinic water column where the molybdate anion is transformed to highly reactive thiomolybdates which are easily sequestered to sediments. Mo isotopes are also used to reconstruct water column redox conditions as light δ^{98}Mo typically adsorbs to sedimentary minerals imparting a light isotopic signature in the sedimentary record (Goldberg et al., 2009; Poulson Brucker et al., 2009; Siebert et al., 2006). Conversely, euxinic sediments typically display the heavy isotopic signature of seawater due to the quantitative removal of Mo from the water column to sediments in these environments (Chen et al., 2015; Dahl et al., 2010; Poulson et al., 2006). While a significant amount of research has been completed into the sequestration of Mo in euxinic sediments, other than the Mn and Fe (oxyhydr)oxide shuttle which has been explored both experimentally and in marine sediments, little is known about other potential sequestration pathways of Mo beneath an oxic water column. To explore these pathways in a continental margin setting, a novel Mo sequential extraction method is combined with Mo isotopes, Mo XANES and Fe speciation to highlight likely Mo-mineral phase associations in sediments from Aarhus Bay, a well-characterised continental margin setting with an oxic water column overlying sulfidic porewaters (Fossing et al., 2004; Thamdrup et al., 1994). By

combining these methods, insights have been gained into the behaviour and sequestration pathways of Mo in sulfidic porewaters and new data are presented that may have implications for the use of Mo isotopes as a palaeoredox proxy.

6.2 Methods

6.2.1 Sampling site

The Aarhus Bay samples used here are described in detail in Section 2.1.1.4. The sampling site is on the Baltic Sea-North Sea transition on the East Coast of Jutland, Denmark (56°07.0866N, 10°20.7807E).

6.2.2 Mo sequential extraction

The Mo sequential extraction method outlined in Chapter 3 targeted eight Mo fractions: 1) weakly adsorbed Mo (Mo_{WA}); 2) strongly adsorbed Mo (Mo_{SA}); 3) Mo incorporated into Mn and Fe (oxyhydr)oxides, calcium carbonates, AVS and other reduced phases (Mo_{ox1}); 4) Mo incorporated into crystalline Fe-oxides (Mo_{ox2}); 5) Mo incorporated into magnetite (Mo_{mag}); 6) Mo incorporated into silicates (Mo_{sil}); 7) Mo incorporated into organic material (Mo_{org}); 8) Mo incorporated into pyrite (Mo_{py}). A wash was performed after each of the extractions 3-8 by shaking with pH 5.5 MQ for 1 h to remove any readsorbed Mo. Once centrifuged, the supernatants removed from samples were diluted and analysed by inductively coupled plasma mass spectrometry on a Thermo iCAP Qc ICP-MS. Six replicate samples were used for precision to give RSD values (Appendix A) and underwent the entire sequential extraction.

6.2.3 Other methods

The methods for the Fe sequential extraction, total digests, TOC analysis, porewater and water column analysis and Mo isotopes are outlined in Chapter 2.

6.2.4 XANES data collection and analysis

Micro-focus XANES spectra at the Mo K-edge (20,000 eV) for AB-1B-2 were collected during a beamline session in March 2017 on the hard X-ray beamline I18 at Diamond Light Source Ltd (DLS). Methods for XANES collection and processing and matching samples to the library of standards are outlined in Chapter 4. The sample analysed was bulk, untreated sediment from sample AB-1B-2 (1.5 cm depth) and was presented to the beam embedded in a polished micro-thin section (<100 µM thick) made from X-ray amorphous resin. Details on thin section sample preparation can be found in Chapter 2.

6.3 Results

6.3.1 Porewater redox geochemistry

Figure 6.1 and Table 6.1 show the results for porewater geochemistry. Manganese (Mn) is high in the upper core, starting at 47.9 µM at 0.5 cm, but concentrations progressively decrease downcore to 2.2 µM at 18 cm. Porewater Fe concentrations are very high in the upper core (up to 161.7 µM) but decrease sharply to a depth of 5 cm, after which concentrations do not exceed 0.55 µM. Dissolved sulfide starts to be detectable from a depth of 1.5 cm, at 0.05 µM. Sulfide concentrations gradually rise to 21.9 µM at 7 cm depth, after which sharp increases are observed with an abrupt increase from 159.2 µM at 12 cm to >300 µM at the base of the core.

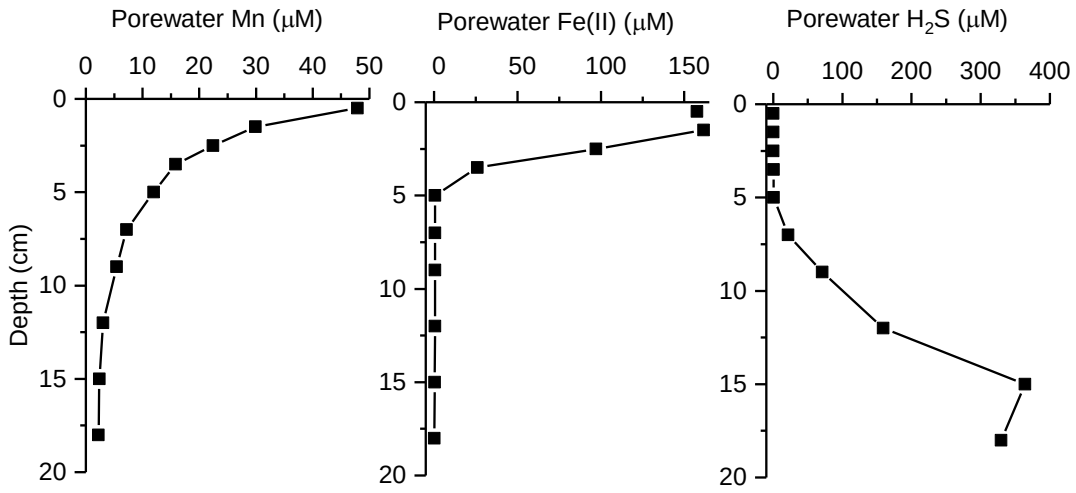

Figure 6.1 *Dissolved phase Mn, Fe(II) and H_2S for AB-1B (Goldberg, 2019).*

Table 6.1 *Porewater core data for AB-1B.*

Depth (cm)	Mn (μM)	Fe (μM)	S (μM)
0.5	47.91	157.68	0.00
1.5	29.89	161.72	0.05
2.5	22.46	97.16	0.15
3.5	15.83	25.98	0.40
5.0	11.99	0.50	0.35
7.0	7.18	0.55	21.85
9.0	5.40	0.54	71.02
12.0	3.03	0.55	159.19
15.0	2.37	0.27	364.27
18.0	2.23	0.25	329.57

6.3.2 Sediment geochemistry

Tables 6.2 and 6.3, and Figure 6.2 show the sediment geochemistry for AB-1B. The sediments are organic-rich with TOC generally ranging between 3.09 to 4.06 wt% (Table 6.2). Concentrations are variable over the top 5 cm, followed by a progressive decrease downcore. Mn concentrations decrease downcore from 0.026 wt% at the top of the core to 0.010 wt% at the base. Although the highest Mn concentrations are observed at the top of the core (0.5 cm) there is another peak at 3.5 cm where concentrations reach 0.025 wt%. Total Fe ranges from 2.29 to 3.30 wt% with the highest concentrations observed at a depth of 5 cm (Table 6.2).

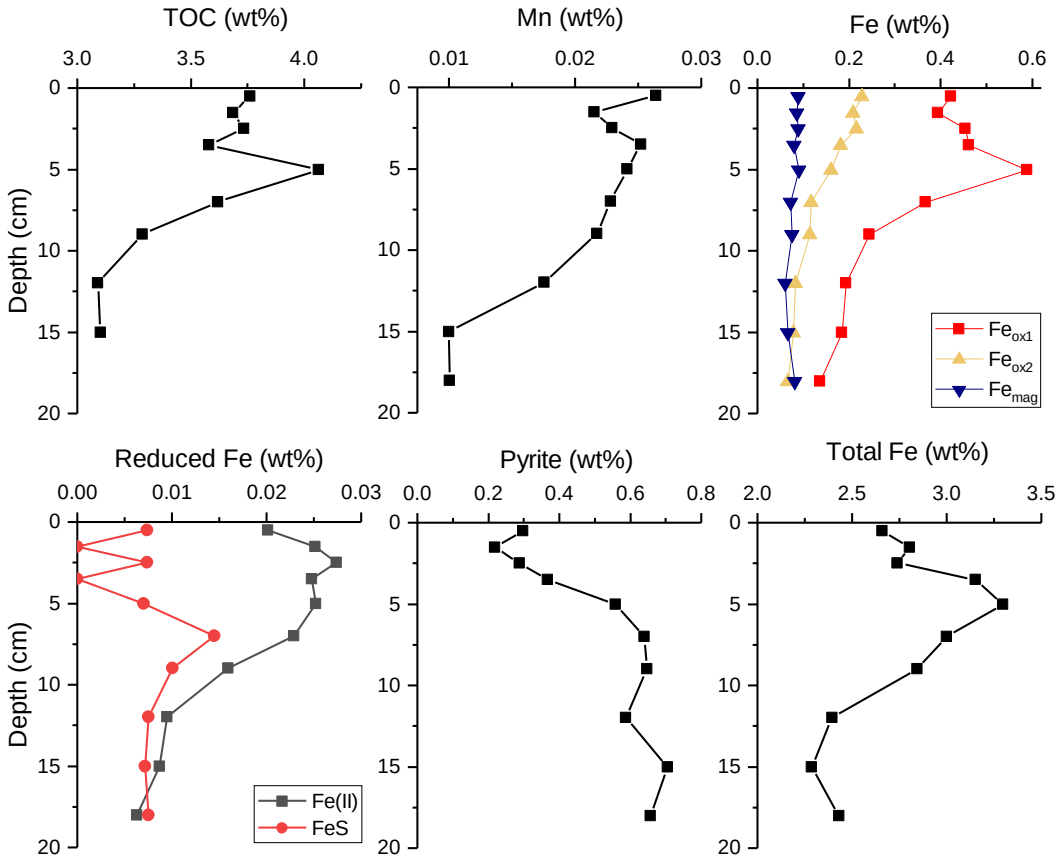

Figure 6.2 *Solid phase geochemistry for AB-1B (Goldberg, 2019).*

Table 6.2 *Sediment core data for AB-1B.*

Depth (cm)	TOC (wt%)	Mn_T (wt%)	Fe_T (wt%)	Fe(II) (wt%)	FeS (wt%)	Fe_{ox1} (wt%)	Fe_{ox2} (wt%)	Fe_{mag} (wt%)	Fe_{py} (wt%)
0.5	3.76	0.03	2.66	0.02	0.007	0.42	0.23	0.09	0.30
1.5	3.69	0.02	2.80	0.03	0.000	0.39	0.21	0.09	0.22
2.5	3.73	0.02	2.74	0.03	0.007	0.45	0.22	0.09	0.29
3.5	3.58	0.03	3.15	0.02	0.000	0.46	0.18	0.08	0.37
5.0	4.06	0.02	3.30	0.03	0.007	0.59	0.16	0.09	0.56
7.0	3.62	0.02	3.00	0.02	0.014	0.37	0.12	0.07	0.64
9.0	3.29	0.02	2.84	0.02	0.010	0.24	0.11	0.07	0.65
12.0	3.09	0.02	2.40	0.01	0.008	0.19	0.08	0.06	0.59
15.0	3.10	0.01	2.29	0.01	0.007	0.18	0.08	0.07	0.71
18.0	ND	0.01	2.43	0.01	0.008	0.14	0.07	0.08	0.66

Total Fe concentrations in the uppermost sediments (0.5 cm) start at 2.66 wt% before increasing to maximum concentrations at 5 cm, after which they gradually decrease downcore.

A slight increase is observed at the base of the core (18 cm). Fe speciation data indicate that within the oxidised Fe-species, poorly crystalline Fe-oxides dominate (e.g., ferrihydrite; Fe_{ox1}), followed by crystalline Fe-oxides (e.g., goethite, hematite; Fe_{ox2}), then magnetite (Fe_{mag}). Pyrite is lower than Fe_{ox1} in the top 5 cm (but higher than Fe_{ox2} and Fe_{mag}) but below 5 cm becomes the dominant Fe-species, reaching concentrations of 0.71 wt% towards the base of the core. Fe(II) concentrations are relatively high (0.02 to 0.03 wt%) in the upper 5 cm, but below this depth concentrations gradually decline to 0.01 wt% at the base of the core (Table 6.2). FeS concentrations are relatively stable for most of the core at around 0.07 wt%, other than two points at 1.5 cm and 3.5 cm where no FeS was detected, and 7cm and 9 cm where FeS concentrations increase to 0.014 wt% and 0.010 wt% respectively.

6.3.3 Molybdenum geochemistry

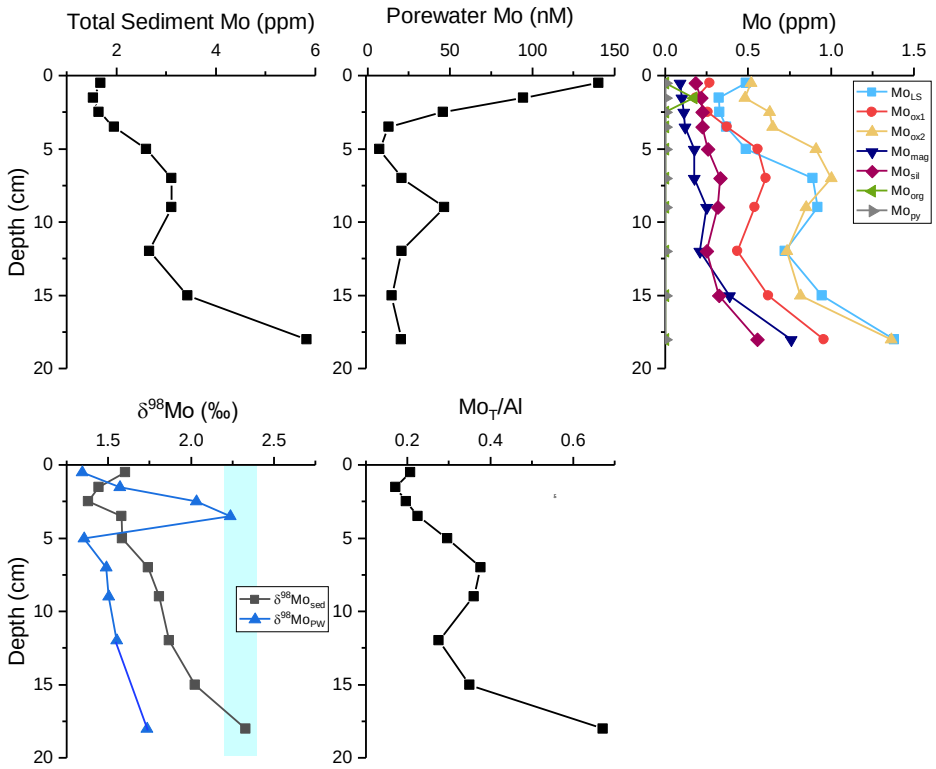

Figure 6.3 *Mo geochemistry for AB-1B (the blue shaded area in the δ^{98}Mo graph indicates seawater values).*

Table 6.3 *Sediment and porewater Mo data for AB-1B.*

Depth (cm)	Total Mo (ppm)	Sediment δ^{98}Mo (‰)	Porewater Mo (nM)	Porewater δ^{98}Mo (‰)
0.5	1.68	1.60	140.30	1.34
1.5	1.53	1.44	94.69	1.57
2.5	1.65	1.38	45.70	2.03
3.5	1.96	1.58	12.81	2.24
5.0	2.60	1.58	7.28	1.36
7.0	3.11	1.74	20.70	1.49
9.0	3.11	1.81	46.60	1.50
12.0	2.66	1.87	20.71	1.55
15.0	3.43	2.02	14.74	
18.0	5.83	2.33	20.49	1.73

Table 6.4 *Sediment Mo speciation data for AB-1B.*

Depth (cm)	Mo_{WA} (ppm)	Mo_{ox1} (ppm)	Mo_{ox2} (ppm)	Mo_{mag} (ppm)	Mo_{sil} (ppm)	Mo_{org} (ppm)	Mo_{py} (ppm)
0.5	0.49	0.27	0.52	0.09	0.18	ND	ND
1.5	0.32	0.19	0.48	0.10	0.22	0.17	ND
2.5	0.33	0.26	0.63	0.11	0.22	ND	ND
3.5	0.37	0.37	0.65	0.12	0.22	ND	ND
5.0	0.49	0.56	0.91	0.18	0.26	ND	ND
7.0	0.89	0.61	1.00	0.17	0.33	ND	ND
9.0	0.92	0.54	0.85	0.25	0.32	ND	ND
12.0	0.72	0.44	0.73	0.21	0.25	ND	ND
15.0	0.95	0.62	0.82	0.39	0.32	ND	ND
18.0	1.38	0.96	1.36	0.76	0.55	ND	ND

Porewater Mo is slightly higher than average seawater Mo (~105 nM; Collier, 1985) in the upper 0.5 cm, but concentrations decrease below this value from a depth of 1.5 cm. An increase is observed mid-core where Mo concentrations rise to 46.6 nM before decreasing back to 20.5 nM at the base of the core. Porewater δ^{98}Mo ($\delta^{98}Mo_{PW}$) values are generally lighter than typical seawater values for oxygenated waters (~ 2.3‰; Siebert et al., 2003) throughout most of the core, with the lightest value observed at a depth of 0.5 cm (1.34‰). A sharp increase in $\delta^{98}Mo_{PW}$ is observed at 2.5 cm and 3.5 cm depths where values increase up

to a near seawater value of 2.24‰ before a sharp decrease to 1.36‰ followed by a steady increase downcore (Figure 6.3; Table 6,3).

Tables 6.3 and 6.4, and Figure 6.3 show Mo sediment geochemistry. Total sediment Mo concentrations range from 1.53 ppm in upper sediments (1.5 cm) to 5.83 ppm at the base of the core (18 cm) and generally increase downcore, but with mid-depth samples showing some scatter and little overall increase. Mo speciation data indicate that both loosely adsorbed Mo (Mo_{WA}) and Mo incorporated into crystalline Fe-oxides (Mo_{ox2}) are the foremost sequestration pathways for Mo throughout the core, with Mo_{ox2} generally dominating over Mo_{WA} (Table 6.4; Figure 6.3). Speciation data also indicate that Mo strongly adsorbed or incorporated into Mn and Fe (oxyhydr)oxides (Mo_{ox1}), Mo associated with AVS and other reduced Fe mineral phases and Mo associated with calcium carbonate; Mo incorporated into magnetite (Mo_{mag}); and Mo incorporated into silicates (Mo_{sil}) are hosts for Mo, although Mo in silicates is most likely delivered to sediments through terrestrial erosion of silicate rocks. Mo incorporated into organic matter (Mo_{org}) or pyrite (Mo_{py}) do not appear to be important sequestration pathways in this environment as, other than one value for Mo_{org} (0.17 ppm Mo at 1.5 cm), all results were below detection limits (0.046 ppb) for these fractions. Overall sediment δ^{98}Mo values become heavier downcore, but there are two sharp decreases in the upper sediments at 1.5 cm (1.59‰) and 3.5 cm (1.60‰). Values then peak at 7 cm (2.31‰), before a gradual decrease followed by a further peak at the base of the core (18 cm) to 2.60‰.

6.3.4 XANES

XANES were collected for a bulk, untreated sample from the Aarhus Bay core (specifically AB-1B-2, 1.5 cm depth; Figure 6.4; Table 6.5). This sample is representative of Mo sequestration to minerals during reductive cycling in upper sediments. The XANES spectra indicates that the main edge and associated spectral parameters are present at: E_M = 20031.6 eV; E0 = 20007.4

eV; and E_S = -9.6 eV. The pre-edge region is characterised by an absence of any pre-edge peaks or humps and the spectra displays an edge shoulder. The post-edge region is characterised by: E_C = 20056.7 eV and E_D = 20093.5 eV. These spectral characteristics indicate that AB-1B contains largely reduced Mo in mainly octahedral coordination adsorbed to pyrite as MoS_4 (Chapter 4).

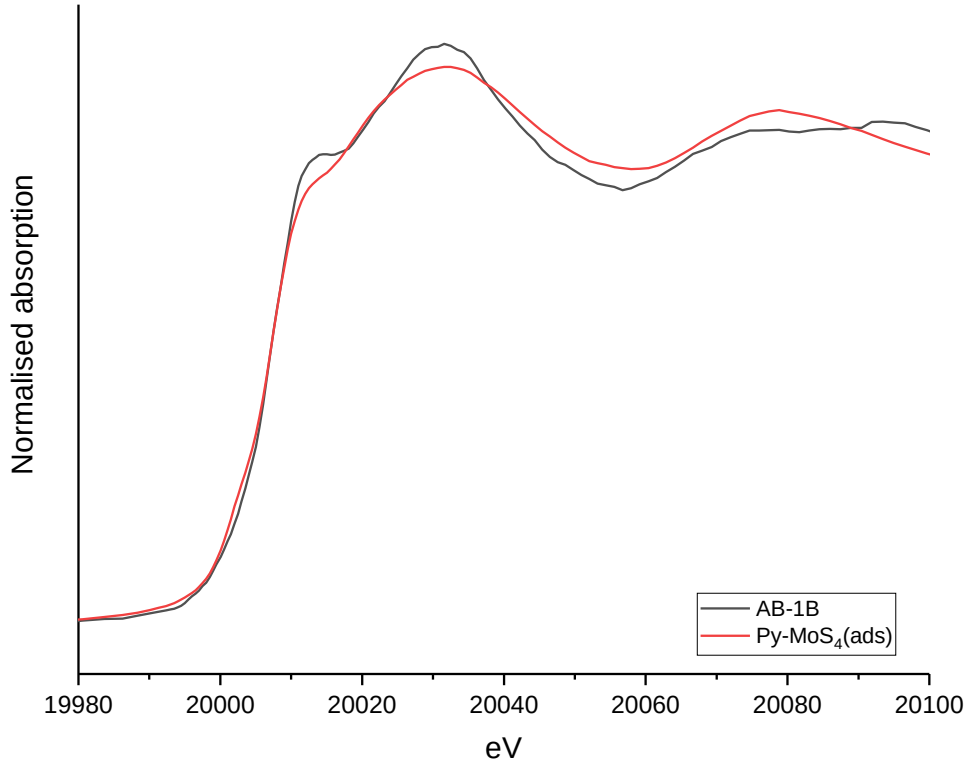

Figure 6.4 *XANES spectra for bulk, untreated sample from the Aarhus Bay core (AB-1B) and the Py-MoS_4(ads) standard showing similarities in spectral shape and features.*

Table 6.5 *XANES spectral values for AB-1B-2 and the Py-MoS_4(ads) standard.*

	AB-1B	**Py-MoS_4(ads) standard**
E0 (eV)	20007.4	20007.2
E_M (eV)	20031.6	20032.0

E_S (eV)	-9.6	-9.8
E_C (eV)	20056.7	20059.0
E_D (eV)	20093.5	20079.0

6.4 Discussion

6.4.1 Sediment Geochemistry

Aluminium generally acts conservatively during sedimentation and diagenesis, and therefore, to determine whether fluctuations in Fe, Mn and Mo concentrations are dominated by authigenic processes, total element concentrations are compared with *element*/Al ratios (Figure 6.5). All three total element concentration profiles show the same general trend as the element/Al profiles, and consequently the element concentrations are likely dominantly controlled by diagenetic mobilisation.

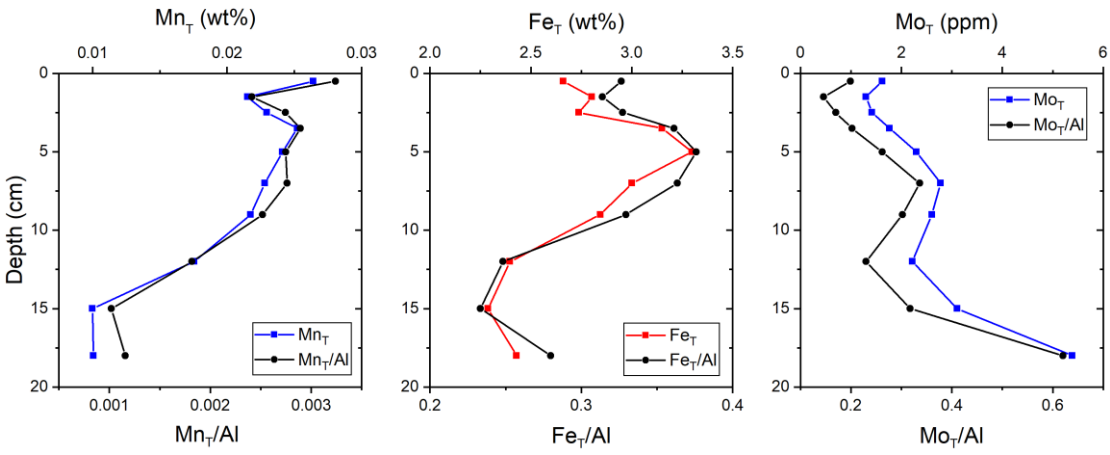

Figure 6.5 *Total Mn, Fe and Mo concentrations compared with Mn/Al, Fe/Al and Mo/Al respectively.*

6.4.2 Biogeochemical cycling

The data collected are broadly consistent with the previous studies of the area (Fossing et al., 2004; Thamdrup et al., 1994). The core displays evidence of Mn, Fe and Mo cycling,

particularly in the upper sediments (defined here as 0-5 cm depth). Porewater Mn concentrations are relatively high in the upper sediments, displaying a steep decline downcore indicative of the reductive dissolution of Mn from Mn^{4+} to Mn^{2+}, which is then released into porewaters before undergoing upward diffusion to be re-oxidised at the surface (Figure 6.5; e.g. Goldberg et at., 2012; Thamdrup et al., 1994). Reductive dissolution of MnO_2 is likely largely due to organic matter remineralization but may also be linked to reaction with Fe^{2+} and H_2S (Table 6.6, equations a-c; Fossing et al., 2004), and although sulfide is not detectable in the porewaters of the upper sediments, this is likely due to its consumption in redox reactions (Thamdrup et al., 1994), as evidenced by the presence of both AVS and pyrite in shallow sediments. Sediment Mn concentrations are also relatively high in upper sediments, reflective of the transient enrichments observed in zones of biogeochemical cycling (Figure 6.2; Burdige, 1993), and Mn steadily declines downcore as reduced Mn undergoes upward diffusion and oxidation. The porewater and solid phase Mn profiles suggest that Mn reduction is a dominant redox process to 1.5 cm but occurs at all depths. Fe porewater concentrations also display a steep decline in the upper sediments, again indicative of mineral cycling as Fe-oxides are reductively dissolved, releasing Fe(II) into porewaters where it undergoes upward diffusion to be reoxidised at the surface (Table 6.6, equations g-k; Goldberg et al., 2012, Fossing et al., 2004; Thamdrup et al., 1994). Sedimentary Fe sequential extraction data indicate high levels of Fe oxides in the upper sediments that then decrease below the redox boundary, particularly in the Fe_{ox1} phase (Figure 6.2). These higher concentrations are most likely the result of reoxidation of porewater Fe(II) by Mn oxides (Thamdrup et al., 1994). This observation is consistent with the sharp decrease in porewater Fe(II) in the upper sediments above the redox boundary and the data suggest that Fe redox processes dominate from 1.5 to 5 cm but occur throughout the core.

Porewater sulfide is very low in the upper sediments, with a steady increase from 5 cm downcore (Figure 6.1). This most likely reflects the near complete consumption of sulfide by Mn and Fe redox reactions (Thamdrup et al., 1994) and Mo redox reactions may also be a minor contributor to this depletion of sulfide, as MoO_4 forms thiomolybdates ($MoO_4^{2-} + xHS^- \leftrightarrow MoO_xS_{4-x}^{2-} + xOH^-$, $1<x<4$; Bostick et al., 2003) in the presence of sulfide.

Table 6.6 *Redox reactions for Mn and Fe (after Fossing et al., 2004).*

Manganese		
Reduction	$MnO_2 + 2Fe_2 + 2H_2O \rightarrow Mn^{2+} + 2FeOOH + 2H^+$	(a)
	$MnO_2 + H_2S + 2H^+ \rightarrow Mn^{2+} + S^0 + 2H_2O$	(b)
	$2MnO_2 + CH_2O + 4H^+ \rightarrow 2Mn^{2+} + CO_2 + 3H_2O$	(c)
Oxidation	$Mn^{2+} + 2FeOOH + 2H^+ \rightarrow MnO_2 + 2Fe_2 + 2H_2O$	(d)
	$Mn^{2+} + S^0 + 2H_2O \rightarrow MnO_2 + H_2S + 2H^+$	(e)
	$2Mn^{2+} + O_2 + 2H_2O \rightarrow 2MnO_2 + 4H^+$	(f)
Iron		
Reduction	$2FeOOH + Mn^{2+} + 2H^+ \rightarrow 2Fe^{2+} + MnO_2 + 2H_2O$	(g)
	$2FeOOH + H_2S + 4H^+ \rightarrow 2Fe^{2+} + S^0 + 4H_2O$	(h)
	$4FeOOH + CH_2O + 8H^+ \rightarrow 4Fe^{2+} + CO_2 + 7H_2O$	(i)
Oxidation	$2Fe^{2+} + MnO_2 + 2H_2O \rightarrow 2FeOOH + Mn^{2+} + 2H^+$	(j)
	$S^0 + 2Fe^{2+} + 4H_2O \rightarrow H_2S + 2FeOOH + 4H^+$	(j)
	$4Fe^{2+} + O_2 + 2H_2O \rightarrow 4FeOOH + 8H^+$	(k)

Biogeochemical cycling is also evident in the Mo isotope data (Figure 6.3), with generally light δ^{98}Mo values for porewaters and heavy δ^{98}Mo values for bulk sediment in the upper sediments. Although seawater δ^{98}Mo is 2.3‰ (Scholz et al., 2013), the first value recorded for porewaters at 0.5 cm deep is 1.34‰. This likely reflects the initial reductive dissolution of Mn and Fe-oxides, which would release isotopically light adsorbed Mo into porewaters. However, as Mo is readsorbed to Mn and Fe (oxyhydr)oxides during cycling, it removes additional light δ^{98}Mo, pushing porewaters to heavier values, the maximum extent of which occurs at ~3.5 cm depth, with a δ^{98}Mo value (2.24‰) that is close to the seawater value.

6.4.3 Molybdenum sequestration pathways

In an oxic water column Mo is predominantly delivered to sediments adsorbed to Mn and Fe-oxides where it may then be released to porewaters upon reductive dissolution of these minerals (Goldberg et al., 2012; Scholz et al., 2013; Shimmield and Price, 1986) and the Mo sequential extraction data provide support for this process (Figure 6.3). In the upper 3.5 cm, porewater Mo declines steeply as Mo released from Mn and Fe-oxides is readsorbed in sediments (Figure 6.3). This trend coincides with a near-complete depletion of porewater sulfide (Figure 6.1) which, as mentioned above, is likely a result of almost total consumption of sulfide in the production of Fe sulfides, which is itself also a likely sequestration pathway for Mo (Ardakani et al., 2016; Bostick et al., 2003; Tribovillard wt al., 2004). Although Fe redox processes dominate at these depths, the initial presence of sulfide before its depletion also facilitates the formation of thiomolybdates, and this is evident in the Mo XANES which indicate that MoS_4 is present at 1.5 cm. These thiomolybdates are highly reactive to particle scavenging and ultimately increase the sequestration of Mo to sediments (Erickson and Helz, 2000; Wagner et al., 2017).

Mo_{WA} is one of the most dominant phases identified by sequential extraction (Figure 6.3) and when observing this Mo pool as a percentage of total Mo (Figure 6.6) the data indicate that the overall proportion of Mo_{WA} increases below 5 cm. When Mo_{WA} is normalised to the potential Fe pools that may be involved in the sequestration of this Mo fraction (Fe_{ox1}, Fe_{ox2}, Fe_{mag} and Fe_{py}; Figure 6.7a), Mo_{WA}/Fe_{py} displays a relatively constant ratio throughout the core suggesting that pyrite concentrations may exert a control over Mo sequestration to sediments (i.e. where pyrite concentrations increase so do authigenic Mo concentrations). Normalisation of this Mo phase to Fe_{ox1}, Fe_{ox2} and Fe_{mag} display profiles similar to that of Mo_T, suggesting that these phases exert less of a control over Mo sequestration. Given that the Mo XANES indicate that Mo is adsorbed to pyrite (Figure 6.4, Table 6.5), and yet no Mo was recovered in the Mo_{py} extraction (Figure 6.3), the relationship between the Fe_{py} and Mo_{WA} profiles was also investigated on the basis that Mo may be weakly adsorbed to this phase by directly comparing the Mo_{WA} profile to that of Fe_{py} (Figure 6.7c). The Mo_{WA} and Fe_{py} profiles match well in the upper sediments and to a slightly lesser degree in the sediments below (Figure 6.7c). Fe_{py} concentrations increase in the upper sediments, and this could account for the reduction in porewater Mo as it adsorbs to pyrite. Pyrite is being constantly formed in these sediments via the reduction of Fe^{3+} in FeOOH to Fe^{2+} which is released to porewaters where it then reacts with sulfide to form FeS and ultimately FeS_2 (Thamdrup et al., 1994; Fossing et al., 2004). Pyrite has been highlighted as an important sink for Mo in other studies (Ardakani et al., 2016; Bostick et al., 2003; Tribovillard et al., 2004) and the data suggest that a significant proportion of the Mo in Mo_{WA} is associated with the pyrite fraction, but only weakly adsorbed. The XANES indicate that MoO_4 adsorbed to pyrite at 1.5 cm has been transformed to MoS_4, which could only have occurred in the porewaters (as the water column is oxic), but it is unclear whether this happened before or during adsorption to pyrite. The transformation of MoO_4 to MoS_4 may play a minor role in the consumption of porewater sulfide in the upper sediments. The sedimentation rates in this location are ~3.2 mm/y (Rasmussan and Jørgensen, 1992) and

therefore the sample was deposited ~4.7 y prior to collection. This deposition period exceeds the calculated period for transformation of MoO_4 to MoS_4 in sulfidic porewaters by ~3.2 y (Erikson and Helz, 2000). This Mo_{py} phase was not detected in the Mo sequential extraction, likely because it was desorbed in the Mo_{WA} extraction which removes loosely adsorbed Mo from the mineral surface, therefore showing that MoS_4 was only loosely adsorbed at the pyrite surface rather than incorporated into the structure.

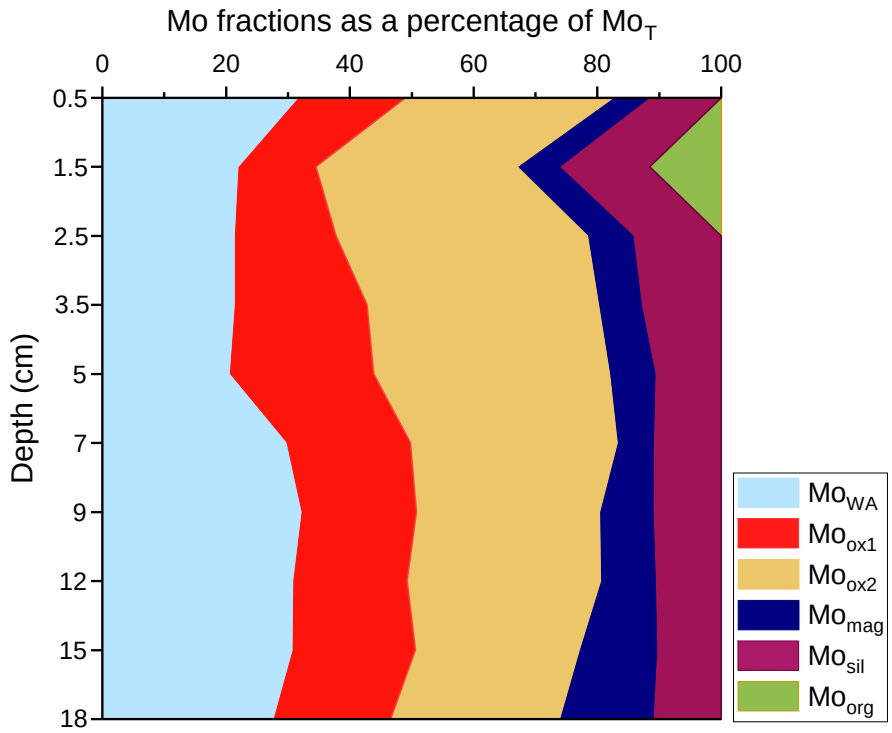

Figure 6.6 *Mo sequential extraction fractions as a percentage of total Mo.*

Another dominant phase identified by the Mo sequential extraction in the upper sediments, that persists downcore, is Mo_{ox1}, which includes Mo strongly adsorbed or incorporated into Mn and Fe (oxyhydr)oxides. Mo is shuttled to sediments adsorbed to these minerals before being released to porewaters when they are reductively dissolved, but reoxidation following upwards migration of dissolved species may result in re-precipitation of Mn and Fe (oxyhydr)oxides (Thamdrup et al., 1994), providing a mechanism for readsorption of Mo. The

overall proportion of Mo in the Mo_{ox1} phase decreases slightly at 1.5 cm, likely as a result of reductive dissolution of Fe (oxyhydr)oxides in (which is also reflected in the Fe_{ox1} profile, Figure 6.2) but is otherwise fairly constant throughout the core (Figure 6.6). When normalising Mo_{ox1} to Fe_{ox1} (Figure 6.7b) ratios are relatively constant in the top 5 cm but become less consistent below this point. The Fe_{ox1} profile shows that, although this pool persists at depth, it does decrease downcore. However, the Mo_{ox1} pool is proportionately consistent throughout the core suggesting that Fe_{ox1} concentrations are not directly influencing the levels of Mo sequestration in this environment. When comparing the Mo_{ox1} and Fe_{ox1} profiles (Figure 6.7d) they correlate reasonably well to 5 cm before Fe_{ox1} concentrations decrease sharply while Mo_{ox1} concentrations continue to generally increase. The Mn_T profile was also compared to consider Mo adsorbed to Mn-oxides and this correlates well to 3.5 cm, before Mn_T begins to decrease downcore (Figure 6.7d). This depth is consistent with Mn redox cycling in the upper sediments where, in a similar fashion to Fe, Mn-oxides are reduced to release Mn^{2+} to porewaters which is then available for reoxidation. Although this Mo-Mn phase likely contributes to the Mo_{ox1} profile, total Mn concentrations are an order of magnitude lower than Fe_{ox1} concentrations and Fe (oxyhydr)oxides are therefore likely to be the dominant Mo sequestration mechanism for Mo_{ox1}. Mo adsorption to either of these mineral phases is likely to have occurred in sediments rather than the water column, as Fe and Mn are vigorously recycled in the upper sediments (Thamdrup et al., 1994; Fossing et al., 2004) which would have released Mo to porewaters for readsorption to reoxidised Mn and Fe-oxides.

The dominant Mo phase identified in the sequential extraction is Mo_{ox2} (Figure 6.3) which extracts Mo strongly adsorbed or incorporated into crystalline Fe oxides. The overall proportion of Mo_{ox2} generally increases in the top 5 cm and then decreases below this depth and is the most dominant fraction to a depth of 7 cm (Figure 6.6). When Mo_{ox2} is normalised to Fe_{ox2}, ratios are not constant in the core as Mo_{ox2} concentrations increase relative to Fe_{ox2}

concentrations (Figure 6.7b). When comparing the Mo_{ox2} and Fe_{ox2} fractions (Figure 6.7e), the only observed correlation is from 7 cm to 12 cm and this evidence, combined with the Mo_{ox2}/Fe_{ox2} profile suggests that Fe_{ox2} concentrations do not generally exert a major influence on Mo adsorption to crystalline Fe-oxides in this setting. The Fe_{ox2} fraction is lower than Fe_{ox1} yet accounts for more Mo adsorption (indicated in the Mo sequential extraction data), potentially because of the capacity of Mo, on goethite in particular, to form inner and outer sphere complexes, which begins on outer absorption sites, followed by diffusion into pore spaces, leaving outer sites available for further adsorption (Lang et al., 2000; Lang and Kaupenjohann, 2003). Incorporation of Mo by the formation of inner-sphere complexes has also been observed in hematite (Das and Hendry, 2013; Das et al., 2016) and this may act to retain Mo and prevent release and subsequent readsorption to other mineral phases. The association of Mo with crystalline Fe-oxides has not previously been documented in anoxic, sulfidic sediments of this nature, with most work favouring Mo sequestration with pyrite or organic matter (Dahl et al., 2017; Hetzel et al., 2009; Tribovillard et al., 2004). This new data thus highlights the importance of Fe-oxides in Mo sequestration in such environments.

The Mo sequential extraction also shows that Mo is strongly adsorbed or incorporated into magnetite, although to a lesser extent than Mo_{WA}, Mo_{ox1} and Mo_{ox2}. When considered as a percentage of total Mo (Figure 6.6), Mo_{mag} gradually increases downcore, particularly below 12 cm which coincides with an increase in Fe_{mag} concentrations. The Mo_{mag} and Fe_{mag} profiles also become well correlated towards the base of the core from 12 cm (Figure 6.7f). Although Fe_{mag} is a relatively minor fraction of the total Fe pool, the data appear to suggest that Fe_{mag} concentrations are linked to Mo_{mag} concentrations below 12 cm with higher Fe_{mag} leading to higher Mo_{mag} concentrations, and this may reflect the increasing crystallinity of magnetite with depth. Magnetite has not been previously identified as a sequestration pathway for Mo, but research shows that Mo bonds with Fe(III) in magnetite and forms an inner-sphere complex

(Verbinnen et al., 2012) and these data highlight that it does play a minor role in Mo sequestration.

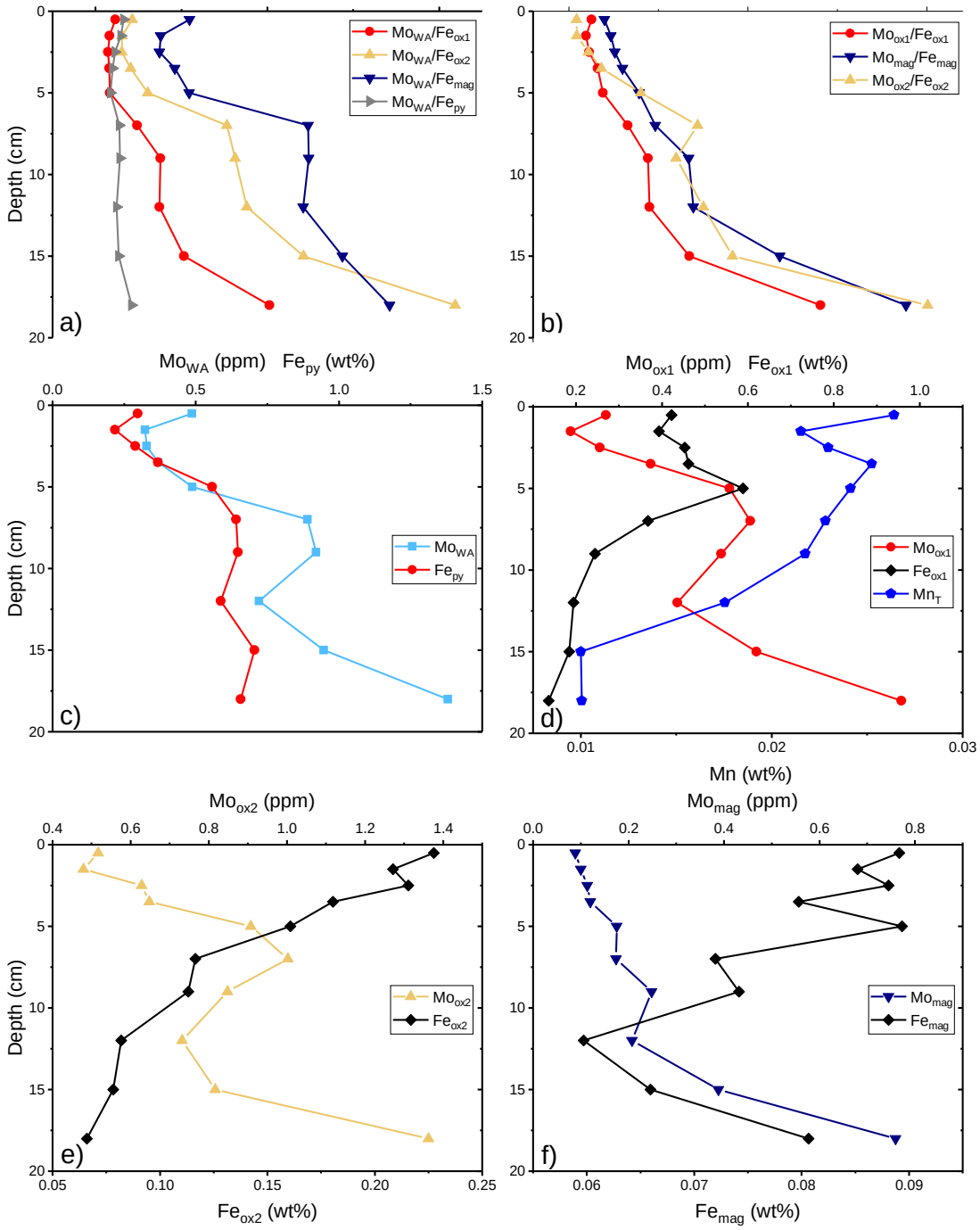

Figure 6.7 *a) and b) show Mo sequential extraction fractions normalised to the relevant Fe sequential extraction fractions; c) to f) show comparisons of Fe and Mo pools identified by sequential extraction.*

6.4.4 Molybdenum isotopes

Initial porewater δ^{98}Mo is 1.34‰, which is below the expected seawater δ^{98}Mo value of 2.3‰ (Siebert et al., 2003). A higher resolution study of Aarhus Bay sediments (Thamdrup et al., 1994) identified that Mn and Fe cycling is occurring from 0.5 and the data here support that. The first porewater sample is from 0.5 cm and it is likely that reductive dissolution of Mn and Fe at this depth released light δ^{98}Mo that was previously adsorbed to Mn and Fe-oxides in the water column, to porewaters, reducing the initial δ^{98}Mo value. From 0.5 cm, porewater δ^{98}Mo increases sharply as light δ^{98}Mo is readsorbed to minerals, removing it from the porewater pool and driving porewater δ^{98}Mo values higher. At 3.5 cm porewater δ^{98}Mo reaches seawater values (2.24‰) followed by a steep decrease which coincides with an increase in bulk sediment δ^{98}Mo which can be explained by the adsorption of heavy δ^{98}Mo to solid phases. A near constant fractionation of ~0.28 ‰ between bulk sediment δ^{98}Mo and porewater δ^{98}Mo ($\delta^{98}Mo_{sed}$ - $\delta^{98}Mo_{PW}$) is observed from 5 to 15 cm, suggesting that the adsorption of heavy δ^{98}Mo to solid phases is the result of equilibrium reactions in deeper sediments, rather than kinetic reactions that likely dominate in the upper sediments and which result in the adsorption of light δ^{98}Mo.

The reported bulk sediment δ^{98}Mo values range from 1.38 to 2.33‰, generally increasing downcore (Figure 6.3). While the Mo sequential extraction and XANES data suggest that Fe-oxides and pyrite are the dominant sequestration pathways in sediments below 5 cm, experimental work indicates that light δ^{98}Mo is preferentially adsorbed to these phases (Goldberg et al., 2009; Poulson Brucker et al., 2012). However, this may be a reflection of the kinetic reactions occurring in upper sediments that adsorb light δ^{98}Mo rather than the equilibrium reactions thought to be occurring in deeper sediments in this core, as the experimental work did not include observations of aged sediments. Mineral crystallinity, which increases with depth, may also affect the δ^{98}Mo signature in sediments as fractionation

between the original seawater δ^{98}Mo value and adsorbed δ^{98}Mo decreases with increasing crystallinity. This applies to Mo adsorbed to pyrite and other phases, predominantly the Fe_{ox2} phase identified in the sequential extraction.

It is interesting to note that the similarity between the δ^{98}Mo signature observed at depth in this core to seawater δ^{98}Mo, implies that, like sediments deposited under a euxinic water column, sulfidic continental margin sediments deposited beneath an oxic water column may ultimately record the isotopic composition of seawater. This highlights the major importance of utilising independent techniques to characterise the redox state of the water column and sediments when utilising Mo isotope systematics as a palaeoredox proxy (e.g., Chen et al., 2015; Dahl et al., 2010; Kendall et al., 2010).

6.5 Conclusions

A novel Mo sequential extraction method has been used in combination with XANES fingerprinting using a new library of Mo XANES standards for the first time alongside existing Fe speciation and Mo isotope methods to investigate and identify Mo sequestration pathways in marine sediments deposited beneath an oxic water column from a continental margin setting. The use of Fe sequential extraction together with Mo sequential extraction which target similar sedimentary pools facilitates a greater understanding of the Mo data through comparison with individual Fe pools. In combination these methods show that Fe oxides play a large role in sequestering Mo to sediments with sulfidic porewaters, particularly crystalline Fe oxides which are the dominant Mo fraction identified by sequential extraction in the upper sediments. However, pyrite is also responsible for Mo sequestration, potentially dominating in the lower sediments and data suggest that pyrite concentrations exert a control over Mo concentrations in this setting. The Mo sequential extraction also highlights magnetite as a minor sink for Mo which is currently unreported in terms of Mo sequestration pathways. The utilisation of Mo XANES alongside these methods also shows that MoO_4 has been transformed

to MoS_4 in relatively shallow sediments with porewater sulfide. The XANES further indicate that Mo is adsorbed to pyrite at a depth of 1.5 cm with a change in coordination chemistry to octahedral coordination.

Perhaps the most important finding highlighted by this work is that sediments deposited beneath an oxic water column can return seawater δ^{98}Mo values. Use of these data based on δ^{98}Mo values alone would usually lead to an interpretation of deposition beneath a euxinic water column. These new isotope data therefore highlight the importance of using multiple proxies for palaeoredox reconstruction of the water column and may require that some historic interpretations based on Mo isotopes alone are revisited.

6.6 References

Adelson, J. M., Helz, G. R., and Miller, C. V. 2001. Reconstructing the rise of recent coastal anoxia: molybdenum in Chesapeake Bay sediments. *Geochimica et Cosmochimica Acta.* **65** (2), pp. 237-252.

Ardakani, O. H., Chappaz, A., Sanei, H., and Mayer, B. 2016. Effect of thermal maturity on remobilization of molybdenum in black shales. *Earth and Planetary Science Letters*. **449**, pp. 311-320.

Bostick, B. C., Fendorf, S., and Helz, G. R. 2003. Differential Adsorption of Molybdate and Tetrathiomolybdate on Pyrite (FeS_2). *Environmental Science & Technology*. **37**, pp. 285-291.

Burdige, D. J. 1993. The biogeochemistry of manganese and iron reduction in marine sediments. *Earth-Science Reviews*. **35,** pp. 249-284.

Chen, X., Ling, H., Vance, D., Shields-Zhou, G. A., Zhu, M., Poulton, S. W., Och, L. M., Jiang, S., Li, D., Cremonese, L., and Archer, C. 2015. Rise to modern levels of ocean oxygenation coincided with the Cambrian radiation of animals. *Nature Communications.* **6** (7142), pp. 1-7.

Collier, R. W. 1985. Molybdenum in the Northeast Pacific Ocean. *Limnology and Oceanography.* **30** [6], pp. 1351-1354.

Dahl, T. W., Anbar, A. D., Gordon, G. W., Rosing, M. T., Frei, R., and Canfield, D. E. 2010. The behaviour of molybdenum and its isotopes across the chemocline in the sediments of Lake Cadagno, Switzerland. *Geochimica et Cosmochimica Acta.* **74**, pp. 144-163.

Dahl, T. W., Chappaz, A., Hoek, J., McKenzie, C. J., Svane, S., and Canfield, D. E. 2017. Evidence of molybdenum association with particulate organic matter under sulfidic conditions. *Geobiology*. **15** (2), pp. 311-323.

Das, S., and Hendry, M. J. 2013. Adsorption of molybdate by synthetic hematite under alkaline conditions: Effects of aging.

Das, S., Essilfie-Dughan, J., and Jim Hendry, M. 2016. Sequestration of molybdate during transformation of 2-line ferrihydrite under alkaline conditions. *Applied Geochemistry*. **73**, pp. 70-80.

Erickson, B. E., and Helz, G. R. 2000. Molybdenum (VI) speciation in sulfidic waters: Stability and lability thiomolybdates. *Geochimica et Cosmochimica Acta*. **64** (7), pp. 1149-1158.

Fossing, H., Berg, P., Thamdrup, B., Rysgaard, S., Sørensen, H. M., Nielsen, K. 2004. A model set-up for an oxygen and nutrient flux model for Aarhus Bay (Denmark). *National Environmental Research Institute Technical Report.* **483**, pp. 1-68.

Goldberg, T., Archer, C., Vance, D., Thamdrup, B., McAnena, A., and Poulton, S. W. 2009. Mo isotope fractionation during adsorption to Fe (oxyhydr)oxides. *Geochimica et Cosmochimica Acta.* **73**, pp. 6502-6516.

Goldberg, T., Archer, C., Vance, D., Thamdrup, B., McAnena, A., and Poulton, S. W. 2012. Controls on the Mo fractionations in a Mn-rich anoxic marine sediment, Gulmar Fjord, Sweden. *Chemical Geology*. **296**, pp. 73-82.

Goldberg, T. 2019. *Email to Jennifer Rodley 30 May.*

Hetzel, A. Böttcher, M. E., Wortmann, U. G., and Brumsack, H. 2009. Paleo-redox conditions during OAE 2 reflected in Demerara Rise sediment geochemistry (ODP Leg 207). *Palaeogeography, Palaeoclimatology, Palaeoecology.* **273**, pp. 302-328.

Kendall, B., Reinhard, C. T., Lyons, T. W., Kaufman, A. J., Poulton, S. W., and Anbar, A. D. 2010. Pervasive oxygenation along late Archean ocean margins. *Nature Geoscience*. **3**, pp. 647-652.

Lang, F., Pohlmeier, A., and Kaupenjohann, M. 2000. Mechanism of molybdenum sorption to iron oxides using pressure-jump relaxation. *Plant Nutrient & Soil Science.* **163**, pp. 571-575.

Lang, F., and Kaupenjohann, M. 2003. Immobilisation of molybdate by iron oxides: effects of organic coatings. *Geoderma*. **113**, pp. 31-46.

März, C., Beckmann, B., Franke, C., Vogt, C., Wagner, T., and Kasten, S. 2009. Geochemical environment of the Coniacian-Santonian western tropical Atlantic at Demerara Rise. *Palaeogeography, Palaeoclimatology, Palaeoecology.* **273**, pp. 286-301.

Poulson, R. L., Siebert, C., McManus, J., and Berelson, W. M. 2006. Authigenic molybdenum isotope signatures in marine sediments. *Geology*. **34** (8), pp. 617-620.

Poulson Brucker, R. L., McManus, J., Severmann, S., and Berelson, W. M. 2009. Molybdenum behaviour during early diagenesis: Insights from Mo isotopes. *Geochemistry Geophysics Geosystems.* **10** (6), pp. 1-25.

Poulson Brucker, R. L., McManus, J., and Poulton, S. W. 2012. Molybdenum isotope fractionation observed under anoxic experimental conditions. *Geochemical Journal*. **46**, pp. 201-209.

Ramussen, H. and Jørgensen, B. B. 1992. Microelectrode studies of a seasonal oxygen uptake in a coastal sediment: role of molecular diffusion. *Marine Ecology Progress Series.* **81**, pp. 289-303.

Scholz, F., McManus, J., and Sommer, S. 2013. The manganese and iron shuttle in a modern euxinic basin and implications for molybdenum cycling at euxinic ocean margins. *Chemical Geology.* **355**, pp. 56-68.

Shimmield, G. B., and Price, N. B. 1986. The behaviour of molybdenum and manganese during early sediment diagenesis – offshore Baja California, Mexico. *Marine Chemistry*. **19**, pp. 261-280.

Siebert, C., Nägler, T. F., von Blanckenburg, F., and Kramers, J. D. 2003. Molybdenum isotope records as a potential new proxy for paleoceanography. *Earth and Planetary Science Letters*. **211**, pp. 159-171.

Siebert, C., McManus, J., Bice, A., Poulson, R., and Berelson, W. M. 2006. Molybdenum isotope signatures in continental margin marine sediments. *Earth and Planetary Science Letters.* **241**, pp. 723-733.

Thamdrup, B., Fossing, H., and Jørgensen, B. B. 1994. Manganese, iron and sulfur cycling in coastal marine sediment, Aarhus Bay, Denmark. *Geochimica et Cosmochimica Acta.* **58** (23), pp. 5515-5129.

Tribovillard, N., Riboulleau, A., Lyons, T., and Baudin, F. 2004. Enhanced trapping of molybdenum by sulfurized organic matter of marine origin in Mesozoic limestones and shales. *Chemical Geology*. **213**, pp. 385-401.

Verbinnen, B., Block, C., Hannes, D., Lievens, P., Vaclavikova, M., Stefusova, K., Gallios, G., and Vandecasteele, C. 2012. Removal of Molybdate Anions from Water by Adsorption on Zeolite-Supported Magnetite. *Water Environment Research.* **84** (9), pp. 753-760.

Viollier, E., et al., 2000. The ferrozine method revisited: Fe(II)/Fe(III) determination in natural waters. *Applied Geochemistry.* **15**, pp. 785-790.

Wagner, M., Chappaz, A., and Lyons, T. W. 2017. Molybdenum speciation and burial pathway in weakly sulfidic environments: Insights from XAFS. *Geochimica et Cosmochimica Acta*. **206**, pp. 18-20.

Chapter 7 Conclusions

This chapter provides an overview of the findings presented in this thesis and how they impact on our current understanding of Mo behaviour in sedimentary environments and its use as a palaeoredox proxy. The development of new methods provides opportunities for future research which are also explored here.

7.1 Development of a Mo sequential extraction method

A novel Mo sequential extraction technique has been developed that can provide details of Mo partitioning within sediments for modern and ancient sediments (Chapter 3). Eight Mo pools were identified which can be measured in terms of Mo concentrations to very low levels (0.09 ppm ±0.01). In addition to the redox environments used in the method development, the sequential extraction was used for a full core of sediments deposited beneath an oxic water column (Chapter 6), in combination with Mo XANES, Mo isotopes and Fe sequential extraction, to identify the Mo sequestration pathways in this setting. For the first time Mo is shown to be associated with magnetite across all environments studied, which to date has been under-represented as a Mo sequestration pathway in sediments in the literature. The sequential extraction data in Chapters 3 and 6 also illustrate the importance of Fe (hydr)oxides in sequestering Mo to sediments across redox environments, including in sediments deposited beneath euxinic water columns. This is generally an overlooked long-term sequestration mechanism for Mo in euxinic environments which warrants further research.

The development of the method indicated that a significant portion of Mo is loosely adsorbed to minerals in sediments and therefore easily removed in any initial sequential extraction step. This highlights the importance of the initial Mo_{WA} and Mo_{SA} extractions which are essential to avoid misinterpretation of early extractions which could potentially include Mo from other pools. The

data also indicate that wash steps are required between sequential extraction steps to capture any Mo that is readsorbed following an extraction. This again highlights the importance of these steps between extractions to avoid misinterpretation of later Mo pools.

This new method provides a research tool that can be used to explore Mo sequestration pathways in a range of environments where before, outside of Mo XANES and EXAFS, only Mo concentrations or isotope methods have generally been utilised. The sequential extraction can be applied to modern and ancient sediments, which ultimately provides the means to develop a model of Mo behaviour in known geochemical settings to use as a proxy for ancient settings.

7.2 The development of XANES as a tool to identify Mo sequestration pathways

Although XANES have been used to explore Mo behaviour in sediments and soils, this is the first XANES library that includes a comprehensive collection of potential Mo pools in marine sediments with clear and specific methods for matching sample XANES to standards to identify Mo phase associations (Chapter 4). The library also provides the means to indicate whether Mo has been reduced and identify Mo coordination.

Mo XANES were collected from sediments deposited beneath oxic and euxinic water columns and, for the first time, from sediments under nitrogenous and ferruginous water columns (Chapter 5). Using the library of standards, these XANES show that Mo is not limited to a single sequestration pathway in most of these environments and multiple Mo phase associations were identified in all four of the redox settings studied (oxic, nitrogenous, ferruginous and euxinic). The XANES from sediments deposited beneath an oxic water column indicate that Mo has been transformed from MoO_4 in the water column to MoO_xS_{4-x} and MoS_4 in the sulfidic porewaters, demonstrating that a euxinic water column is not a requirement for the thiolation of MoO_4. Mo sequestered under an

oxic water column was also shown to be adsorbed to pyrite, although it is likely it was initially delivered to sediments adsorbed to Mn and Fe oxides (Scholz et al., 2013; Scholz et al., 2017; Shimmield and Price, 1986). This suggests that upon reductive dissolution of these minerals in anoxic porewaters, Mo is subsequently sequestered by pyrite, potentially in its thiolated form. Pyrite was also indicated as a host mineral for Mo sequestration in XANES for sediments deposited beneath a nitrogenous water column, which is in agreement with work by Scholz et al. (2017) who suggest that Mo is delivered to sediments by Fe (oxyhydr)oxides in the same way as suggested for the oxic setting and then retained by Fe sulfide minerals. However, the XANES presented here also indicate that Mo is retained in these sediments adsorbed to magnetite, which has not been significantly explored as a sequestration mechanism for Mo, other than experimental work into isotopic fractionations (Goldberg et al., 2009). XANES collected for sediments deposited beneath a ferruginous water column indicate that Mo has been fully transformed to MoS_4 adsorbed to magnetite and complexed with organic matter. These data again demonstrate the potential importance of magnetite as a host for Mo in these environments, which are under-explored in terms of Mo cycling and deposition. The XANES for sediments deposited beneath a euxinic water column are in line with existing research, indicating that Mo is associated with organic matter and pyrite which are well-explored sequestration pathways (e.g. Chappaz et al., 2014; Dahl et al., 2010, Wagner et al., 2017). It is interesting that Mo is observed in various states of thiolation from MoO_4 to MoS_4, which demonstrates that not all Mo is fully or partially thiolated in the euxinic water column. Overall the library of standards provides a means to identify sequestration pathways for Mo across a range of environments at bulk sediment concentrations down to 1.5 ppm.

7.3 Combining techniques to expand the use of Mo as a palaeoredox proxy

In Chapter 6 the sequential extraction method and techniques outlined for use of the library of standards were combined with Mo isotope and Fe sequential extraction data to explore Mo sequestration in a sediment core deposited beneath an oxic water column in Aarhus Bay, Denmark.

The combined methods indicate that, in addition to Fe (hydr)oxides, Mo is sequestered with pyrite, an observation which is supported by XANES collected from sediments deposited beneath an oxic water column in the Eastern Mediterranean in Chapter 4. In combination with Fe sequential extraction data, the Mo sequential extraction data suggest that Fe (hydr)oxides are an important sequestration pathway for Mo in Aarhus Bay but also show that magnetite is one of these pathways, again highlighting this phase association for Mo. An important result from this research is that Mo isotope values increase downcore, eventually reaching seawater values. Alone, these data would suggest deposition beneath a euxinic water column, and this finding therefore emphasises the importance of using multiple redox proxies to characterise environments to prevent misinterpretation.

7.4 Future work

To develop a greater understanding of Mo sequestration pathways in different redox environments, it would be useful to collect data from a range of these settings using the new Mo sequential extraction method, to develop a model of Mo-mineral phase associations and associated concentrations that could be used as a palaeoredox tool.

Similarly, the development of the Mo XANES library of standards facilitates further research into Mo phase associations in different redox environments. Further research to collect Mo XANES from oxic, nitrogenous and ferruginous environments would be beneficial, again to contribute to the development of a model that could be used as a palaeoredox tool. It would also improve the current understanding of Mo behaviour in different redox environments if XANES were collected on water column samples to ascertain how Mo is delivered to sediments, particularly outside of the Mn-Fe shuttle. XANES collected for sediments deposited beneath a euxinic water column indicate that Mo is not always fully thiolated and water column XANES from this environment may help to understand whether this is a result of Mo-mineral phase associations. It may also be beneficial to explore the

possibility of adding standards to the library for the Mo-polysulfide species described by Vorlicek et al., (2004) and the Mo-Fe-S colloid described by Vorlicek et al. (2018).

The research presented here highlights magnetite as a Mo sequestration pathway. This has been studied very little and further investigation into the association of Mo with magnetite would be beneficial, including but not limited to, pH sorption experiments.

7.5 References

Chappaz, A., Lyons, T. W., Gregory, D. D., Reinhard, C. T., Gill, B. C., Li, C., and Large, R. R. 2014. Does pyrite act as an important host for molybdenum in modern and ancient euxinic sediments? *Geochimica et Cosmochimica Acta*. **126**, pp. 112-122.

Dahl, T. W., Anbar, A. D., Gordon, G. W., Rosing, M. T., Frei, R., and Canfield, D. E. 2010. The behaviour of molybdenum and its isotopes across the chemocline in the sediments of Lake Cadagno, Switzerland. *Geochimica et Cosmochimica Acta.* **74**, pp. 144-163.

Goldberg, T., Archer, C., Vance, D., Thamdrup, B., McAnena, A., and Poulton, S. W. 2009. Mo isotope fractionation during adsorption to Fe (oxyhydr)oxides. *Geochimica et Cosmochimica Acta.* **73**, pp. 6502-6516.

Scholz, F., McManus, J., and Sommer, S. 2013. The manganese and iron shuttle in a modern euxinic basin and implications for molybdenum cycling at euxinic ocean margins. *Chemical Geology.* **355**, pp. 56-68.

Scholz, F., Siebert, C., Dale, A. W., and Frank, M. 2017. Intense molybdenum accumulation in sediments underneath a nitrogenous water column and implications for the reconstruction of paleo-redox conditions based on molybdenum isotopes. *Geochimica et Cosmochimica Acta*. **213**, pp. 400-417.

Shimmield, G. B., and Price, N. B. 1986. The behaviour of molybdenum and manganese during early sediment diagenesis – offshore Baja California, Mexico. *Marine Chemistry*. **19**, pp. 261-280.

Vorlicek, T. P., Kahn, M. D., Kasuya, Y., and Helz, G. R. 2004. Capture of molybdenum in pyrite-forming sediments: Role of ligand-induced reduction by polysulfides. *Geochimica et Cosmochimica Acta*. **68** (3), pp. 547-556.

Vorlicek, T. P., Helz, G. R., Chappaz, A., Vue, P., Vezina, A., and Hunter, W. 2018. Molybdenum Burial Mechanism in Sulfidic Sediments: Iron-Sulfide Pathway. *ACS Earth and Space Chemistry.* **2** (6), pp. 565-576.

Wagner, M., Chappaz, A., and Lyons, T. W. 2017. Molybdenum speciation and burial pathway in weakly sulfidic environments: Insights from XAFS. *Geochimica et Cosmochimica Acta*. **206**, pp. 18-20.

Appendix A – Repeatability (%RSD) for each step of the Mo sequential extraction method

Table A.1 *Reproducibility for each step of the Mo sequential extraction method.*

Mo_{WA}					
Sample	**Mo (ppm)**	**±**	**%RSD**	***n***	**Stdev**
DR-1261-4-5	31.39	1.33	4.03	6	1.27
DR-1261-18-19	20.44	0.33	1.55	6	0.32
DR-1258-1	25.59	0.64	2.38	6	0.61
DR-1258-4	51.19	1.90	3.54	6	1.81
USGS-GRS	11.24	0.69	5.85	6	0.66
AB-1B-3	0.33	0.03	7.99	5	0.03
LC-1A-5	7.98	0.42	5.01	6	0.40
LC-1A-6	47.95	3.00	5.96	6	2.86
		Average RSD	**4.54**		

Mo_{SA}					
Sample	**Mo (ppm)**	**±**	**%RSD**	***n***	**Stdev**
DR-1261-4-5	4.02	0.20	4.63	6	0.19
DR-1261-18-19	2.49	0.06	2.12	6	0.05
DR-1258-1	4.03	0.15	3.53	6	0.14
DR-1258-4	6.66	0.54	7.71	6	0.51
USGS-GRS	1.57	0.10	5.03	5	0.08
AB-1B-3	0.00	0.00	n/a	6	n/a
LC-1A-5	8.49	0.42	4.68	6	0.40
LC-1A-6	6.22	0.52	7.99	6	0.50
		Average RSD	**5.10**		

Mo_{ox1}					
Sample	**Mo (ppm)**	**±**	**%RSD**	***n***	**Stdev**
DR-1261-4-5	22.26	0.41	1.78	6	0.40
DR-1261-18-19	19.42	0.77	3.76	6	0.73
DR-1258-1	4.90	0.10	2.00	6	0.10
DR-1258-4	11.47	0.53	4.42	6	0.51
USGS-GRS	4.66	0.10	1.98	6	0.09
AB-1B-3	0.26	0.01	2.56	6	0.01
LC-1A-5	25.04	1.81	6.89	6	1.73
LC-1A-6	11.19	0.39	3.30	6	0.37
		Average RSD	**3.33**		

Mo_{ox2}					
Sample	**Mo (ppm)**	**±**	**%RSD**	***n***	**Stdev**
DR-1261-4-5	5.96	0.21	3.33	6	0.20
DR-1261-18-19	4.52	0.04	0.59	4	0.03
DR-1258-1	2.23	0.17	4.67	4	0.10
DR-1258-4	7.33	0.88	7.57	4	0.55
USGS-GRS	0.88	0.08	7.34	5	0.06
AB-1B-3	0.63	0.03	3.44	5	0.02
LC-1A-5	25.54	1.11	3.49	5	0.89
LC-1A-6	15.30	1.05	4.30	4	0.66
		Average RSD	**4.34**		

Mo_{mag}					
Sample	**Mo (ppm)**	**±**	**%RSD**	***n***	**Stdev**
DR-1261-4-5	3.95	0.12	2.77	6	0.11
DR-1261-18-19	2.84	0.05	1.52	6	0.04
DR-1258-1	2.45	0.06	2.18	6	0.04
DR-1258-4	5.93	0.25	3.96	6	0.23
USGS-GRS	1.42	0.08	4.54	5	0.06
AB-1B-3	0.12	0.01	2.72	4	0.00
LC-1A-5	7.71	0.35	3.67	5	0.28
LC-1A-6	6.84	0.23	2.14	4	0.15
		Average RSD	**2.94**		

Mo_{sil}					
Sample	**Mo (ppm)**	**±**	**%RSD**	***n***	**Stdev**
DR-1261-4-5	10.52	0.46	4.17	6	0.44
DR-1261-18-19	8.37	0.27	2.58	5	0.22
DR-1258-1	5.93	0.23	3.69	6	0.22
DR-1258-4	8.85	0.38	4.09	6	0.36
USGS-GRS	2.54	0.40	6.31	3	0.16
AB-1B-3	0.22	0.01	4.47	6	0.01
LC-1A-5	9.63	0.52	4.31	5	5.00
LC-1A-6	10.68	0.65	4.89	5	0.52
		Average RSD	**4.31**		

Mo_{org}					
Sample	**Mo (ppm)**	**±**	**%RSD**	***n***	**Stdev**
DR-1261-4-5	14.92	0.93	5.01	5	0.75
DR-1261-18-19	9.49	0.36	3.65	6	0.35
DR-1258-1	7.48	0.23	2.87	6	0.21
DR-1258-4	7.32	0.66	5.66	4	0.41
USGS-GRS	7.94	1.16	5.89	3	0.47
AB-1B-3	0.00	0.00	n/a	6	0.00
LC-1A-5	2.46	0.21	6.93	5	0.17
LC-1A-6	2.65	0.08	2.90	6	0.08
		Average RSD	**4.70**		

Mo_{py}					
Sample	**Mo (ppm)**	**±**	**%RSD**	***n***	**Stdev**
DR-1261-4-5	15.77	1.12	6.79	6	1.07
DR-1261-18-19	11.24	0.55	4.63	6	0.52
DR-1258-1	11.19	0.98	5.48	4	0.61
DR-1258-4	15.13	0.86	5.44	6	0.82
USGS-GRS	2.85	0.39	8.65	4	0.25
AB-1B-3	0.00	0.00	n/a	6	0.00
LC-1A-5	0.00	0.00	n/a	2	0.00
LC-1A-6	2.04	0.17	6.64	5	0.14
		Average RSD	**6.27**		

Appendix B – X-ray diffraction patterns

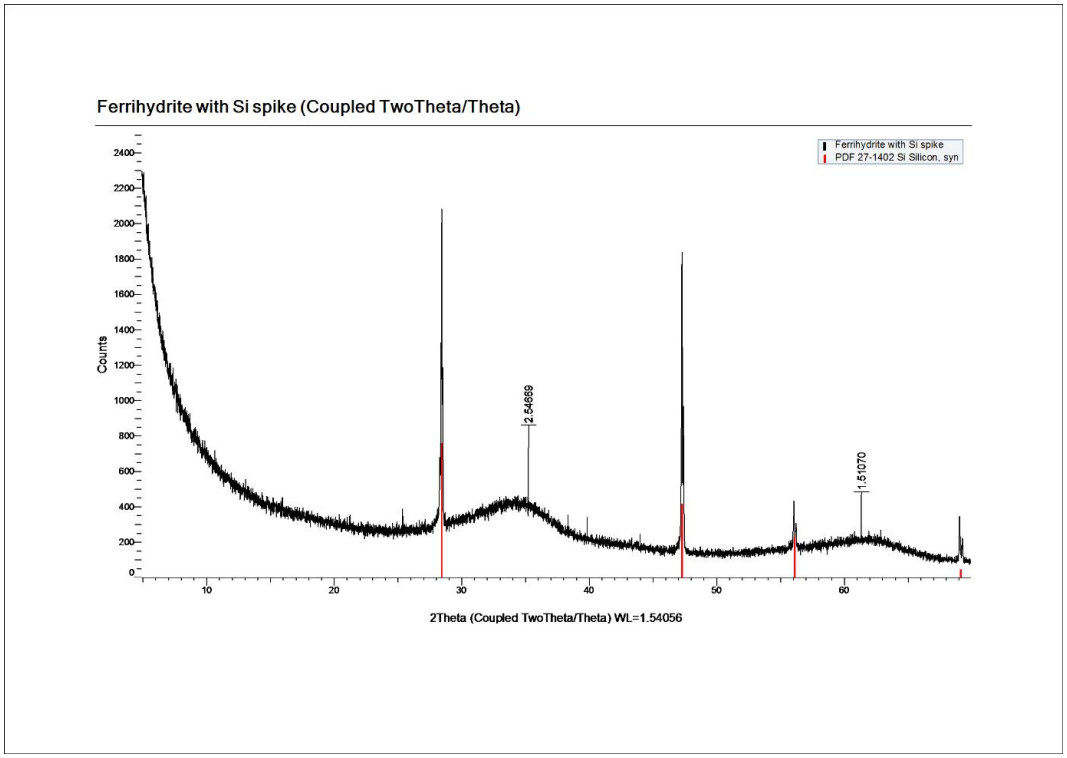

Figure B.1 *XRD Scan for synthetic ferrihydrite.*

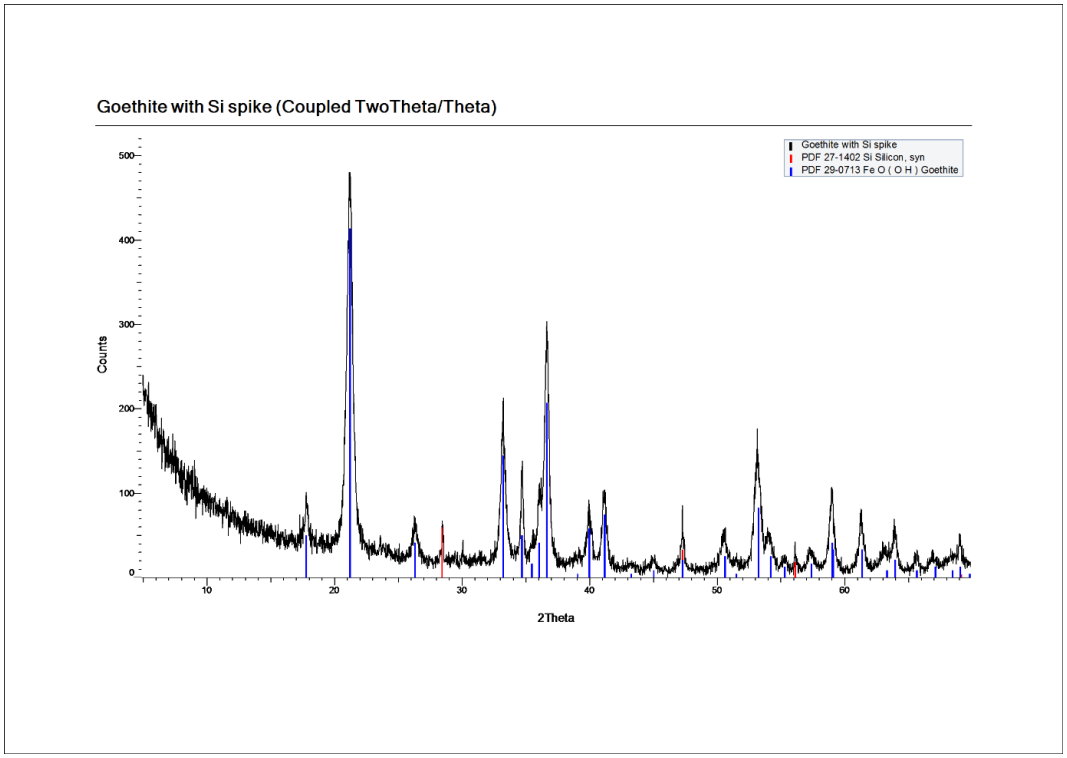

Figure B.2 *XRD scan for synthetic goethite.*

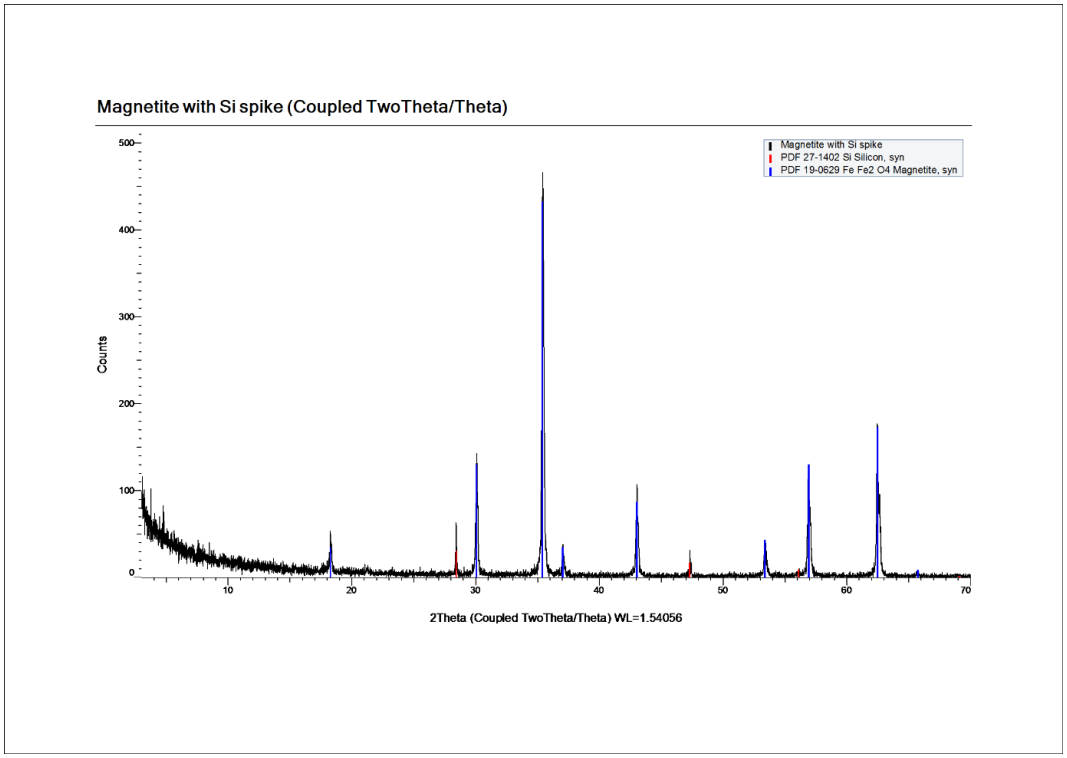

Figure B.3 *XRD scan for synthetic magnetite.*

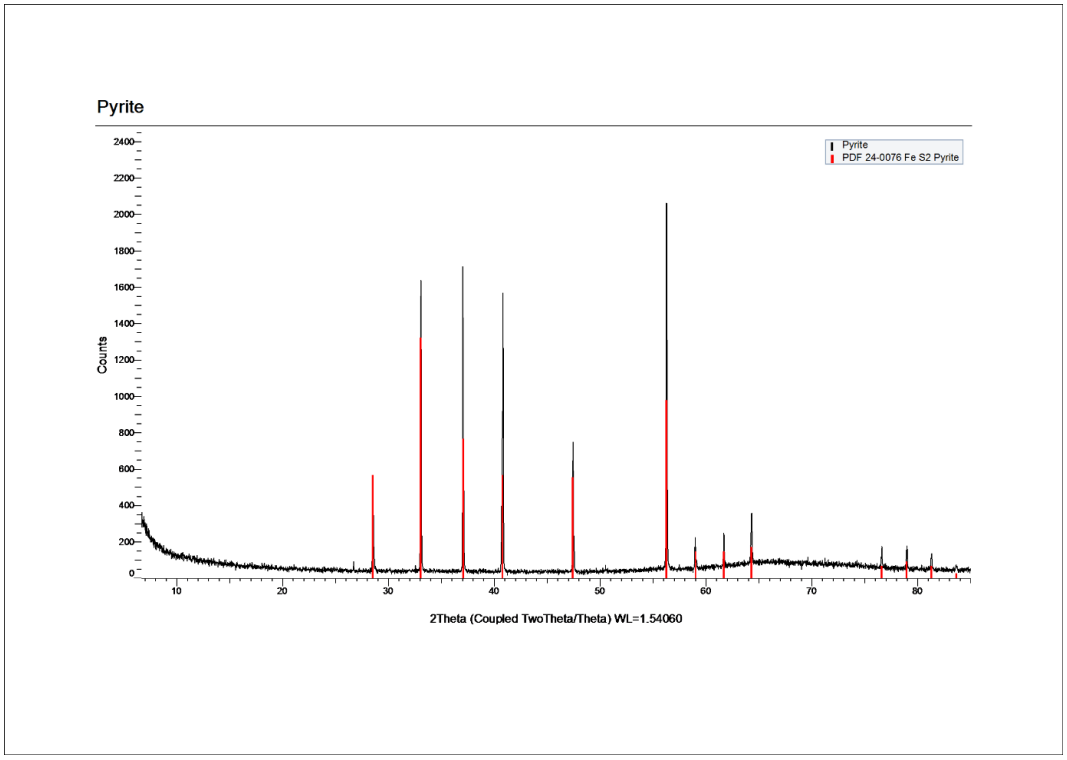

Figure B.4 *XRD scan for synthetic pyrite.*

Appendix C – XANES Library of standards spectral values

Table C.1 *Spectral values for the XANES library of standards.*

TD	E_M (eV)	E0 (eV)	E_S (eV)	E_A (eV)	E_B (eV)	E_C (eV)	E_D (eV)	Pre-edge hump	Flattened edge	Edge shoulder
$Mo(VI)O_4$(aq) reference	20043.0	20017.0	-	20005.5	20010.0	20083.0	20129.0	-	yes	-
$Mo(VI)O_xS_{4-x}$(aq) reference	20040.0	20009.3	7.7	-	-	20063.0	20099.0	yes	yes	-
$Mo(VI)S_4$(aq) reference	20045.0	20010.6	6.4	-	-	20069.0	20105.0	yes	yes	-
$Mo(IV)S_3$(s) reference	20031.0	20006.6	10.4	-	-	20057.0	20081.0	-	-	-
MnO_2-MoO_4(ads)	20038.0	20015.5	1.5	20006.0	20009.0	20087.0	20119.0	-	-	yes
MnO_2-MoS_4(ads)	20041.0	20017.2	-0.2	20005.0	20009.0	20079.0	20127.0	-	yes	yes
Fh-MoO_4(ads)	20040.0	20016.4	0.6	20005.5	20009.5	20081.0	20133.0	-	yes	-
Fh-MoS_4(ads)	20034.0	20015.6	1.4	-	-	20061.0	20081.0	yes	yes	-
Gt-MoO_4(ads)	20040.0	20016.4	0.6	20005.5	20009.5	20077.0	20133.0	-	yes	-
Gt-MoO_4(inc)	20044.0	20017.0	0.0	20005.5	20010.0	20073.0	20129.0	-	yes	-
Gt-MoS_4(ads)	20035.0	20015.5	1.5	20005.5	20008.0	20071.0	20137.0	-	yes	-
Mag-MoO_4(ads)	20039.0	20015.9	1.1	20006.0	20009.0	20079.0	20133.0	-	yes	yes
Mag-MoO_4(inc)	20044.0	20017.5	-0.5	20006.0	20010.5	20079.0	20131.0	-	yes	-
Mag-MoS_4(ads)	20033.0	20007.3	9.7	-	-	20060.0	20079.0	-	yes	-
Ac-MoO_4(aq)	20038.0	20015.6	1.4	20007.0	20009.5	20075.0	20125.0	-	yes	-
Ac-MoS_4(aq)	20033.0	20008.0	9.0	-	-	20057.0	20081.0	-	yes	-
Ph-MoO_4(aq)	20033.0	20014.2	2.8	20005.5	20007.5	20047.0	20054.0	-	yes	yes
Ph-MoS_4(aq)	20032.0	20007.5	9.5	-	-	20056.0	20079.0	-	yes	-
Tan-MoO_4(aq)	20033.0	20012.0	5.0	20005.0	20007.0	20071.0	20087.0	-	-	yes
Tan-MoS_4(aq)	20032.0	20007.0	10.0	-	-	20057.0	20081.0	-	-	-
Py-MoO_4(ads)	20039.0	20016.8	0.2	20006.0	20010.0	20077.0	20135.0	-	-	-
Py-MoO_xS_{4-x}(ads)	20033.0	20014.4	2.6	-	-	20065.0	20083.0	yes	-	-
Py-MoS_4(ads)	20032.0	20007.2	9.8	-	-	20059.0	20079.0	-	yes	-